Ordering phenomena in nickelate heterostructures studied by elastic and inelastic photon scattering

Von der Fakultät Mathematik und Physik der Universität Stuttgart
zur Erlangung der Würde eines Doktors der Naturwissenschaften
(Dr. rer. nat.) genehmigte Abhandlung

Vorgelegt von

Matthias Hepting

aus Donaueschingen (Deutschland)

Hauptberichter:	Prof. Dr. B. Keimer
Mitberichter:	Prof. Dr. T. Pfau
	Prof. Dr. G. A. Sawatzky
Prüfungsvorsitzender:	Prof. Dr. H. P. Büchler

Tag der Einreichung:	28.10.2016
Tag der mündlichen Prüfung:	29.11.2016

Universität Stuttgart
Max-Planck-Institut für Festkörperforschung
Stuttgart 2016

Contents

Abbreviations

TM	transition metal
TMO	transition metal oxide
ZSA	Zaanen, Sawatzky, Allen
PLD	pulsed laser deposition
MBE	molecular beam epitaxy
REXS	resonant elastic x–ray scattering
MIT	metal-insulator transition
SB	short bonds
LB	long bonds
XAS	x-ray absorption spectrum
LNO	$LaNiO_3$
PNO	$PrNiO_3$
NNO	$NdNiO_3$
SNO	$SmNiO_3$
DSO	$DyScO_3$
LSAT	$[LaAlO_3]_{0.3}[Sr_2AlTaO_6]_{0.7}$
LSAO	$LaSrAlO_4$
IR	infrared
XRD	x-ray diffraction
FY	fluorescence yield
TEY	total electron yield
NA	numerical aperture
SERS	surface enhanced Raman spectroscopy
TERS	tip enhanced Raman spectroscopy
u.c.	unit cells
PEEM	photoemission electron microscopy
PAO	$PrAlO_3$
MPI–FKF	Max Planck Institut für Festkörperforschung
STEM	scanning transmission electron microscopy
HAADF	high angle annular dark field
LAADF	low angle annular dark field
EELS	electron energy loss spectroscopy
ABF	annular bright field
RIXS	resonant inelastic x–ray scattering

Abstract

Ordering phenomena in nickelate heterostructures
studied by elastic and inelastic photon scattering

Heterostructures composed of transition metal oxides such as rare-earth nickelates have recently attracted widespread interest. Their targeted synthesis provides unique opportunities of controlling and manipulating the charge, spin, orbital, and lattice degrees of freedom in the components such that novel phenomena can emerge which are not present in the constituent materials alone [1]. Furthermore, model systems can be created where the systematic tuning of specific interaction parameters leads to specific responses which give new insights about intrinsic phenomena observed in the bulk of the materials.

The present doctoral thesis describes an experimental study of ordering phenomena in rare-earth nickelate based heterostructures by means of inelastic Raman light scattering and elastic resonant x-ray scattering. The two key results of the thesis are: (a) The demonstration of full control over the charge/bond and spin order parameters in specifically designed $PrNiO_3$ heterostructures and evidence of a novel spin density wave phase induced through spatial confinement of the conduction electrons. (b) The thickness-induced crossover between collinear and non-collinear spin structures in $NdNiO_3$ slabs designed as an elementary magnetic model system. In addition, the amplitude ratio of magnetic moments in neighboring NiO_6 octahedra can be controlled experimentally through the crystallographic symmetry of confining layers.

(a) Recently it has been demonstrated by electrical transport measurements that the metal-insulator transition in nickelates can be controlled by epitaxial strain imposed through a substrate [2,3]. Further, it was shown that also the magnetic order is affected by the parameters strain and spatial confinement when the effective nickelate layer thickness approaches the thin or ultra-thin regime [4]. However, experimental evidence of the structural symmetry breaking concurrent with the metal-insulator transition remained elusive in thin heterostructures, since the application of conventional diffraction techniques such as neutron or x-ray scattering is difficult when the effective scattering volume is small and/or only few Bragg reflexes are accessible.

The present work employs polarized Raman scattering on thin nickelate heterostructures to detect faint changes in the crystal symmetry coinciding with electronic and magnetic phase transition. To this end, a special measurement technique was developed combining the narrow depth-of-field of confocal Raman spectroscopy with vertical scans (z-scans) of the sample. The technique strongly reduces the substrate contribution to the Raman spectrum and the measurement of phonon spectra of nickelate layers with thicknesses of only a few nanometers became feasible. Moreover, laser wavelengths located in the optical range can be used what makes confocal Raman z-scans a powerful and versatile alternative to ultraviolet Raman spectroscopy [5].

The most relevant measurements of part (a) of the thesis were conducted on a series of $PrNiO_3$ heterostructures. $PrNiO_3$ exhibits coinciding structural, electronic, and magnetic transitions in the bulk while in the phase diagram it is located in proximity to the paramagnetic metallic $LaNiO_3$. This position makes $PrNiO_3$ prone to changes of its electronic and magnetic ground state. To this effect we have grown $PrNiO_3$ films on substrates inducing compressive and tensile biaxial strain along the in-plane directions. As next step the $PrNiO_3$ was sandwiched in between layers of the band-insulator $PrAlO_3$ to impose spatial confinement to the conduction electrons. The confocal Raman measurements were complemented by electrical transport measurements and magnetic resonant elastic x-ray scattering (REXS) probing the occurrence of the magnetic order parameter.

In nickelate films and superlattices under tensile strain which undergo a metal-insulator transition upon cooling, the Raman spectra reveal phonon modes characteristic of charge/bond ordering. These anomalous phonons do not appear in compressively strained films which remain metallic at all temperatures. Hence, the behavior of the tensile strained films and superlattices is similar to bulk $PrNiO_3$ whereas the compressively strained film resembles bulk $LaNiO_3$. For superlattices under compressive strain, the Raman spectra show no evidence of anomalous phonons indicative of charge/bond ordering and the increase in resistivity is only marginally upon cooling, while REXS data reveal antiferromagnetic order.

Conclusively, three different states are identified, only two of which were observed before in bulk nickelates: first an insulating state with robust charge/bond and spin order and second a metallic state with neither form of order. The superlattices under compressive strain, however, show evidence of spin order evolving without concurrent charge/bond order which corresponds to a novel state without bulk analog. A similar metallic spin density wave phase driven by spatial confinement of the conduction electrons and with charge/bond order as secondary order parameter has been predicted by theory calculations [6].

Spin density waves have been directly observed and characterized only in few bulk metals, including elemental chromium and its alloys, organic charge-transfer salts, and recently the iron pnictides [7]. The separate control of magnetic and charge order opens up new opportunities for device applications, including designs in which metallic antiferromagnets serve as active elements. In addition, the determination of the energies and symmetries of the vibrational modes characteristic of charge ordering, as well as their dependence on strain and spatial confinement, provides specific input for models of charge ordering and electron-phonon interactions in the nickelates and related transition metal oxides

(b) Experiments on nickelate heterostructures have stimulated theoretical research addressing the mechanisms driving the metal-insulator transition. The nature of the antiferromagnetic ground state, however, remains unresolved. Whereas it is consensus that the magnetic order is characterized by the wave vector

$\mathbf{q}_0 = (1/4,\ 1/4,\ 1/4)$ in pseudocubic notation, neutron diffraction experiments were not able distinguish between collinear (↑↑↓↓) and non-collinear (↑→↓←) spin arrangements [8]. As a consequence, theoretical descriptions vary from localized spin models [9] with antisymmetric exchange interactions to itinerant models [6] where the spin order arises from a nesting instability of the Fermi surface, and yield diverse collinear and non-collinear ground states. Moreover, several scenarios describing the magnetization of the Ni sublattices were proposed in neutron studies and theory calculations: (i) two distinct Ni magnetic moments [8], (ii) equal moments sizes [10], and (iii) one of the Ni sublattices carrying zero moment [11]. Considering these discrepancies, experiments probing the spin configuration and test the validity of theoretical concepts are of great importance.

Lately, the presence of the non-collinear (↑→↓←) spiral has been confirmed by means of REXS, assessing the azimuthal dependence of the (1/4, 1/4, 1/4) magnetic Bragg reflection. The seminal experiment was performed in resonance to the Ni L_3 edge with π -and σ-polarized x-rays [12]. Matching the resonance condition greatly enhanced the magnetic scattering cross section and provided an element specific probe of the Ni magnetism. With polarized x-rays the relative orientation between the magnetic moments and incident photons polarization could be changed as the sample was rotated around the azimuthal angle ψ. The intensity of the magnetic Bragg reflection depends on this relative orientation and in consequence a comparison of the characteristic azimuthal dependence of the scattered intensity with model calculations could reveal the non-collinear spin arrangement in the nickelate. Along these lines, the REXS experiments described in the present doctoral thesis probe the complex magnetism in the nickelates with the goal of investigating the effects of heterostructuring and truncation along the $\mathbf{q}_0$ direction. Additionally, a newly developed analysis method was used to extract the absolute magnetic moment amplitudes of the Ni sites.

In more detail, $NdNiO_3$ was synthesized in [111] oriented slabs comprising $N = 55$, 45, 14, and 8 consecutive Ni layers sandwiched epitaxially in between layers of $NdGaO_3$. The $NdNiO_3$-$NdGaO_3$ heterostructure serves as an elementary magnetic model system which allows to preclude external influences on the nickelate's magnetism such as charge transfer to the Ni, polar discontinuities at interfaces, or orbital polarizations. As a consequence the pure effect of truncation along the [111] direction coinciding with the $\mathbf{q}_0 = (1/4,\ 1/4,\ 1/4)$ magnetic wave vector direction can be studied.

As central result a crossover from non-collinear to collinear spin structures is found when the nickelate crystal structure is truncated to two magnetic periods or less. The non-collinear spin structure is similar to the orthogonal (↑→↓←) spiral which has been identified previously in bulk-like $NdNiO_3$ films. The collinear spin configuration of the thin $NdNiO_3$ slab corresponds to an unusual antiferromagnetic up-up-down-down arrangement. The crossover between the spin structures is correctly predicted by density functional theory, confirming the model system's suitability as new testing ground for *ab-initio* calculations. Moreover, it is expected that the observation of the existence of non-collinear and collinear spin order within the same material system has profound implications on theories attempting to establish a uniform picture of the complex magnetism in rare-earth nickelates.

In addition to the changes in the spin orientation the Ni magnetic moment amplitudes are extracted from the azimuthal dependences. Contrary to previous REXS experiments, a systematic anomaly in the energy dependence of the (1/4, 1/4, 1/4) peak for particular ψ angles is observed, reflected in a non-constant ratio of the scattered intensity for π -and σ polarized incident photons. We identify the anomaly as the unique signature of scattering from two inequivalent Ni sites with distinct magnetic scattering tensors, which requires an advanced modeling of the magnetic form factors of the two sites. To this end, we use a newly developed double cluster model [13], which is based on the negative charge transfer concept [14] that starts from a Ni $3d^8$ electron configuration with a ligand hole at the oxygen. For the thick $N = 55$ sample magnetic moments of $m_1 = 0.80\ \mu_B$ and $m_2 = 1.44\ \mu_B$ are obtained, while fits for the thinner $NdNiO_3$ slabs yield a reduced imbalance between the moments m_1 and m_2. For the thinnest $N = 8$ sample the imbalance has vanished, in correspondence to uniformly sized NiO_6 octahedra. The equalization of the moment magnitudes for $N = 8$ is in accordance with the absence of the energy scan anomaly and indicates the presence of only one crystallographic Ni site.

This is further supported by scanning transmission electron microscopy imaging of the oxygen positions revealing a full structural pinning of the NiO_6 octahedral network to the confining $NdGaO_3$ layers for $N = 8$, whereas subtle relaxations in the Ni-O-Ni bond angles are observed for the thick $N = 55$ film. Such structural pinning might be particularly strong due to the enhanced octahedral interconnectivity of the [111] interfaces. Accordingly the orthorhombic $NdGaO_3$ symmetry can be imposed on thin $NdNiO_3$ slabs and hamper the structural symmetry breaking at low temperatures, resulting in antiferromagnetic order with equivalent Ni moment sizes.

Finally, the results of the analysis are incompatible with theories restricted to the picture of one Ni sublattices carrying zero moment and provide new, specific indicators for testing future models.

The thesis introduces a particular combination of methods, ranging from confocal Raman scanning, to resonant x-ray scattering, to first-principles calculations, and to modeling based on correlated cluster calculations. This composition of approaches provides deep insights into the mechanisms and physics behind the complex ordering phenomena in rare-earth nickelates. Along these lines, such combination can possibly open up novel perspectives for the systematic investigation of other transition metal oxide heterostructures such as managanites, ruthenates, and iridates.

Deutsche Zusammenfassung

Untersuchung von Ordnungsphänomenen in Nickelat-Heterostrukturen mittels elastischer und inelastischer Photonenstreuung

Heterostrukturen bestehend aus Übergangsmetalloxiden wie beispielsweise den Seltenerd-Nickelaten haben in den letzten Jahren große Aufmerksamkeit auf sich gezogen. Ihre gezielte Synthese bietet einzigartige Möglichkeiten Ladungs-, Spin-, Orbital- und Gitter-Freiheitsgrade zu kontrollieren und zu beeinflussen, so dass neue Phänomene auftreten, die in den Ausgangsmaterialien nicht existieren [1]. Darüber hinaus können Modellsysteme kreiert werden, in denen die systematische Veränderung bestimmter Wechselwirkungsparameter zu speziellen Reaktionen des Materials führt, was neue Erkenntnisse zu intrinsischen Phänomenen in den Ausgangsmaterialien liefern kann.

Die vorliegende Dissertation beschreibt die experimentelle Untersuchung von Ordnungsphänomenen in Seltenerd-Nickelat-basierten Heterostrukturen mittels inelastischer Raman-Licht-Streuung und elastischer resonanter Röntgenstreuung. Die beiden zentralen Ergebnisse der Arbeit sind: (a) Die vollständigen Kontrolle über die Ladungs/Bindungs- und Spin-Ordnungsparameter in speziell konstruierten $PrNiO_3$-Heterostrukturen und der Nachweis einer neuartigen Spindichtewelle, die durch räumliche Beschränkung der Leitungselektronen hervorgerufen wird. (b) Der schichtdickeninduzierte Übergang zwischen nicht-kollinearen und kollinearen Spinstrukturen in einer $NdNiO_3$-Heterostruktur, die als magnetisches Modellsystem konzipiert ist. Zusätzlich kann das relative Größenverhältnis der magnetischen Momente in den Ni-Untergittern durch die Kristallsymmetrie der benachbarten Schichten beeinflusst werden.

(a) Elektrische Transportmessungen an Heterostrukturen haben gezeigt, dass der intrinsische Metall-Isolator Übergang einiger Vertreter der Seltenerd-Nickelate mittels der Parameter Verspannung und räumliche Beschränkung beeinflusst werden kann [2,3]. Im Regime sehr dünner Nickelat-Schichten konnten resonante Röntgendiffraktionsexperimente aufzeigen, dass diese Parameter auch Einfluss auf die magnetische Ordnung haben [4]. Jedoch war es für Heterostrukturen mit effektiven Schichtdicken von 10 nm oder weniger bisher nicht möglich, einen strukturellen Phasenübergang und die einhergehende Ladungs/Bindungs-Ordnung nachzuweisen, da für Messungen mit herkömlichen Diffraktionsmethoden im Allgemeinen ein größeres Streuvolumen benötigt wird.

In der vorliegenden Doktorarbeit wird Raman-Spektroskopie zum Nachweis von Veränderungen der Kristallsymmetrie verwendet, die in enger Verbindung mit dem Auftreten von Ladungs/Bindungs-Ordnung sowie magnetischer Ordnung stehen. Hierzu wird eine spezielle Technik entwickelt, welche die geringe Tiefenschärfe der konfokalen Raman-Spektroskopie mit vertikalen Scans der Probe (z-scan) kombiniert, um Messungen an dünnen Materialschichten zu ermöglichen.

Die Methode reduziert den Substrat-Beitrag im Raman-Spektrum so stark, dass das Signal von Nickelat-Filmen mit einer Dicke von nur wenigen Nanometern detektiert werden kann. Die hier eingeführte Technik verwendet Laserlicht aus dem sichtbaren Bereich und erweist sich als leistungsfähige und vielseitige Alternative zur Ultraviolett-Raman-Spektroskopie [5].

In *bulk* $PrNiO_3$ weisen der strukturelle, elektronische und magnetische Phasenübergang dieselbe Ordnungstemperatur auf. In epitaktisch verspannten $PrNiO_3$ Filmen und Übergittern, bestehend aus $PrNiO_3$ und dem Band-Isolator $PrAlO_3$, kann das Auftreten der verschiedenen Ordnungsparameter und ihre Kopplung untereinander verändert werden. Mittels konfokaler Raman z-scans werden kollektive Gitterschwingungen (Phononen) als Funktion der Temperatur gemessen und mit komplementären elektronischen Transportmessungen verglichen. Zusätzlich wird mit Hilfe von magnetischer resonanter Röntgenstreuung die Präsenz des magnetischen Ordungsparameters nachgewiesen. In Nickelat-Filmen und Übergittern unter Zugspannung, die einen Metall-Isolator-Übergang beim Abkühlen aufweisen, zeigen die Ramanspektren Phonon-Moden des strukturellen Phasenübergangs, die charakteristisch für Ladungs/Bindungs-Ordnung sind. Diese anomalen Phononen treten nicht in Filmen unter Druckspannung auf, die bei allen Temperaturen metallisch bleiben. Die Filme verhalten sich daher ähnlich wie *bulk* $LaNiO_3$, das keinen Phasenübergang aufweist. In Übergittern unter Druckspannung weisen die Ramanspektren keine anomalen Phononen auf und der elektrische Widerstand erhöht sich nur geringfügig beim Abkühlen. Hingegen enthüllt resonante Röntgenstreuung die Existenz antiferromagnetischer Ordnung. Es werden also drei verschiedene Zustände identifiziert, von denen nur zwei vorher bei *bulk*-Nickelaten beobachtet wurden: Erstens ein isolierender Zustand mit robuster Ladungs/Bindungs- und Spin-Ordnung und zweitens einen metallischen Zustand mit keiner der beiden Ordnungformen. Die Übergitter unter Druckspannung zeigen jedoch Spin-Ordnung, die sich ohne gleichzeitige Ladungs/Bindungs-Ordnung entwickelt. Dieser Phasenzustand entspricht einer metallischen Spindichtewelle, die bisher im *bulk* oder in *bulk*-ähnlichen Nickelat Strukturen noch nicht nachgewiesen wurde.

Das Erzeugen einer Spindichtewellen-Phase durch die räumliche Beschränkung der Leitungselektronen bestätigt theoretische Vorhersagen eines Phasenübergangs, bei dem die Ladungs/Bindungs-Ordnung lediglich der sekundäre Ordnungsparamter ist [6]. Spindichtewellen wurden bisher nur in wenigen *bulk*-Metallen direkt beobachtet und charakterisiert, beispielsweise in Chrom-Verbindungen, organischen Ladungstransfersalzen und den Eisenpniktiden [7]. Die voneinander unabhängige Kontrolle der magnetischen und Ladungs/Bindungs-Ordnung eröffnet neue Möglichkeiten für den Einsatz von Nickelaten im Bereich der Spinelektronik, wo metallische Antiferromagnete als aktive Steuerelemente verwendet werden können. Darüber hinaus bietet die Bestimmung der Energien und Symmetrien der Phononen, die charakteristisch für die Ladungs/Bindungs-Ordnung sind, sowie deren Abhängigkeit von Gitterverspannung und räumlicher Beschränkung, spezifische Vorgaben für theoretische Modelle, die den Metall-

Isolator Übergang und die Elektron-Phonon-Wechselwirkungen in den Nickelaten und verwandten Übergangsmetalloxiden beschreiben.

(b) Erkenntnisse aus Messungen an Nickelat-Heterostrukturen haben in den letzten Jahren zu einem besseren Verständnis des Metall-Isolator Übergangs beigetragen. Wichtige Merkmale des antiferromagnetischen Grundzustands, der durch den Wellenvektor $\mathbf{q}_0$=(1/4, 1/4, 1/4) charakterisiert ist, sind jedoch größtenteils ungeklärt. Beispielsweise konnten Neutronenstreuexperimente nicht zwischen kollinearen und nicht-kollinearen Spinanordnungen unterscheiden [8]. Theoretische Beschreibungen der magnetischen Phase variieren von lokalisierten Spin-Modellen mit antisymmetrischen Austauschwechselwirkungen [9] bis zu itineranten Modellen, in denen die Spin-Ordnung aus einer *Nesting*-Instabilität der Fermi-Fläche hervorgeht [6]. Darüber hinaus werden in Neutronenstudien mehrere Szenarien bezüglich der Magnetisierung der Ni-Untergitter vorgeschlagen: (i) identische magnetische Momente in den zwei Untergittern [8], (ii) unterschiedliche Momentgrößen in den Untergittern [10] und (iii) eines der Ni-Untergitter trägt effektiv ein Nullmoment [11]. Die verschiedenen Möglichkeiten finden sich auch in diversen *mean field* und *ab-initio*-Berechnungen wieder und bisher besteht kein Konsens daüber, welches Szenario tatsächlich vorliegt. Folglich sind Experimente, die eine klare Bestimmung der Spinanordnung und der magnetischen Momente zulassen, von hoher Relevanz.

Erst kürzlich haben elastische Röntgenstreuungsexperimente die nicht-kollineare Spinanordnungen in *bulk*-ähnlichen $NdNiO_3$ Filmen bestätigt. Hierbei wurde die Abhängigkeit der magnetischen (1/4, 1/4, 1/4) Bragg-Reflektion vom azimuthalen Winkel ψ gemessen [12]. Während des Experiments wird die Probe um den Winkel ψ gedreht, was die relative Orientierung zwischen den magnetischen Momenten in der Probe und der π -bzw. σ-Polarisierung der einfallenden Photonen systematisch ändert. Da die gestreute Intensität von ebendieser relativen Orientierung abhängt, kann mittels Modellierung der azimuthalen Abhängigkeit die Spinanordnung in der Probe bestimmt werden. Basierend auf dieser Methode werden in der vorliegenden Dissertation die Einflüsse von Heterostrukturierung auf die Spinanordnung untersucht. Zusätzlich wird eine neu entwickelten Analysemethode verwendet, um die magnetische Momente der Ni Untergitter zu extrahieren.

Die untersuchten Heterostrukturen bestehen aus $NdNiO_3$-Schichtsystemen, die entlang des magnetischen Wellenvektors $\mathbf{q}_0$ orientiert und in eine nichtmagnetische $NdGaO_3$-Matrix eingebettet sind. Dieses spezielle Schichtsystem entspricht einem elementaren magnetischen Modellsystem, in dem die effektiven magnetischen Wechselwirkungen und die relativen magnetischen Momente der Spin-Untergitter gesteuert und erforscht werden können. Insbesondere werden externe Einflüsse auf den Magnetismus, wie beispielsweise Ladungstransfer und orbitale Polarisation, vermieden, so dass allein die Auswirkung einer zunehmenden räumlichen Beschränkung entlang der $\mathbf{q}_0$ Richtung untersucht werden kann.

Das Hauptergebnis der Studie ist der Übergang der Spin-Ordnung von einem nicht-kollinearen zu einem kollinearen Zustand, sobald die Nickelat-Kristallstruktur räumlich auf zwei magnetische Perioden oder weniger begrenzt wird. Die nicht-kollineare Spinstruktur der dicken $NdNiO_3$ Schichtsysteme ist vergleichbar mit der orthogonalen Spin-Spirale, die zuvor in *bulk*-ähnlichen $NdNiO_3$ Filmen identifiziert wurde. Der kollineare Zustand entspricht einer antiferromagnetischen *up-up-down-down* Ordnung, die bisher nur in wenigen Materialen beobachtet wurde. Der Nachweis beider Arten von Spinstrukturen innerhalb eines Nickelat-Materialsystems und als Funktion der räumlichen Beschränkung entlang der $\mathbf{q}_0$ Richtung, liefert wichtige neue Erkenntnisse über die intrinsische magnetische Ordnung der Nickelate, welche seit Jahrzehnten debattiert wird. Darüber hinaus wird der Übergang korrekt mittels Dichtefunktionaltheorie vorhergesagt, was das $NdNiO_3$-$NdGaO_3$ Modellsystem als interessantes neues Versuchsfeld für *ab-initio* Berechnungen bestätigt.

Die zweite wichtige Beobachtung der Studie ist eine Anomalie in der Energieabhängigkeit der magnetischen (1/4, 1/4, 1/4) Bragg-Reflektion in der Nähe der Ni L_3-Kante, die sich durch ein nicht-konstantes Verhältnis zwischen der π -und σ-gestreuten Intensität äußert. Die Anomalie wird als Folge zweier nicht-äquivalenter Ni Atom-Positionen im Grundzustand interpretiert, was letztendlich zu einer komplexen Energieabhängigkeit in der magnetischen Streuung führt. Die nicht-Äquivalenz der Ni Positionen muss auch in der Modellierung der azimuthalen Streuabhängigkeit berücksichtigt werden und die entsprechend unterschiedlichen magnetischen Streutensoren werden mit Hilfe eines neu entwickelten korrelierten Doppel-Cluster-Modells berechnet [13]. Das Cluster-Modell behandelt das Nickelat als *negative charge-transfer* Material [14], d.h. die nicht-Äquivalenz korrespondiert mit der Umverteilung von Liganden-Löchern zwischen benachbarten NiO_6-Oktaedern. Mit diesem Ansatz lassen sich aus der azimuthalen Abhängigkeit auch die absoluten magnetischen Momente in den Ni Untergittern extrahieren. Während sich in den dicken Proben deutlich unterschiedliche Momente ergeben, verschwindet das Ungleichgewicht mit abnehmender Schichtdicke. Diese Beobachtung wird durch die strukturelle Fixierung der Sauerstoffpositionen in den Oktaedern an der Grenzfläche der Heterostruktur erklärt, was mit Hilfe von Rastertransmissionselektronenmikroskopie-Aufnahmen der Sauerstoff- und Kation-Positionen bestätigt wird.

In der Doktorarbeit wird eine besondere Kombination von Methoden eingeführt, die konfokale Ramanstreuung, resonante Röntgenstreuung, *ab-initio* Rechnungen und Cluster-Rechnung basierte Modellierung umfasst. Ebendiese Verknüpfung verschiedener Ansätzen liefert tiefe Einblicke in die Mechanismen und Physik der komplexen Ordnungsphänomene in Seltenerd-Nickelaten. Im weiterführenden Sinne kann eine solcher Ansatz neue Perspektiven für die systematische Untersuchung anderer Übergangsmetalloxid-Heterostrukturen wie Managanate, Ruthanate und Iridate eröffnen.

Chapter 1

Introduction: transition metal oxides and their heterostructures

Compounds incorporating transition metal (TM) elements are a unique and diverse class of solids [15]. Amongst them a plethora of strongly correlated electron systems is found with properties primarily governed by the anisotropically shaped d-orbital electrons. A selection of the most exciting TMOs certainly comprises the $3d$ elements Ti, Co, Cu, Mn, and Ni, the $4d$ elements Y, Nb, and Ru, and the $5d$ elements W and Ir. Unlike standard metals such as Al or semiconductors such as Si, most TM compounds with narrow $3d$ bands cannot be described in a traditional single-electron band picture since the presence of strong Coulomb interactions and the consequences of partial filling of the d-shell add another level of complexity to the systems. The importance of additional charge, spin, lattice, and orbital degrees of freedom gives rise to intriguing phenomena like metal-insulator transitions [16], orbital order [17], frustrated magnetism [18], colossal magnetoresistance [19], and high-T_c superconductivity [20]. At the same time this complexity makes the understanding of the underlying physics a challenging task which in turn has spawned the dialog between theory and experiment since more than six decades [21–23].

In case of $3d$ transition metal oxides (TMOs) strong hybridization between the TM and oxygen ligands are possible and the electronic character of the compound can range from itinerant to highly localized. Moreover, several valence states and electronic configurations can be realized through different bonding geometries and for different stoichiometric compositions. Of all structural variations, in particular layered lattice structures derived from the perovskite building blocks [see inset in Fig. 1.1] are of paramount importance. Prominent examples are ferroelectric $\mathrm{PbZr_{0.2}Ti_{0.8}O_3}$ [24], magnetostrictive $\mathrm{Co_{0.8}Fe_{2.2}O_4}$ [25], and multiferroic $\mathrm{BiMnO_3}$ [26]. Generically, many of these crystal structures descend from the Ruddlesden-Popper homologous series $A_{N-1}A'_2B_N\mathrm{O}_{3N+1}$, where A and A' represent alkali, alkaline earth, or rare-earth metals while B refers to a TM [27]. For $A = A'$ and $N = 1$ one obtains the common $A_2B\mathrm{O}_3$ phase (corresponding to $\mathrm{K_2NiF_4}$-like structures) and for $N = 2$ the $A_3B_2\mathrm{O}_7$ structure results. In this work we focus on $N = \infty$, corresponding to the $AB\mathrm{O}_3$ perovskites. A multitude of TMO compounds of this composition has been intensively studied and efforts have been made to rationalize their electronic properties and the origin of the

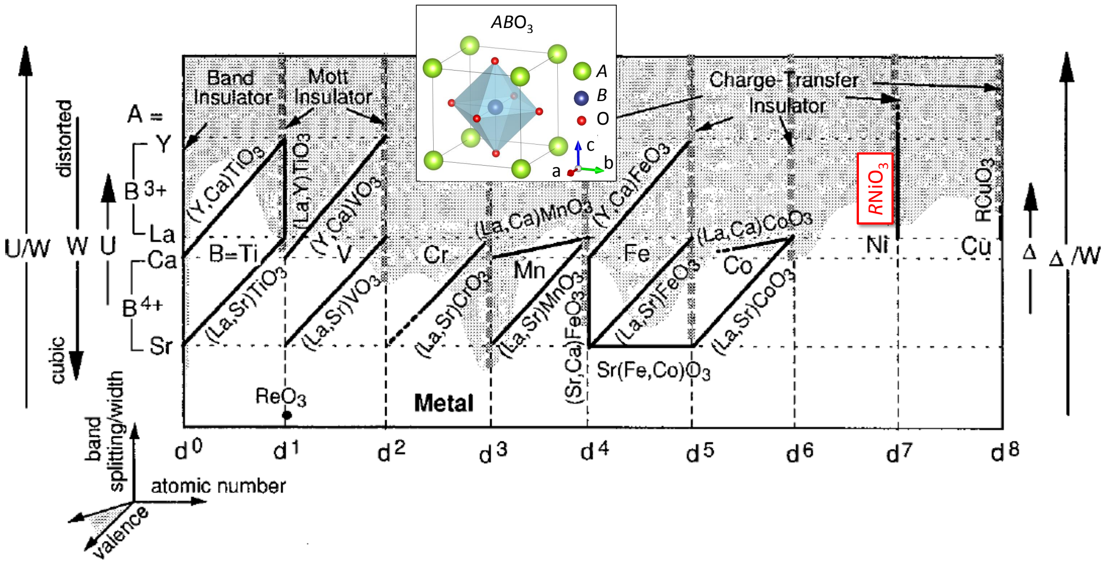

Figure 1.1 Metal-insulator diagram of $3d^n$ perovskite TMOs. The A-site cation is plotted as a function of the d-band filling n. Band-gap closure occurs along vertical lines, valence control is realized along oblique directions, and atomic-number control along the horizontal direction. U is the dd-Coulomb interaction, W is the electronic bandwidth, and Δ is the oxygen-p to TMO-d charge-transfer energy. The figure is reproduced from Ref. [28]. The inset shows the ABO_3 perovskite building block. The position of the rare-earth nickelates $R\mathrm{NiO}_3$ with R being a rare-earth element is indicated by the red box.

band gap within an universal scheme [Fig. 1.1].

A major puzzle in these and related compounds was the occurrence of an insulating ground state in spite of partially filled d-levels. Several theory concepts have been developed to explain the origin of such behavior, starting from Slater's early suggestion of possible gap openings due to antiferromagnetic order [29] and Mott's idea of electron localization for sufficiently large on-site Coulomb interaction strength U [30], which subsequently was further developed by Hubbard [31]. In the simplest case the balance between the parameter U and the single-electron bandwidth W, together with the d-band filling n [Fig. 1.1] controls whether the ground state is insulating or metallic. The early $3d$ TMO compounds in Fig. 1.1 can be well described in such a classical Mott-Hubbard insulator picture while for the late TMOs hybridization between the TM's $3d$ and oxygen $2p$ levels can become crucial [16, 32]. Here, another energy scale, the so-called charge transfer Δ, has to be introduced and compared to other relevant energies. In Fig. 1.1 predominately the late $3d$ TMO compounds are assigned to the regime of charge transfer insulators.

An evaluation of the strength and shortcoming of the aforementioned approaches finally lead to the Zaanen, Sawatzky, Allen (ZSA) scheme [33] which predicts a systematic change of Δ and U along the series of TMOs and classifies them into two groups: materials with $\Delta > U$ in which the energy gap at the Fermi level results from a Mott-Hubbard type splitting of the TM d-band due to the U, and materials with $\Delta < U$ in which the gap separates transition metal d states from ligand p states (charge transfer gap). As indicated by the solid lines in Fig. 1.1, TMOs can at least partly traverse regimes by substitution of the A-site cation. The shift in the phase diagram is

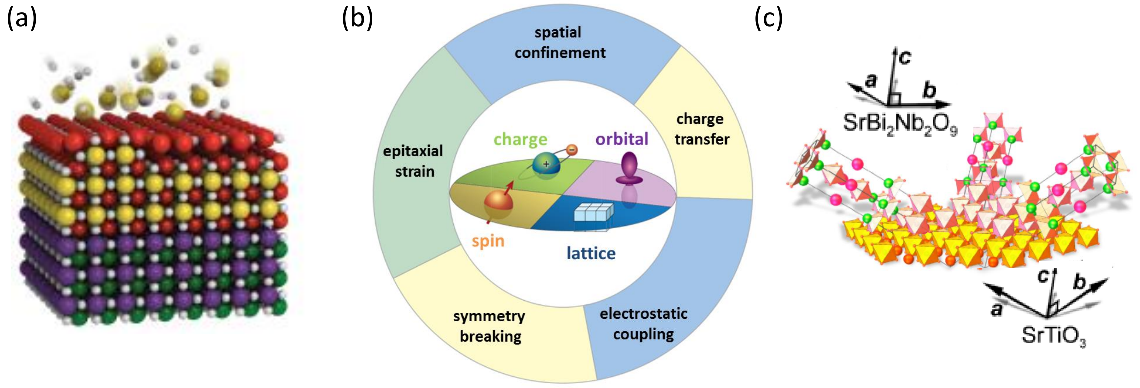

Figure 1.2 Tunable interactions in TMO heterostructures (a) Schematic of atomic layer-by-layer synthesis of multicomponent TMO heterostructures as realized for instance by molecular beam epitaxy. (b) The intrinsic balance between charge, spin, orbital, and lattice degrees of freedom of TMOs can be influenced by external control parameters such as epitaxial strain, spatial confinement, interfacial symmetry breaking, etc. (c) The crystallographic orientation of the substrate governs the resulting lattice symmetry of the deposited TMO layer. Electronic and magnetic properties of such geometrically engineered crystal structures can be very different from common [001] oriented heterostructures. The example shows the deposition of three tetragonal $SrBi_2Nb_2O_9$ unit cells on $SrTiO_3$ substrate in the pseudocubic [111] cut. Panel (a), (b), and (c) are adapted from Refs. [34–36], respectively.

a consequence of the sensitivity of the Δ/U ratio to crystal chemistry and structural distortions. It follows that Δ/U is also sensitive to external control parameters such as hydrostatic pressure [16] making the interaction parameters accessible in experimental studies where the controlled tuning of interactions can yield new fundamental insights on the materials.

Along these lines, a very versatile platform for designing and manipulating TMOs and their properties are heterostructures [1]. In particular the ablation techniques pulsed laser deposition (PLD), magnetron sputtering, and molecular beam epitaxy (MBE) [36, 37] allow to grow materials of unprecedented stoichiometry and to combine different constituents in artificial multilayer systems with atomically sharp interfaces [Fig. 1.2(a)]. In such heterostructures the balance and the interplay between charge, spin, orbital, and lattice degrees of freedom can be significantly altered [Fig. 1.2(b)] and consequences are an enhancement or suppression of certain bulk properties. In some cases even new phenomena can emerge which are not present in the constituent materials alone.

In particular interfaces play a crucial role in TMO heterostructures. Whereas already a free interface breaks inversion symmetry and reshapes the Fermi surface which can lead to a modification of electronic properties, the interface between two complex oxides is host of a multitude of new phenomena. Atomic reconstructions can be influenced by the structure of the adjacent material, yielding new possibilities of local symmetry breaking or modified rotations of the BO_6 octahedra which can have profound impact on magnetic properties, for instance in $La_{2/3}Sr_{1/3}MnO_3$ [38] and $SrRuO_3$ heterostructures [39]. In general, perovskites can exhibit a polar surface termination and/or charge transfer can take place across the interface to a second-component material. Along these lines, the $LaAlO_3/SrTiO_3$ interface has attracted the attention of a whole scientific community when it was discovered that the interface between the two band insulators exhibits an ultra-high electron mobility and even the novel phenomenon of interface superconductivity can occur [40].[1] Another example is the interface between antiferromagnetic $CaMnO_3$ and paramagnetic $CaRuO_3$ where a net ferromagnetic spin polarization arises [42]. Further, the interface between the superconductor $YBa_2Cu_3O_7$ and ferromagnetic $La_{2/3}Ca_{1/3}MnO_3$ fosters the charge transfer between Mn and Cu ions which induces a major reconstruction of the d-orbital occupation and orbital symmetry in the interfacial CuO_2 layers [43]. Nonetheless, heterostructure effects are not only restricted to interfacial regions but can also have a rather long-range character. This was observed in $YBa_2Cu_3O_7$–$La_{2/3}Ca_{1/3}MnO_3$ superlattices, where a Raman vibrational mode of the MnO_6 octahedra experiences superconductivity-induced line-shape anomalies even in 10 nm thick $La_{2/3}Ca_{1/3}MnO_3$ layers [44]. Epitaxial strain due to mismatch of lattice parameters of two TMOs generally relaxes within tens of nanometers, when the mismatch is moderate. The controlled imposition of compressive or tensile strain states induces lattice distortions which in turn influence the electronic degrees of freedom. Hence, so-called strain engineering is a powerful method for adjusting materials' properties and stabilizing alternative ground states [45]. Another route to access unprecedented electronic and topological phases is a change of the geometric motif of the underlying crystal lattice. In TMO heterostructures this can be realized by epitaxial growth on substrates of surface orientation other than the common pseudocubic [001] direction [Fig. 1.2(c)]. For instance the growth and/or confinement along the [111] direction renders the ABO_3 perovskite structure into a graphenelike buckled honeycomb lattice. Following this notion, the synthesis of $SrIrO_3$-$SrTiO_3$ superlattices on [111] oriented $SrTiO_3$ substrates can yield exotic non-trivial band topologies in the iridate component [46]. More examples of emerging phenomena in TMO heterostructures can be found in the reviews in Refs. [1, 18, 35, 47–49]

Finally, TMO heterostructures are not only fascinating from the perspective of basic research but also due to their potential of being integrated into modern electronic devices. The TMO growth techniques allow to synthesize the active layers in atomically thin fashion with sharp interfaces and often the electronic correlation strength can be tuned over several orders of magnitude. These advantages over conventional semiconductor based heterostructures might eventually promote oxide electronics as new workhorse of mainstream electronics [50]. Further, TMO heterostructures find application in the field of spintronics where an active control and manipulation of spin degrees of the charge carriers provides additional functionalities for the devices [51].

In the focus of this thesis are ternary nickel oxides $RNiO_3$, whose heterostructures have been subject of a multitude of studies during the last years. In the perovskite unit cell the TM Ni is coordinated with oxygen atoms in an octahedral crystal field environment, together with an element of the rare-earth series R = La, Ce, Pr, Nd, Sm, etc. In Fig. 1.1 bulk $RNiO_3$ is found in the regime of the charge transfer insulators

---

[1] It is noted that in another set of models the high conductivity at the $LaAlO_3/SrTiO_3$ interface is explained by the presence of oxygen vacancies [41].

(except for R = La). According to modern theory concepts this classification later will be refined to *negative charge transfer* material [14, 52].

Generally, experimental tests of theoretical predictions such as the emergence or absence of electronic, magnetic, and structural order parameters are challenging in thin films and heterostructures of TMOs since the probing volume is naturally very small. Whereas resonant elastic x-ray scattering (REXS) has successfully detected magnetic order in epitaxially strained nickelate superlattices and ultra-thin films, [2–4, 53] direct evidence of a structural symmetry breaking concomitant to the MIT has not been reported in such systems yet. As first key result of the present doctoral thesis it is demonstrated that a combination of confocal Raman spectroscopy and a vertical scan of the focus position can be used to detect such a symmetry breaking in nickelate heterostructures with an effective layer thickness of 10 nm or less [54, 55]. In $PrNiO_3$ heterostructures it is then shown—together with complementary electrical transport and magnetic REXS measurements—that the emergence of the structural, electronic, and magnetic order parameters can be widely tuned through the external control parameters epitaxial strain and spatial confinement. Further, it is found that in compressively strained $PrNiO_3$-$PrAlO_3$ superlattices the spin order can evolve independently of the charge/bond order parameter, corresponding to a novel spin density wave phase [6, 56] with no bulk analog.

In many TMO systems with strong electronic correlations magnetic ordering phenomena have profound influence on the macroscopic properties. However, the realistic prediction of magnetic interactions and spin orientation in complex systems remains a formidable challenge. One archetypical example is the nickelates-family, where proposals of collinear (↑↑↓↓) and non-collinear (↑→↓←) magnetic structures and the amplitude of magnetic moments on different Ni sublattices have been subjects of debate for decades [4, 8, 10–12, 57]. In the second part of the thesis polarized REXS is employed to investigate complex magnetic ordering phenomena in $NdNiO_3$ heterostructures that are oriented along the crystallographic [111] direction which coincides with the $\mathbf{q}_0 = (1/4,\ 1/4,\ 1/4)$ magnetic wave vector. Particular $NdNiO_3$ slabs embedded in a non-magnetic $NdGaO_3$ matrix are introduced as an elementary model system that allows to tune and study the nickelates' antiferromagnetic interactions. The central result of the series of experiments is a crossover between a non-collinear spin spiral and a collinear spin configuration when the nickelate slab is truncated along $\mathbf{q}_0$ to two magnetic periods or less. The crossover between both spin structures is correctly predicted by density functional theory. It is further demonstrated that the amplitude ratio of magnetic moments in neighboring NiO_6 octahedra can be accurately determined by REXS in combination with a correlated double cluster model, and controlled experimentally through the crystallographic symmetry of the confining layers.

Chapter 2

The rare-earth nickelates

2.1 Bulk electronic, magnetic, and structural properties

The rich phase diagram of rare-earth nickelates $R\mathrm{NiO}_3$ (with R=rare-earth or Y), has been subject of interest in a great variety of studies since more than 20 years [58–60]. The phase space of bulk $R\mathrm{NiO}_3$ spans from a Pauli paramagnetic metal to paramagnetic insulator to unconventional period-four antiferromagnet [Fig. 2.1]. The phase diagram's complexity originates from a fine balance between bandwidth and correlation energies that is mediated by the perovskite lattice distortions.

The properties of rare-earth nickelates are determined by the ionic radius r_R of the rare-earth R. The ground state of the family member with the largest radius, LaNiO_3, is paramagnetic metallic with space group $R\bar{3}c$ [Fig. 2.1(a),(b)]. All other members exhibit a relatively sharp metal-insulator transition (MIT) with the transition temperature $T_{\mathbf{MI}}$ monotonically increasing with decreasing rare-earth ionic radius - from PrNiO_3 with ~130 K, to NdNiO_3 with ~200 K, to SmNiO_3 with ~400 K, up to YNiO_3 with ~560 K [8]. For PrNiO_3 and NdNiO_3 the MIT coincides with an antiferromagnetic phase transition, whereas the magnetic onset temperature $T_{\mathbf{N}}$ is lower than $T_{\mathbf{MI}}$ for smaller rare-earths, with an intermediate paramagnetic insulating phase. For $R \neq \mathrm{La}$ the space group of the high-temperature metallic phase is of orthorhombic $Pbnm$ symmetry, which is reduced to monoclinic $P2_1/n$ when the nickelate undergoes the transition to the insulating state. For PrNiO_3 and NdNiO_3 the monoclinic distortion is relatively faint and only one Raman study [63] and recent state-of-the-art high-resolution powder x-ray and neutron diffraction have found clear evidence for its presence [64, 65].

Another parameter classifying the rare-earth nickelates is the so-called *tolerance factor* t [Fig. 2.1(a)]. The tolerance factor is generally used to characterize perovskite structures [66] and is defined as $t = d_{R-O}/\sqrt{2}d_{Ni-O}$, where d_{R-O} and d_{Ni-O} are the ionic bond distances. The ideal undistorted perovskite structure manifests itself by $t = 1$. The ionic radii of the rare-earth ions of the $R\mathrm{NiO}_3$ family, however, are generally not large enough to accommodate the cubic lattice. Hence, t is smaller than unity throughout the entire phase diagram of Fig. 2.1(b), except for a small pocket

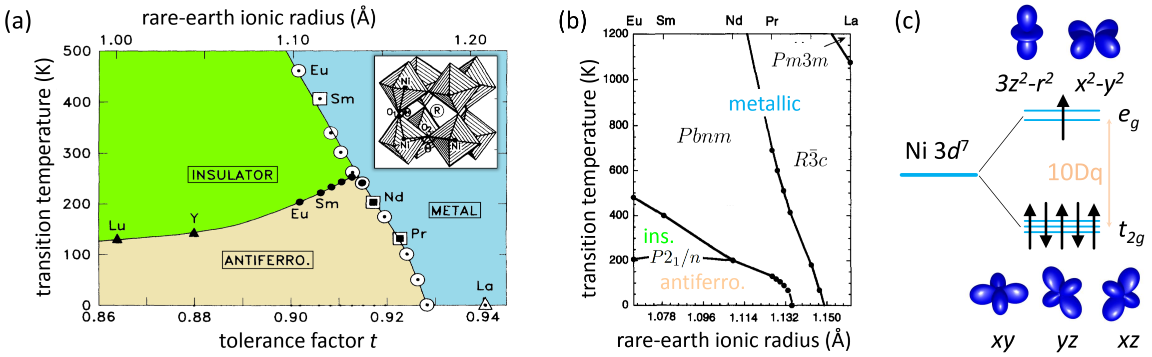

Figure 2.1 Rare-earth nickelates in bulk. (a) Insulator-metal-antiferromagnetic phase diagram of the RNiO$_3$ family as a function of the ionic radius of the rare-earth R or the tolerance factor t. Data points in-between the RNiO$_3$ family members correspond to compounds with mixed rare-earth composition. (b) Crystallographic symmetries of the rare-earth nickelates. (c) The formal Ni^{3+} $3d^7$ state in low-spin configuration. An O_h symmetry crystal field ($10D_q$) splits the 5-fold degenerate orbitals are split into an e_g and t_{2g} manifold. Panel (a) and (b) are from Refs. [61,62], respectively.

corresponding to space group $Pm3m$ in the case of LaNiO$_3$ at very high temperatures. In first approximation, a reduction in the tolerance factor is accommodated by the tilts of the NiO$_6$ octahedra. In a simplified picture, the bending of the Ni-O-Ni angle (see inset in Fig. 2.1(a)) reduces the orbital overlap of Ni $3d$ and oxygen $2p$ and promotes the insulating state over the metallic one, rendering LaNiO$_3$ with the straightest bond angles metallic down to lowest temperatures.

In the ABO$_3$ stoichiometric composition the Ni ion formally exhibits a 3+ valence with low-spin $3d^7$ ($t_{2g}^6 e_g^1$) configuration and one electron in the twofold degenerate e_g orbitals [Fig. 2.1(c)]. Naturally, this electron interacts with the crystal field environment and in correspondence to similar TMO systems [67] the degeneracy of the e_g levels is expected to be split by a Jahn-Teller distortions of the oxygen octahedra [8,68,69]. However, the fingerprints of such lattice distortion and the concurrent orbital order could not be detected in bulk and bulk-like samples [70]. Instead it was suggested that a charge disproportionation between adjacent Ni^{3+} ions of the form Ni$^{3+\delta}$ and Ni$^{3-\delta}$ could lift the degeneracy, in correspondence to the two inequivalent Ni sites of the monoclinic $P2_1/n$ ground state. The $P2_1/n$ structure exhibits two types of NiO$_6$ octahedra, one set is compressed and has short Ni-O bonds (SB), and the other set of octahedra is expanded and has long Ni-O bonds (LB) [Fig. 2.2(a)]. Generally, a charge transfer between the Ni ions should be suppressed by the on-site Coulomb repulsion U, however, in presence of a sizable Hund's coupling a disproportionated can be stabilized if the system is close to the itinerant limit [71].

The picture relating the MIT and the concomitant structural transition to the occurrence of an order parameter equivalent to the Ni charge disproportionation was supported by resonant x-ray scattering experiments at the Ni K-edge at 8340 eV [70]. Staub *et al.* measured a modulated intensity of specific Bragg reflections when the incident x-ray energy was tuned through the Ni K-edge. This was interpreted as a signature of Ni being present in two different valence states. In the study reflections of $(h0l)_{or}$ and $(0hl)_{or}$ type with h and l odd [Fig. 2.2(b)] are considered (here orthorhom-

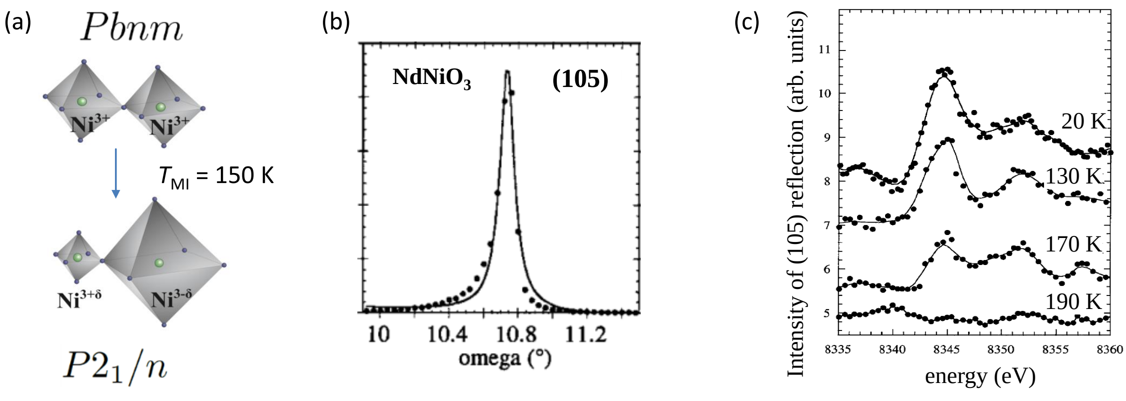

Figure 2.2 Structural phase transition and charge order. (a) Orthorhombic space group *Pbnm* exhibits uniformly sized NiO_6 octahedra. Concomitant with the MIT the volume of one set of octahedra collapses while the other set expands, corresponding to space group $P2_1/n$. In some models the transition is related to a charge disproportionation of Ni^{3+} ions to $Ni^{3+\delta}$ and $Ni^{3-\delta}$. For the $NdNiO_3$ in Ref. [70] $T_{\mathbf{MI}}$ is 150 K upon cooling. (b) Rocking scan of the $(105)_{or}$ Bragg reflection at 190 K. (c) Intensity of the $(105)_{or}$ reflection in dependence of the energy for selected temperatures below and above the MIT. Panel (b) and (c) are from Ref. [70].

bic indexing is used). In *Pbnm* symmetry with a single Ni site the structure factor of these reflections is not sensitive to the considered resonance effects, i.e. in first approximation the peak intensity is independent of the energy.[1] In $P2_1/n$, on the other hand, the presence of two inequivalent Ni sites and their structure factors leads to a complex interference when the phase shifts of the x-ray wavefronts add up, with the real and imaginary part simultaneously playing a role in the scattered intensity. This yields the wiggly lineshape in Fig. 2.2(c) as the energy is scanned through the resonance. Note that it is difficult to detect the presence of slightly different structure factors in the corresponding K-edge absorption experiments [73]. In more detail, each Ni site exhibits a different core potential, slightly shifting the position of the absorption edge in the x-ray absorption spectrum (XAS). Since the absorption is proportional to the imaginary part of the scattering factor, which here is a simple superposition of the two, only the average of the two sites is measured. Thus possible differences between them are just washed out into a slightly broader spectrum.

Also note that the occurrence of two inequivalent Ni sites basically doubles the size of the pseudocubic unit cell which can result in superstructure peaks of $\boldsymbol{q}_{CO} = \left(\frac{h}{2}, \frac{k}{2}, \frac{l}{2}\right)$ (now pseudocubic indexing is used). However, the soft x-ray regime employed in this thesis (comprising e.g. the Ni L-edges with $2p \rightarrow 3d$ transition) does not provide sufficient momentum transfer to access this point in reciprocal space experimentally. Conversely, the momentum transfer in hard x-ray K-edge experiments is high, but the electronic transition corresponds to $1s \rightarrow 4p$, i.e. the states close to the Fermi level of $3d$ TMOs are not probed directly. Still, these experiments can be sensitive to the local electronic and crystallographic environment of the respective TMO ions with complex resonant lineshapes arising from details of the scattering tensor [72, 74–76].

---

[1] Recently it has been shown by Lu *et al.* that also mere octahedral tilt distortions yield an energy dependence of the Bragg peaks at the Ni K-edge [72].

Figure 2.3 Negative charge transfer gap character of nickelates. (a),(b) Single electron excitation spectra in terms of charge removal and charge addition for different regimes of effective charge-transfer Δ'. The charge transfer energy, i.e. the cost for transferring an electron/hole from the ligand band to the Ni $3d$ band, is Δ. The (Hubbard) U is the cost needed to remove an electron from the occupied $3d$ band and to add it to the unoccupied $3d$ band. (a) Positive charge transfer compound ($\Delta' > 0$). The lowest energy removal states are ligand-based and the lowest energy addition states are transition metal based, leading to a charge transfer derived energy gap (O $2p$ – Ni $3d$ like) and a $3d^7$ ground state. (b) In negative charge transfer compounds ($\Delta' < 0$), one hole per Ni is doped into the ligand band, giving a density of ligand holes n, L^n. The ground state is $d^8\underline{L}^n$. The red-dashed contour bands are a cartoon-like demonstration of the opening of the gap in the mainly O $2p$ continuum resulting in the MIT. Here, the lowest energy removal and addition states are both ligand-based, leading to an O $2p$ – O $2p$ like gap. Ni-O hybridization are neglected to provide clear distinction between the regimes. The figure is from Ref. [52].

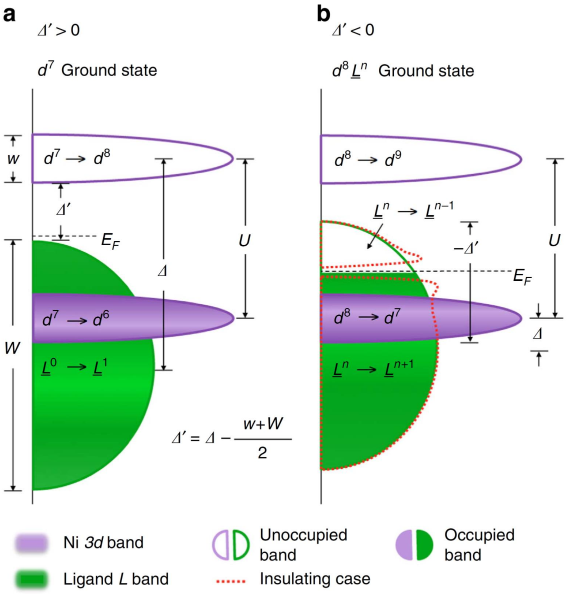

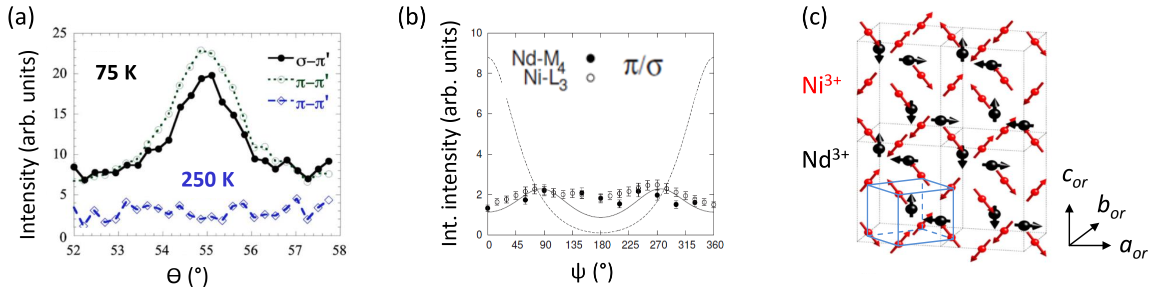

Figure 2.4 Resonant magnetic x-ray scattering. (a) Rocking scans of the magnetic Bragg reflection of $NdNiO_3$ at $\mathbf{q}_0$=(1/4, 1/4, 1/4) below (75 K) and above (250 K) $T_\mathbf{N}$ for π and σ photon polarizations. The energy is tuned to the Ni L_3 edge. (b) Azimuthal dependence of the π/σ ratio measured in resonance to the Ni L_3 and the Nd M_4 edge, respectively. The superimposed solid and dashed lines are the simulated dependencies of non-collinear ($\uparrow\rightarrow\downarrow\leftarrow$) and collinear ($\uparrow\uparrow\downarrow\downarrow$) spin order, respectively. The collinear order corresponds to spins oriented within the *ab* plane of the orthorhombic unit cell. The non-collinear spin configuration is shown in (c). In addition to the four orthorhombic unit cells (black dashed lines) the pseudocubic unit cell is indicated (solid blue lines). Panel (a) is from Ref. [12] and panel (b) and (c) are from Ref. [57].

From a theoretical point of view there are many studies that have reassessed the traditional interpretation of the charge-ordered state in terms of $Ni^{3+\delta}$ and $Ni^{3-\delta}$ valence states stabilized by Hund's rule interactions [71,77–80]. One set of models has invoked an unusual electron-phonon interaction that modulates the covalency of the Ni-O bond so that the charge transfer, δ, between adjacent Ni sites vanishes both above and below the MIT [13,52,81–84]. The approach treats the nickelate as *negative charge transfer* material, as introduced by Mizokawa *et al.* [14,85], and starts with a Ni $3d^8$ electron configuration with a ligand hole $\underline{L}$ at the oxygen [Fig. 2.3]. In the extreme limit the disproportionation then corresponds to

$$2\,(\mathrm{Ni}\,d^8\underline{L})_{S=1/2} \rightarrow \mathrm{Ni}\,(d^8\underline{L}^2)_{S=0} + \mathrm{Ni}\,(d^8)_{S=1}, \tag{2.1}$$

with the total spin S. Hence the charge disproportionation rather happens at the ligand oxygen state than at the Ni. Also in this picture the uniformly sized NiO_6 octahedra of the metallic phase split into sets of collapsed (SB, $d^8\underline{L}^2$) and expanded octahedra (LB, d^8). In the strong-coupling limit the SB sites correspond to a Kondo insulator and the LB sites to a Mott insulator, which is why the transition has been called 'site-selective Mott transition' by the authors of Ref. [83]. This associates the MIT with a change of the covalency of the bonds rather than an actual charge transfer [68,86]. Therefore the ground state has been coined *bond ordered* instead of *charge ordered.*

According to another model, the MIT of the more itinerant members with R = Nd and Pr is caused by spin density density wave formation, with charge/bond order as a secondary order parameter in some (but not all) lattice structures [6,56]. However, the antiferromagnetic order of the nickelates with an unusually large periodicity is generally subject of an ongoing discussion. Whereas other perovskite TMOs show the tendency to form antiferromagnetic order via dominant next-nearest neighbor superexchange which leads to a doubling of the pseudocubic unit cell neutron studies of nickelates consistently found an unusual period-four antiferromgentic order along the pseudocubic (111) body diagonal, i.e. the propagation vector was determined as $\mathbf{q}_0$=(1/4, 1/4, 1/4) [11, 69], corresponding to $(1/2, 0, 1/2)_{or}$ in orthorhombic notation. From the neutron powder diffraction data collinear (↑↑↓↓) and non-collinear (↑→↓←) spin configurations could not be discerned. What could be resolved, however, were the Ni magnetic moments corresponding to distinct Ni sites of the SB and LB octahedra with 1.4 and 0.6 μ_B for $HoNiO_3$ and 1.4 and 0.7 μ_B for $YNiO_3$ [8, 87]. Early neutron studies investigating the larger rare-earths were not able to distinguish different moment sizes and detected 0.9 μ_B in case of $NdNiO_3$ and $PrNiO_3$ [88] which is close to the purely ionic value of 1 μ_B of Ni^{3+} but inconsistent with a charge/bond disproportionation scenario with SB and LB sites.

Scagnoli *et al.* addressed the open question of spin collinearity vs. non-collinearity by magnetic resonant x-ray diffraction experiments on bulk-like $NdNiO_3$ films [12, 57]. As described in chapter 3 the intensity of a magnetic Bragg reflection depends on the relative orientation between the incident x-rays and the local orientation of the magnetic moments. When the sample is rotated around the azimuthal angle ψ this relative orientation changes and from the modulation of the intensity the spin configuration can be deduced. The experimental results shown in Fig. 2.4(b) indicated an orthogonal spin spiral of the type (↑→↓←) and ruled out a collinear (↑↑↓↓) model.

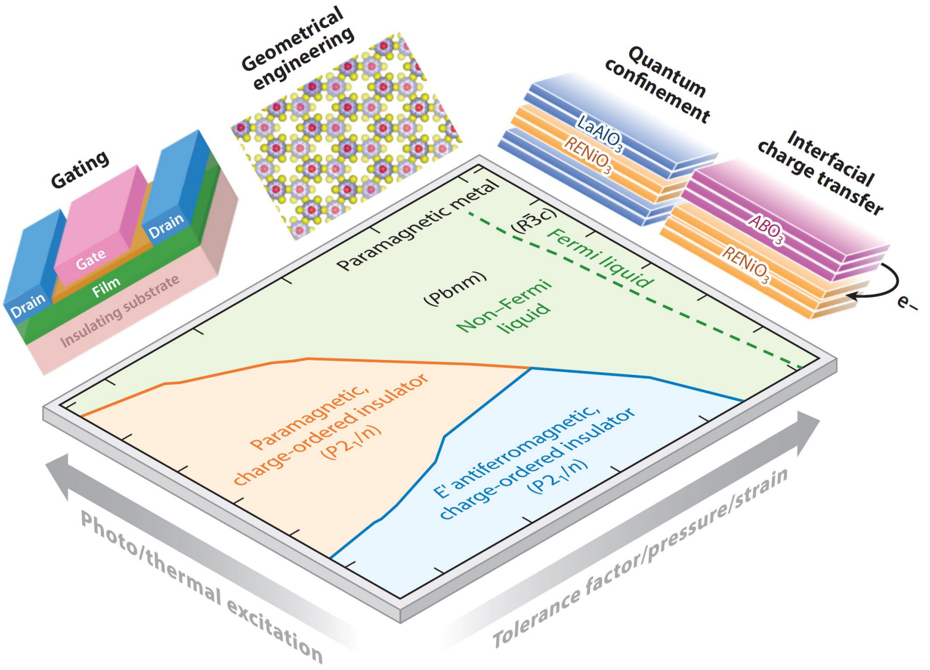

Figure 2.5 Nickelate heterostructures. Schematic diagram illustrating various experimental ways to alter and control the phases and properties of the bulk nickelates phase diagram via heterostructuring. The figure is from [91].

2.2 Nickelate heterostructures

Specifically designed heterostructures offer alternative routes to study the manifold physics of strongly correlated TMOs. Beside the possibility to stabilize chemical phases, which are hard or impossible to grow in bulk form,[2] structural distortions can be systematically influenced by the epitaxial relationship with the underlying substrate or a second-component material, confinement of the electron system can be realized through reduced layer thicknesses, and interfacial reconstructions and interactions might occur depending on the combination of different materials [1].

Heterostructures comprising rare-earth nickelates as component are particularly intriguing since the material class features a delicate competition between spin, charge, orbital, and lattice degrees of freedom. In such an environment a pronounced susceptibility to external control parameters influencing this competition comes naturally. Over the last years an impressive number of studies has demonstrated how the microscopic and macroscopic properties of nickelates can be widely influenced and controlled [Fig. 2.5] via epitaxial strain [3, 92–95], external electric fields [96], chemical doping

---

[2] Note that the synthesis of large single crystals of rare-earth nickelates has not been achieved yet with common crystal growth methods, as an extremely high oxygen pressure at high temperatures would be required to stabilize Ni in its 3+ state of oxidation. Few exceptions are reported in Refs. [89, 90], with very small and heavily twinned crystals. The feasibility of stabilizing nickelates as powders or as films on a substrate up to a critical thickness, however, is long known. In specific cases the films resemble the bulk-like properties in other cases the epitaxy to the substrate alters the nickelate's properties.

and electrolyte gating [59,97,98], light induced lattice distortions [53,99,100], reduced thickness of the active layer [101], spatial confinement of the conduction electrons through proximity to a band insulator [102], altered geometrical motifs of the underlying crystal lattice [60,103–106], and interfacial exchange interactions [107,108]. A recent review on the topic is given in Ref. [91]. A selection of the key findings in nickelate heterostructures is discussed in the following.

- **Suppressed order parameters:** Epitaxy and lattice mismatch to a substrate can have severe impact on the intrinsic lattice distortions of nickelates. This allows for a tuning of the strength of electronic and magnetic correlations and therewith the transition temperatures $T_{\mathbf{MI}}$ and $T_{\mathbf{N}}$. Whereas the transitions of [001] oriented thin films under tensile strain are similar to bulk, $T_{\mathbf{MI}}$ and $T_{\mathbf{N}}$ can be suppressed down to lowest temperatures for sufficiently large compressive strain [2,3]. Table A.1 and Table A.2 in Appendix A give an overview on the lattice parameters of nickelates and common oxide substrates. Substrates with larger lattice parameters induce tensile strain to the nickelate while smaller lattice parameters induce compressive strain.

  In addition, femtosecond pump-probe experiments demonstrated a melting of the magnetic ground state and an increase of the electrical conductivity by five orders of magnitude through light pulses resonant with specific lattice vibrational modes [53,99,100]. These observations confirm a strong coupling between the lattice and the electronic degrees of freedom and provide a new way of dynamically controlling the nickelates' ground state.

- **Induced order parameters:** In bulk, the ground state of $LaNiO_3$ is paramagnetic metallic. Boris *et al.* have shown that $LaNiO_3$ layers in $LaNiO_3$-$LaAlO_3$ superlattices as thin as two unit cells undergo a sequence of collective metal-insulator and antiferromagnetic transitions as a function of decreasing temperature, whereas samples with thicker $LaNiO_3$ layers retain bulk properties. The transition to the antiferromagnetic state was later confirmed by Frano *et al.* by REXS and the magnetic spin configuration in the heterostructures was revealed, as described in more detail later in the text.

- **Separated order parameters:** For bulk $NdNiO_3$ and films grown under tensile strain on [001] oriented substrates the MIT and the antiferromagnetic transition coincide. Catalano *et al.* found $T_{\mathbf{MI}}$ and $T_{\mathbf{N}}$ widely separated in the particular case of $NdNiO_3$ grown on [111] oriented $NdGaO_3$ substrates [103]. Here $NdNiO_3$ resembles the bulk properties of $SmNiO_3$. The study will be described further below.

- **Orbital polarization:** Distortions of the local symmetry of the NiO_6 octahedra can lift the degeneracy of the Ni e_g orbitals [Fig. 2.6] [109,110]. Benckiser *et al.* could resolve orbital polarization profiles in the atomic layers of $LaNiO_3$-$LaAlO_3$ heterostructures and disentangle the influence of epitaxial strain from interfacial effects controlled by the chemical composition of the insulating blocking layers [111] [Fig. 2.6(c)]. Later it was shown by Wu *et al.* that the occupation of the

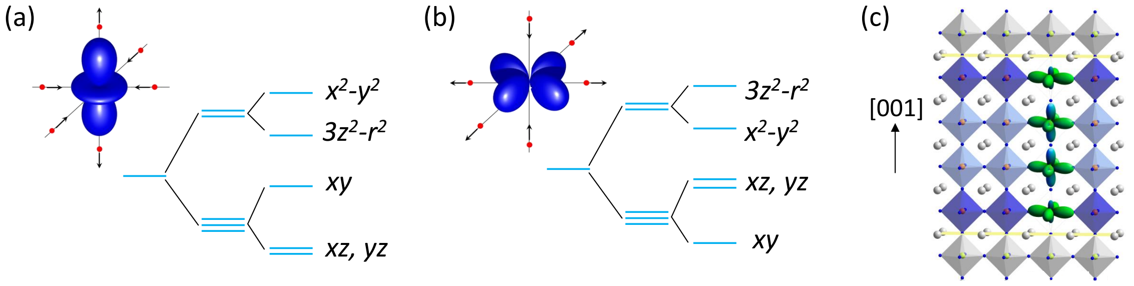

Figure 2.6 Orbital polarization induced by tetragonal lattice distortions and interfacial coupling. (a) Tetragonal (D_{4h}) distortion of the NiO_6 octahedron lifting the degeneracy of the e_g and t_{2g} orbitals. A compression along the in-plane directions yields preferred occupation of the $d_{3r^2-z^2}$ orbital. (b) Elongation along the in-plane directions yields preferred occupation of the $d_{x^2-y^2}$ orbital. (c) Spatially resolved orbital polarization profiles along the pseudocubic [001] direction reveal a reduced out-of plane orbital occupation at the interface to a band insulator as compared to the inner layers. Panel (c) is from [111].

$d_{x^2-y^2}$ orbital can be enhanced by about 25% predominantly through the tensile strain imposed through substrate mismatch [112, 113]. .

- **Orbital order:** Middey *et al.* suggest the presence of a novel type of orbital order in $NdNiO_3$-$LaAlO_3$ superlattices composed of two Ni layers along the [111] direction [60]. The antiferro-orbital ordered state which manifests as staggered planes of Ni $d_{3z^2-r^2}$ and $d_{3x^2-r^2}$ orbitals is unattainable in bulk nickelates and nickelate based heterostructures grown along the [001] direction. Hence the altered geometric motif of the [111] oriented crystal structure (buckled honeycomb lattice) can induce novel orbital states when combined with the spatial confinement of the electronic system.

- **Interfacial charge transfer:** Charge transfer and electronic reconstructions are common phenomenon at (polar) TMO heterointerfaces. Substantial effects have been observed in nickelate multilayer systems containing RXO_3 layers with X=Ti [114]. Charge is transferred across the interface from Ti to Ni which yields 50% enhanced occupation of the $d_{3r^2-z^2}$ orbitals in case of $LaTiO_3$-$LaNiO_3$-$LaAlO_3$ tricomponent superlattices [115, 116]. This kind of orbital engineering based on symmetry-breaking and polar fields thus leads to large orbital polarizations and provides the possibility to create unique electronic systems.

  Another example for interfacial charge transfer are nickelate/manganite multilayers [107], allowing the Ni ion to adopt its preferred Ni^{2+} state by accepting an electron from the Mn. Such systems which can induce specific types of magnetic order in the nickelate will be discussed in more detail further below.

- **Stabilized non-equilibrium states:** Kim *et al.* designed [111] oriented $NdNiO_3$-$LaAlO_3$ heterostructures where polar displacements of the Nd cations can be stabilized because the $LaAlO_3$ octahedral tilt pattern counteracts that in

$NdNiO_3$ [117]. The result is a ferroelectric polarization in the metallic phase of $NdNiO_3$. Such an exotic state corresponding to a polar metal contradicts Gauss's law which dictates that the net electric field inside a conductor is zero by effective charge screening. The study combining experiments and first-principles calculations is an intriguing example of atomic-scale engineering leading to the emergence of novel and unprecedented states.

- **Predicted multiferroicity:** The charge/bond ordered ground state of the nickelates together with the period-four antiferromagnetic order is in principal prone to so-called type II multiferroicity [118, 119]. In that case a ferroelectric polarization can occur in the magnetically ordered state due to magnetostriction effects and is expected to be strongest when the spin order is of collinear (↑↑↓↓) type. However, to this day no conclusive experimental evidence for multiferroicity in the nickelates has been presented.

- **Predicted superconductivity:** The high-T_c cuprates exhibit an electronic configuration of Cu d^9 with one hole in the $d_{x^2-y^2}$ orbital. The quasi-two-dimensional electronic structure in the CuO_2 planes and the strong antiferromagnetic correlations between the Cu 1/2 spins are believed to be essential for their high-T_c superconducting state. Chaloupka, Khaliullin and other pointed out that in $LaNiO_3$-$LaAlO_3$ superlattices with a nickelate layer thickness of only one unit cell the $d_{3r^2-z^2}$ level could be pushed above the Fermi surface, leaving only the $d_{x^2-y^2}$ relevant [120, 121]. In consequence all aforementioned ingredients might be present in a nickelate heterostructure. From the experimental side, however, a superconducting transition has not yet been observed in nickelate based superlattices.

2.2.1 Orbital control of non-collinear magnetic order

Frano *et al.* have used REXS to probe the antiferromagnetic spin configuration of nickelate heterostructures under (i) tensile strain, (ii) compressive strain, and (iii) additional spatial confinement [Fig. 2.7] [4]. The methodology of extracting the spin order from the azimuthal dependence of the (1/4, 1/4, 1/4) reflection is similar to the experiments of Refs. [12, 57] mentioned above. The concept will be elucidated in detail in chapter 3 and is employed for the magnetic REXS measurements of this thesis. The heterostructures investigated by Frano *et al.* were oriented along the [001] pseudocubic direction whereas the bulk-like nickelate films of Refs. [12, 57] were oriented along the [111] direction, coinciding with the $\mathbf{q}_0$=(1/4, 1/4, 1/4) magnetic propagation vector direction. Thus, Frano *et al.* had to use a tilted wedge scattering geometry in order to access the corresponding scattering plane. Figs. 2.7(a)-(c) show the ratio of the intensity of the (1/4, 1/4, 1/4) reflection for π and σ polarized incident x-rays as a function of the azimuthal angles ψ. Since in the wedge geometry the illuminated sample area changes with ψ the ratio of the intensities was evaluated for extracting the spin orientation. Model calculations (solid lines) then confirmed the non-collinearity of the spin spiral for nickelate heterostructures, but relative spin angles between the Ni sublattices and the spiral's polarization plane were revealed to be different than in the orthogonal (↑→↓←) spiral of the bulk [Figs. 2.7(g),(h)].

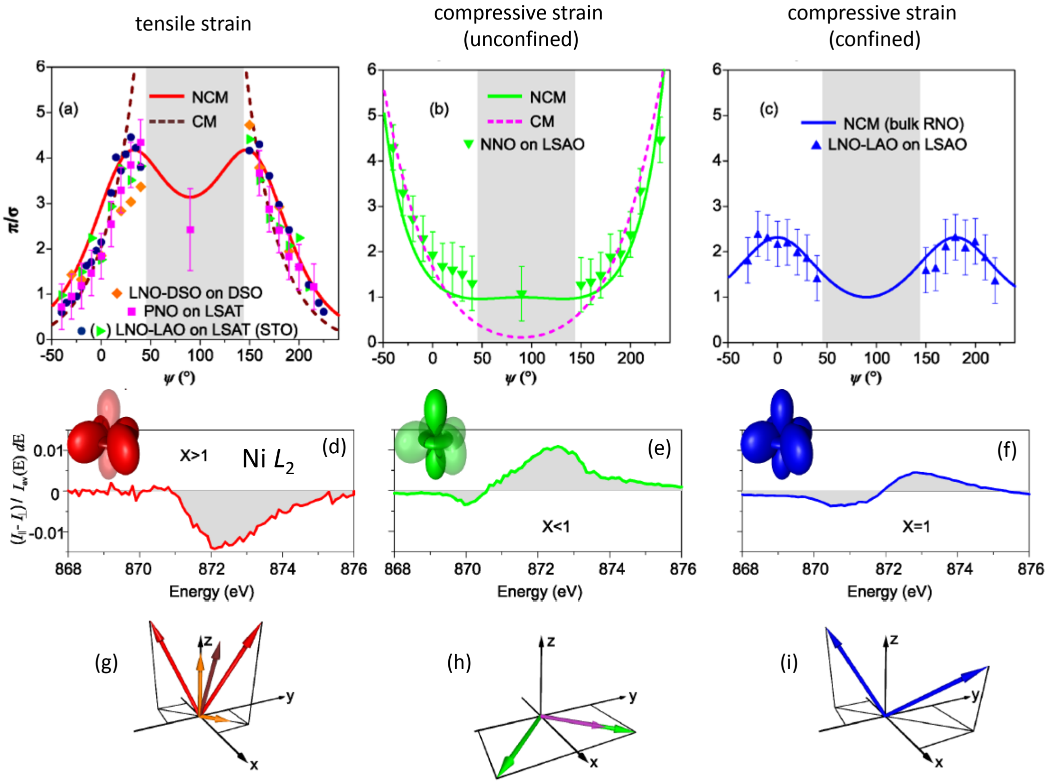

Figure 2.7 Orbital polarization and its influence on the spin order. (a)-(c) Azimuthal dependencies of magnetic scattering intensities for π and σ polarized x-rays. The [001] oriented heterostructures are composed of $LaNiO_3$ (LNO), $PrNiO_3$ (PNO), $NdNiO_3$ (NNO), $LaAlO_3$ (LAO), and $DyScO_3$ (DSO) and grown on DSO, LSAT, and LSAO substrates. Gray shaded areas correspond to azimuthal angles ψ where the incident or outgoing beams are below the sample horizon. (d)-(f) X-ray linear dichroism. The normalized difference spectra $(I_\parallel - I_\perp)/I_{av}(E)dE$ are obtained from the XAS around the Ni L_2 edge with incoming light polarization in and out of the (001) plane. The sign of the hole ratio X is stated in each panel. Insets with the color-coded solid and semitransparent e_g orbitals illustrate the corresponding imbalance of orbital occupancy, i.e. the orbital polarization. (g)-(i) Cartoons of the spin order influenced by orbital polarization. The axis x, y and z correspond to the pseudocubic [001] reference frame and the color-coding refers to panels (a)-(c). For simplicity only the first two spins of the period-four antiferromagnetic spin spiral are shown. The two omitted spins are the corresponding negative vectors. Spins of different color (orange and dark red in (g) and purple in (h)) are alternative spin configurations from the model calculations. The configuration of the blue spins in (i) is similar to the orthogonal (↑→↓←) spiral found in bulk-like nickelate films [12, 57]. The figure is adapted from [4].

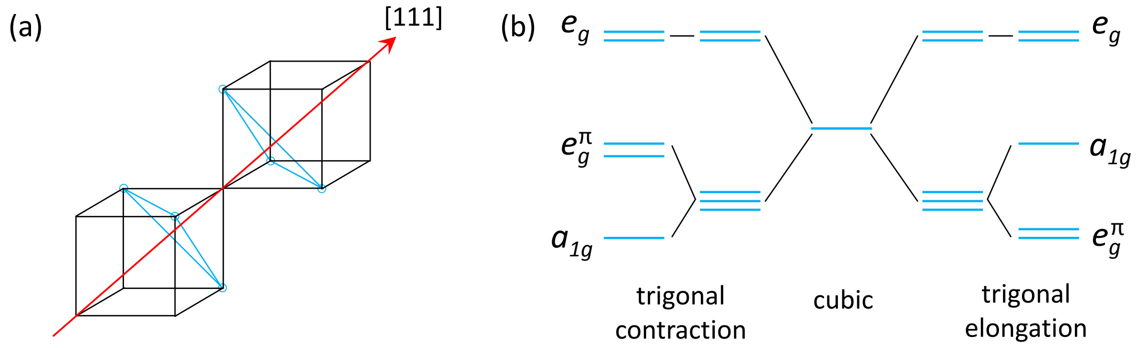

Figure 2.8 Orbital polarization for trigonal distortions. (a) Two pseudocubic unit cells with the [111] direction and two (111) planes indicated. Trigonal (D_{3d}) lattice distortions within the (111) plane of a heterostructure can possibly be induced by the compressive or tensile strain mismatch to a [111] oriented substrate. (b) The t_{2g} levels are split into a e_g^π doublet and an a_{1g} singlet while the e_g manifold is unaffected and stays degenerate.

In addition to the magentic scattering (at the Ni L_3 edge), the x-ray linear dichroism, a measure of the orbital polarization, was recorded at the Ni L_2 edge [Figs. 2.7(d)-(f)]. Note that the intrinsically stronger L_3 edge XAS signal could not be evaluated due to large overlap with the La M_4 line. The change in the hole ratios X (further explanation in chapter 3) indicate different relative occupations of the Ni e_g orbitals which in turn govern the local spin orientation via the spin-orbit coupling. Accordingly, the spiral polarization plane can be controlled by adjusting the Ni d-orbital occupation via two independent mechanisms: epitaxial strain and spatial confinement of the valence electrons.

2.2.2 Heterostructures oriented along the [111] direction

Studies exploring the [111] crystallographic orientation of nickelates are sparse compared to research on [001] heterostructures which is partly due to difficulties of synthesizing the materials along this highly polar direction. However, the occurrence of novel properties in [111] heterostructures has been reported in Refs. [60,103,105,107,117,122].

In chapter 5 we will present magnetic REXS measurements on nickelate heterostructures grown on [111] oriented substrates. Since one of the major results of the study by Frano *et al.* [4] was that orbital polarization controls the nickelates' magnetocrystalline anisotropy via the spin-orbit coupling the possible orbital polarization of [111] heterostructures is of particular interest. A trigonal lattice distortion corresponding to epitaxial strain within the (111) plane as possibly imposed by a [111] substrate mismatch does not lift the degeneracy of the e_g manifold [Fig. 2.8]. Thus no orbital polarization and therewith no major effect on the spin configuration is expected for such heterostructures. However, other effects that might have an impact on the magnetic configuration of [111] heterostructures are to be discussed.

Important experiments investigating induced magnetic order in [111] oriented nickelates were performed on superlattices consisting of $LaNiO_3$ sandwiched by layers

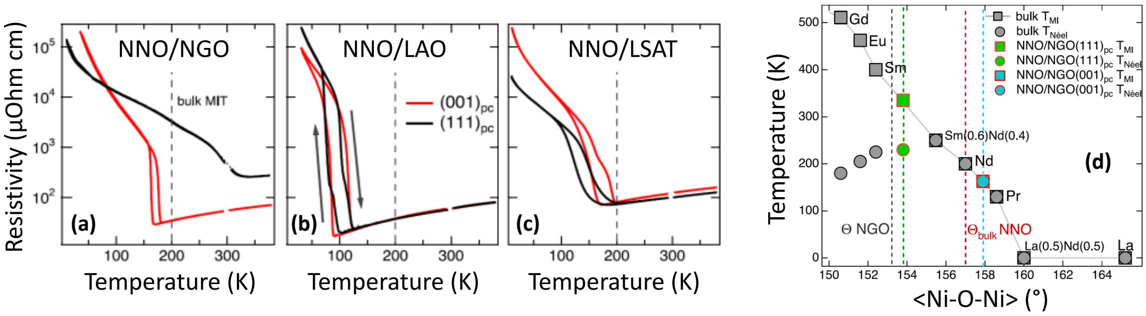

Figure 2.9 **Enhanced $T_{\mathbf{MI}}$ in [111] oriented $\mathbf{NdNiO_3}$ on $\mathbf{NdGaO_3}$.** (a)-(c) Electrical transport of $NdNiO_3$ in the [001] and the [111] orientation on various substrates (red and black curve, respectively), as observed in Ref. [103]. Only the system $NdNiO_3$ on $NdGaO_3$ shows distinct behavior for the [111] orientation and the metal-insulator transition is shifted to ~ 325 K whereas the small kink in the resistivity indicating $T_{\mathbf{N}}$ is at ~ 210 K. The dashed vertical lines represent $T_{\mathbf{MI}} = T_{\mathbf{N}}$ of bulk $NdNiO_3$. (d) $T_{\mathbf{MI}}$ and $T_{\mathbf{N}}$ as a function of the Ni-O-Ni bond angle. The figure is adapted from Ref. [103].

of ferromagnetic $LaMnO_3$ [107, 108]. Gibert *et al.* found an unusual exchange bias effect implying an interface induced magnetic structure in the otherwise non-magnetic $LaNiO_3$. Induced magnetism in $LaNiO_3$ heterostructures has been reported before [102], however it is pointed out in Ref. [107] that the observed exchange bias provides a unique tool to probe the interfacial coupling between $LaNiO_3$ and $LaMnO_3$. Moreover, the exchange bias effect is exclusively present in [111] heterostructures because here the interfacial coupling is enhanced as compared to [001] interfaces. The enhanced coupling does not only apply to structural properties, but also the charge transfer between Mn and Ni is more pronounced across the [111] interface [123]. First-principles simulations of superlattices with different periodicities indicate a spin density wave like modulation of the Ni magnetic moments with a ferromagnetic coupling of the Ni moments at the interface to the Mn. Recently, the follow-up study showed that the interlayer magnetic coupling depends on the exact thickness of the $LaNiO_3$ layer [108]. Specifically for $N = 7$ atomic layers of Ni, negative and positive exchange bias occurs, as well as antiferromagnetic interlayer coupling in different temperature windows.

Interestingly, nickelate films show similar behavior in electronic transport when grown on [001] and [111] oriented $LaAlO_3$ (or LSAT) substrates, whereas the specific combination of $NdNiO_3$ on [111] oriented $NdGaO_3$ substrate significantly enhances $T_{\mathbf{MI}}$ up to 335 K [Fig. 2.9(a)-(c)] [103]. This strengthening of the electronic correlations gives rise to a unprecedented paramagnetic insulating phase, since now $T_{\mathbf{MI}}$ and $T_{\mathbf{N}}$ are widely separated. Catalano *et al.* attributed the effect to a structural modification of the $NdNiO_3$ imposed by the $NdGaO_3$ substrate which is possible for $NdNiO_3$-$NdGaO_3$ due to a close matching of the lattice constants as well as the B-O-B tilt angles. A highly increased propagation length of the substrate's octahedra tilts across the [111] interface was suspected and it is proposed that the octahedra tilt angles of the $NdGaO_3$ propagate throughout the whole 17 nm thick $NdNiO_3$ film. This would be in contrast to findings for [001] oriented heterostructures where the propagation length is usually only of the order of a few unit cells [124]. Thus, the enhanced octahedral interconnectivity of the [111] interface and the tilt propagation [Fig. 5.3(c)] is an important issue, that is addressed by scanning transmission electron microscopy imaging of the octahedral oxygen positions within the scope of this thesis (see chapter 5).

Chapter 3

Experimental techniques

3.1 Inelastic Raman light scattering

Vibrational spectroscopy has a long history as fundamental technique to study the structure, dynamics and reactivity of crystalline materials, liquids and molecules. First spectra of molecular vibrations were recorded by W. Abney and E.R. Festing in 1881 [125]. In their pioneer study they observed characteristic absorption bands of organic liquids in the near infrared region. Later, when infrared (IR) spectroscopy was already an established technique, C.V. Raman and K.S. Krishnan detected inelastic scattering of light by a fluid [126] – a concept which was honored with the Nobel prize for physics in 1930. In these early days it could easily take more than 24 hours to record a single spectrum and Raman scattering was rather considered as a curiosity only used by a few specialized research laboratories. Today, Raman spectroscopy is one of the major analysis techniques in the fields of physics, chemistry, and material research. The technique is even employed in the quality control of industrial production cycles, where automated searching algorithms can identify characteristic Raman bands of spectra recorded within milliseconds of time. The diversity of modern-day applications is a consequence of substantial technical advances of the Raman instrumentation. Photographic plates were replaced by photomultipliers and charge-coupled device (CCD) elements, scanning grating spectrometers replaced the prism spectrographs, and the development of triple monochromators significnatly improved the quality of the spectra and the convenience of recording them. However, the major breakthrough was the introduction of laser light sources, increasing the signal to noise ratio by more than 10 orders of magnitude, as compared to C.V. Raman's original light source: monochromatized sunlight.

In the field of condensed matter physics, Raman spectroscopy is a prominent tool. Light scatters inelastically from many different types of elementary excitations such as collective crystal lattice vibrations and spin waves, and their properties then can be studied in the Raman spectrum. In this thesis, we examine phonon excitations in rare-earth nickelates, which are indicative of particular structural and electronic phases of the material.

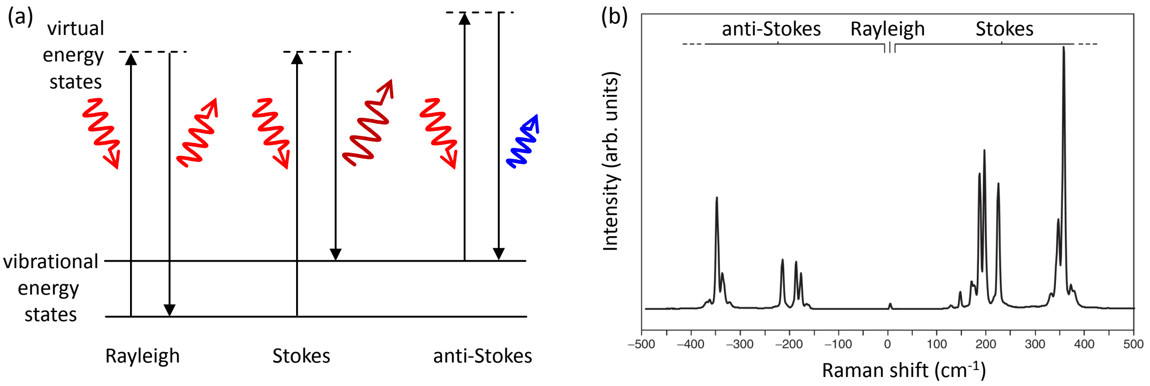

Figure 3.1 Raman scattering process and Raman spectra. (a) Energy-level diagram of photon-in photon-out processes related to Raman spectroscopy. (b) Raman spectrum of the mineral As_4S_4 with anti-Stokes, Rayleigh and Stokes contributions. The Rayleigh line (elastic scattering) is strongly suppressed by a holographic filter. Its unfiltered intensity is more than 10^6 times higher than the inelastically scattered contributions. The Stokes intensity is generally higher than the anti-Stokes contribution as the latter is proportional to a finite population of thermally excited (phononic) states. Panel (b) is from Ref. [127].

3.1.1 Classical description of Raman scattering

Electromagnetic radiation incident on a condensed matter medium can be reflected, transmitted or absorbed. For monochromatic incident photons, the scattering process is called elastic (*Rayleigh scattering*) when the scattered light exhibits the same energy as the incident photons [Fig. 3.1(a)]. In case of inelastic scattering, energy and momentum can be transferred between the incident photon and the investigated system. Depending on whether the light-matter interaction and the transfer of energy and momentum involves the creation or the annihilation of an elementary excitation, the process is referred to as *Stokes* -or *anti-Stokes* scattering, respectively. Raman spectroscopy detects the energy shift between the incident and the scattered light [Fig. 3.1(b)] which is typically given in units of wavenumbers [cm^{-1}]. The conversion between wavenumbers w and the spectral wavelength λ in nm can be performed via

$$\Delta w(\mathrm{cm}^{-1}) = \left(\frac{1}{\lambda_0(\mathrm{nm})} - \frac{1}{\lambda_1(\mathrm{nm})}\right) \times \frac{(10^7\mathrm{nm})}{(\mathrm{cm})}, \tag{3.1}$$

where λ_0 is the excitation wavelength and λ_1 the Raman spectrum wavelength. In terms of electronvolt energy units, 1 meV corresponds to $\sim$8 cm^{-1}. Typically, Raman scattering experiments are carried out with optical photons ($\sim$1 eV) and low energy excitations like phonons ($\sim$10 meV) or magnons are studied [Fig. 3.2].

The optical photons carry a relatively small momentum ($|\boldsymbol{k}| \sim 10^{-3}$Å), generally much smaller than the reciprocal lattice vectors in a crystal lattice. In consequence the momentum transfer $\boldsymbol{q}$ in the Raman process is negligible $\boldsymbol{k}_{out} - \boldsymbol{k}_{in} = \boldsymbol{q} \approx 0$ and Raman spectroscopy is a probe restricted to the zone center Γ of the first Brillouin zone. Exceptions are second or higher order Raman processes, including two phonons with $\boldsymbol{q}_1 + \boldsymbol{q}_2 = 0$, making it possible to probe the phonon density of states from arbitrary parts of the Brillouin zone.

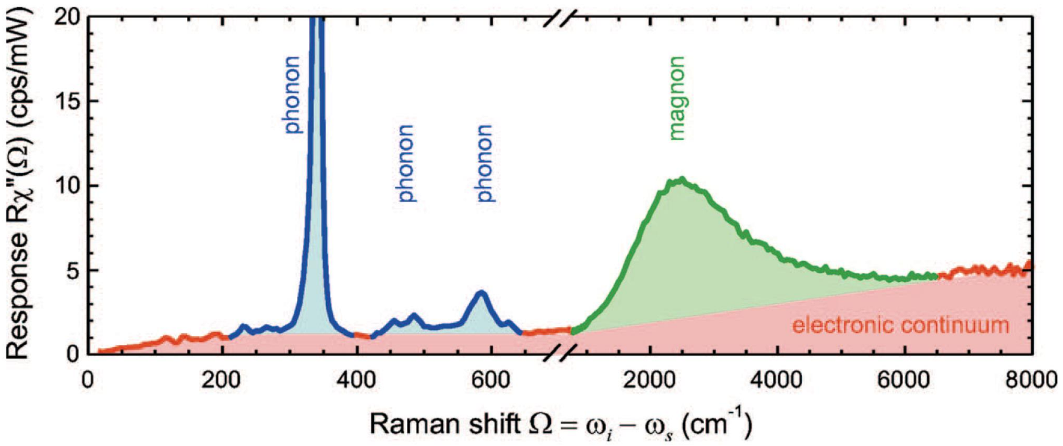

Figure 3.2 Typical excitations in a Raman spectrum. Spectrum showing the inelastic light scattering response of a $(Y_{0.92}Ca_{0.08})Ba_2Cu_3O_{6.3}$ crystal. Characteristic contributions from phonons, magnons, and electrons, colored in blue, green, and red, respectively. The figure is from Ref. [128].

In the following sections a brief review of the classical description phononic Raman scattering is given, based on Refs. [129–133] and references therein. In the simplest case of an external field $\boldsymbol{E}$ perturbing an electron in a medium, the induced macroscopic polarization $\boldsymbol{P}$ is

$$\boldsymbol{P} = \chi \boldsymbol{E}(t), \tag{3.2}$$

with the electrical susceptibility χ. In general, χ is a second-rank tensor containing microscopic information about the medium, also comprising contributions from collective lattice vibrations. The external electromagnetic wave field can be expressed as $\boldsymbol{E}(\boldsymbol{r}, t) = \hat{\boldsymbol{\varepsilon}} E_0 e^{i(\boldsymbol{k}\cdot\boldsymbol{r}-\omega t)}$ with $\hat{\boldsymbol{\varepsilon}}$ being a unit vector along the wave's polarization, the frequency ω and the wave vector $\boldsymbol{k}$.[1] Further, let $\boldsymbol{u}$ be the displacement of the atoms in the medium from their average position which in harmonic approximation corresponds to $\boldsymbol{u}(\omega, \boldsymbol{q}) = \boldsymbol{u}_0 \cos(\boldsymbol{q} \cdot \boldsymbol{r} - \omega t)$. Such displacements are collective lattice waves of frequency ω and are characterized by their wave vector $\boldsymbol{q}$. They represent independent vibrational modes of the lattice, the *normal modes*, exhibiting an appropriate dispersion relation between ω and $\boldsymbol{q}$. In the Born-Oppenheimer or adiabatic approximation electrons follow the slow motion of the atomic nuclei instantaneously but are much lighter move more rapidly. As a consequence χ can be expressed as a function of $\boldsymbol{u}$, since the characteristic electronic frequencies are much larger than ω. A Taylor expansion of χ for lattice vibrations with $\boldsymbol{u}_0$ small compared to the lattice constants yields

$$\chi(\boldsymbol{u}) = \chi_0 + \left.\frac{\partial \chi}{\partial \boldsymbol{u}}\right|_0 \boldsymbol{u} + \frac{1}{2} \left.\frac{\partial^2 \chi}{\partial \boldsymbol{u}^2}\right|_0 \boldsymbol{u}^2 + \ldots \tag{3.3}$$

The subscript 0 on the derivatives indicates that these are to be taken at the equilibrium positions. χ_0 describes the electrical susceptibility without vibrational contribution,

---

[1] Note that we will assume for the entire theoretical description that $|\boldsymbol{k}|$ is much smaller than a reciprocal lattice vector and therefore the incident light is approximately constant within a crystallographic unit cell.

while the term linear in $\boldsymbol{u}$ corresponds to the modulation of the electrical susceptibility by a lattice displacement, i.e. describes a *first order Raman process.* Subsequent terms corresponds to Raman processes of higher orders and include two or more collective lattice vibrations. Inserting the expansion into Eq. 3.2 yields for the polarization vector $\boldsymbol{P}$ of an electron

$$\boldsymbol{P} = \left(\chi_0 + \frac{\partial \chi}{\partial \boldsymbol{u}} \boldsymbol{u} \right) \boldsymbol{E} = \chi_0 \boldsymbol{E} + \frac{\partial \chi}{\partial \boldsymbol{u}} \boldsymbol{u} \cdot \boldsymbol{E}, \tag{3.4}$$

for orders higher than linear neglected. The static term $\chi_0 \boldsymbol{E}$ corresponds to oscillations of the macroscopic polarization which are in phase with the incident radiation. This is basically the elastic light scattering which we will neglect for now in the description of the Raman process, however this term will be important later for the elastic x-ray scattering. Hence, the inelastic scattering is left with

$$\begin{aligned}\boldsymbol{P} = \frac{\partial \chi}{\partial \boldsymbol{u}} \boldsymbol{u} \cdot \boldsymbol{E} = \frac{1}{2} \frac{\partial \chi}{\partial \boldsymbol{u}} \boldsymbol{u}_0 \hat{\boldsymbol{\varepsilon}} E_0 \left[\cos((\boldsymbol{k}_{in} + \boldsymbol{q}) \cdot \boldsymbol{r} - (\omega_{in} + \omega) t) \right. \\ \left. + \cos((\boldsymbol{k}_{in} - \boldsymbol{q}) \cdot \boldsymbol{r} - (\omega_{in} - \omega) t) \right]. \end{aligned} \tag{3.5}$$

In consequence the electric field of the scattered light contains frequencies and wave numbers shifted with respect to the ones of the incident radiation. It thus is of the form

$$\boldsymbol{E}_s(\boldsymbol{k}_s, \omega_s) \sim \boldsymbol{E}_{in} \left[(\boldsymbol{k}_{in} + \boldsymbol{q}), (\omega_{in} + \omega) \right] + \boldsymbol{E}_{in} \left[(\boldsymbol{k}_{in} - \boldsymbol{q}), (\omega_{in} - \omega) \right]. \tag{3.6}$$

The first term corresponds to the *anti-Stokes process* of annihilation of a normal mode excitation ($\omega_s = \omega_{in} + \omega$), while the second describes the *Stokes process* of creation ($\omega_s = \omega_{in} - \omega$) of an excitation.

In general, the *Raman tensor* is defined as

$$R = \left. \frac{\partial \chi}{\partial \boldsymbol{u}} \right|_0 \hat{\boldsymbol{u}}, \tag{3.7}$$

with $\hat{\boldsymbol{u}}$ being a unit vector parallel to the atomic displacement of the lattice vibration. The components of the second-rank tensor are determined by the symmetries of the scattering medium and its lattice vibrations. In other words, χ contains the symmetry of the lattice and R reflects the symmetry of the collective lattice distortion. It can be shown [130] that the differential Raman scattering cross section $\partial^2\sigma/\partial\Omega\partial\omega$, i.e. the probability of an incident photon to be inelastically scattered in a solid angle $d\Omega$ with energy between ω and $\omega + d\omega$, is

$$\frac{\partial^2 \sigma}{\partial \Omega \partial \omega} \sim \omega_s^4 \left| \hat{\boldsymbol{e}}_s \cdot R \cdot \hat{\boldsymbol{e}}_{in} \right|^2 \delta(\omega - \Delta\omega), \tag{3.8}$$

with the Dirac δ-function centered at the Raman shift ω. Therefore the intensity of the Raman scattered light is

$$I_{Raman} \sim \left| \hat{\boldsymbol{e}}_s \cdot R \cdot \hat{\boldsymbol{e}}_{in} \right|^2. \tag{3.9}$$

From Eq. 3.9 it is obvious that the Raman intensity depends on the polarization of incident and scattered light and on the symmetry of the Raman tensor. These are the so-called *Raman selection rules*. In experiment the direction of the light's linear polarization ($\hat{\boldsymbol{e}}_{in}$) can be chosen with respect to the sample orientation and an analyzer can select specific contributions in the scattered light ($\hat{\boldsymbol{e}}_s$). Thus, certain components of R the symmetries of particular normal modes can be probed through Raman polarization analysis. The expected number of normal modes and the relative intensities can be calculated and compared to the experimental spectra.

In principal also the frequency of a normal mode can be calculated by solving the classical equations of motion of the atoms when they undergo small displacements from their equilibrium sites. However, this is only feasible for very simple lattice symmetries. For more complex systems, in harmonic approximation, the dynamical properties of atoms in a Bravais lattice can be mapped onto solving the eigenvalue problem of the so-called *dynamical matrix* [134]. For a crystal with s atoms the system of $3s$ three-dimensional coupled oscillators is transformed into $3s$ decoupled but collective oscillators, and the solutions (*normal modes*) correspond to waves propagating over the entire crystal, exhibiting a dispersion relation $\omega(\boldsymbol{k})$. Therefore, the phonon band structure and its different branches follow from the eigenvalues after diagonalizing the dynamical matrix. More comprehensively, the dynamical matrix derives from the second derivatives of the total energy and one usually exploits first-principles methods for its computation. In the *supercell method* (also called *frozen-phonon approach*) the positions of different atoms are slightly perturbed and the reaction forces on all other atoms are calculated [135]. For systems with long ranged interatomic interaction it is necessary to employ large supercells of the original unit cell to calculate the dynamical matrix with this method at different points of the Brillouin zone. In the supercells the (in principle equivalent) atoms within this larger periodicity are displaced differently, to account for the different phase behavior. Conversely, *linear response calculations* seek to evaluate the dynamical matrix directly for a set of $\boldsymbol{k}$-vectors. The main advantage of the procedure is that there is no need to artificially increase the cell size in order to accommodate small values of the $\boldsymbol{k}$-vectors [136].

3.1.2 Quantum mechanical description of Raman scattering

The framework of the classical description of Raman scattering is basically sufficient to describe the experiments and phenomena observed in the scope of this thesis. It is noted however, that an accurate explanation of resonant Raman scattering, magnon scattering, and electron-phonon and phonon-phonon interaction, requires quantum mechanical treatment e.g. by third-order time-dependent perturbation theory. Then the collective lattice vibration (i.e. the 'phonon') is considered as a quantum of lattice vibration and treated in second quantization formalism [137]. Details can be found in Ref. [130] and in most standard text-books on Raman scattering.

For the sake of completeness, the most important results of a quantum mechanical description, elusive to the classical treatment, are mentioned in the following. The general form of the Hamiltonian is

$$H = H_0 + H_{el-phot} + H_{el-phon} + H_{phon-phon}, \tag{3.10}$$

consisting of two parts: one part describing the unperturbed system and the other part the electron-photon, electron-phonon and phonon-phonon interactions. The interaction terms can account for finite phonon lifetimes (inversely proportional to the phonon linewidth) and for coupling to the electronic continuum which can result in asymmetric phonon lineshapes as e.g. present in Fano profiles [138]. From Fermi's golden rule together with perturbation theory the transition matrix element of two-band scattering scenarios of an electron can be derived and one obtains an expression similar to Eq. 3.8 for the Raman scattering cross section, now including resonance enhancement effects for energies coinciding with the bandgap of an electron-hole excitation. Further, the scattering cross section can also be expressed in terms of a dynamical structure factor $S(\boldsymbol{q}, \omega)$ which is related to the imaginary part of a density-density response function. With χ'' being the imaginary part of the effective Raman response function and the Bose factor $n = 1/(e^{\frac{\hbar\omega}{k_B T}} - 1)$, the structure factor becomes

$$S(\boldsymbol{q}, \omega) = -\frac{\hbar}{\pi}[n+1]\chi''(\boldsymbol{q}, \omega), \tag{3.11}$$

and is directly proportional to the measured Raman intensity. The study of such an electronic background in the spectrum [see also the red colored region in Fig. 3.2] was found to be an important probe in superconducting materials where strong redistributions of spectral weight occur at T_c and depend on the symmetry of the superconducting gap [128].

3.1.3 Raman mode symmetry and selection rules of nickelates

A general classification of collective lattice vibrations is given by group theory [139]. Each normal mode of vibration consists of stretches, bends, and other displacements that form a basis for an *irreducible representation* (irrep) in the character table of the point group with the same symmetry as that of the non-equivalent occupied sites in the crystallographic unit cell. The irreps and character tables for the 32 crystallographic point groups are listed in the *international tables of crystallography* [140]. The number of non-degenerate vibrations is equal to the number of symmetry operations in the unit cell, while the total number of vibrations is given by $3s$, where s is the number of atoms per unit cell. The $3s$ vibrations divide into $3s - 3$ optical and 3 acoustic modes. Usually the irreps are denoted by the so-called Mulliken symbols. The Mulliken symbols relevant for this thesis are explained in Table 3.1.

The complete set of normal vibrational modes then divides into (i) Raman active, (ii) infrared active, and (iii) silent modes. Generally, even modes ($R_{ij} = R_{ji}$) are Raman-allowed in crystal structures containing a center of inversion, while the odd modes ($R_{ij} = -R_{ji}$) are Raman-forbidden. This is opposed to IR modes carrying a dipole moment and coupling directly to light. The universal concept for determining a material's Raman active modes is to first identify its space group and subsequently the position and site symmetry of each atom in the unit cell. Finally the irreps of the zone center phonons resulting from the occupied atomic sites in the unit cell can be derived. A step-by-step recipe for the derivation is given by Rousseau *et al.* in

Table 3.1 Mulliken symbols for irreducible representations. A, B correspond to singly degenerate or one dimensional modes, whereas E is doubly degenerate or two dimensional. In standard convention the z-axis is the principal axis of the system.

A	symmetric with respect to 90° rotation around the principle axis (1D)
B	anti-symmetric with respect to 90° rotation of the principle axis (1D)
E	in-plane mode (2D)
subscript 1	symmetric with respect to a vertical mirror plane perpendicular to the principal axis
subscript 2	anti-symmetric with respect to a vertical mirror plane perpendicular to the principal axis
subscript g	symmetric with respect to the inversion (even mode)
subscript u	anti-symmetric with respect to the inversion (odd mode)

Ref. [141]. The Raman selection rules then follow from the entries of the Raman tensors according to the irreps. For the case of ABO_3 perovskite crystal structures all possible normal modes are derived in Ref. [142]. This overview is particularly useful as the atomic displacement patterns are grouped according to the 15 Glazer tilt systems [143, 144]. Several of these tilt systems were found to be present in the rare-earth nickelates. Moreover, in thin nickelate films and heterostructures the type of the tilt system can me manipulated via the epitaxial relation to the substrate or a second-component material of the heterostructure.

When the shape of the Raman tensor is known for a specific space group it follows from Eq. 3.9 which modes can be probed by different experimental polarization configurations. The scattering configuration is usually described in the *Porto notation*. It has the form $i(kl)j$, where i and j correspond to the propagation directions of the incident and the scattered light respectively, while k and l denote the polarizations of their corresponding electric fields.

In the following the Raman tensors of rare-earth nickelates are discussed for the relevant space groups: $R\bar{3}c$ (No. 167), $C2/c$ (No. 15), $Pbnm$ (No. 62), and $P2_1/n$ (No. 14).

Selection rules of $LaNiO_3$

The rhombohedral $R\bar{3}c$ symmetry of bulk $LaNiO_3$ can be obtained from the undistorted cubic perovskite by a trigonal lattice distortion along the [111]-body diagonal that doubles the primitive unit cell concurrent with octahedral rotations, which are equal in magnitude and alternate in sign about each pseudocubic direction [Fig. 3.3(a)]. This is the $a^-a^-a^-$ tilt system in Glazer notation [143, 144]. The relation between the

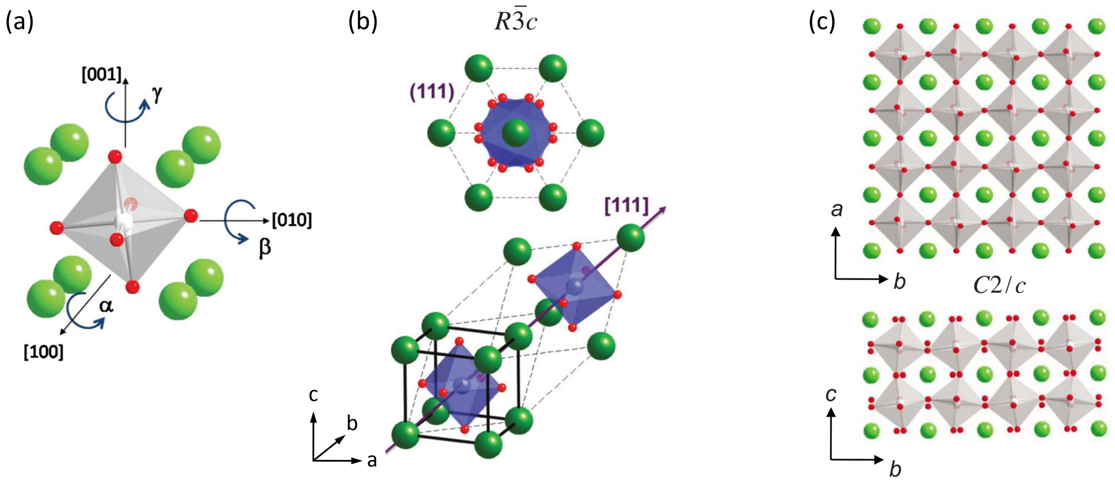

Figure 3.3 LaNiO$_3$ in $R\bar{3}c$ and $C2/c$ symmetry. (a) Schematic of NiO$_6$ octahedron rotation in pseudocubic reference frame. The tilt angles along the pseudocubic directions are α, β, and γ. Subsequent in -or out-of-phase rotations along an axis are characterized in the Glazer notation. La atoms are shown in green, Ni in gray (blue), and oxygen in red. (b) Bulk LaNiO$_3$ in space group $R\bar{3}c$ with the Glazer tilt pattern $a^-a^-a^-$. Tilt angles are $\alpha = \beta = \gamma = 5.2°$. The top panel shows the antiphase octahedra tilts along the [111] direction. The bottom panel relation between the pseudocubic (solid lines) and the rhombohedral (dashed line) unit cell. (c) Projections of the atomic structure of LaNiO$_3$ epitaxially grown on SrTiO$_3$ exhibiting monoclinic space group $C2/c$. Tilt angles are $\alpha = \beta \approx 7.1°$ and $\gamma \approx 0.3°$. Panel (a) and (c) are from Ref. [146] and panel (b) is from Ref. [147].

pseudocubic and the rhombohedral unit cell is illustrated in Fig. 3.3(b)]. Note that the rhombohedral system can equally be described in hexagonal basis. The transformation between the cubic, rhombohedral and hexagonal unit cell is given in Refs. [140, 145].

In bulk, LaNiO$_3$ exhibits space group $R\bar{3}c$ down to lowest temperature. The 10 atoms in the primitive rhombohedral $R\bar{3}c$ unit cell (Schoenflies symbol D_{3d}^6) give rise to 30 zone-center vibrational modes

$$\Gamma = A_{1g} + 4E_g + 2A_{1u} + 3A_{2g} + 4A_{2u} + 6E_u \tag{3.12}$$

with the E_g and E_u modes being two-dimensional irreducible representations. The five Raman active modes are

$$\Gamma_{Raman} = A_{1g} + 4E_g. \tag{3.13}$$

The involvement of the different atomic species in the 30 vibrational modes together with their site symmetries can be found in Ref. [142]. The reference also gives a similar overview on the other crystallographic systems discussed later in the text. Wyckoff positions of bulk LaNiO$_3$ together with fractional atomic coordinates can be found in Ref. [148]. From group theory it can further be shown that the structural transition from high-symmetry cubic $Pm3m$ to rhombohedral $R\bar{3}c$ corresponds to a Γ_{25} phonon soft-mode collapse at the R-point of the cubic lattice [149].

The $R\bar{3}c$ Raman tensors are

$$A_g = \begin{pmatrix} a & 0 & d \\ 0 & a & 0 \\ d & 0 & b \end{pmatrix}, \quad E_{1g} = \begin{pmatrix} c & 0 & 0 \\ 0 & c & d \\ 0 & d & 0 \end{pmatrix}, \quad E_{2g} = \begin{pmatrix} 0 & c & d \\ c & 0 & 0 \\ d & 0 & 0 \end{pmatrix}. \tag{3.14}$$

When $LaNiO_3$ is grown as thin film on a perovskite substrate [Fig. 3.3(c)] it has been reported to exhibit monoclinic space group $C2/c$ [146,150], which is a subgroup of $R\bar{3}c$. Essential group-subgroup relations of perovskite systems can be found in Ref. [151]. In the thin $LaNiO_3$ films of $C2/c$ symmetry the accommodation of epitaxial strain has altered the Glazer tilt pattern from $a^-a^-a^-$ to $a^-b^-b^-$. It is noted that in some studies the setting $I2/c$ is used instead of $C2/c$ [150]. The conversion between the two settings is given in Ref. [140]. For the most part of the thesis we will refer to setting $C2/c$. In more detail, our notation corresponds to $I\frac{2}{c}11$ (cell choice 3 with unique axis a) and $C1\frac{2}{c}1$ (cell choice 1 with unique axis b). The $LaNiO_3$ Wyckoff positions in setting $C2/c$ are given in Ref. [146].

The 10 atoms of the $C2/c$ (C_{2h}^6) unit cell give rise to 30 zone center modes

$$\Gamma = 5A_g + 7B_g + 8A_u + 10B_u. \tag{3.15}$$

The 12 Raman active modes are

$$\Gamma_{Raman} = 5A_g + 7B_g, \tag{3.16}$$

and the $C2/c$ Raman tensors are

$$A_g = \begin{pmatrix} b & 0 & d \\ 0 & c & 0 \\ d & 0 & a \end{pmatrix}, \quad B_g = \begin{pmatrix} 0 & f & 0 \\ f & 0 & e \\ 0 & e & 0 \end{pmatrix}. \tag{3.17}$$

Selection rules of $NdNiO_3$

The high-temperature space group of nickelates other than $LaNiO_3$ is orthorhombic $P\frac{2_1}{b}\frac{2_1}{n}\frac{2_1}{m}$, or in short: $Pbnm$. The corresponding Glazer tilt pattern is $a^-a^-b^+$. The standard setting of the space group is $Pnma$, however often the setting $Pbnm$ is preferred since here the c axis is the long axis. The transformation between $Pbnm$ and $Pnma$ corresponds to a cyclic permutations of the a, b, and c axis

$$\begin{gathered} Pnma \Leftrightarrow Pbnm \\ a \Leftrightarrow b \\ b \Leftrightarrow c \\ c \Leftrightarrow a \end{gathered}$$

Fig. 3.4(b) shows the $Pbnm$ unit cell of $NdNiO_3$. The corresponding structural data and the Wyckoff positions can be found in Ref. [64]. The primitive unit cell contains 20 atoms giving rise to 60 normal modes of vibration at the center of the Brillouin zone. In $Pbnm$ (D_{2h}^{16}) the vibrations are

$$\Gamma = 7A_{1g} + 7B_{1g} + 5B_{2g} + 5B_{3g} + 8A_u + 8B_{1u} + 10B_{2u} + 10B_{3u}. \tag{3.18}$$

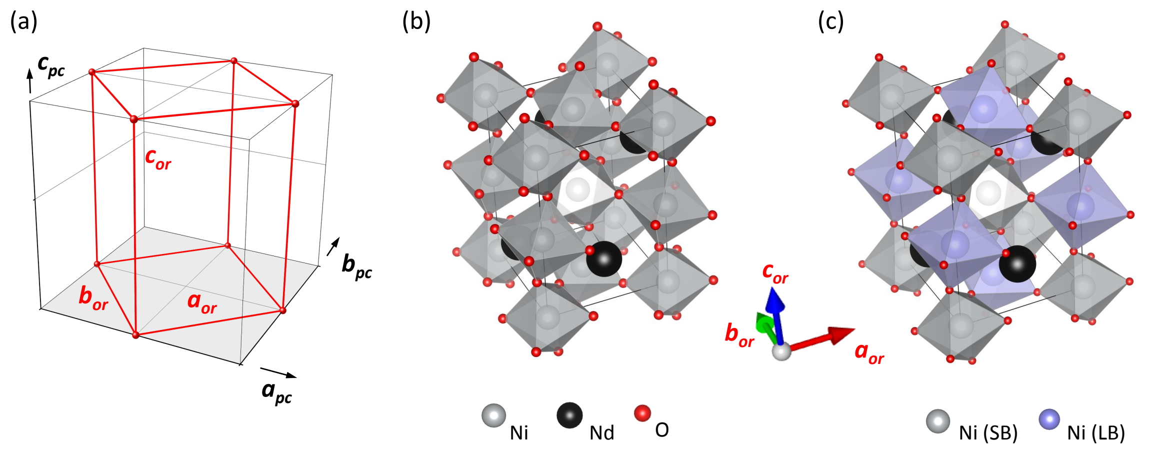

Figure 3.4 $\mathbf{NdNiO_3}$ in *Pbnm* and $P2_1/n$ symmetry. (a) Orthorhombic *Pbnm* unit cell (red) in the pseudocubic reference frame (black). (b) Schematic of the bulk $NdNiO_3$ in space group *Pbnm* with the Glazer tilt pattern $a^-a^-b^+$. (c) Bulk $NdNiO_3$ in space group $P2_1/n$ with short-bond (SB, gray) and long-bond (LB, blue) NiO_6 octahedra. Panel (a) is from Ref. [152]. Panel (b) and (c) are based on structural data from Ref. [64].

All the 24 even modes are Raman active

$$\Gamma_{Raman} = 7A_{1g} + 7B_{1g} + 5B_{2g} + 5B_{3g}. \tag{3.19}$$

For *Pnma* the Raman modes are denoted as $7A_{1g} + 5B_{1g} + 7B_{2g} + 5B_{3g}$. The Raman tensors of *Pbnm* are

$$A_{1g} = \begin{pmatrix} a & 0 & d \\ 0 & b & 0 \\ d & 0 & c \end{pmatrix},$$

$$B_{1g} = \begin{pmatrix} 0 & d & 0 \\ d & 0 & 0 \\ 0 & 0 & 0 \end{pmatrix}, \; B_{2g} = \begin{pmatrix} 0 & 0 & e \\ 0 & 0 & 0 \\ e & 0 & 0 \end{pmatrix}, \; B_{3g} = \begin{pmatrix} 0 & 0 & 0 \\ 0 & 0 & f \\ 0 & f & 0 \end{pmatrix}. \tag{3.20}$$

With decreasing temperature the nickelates experience a structural phase transition from orthorhombic *Pbnm* to monoclinic $P2_1/n$, as the uniformly sized NiO_6 octahedra split into two sets of SB and LB octahedra and the *b* mirror symmetry is lost [Fig. 3.4(c)]. Our notation $P2_1/n$ corresponds to $P1\frac{2_1}{n}1$ (cell choice 2 with unique axis *b*).

The 20 atoms of the $P2_1/n$ (C^5_{2h}) unit cell yield 60 zone center modes

$$\Gamma = 12A_g + 12B_g + 18A_u + 18B_u, \tag{3.21}$$

with 24 Raman active vibrations

$$\Gamma_{Raman} = 12A_g + 12B_g. \tag{3.22}$$

The Raman tensors of $P2_1/n$ are

$$A_g = \begin{pmatrix} a & 0 & d \\ 0 & b & 0 \\ d & 0 & c \end{pmatrix}, \qquad B_g = \begin{pmatrix} 0 & e & 0 \\ e & 0 & f \\ 0 & f & 0 \end{pmatrix}. \tag{3.23}$$

The relative intensity of the Raman lines in different polarization configuration can now be calculated from Eq. 3.9. An overview is given in Table. B.1 in Appendix B. In some cases also Raman frequencies can already be calculated from rather simple lattice dynamical calculations based on a shell model and compared to experimental spectra. A prototypical study was performed by Abrashev *et al.* [153] on orthorhombic $CaMnO_3$ exhibiting space group $Pnma$. Since the material's crystallographic symmetry and the 24 Raman active lattice displacement patterns are closely related to the orthorhombic nickelates, they are shown exemplarily in Fig. 3.5. However a proper calculation of phonon frequencies and eigenvectors of nickelates is more complex, due to the interplay of the lattice dynamics and the electronic bandstructure, and requires treatment by *ab-initio* methods.

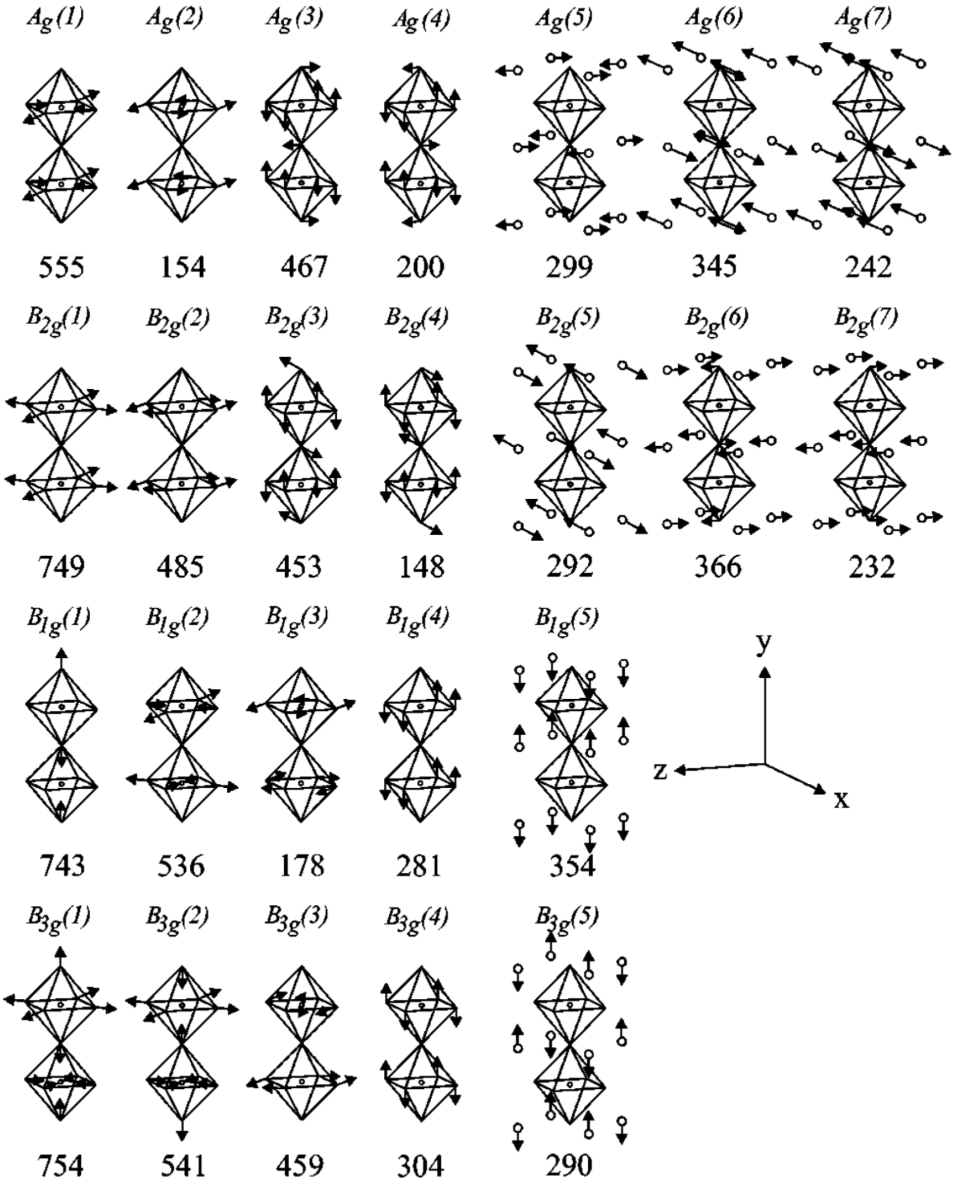

Figure 3.5 Raman active modes of perovskites with *Pnma* space group. Lattice displacement patterns of of Raman active modes of $CaMnO_3$. Mode symmetries and calculated frequencies are indicated. The figure is from Ref. [153].

3.1.4 Raman instrumentation

Different Raman setups are used depending on the type of the investigation. For studies of large crystalline samples or liquids usually *macro Raman setups* are used, sampling cm^3 volumes in different scattering and transmission measurement geometries. *Micro Raman setups* are generally used to probe smaller samples. The incident laser light is focused by an appropriate microscope objective and they mostly operate in backscattering geometry. A more detailed description of the setups and operational modes can be found in Ref. [154]. For our experiments on thin and ultra-thin nickelate heterostructures we have used a commercially available HORIBA JOBIN YVON LabRAM HR800 spectrometer which is an integrated micro Raman system [Fig. 3.6(a)], with the microscope coupled confocally to a 800 mm focal length spectrograph.

The schematic of the optically active elements of the instrument and the laser beam path is shown in Fig. 3.6(b). The laser (632.8 nm in our case) enters the optics compartment at *Iris I1* and a *plasma filter* suppresses any additional laser lines that might be present in the light. Subsequently filters of different opacity can be chosen from the *filter wheel* and attenuate the light to the required degree. A *Fresnel rhomb* then rotates the polarization plane of the linearly polarized beam with respect to the crystallographic orientation of the sample. At the laser injection-rejection system (LIRS) a holographic *notch filter* reflects the beam towards the *microscope*, where it is focused onto the sample. The backscattered light (scattered elastically and inelastically) is guided back to the LIRS component where only the inelastic part is transmitted through the notch filter towards the *confocal hole* and the *spectrograph*. Optional optic elements such as *polarization analyzer* and ultra-low frequency filter (second notch filter) can be inserted to the beam path between the LIRS and the confocal hole. In the spectrograph the diverging beam is first collimated by a spherical mirror (800 mm focal length) and the parallel beam then is reflected onto an optical grating. The diffracted first order is collected by another spherical mirror (800 mm focal length) and focused onto the CCD camera.

Several features distinguish the LabRAM HR800 spectrometer from other micro Raman setups: these are (i) the confocal construction of the beam path in combination with (ii) a highly precise scanning of the focus position in vertical direction, and (iii) an internal laser diode which enables for an extremely accurate alignment of all optical components with respect to the confocal hole. As will be shown in the following section and in chapter 4 the interplay of these three features allows for the detection of Raman signals from TMO heterostructures with an active layer thickness of only a few nm.

3.1.5 The confocal z-scan technique

The confocal optics of the Raman setup illuminate the sample by a diffraction limited spot which is imaged on an ideally point-like detector. Practically, the point-like detector is realized with an adjustable pinhole the so-called *confocal hole* in front of the real detector (or the spectrograph entrance slit). The major effect of confocal sampling is the reduction of the depth of focus which results in a increased discrimination of the

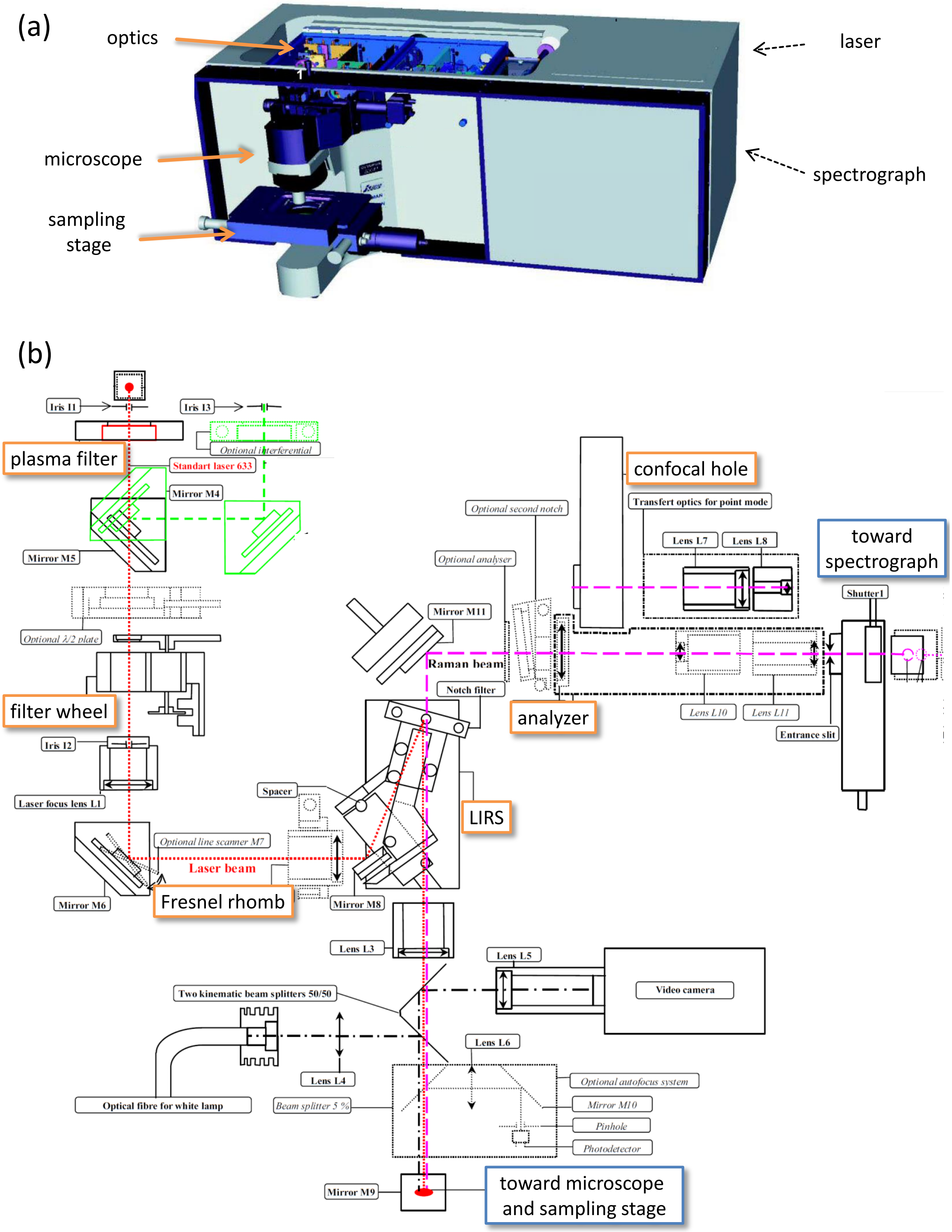

Figure 3.6 The LabRAM HR800 Raman spectrometer. (a) Schematic showing the main components of the Raman spectrometer. In the optics compartment the laser beam is filtered and polarized in the appropriate way for the Raman scattering process. The microscope focusing the beam onto the sample is equipped with a motorized xy stage that also allows translation in z-direction. The backscattered light is guided to the spectrograph where the Raman signal is dispersed into its constituent parts for detection by the CCD detector (not shown here). The laser is mounted externally on an extended chassis at the back of the system (not shown here). (b) Detailed schematic of the optics with the most crucial components indicated in orange boxes. The components are described in the text. The figure is adapted from Ref. [155].

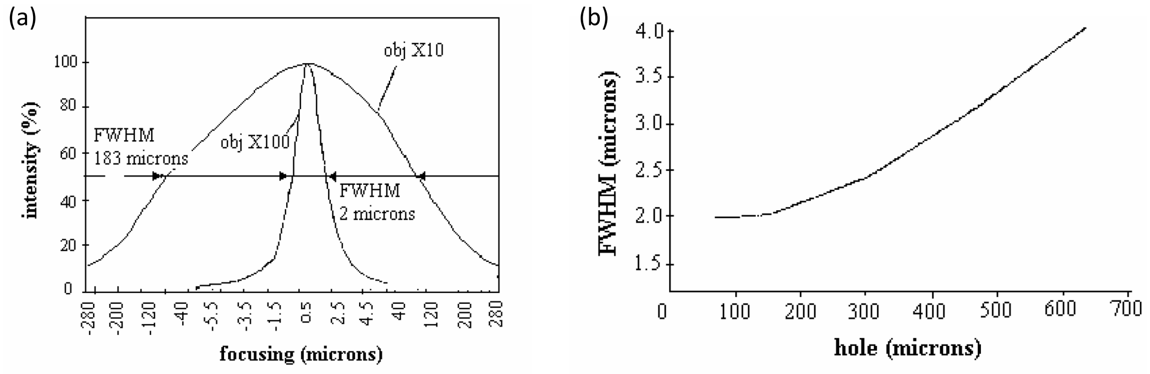

Figure 3.7 Confocal performance of LabRAM HR800 spectrometer. (a) Raman intensity of the 515 cm^{-1} silicon line as the surface of a silicon wafer is scanned through the focus of a ×10 (NA 0.25) and a ×100 (NA 0.9) microscope objective. (b) FWHM for the ×100 objective as a function of the aperture of the confocal hole. The figure is from Ref. [155].

Raman signal along the three spatial directions. In our case of thin heterorstructures grown on a substrate the resolution along the vertical sampling direction (z-direction) is paramount.

The confocality of the LabRAM HR800 has been characterized by tests on a flat silicon wafer as reported in Ref. [155] and shown in Fig. 3.7. The silicon surface was scanned through the focus spot of the microscope objective by the motorized sample stage [see also Fig. 3.8(a)] and the Raman intensity of the 515 cm^{-1} silicon line was tracked. Silicon exhibits a short penetration depth at visible wavelengths, hence such a confocal Raman z-scan basically models a scan of an infinite plane of infinitesimal thickness. The Raman intensity is plotted as function of the sample stage position in Fig. 3.7(a). For large values of z the intensity is low since the image of sample is out of focus on the sharp confocal hole. The maximum intensity is reached when the silicon surface is on the focus of the laser spot. For negative z-values with the focus inside the wafer the intensity decreases again due to the limited penetration depth of the laser light. The full width half maximum (FWHM) of the intensity peak strongly depends on the magnification of the microscope objective, i.e. on the sharpness of the focus. Further, the aperture of the confocal is crucial for a high spatial discrimination of the Raman signal along the z-direction [Fig. 3.7(b)]. The closing mechanism of the confocal hole is motorized and its diameter can be adjusted between 0 and 1000 μm (scaled on the sample by a factor 1.4× objective magnification). The smaller the confocal hole, the higher the z-discrimination, which however comes at the cost of a decreasing overall Raman signal[2]. The curve in Fig. 3.7(b) saturates when hole aperture becomes smaller than the image of the illuminated part of the sample on the hole.

Whereas it is well known that confocal Raman spectroscopy can yield depth profiles of condensed matter material systems and liquid solutions with μm resolution [156–159]

---

[2] In the LabRam HR800 setup the confocal hole acts also as the entrance pinhole of the spectrometer. Therefore, a reduction of the confocal hole diameter is detrimental to the overall signal detection.

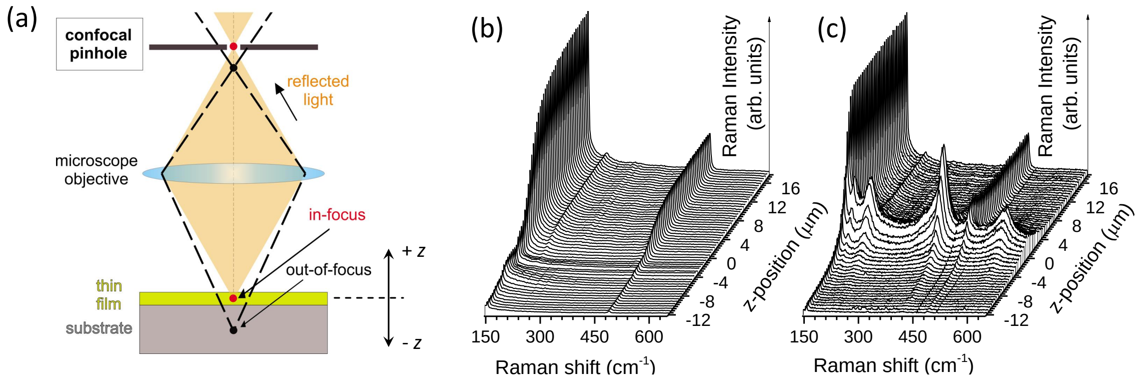

Figure 3.8 The confocal z-scan technique. (a) Schematic of the principle of confocal Raman spectroscopy applied to a thin film on a substrate. The confocal hole rejects residual scattered light from out-of-focus points leading to a suppression of the substrate contribution in the spectrum. The microscope sample stage can be moved in vertical direction (z-scan) in order to precisely attune the focus spot with the thin film position (z=0 μm). (b) z-scan of a $LaAlO_3$ single crystal substrate demonstrating the concept of vertical scanning. (c) The same procedure as in (b) but with a 21 nm $LaNiO_3$ film grown on the surface of the $LaAlO_3$ crystal. The $LaNiO_3$ phonon modes are visible in a narrow range of z values when the focus of the laser coincides with the film ($z = 0$).

there are only few reports on TMO heterostructures achieving a sub-μm resolution [160, 161] and to the best of our knowledge a clear discrimination of signals from layers with thicknesses of the order of 1 - 10 nm has not been reported yet[3,4]. In the following it is demonstrated that the confocal z-scan is a is a powerful tool that allows to discriminate the Raman signal of TMO films with a thickness of only a few nm from the signal of the substrate they are grown on.

In more detail, we have grown and studied nickelate heterostructures on perovskite oxide substrates. For the most part our substrates are transparent with respect to the 632.8 nm excitation line of our HeNe laser, and confocal z-scans of the bare substrates are comparable to the scan of a $LaAlO_3$ single crystal shown in Fig. 3.8(b). The scan is recorded at a confocal hole diameter of 50 μm with a ×100 (NA 0.6) long-working-distance objective at a stepwidth of 0.5 μm in the z-direction. These are the optimized parameters used later for our measurements on nickelate heterostructres with a total thicknesses of $\sim$10 nm or less. The z-scan of the transparent substrate is distinct from the scans of the Si wafer shown in Fig. 3.7(a). When the surface at z=0 is approached the Raman intensity increases and saturates for larger z values instead of decreasing again when the focus spot is in the bulk of the crystal. Note that in our

---

[3] For completeness it is mentioned that the Raman response of different components of thin TMO multilayer systems has been successfully discriminated in specific cases, e.g by using different excitation laser lines, corresponding to different optical penetration depths [162, 163]. Also ultraviolet Raman spectroscopy allows to distinguish the signal of a $\sim$25 nm TMO film from its $SrTiO_3$ substrate [5]. However, the confocal z-scan technique we introduce here is a much more general approach, which is not restricted to a certain laser wavelength or particular compositions of a multilayer system.

[4] Note that the Raman scattering cross section of many TMOs is inherently small, which is in opposition to thin slabs of strong Raman scatterers such as monolayers of graphene. This already makes the measurement of thin TMO layers difficult, let alone the discrimination of the signal from different TMO components.

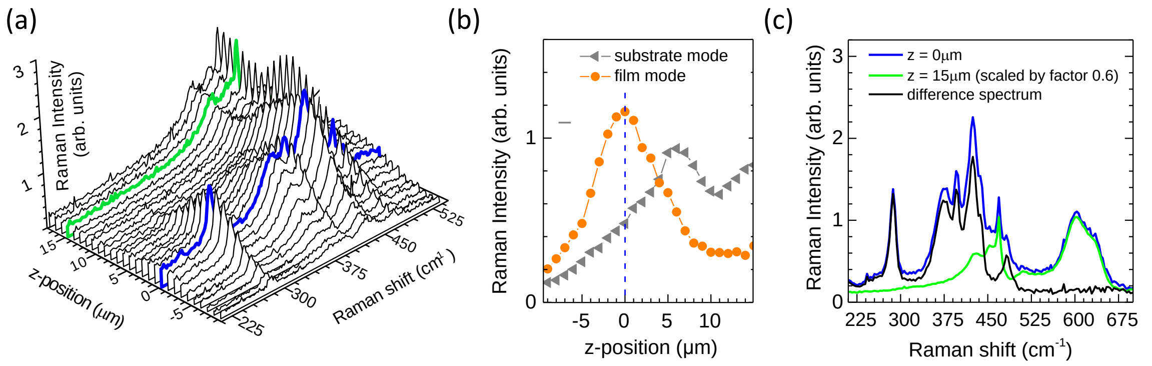

Figure 3.9 Confocal z-scan of $PrNiO_3$ on LSAT. (a) z-scan of 12 nm $PrNiO_3$ on LSAT at $T = 10$ K. $PrNiO_3$ phonon modes are visible in a narrow range when the focus of the laser coincides with the film around z=0 (blue spectrum). For larger z values only LSAT substrate modes are observed (green spectrum). (b) Dependency of the intensity of the film mode at 285 cm^{-1} and the substrate mode at 470 cm^{-1} on the z-position. (c) The z=0 (blue) and z=15 μm Raman spectra (green) from panel (a) and their difference. The spectrum at z=15 μm is scaled by a factor (here 0.6) and subtracted from the one at z=0 μm in order to obtain a spectrum free of substrate contributions and showing only the Raman modes of the film (black). The correct scaling factor is obtained from a spectral range where only substrate modes are present.

definition negative z values correspond to the focus above the sample surface.

Fig. 3.8(c) shows the same scanning procedure applied to a $LaNiO_3$ thin film grown on the $LaAlO_3$ substrate. A pronounced emergence of $LaNiO_3$ phonon modes can be observed in a narrow range of z values when the focus of the laser coincides with the film. The onset z=0 is defined as the position of the maximum intensity of the film Raman modes. A close inspection of Fig. 3.8(c) reveals that at z=0 also the substrate modes give a (small) contribution to the Raman spectrum. A further reduction of the confocal pinhole aperture decreases this contribution, however the overall intensity decreases accordingly.

Thus, we define the following strategy for nickelate films showing an overlap with substrate modes: (i) the confocal hole is closed as much as possible without loosing too much total intensity and (ii) a spectrum of high z value is subtracted from the z=0 spectrum. This concept demonstrated in Fig. 3.9(a)-(c) on a 12 nm $PrNiO_3$ film grown on LSAT: By subtracting the Raman spectrum of $z = 15$ μm (which contains solely substrate phonon modes) from the $z = 0$ spectrum (film modes with small contributions from substrate modes), one can obtain the spectrum of the film free from substrate contributions with no need to measure a reference spectrum from an additional bare substrate. As a consequence also uncertainties and deviations which could occur by misalignment of a reference substrate when it is mounted or moved to measure in different geometries and polarizations can be excluded.

In the following, all film spectra shown are already corrected by the substrate contribution, except for spectra of films grown on $LaAlO_3$ substrates.

Temperature dependent measurements were performed in a CryoVac KONTI-micro cryostat. The sample's mounting position is in vacuum and the focusing optics are

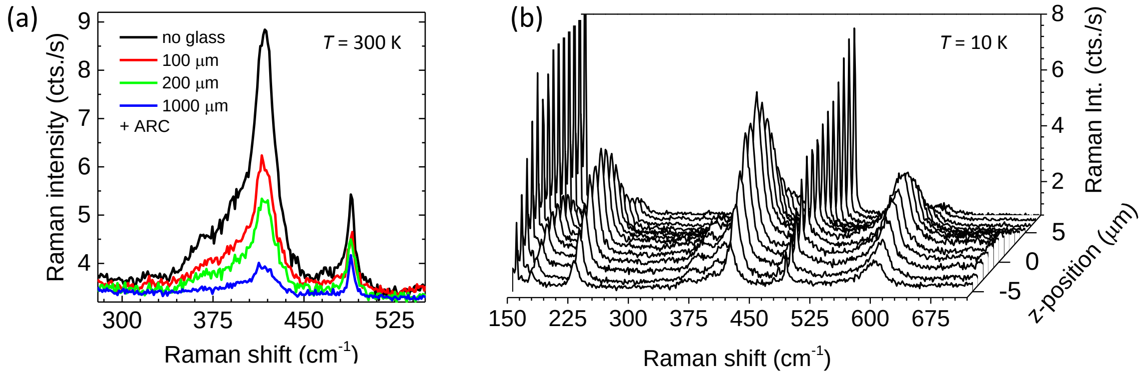

Figure 3.10 Cryostat glass windows and confocal z-scan at low temperatures. (a) Intensity of the Raman spectrum of 21 nm $LaNiO_3$ on $LaAlO_3$ substrate in dependency of the cryostat glass window. The black curve is measured without glass window and the blue curve with the conventional 1000 μm thick suprasil window with anti-reflection coating (ARC). The E_g bending mode of $LaNiO_3$ at 415 cm^{-1} decreases by $\sim$ 90% after the glass window is inserted to the laser light path. The intensity of the substrate mode at 490 cm^{-1} decreases by $\sim$ 50%. By a customized thinning process of the glass windows up to $\sim$ 50% of the intensity of the film mode can be recovered (green and red curve). (b) Demonstration of a confocal z-scan for the 21 nm $LaNiO_3$ on $LaAlO_3$ substrate with a 100 μm thick cryostat window at T = 10 K. Film modes exhibit a peak-like envelope as a function of z whereas $LaAlO_3$ substrate mode increase in intensity for larger z.

outside of the cryostat. Hence, the laser passes the cryostat glass window before and after scattering on the sample. As a consequence the focusing of the laser beam is deteriorated and the signal-to-noise ratio of the film spectrum in a z-scan becomes worse. Fig. 3.10(a) shows a direct comparison of the z=0 spectra of a $LaNiO_3$ film with and without glass window in the laser beam path. The commonly used 1000 μm suprasil glass window which is anti reflection coated reduces the film mode intensity by more than 90%. A careful procedure of mechanical polishing of the glass, thinning it down to 100 μm can recover up to $\sim$ 50% of the original Raman intensity. Additional tests with materials exhibiting other refractive indices than suprasil glass did not bring significant improvements. Hence, for the following low-T measurements the custom-made suprasil windows with thicknesses of 100 μm or less were used [Fig. 3.10(b)].

Moreover the presence of the glass reduces the laser power on the samples allowing for working conditions free from heating effects. In this respect preliminary test measurements were performed with a series of different attenuating filters and it was found that with laser power < 1 mW (measured before the glass) the Raman spectra were not affected by laser heating at least within our detection sensitivity. In particular, by comparing the fast drop of the intensity of new phonon modes only observed below a the critical temperature of a phase transition (see later in the text) for higher laser powers with data acquired with less than 1 mW, we could conclude that our Raman temperatures have an uncertainty not larger than 5 K.

3.1.6 Analysis of the Raman data

A detailed analysis of the recorded Raman spectra was performed by fitting the phonon peaks with Voigt profiles and plotting the evolution of characteristic parameters such as (integrated) intensity, linewidth, and Raman shift as a function of temperature. The correspondence between the experimental peak profiles and the mathematical form of Voigt line-shape is well-established for Raman spectroscopy and is also standard in many spectroscopic techniques. The Voigt profile results from the folding of a Gaussian resolution function and a Lorentzian function

$$I(q) = \int_{-\infty}^{\infty} G(q')L(q-q')dq', \tag{3.24}$$

with $G(x) = \frac{1}{\omega\sqrt{\pi \ln 2}} e^{-(\ln 2\ x^2)/\omega^2}$ and $L(x) = \frac{C}{1+(x/\nu)^2}$, such that 2ω and 2ν are FWHM of the Gaussian and Lorentzian functions, respectively. In the Raman fits the Voigt profiles are a convolution of the Lorentzian phonon lineshape with the Gaussian lineshape imposed by the instrumental resolution function.

The resolution of the LabRAM HR800 spectrometer was determined to be ~ 2 cm^{-1} from measuring the spectrum of a discharge lamp containing Neon gas. The intrinsic linewidth of the Neon emission lines is extremely sharp, i.e. the recorded spectrum of such a line is dominated by the gaussian broadening of the spectrometer and yields the spectrometer's resolution.

During extensive temperature series on the nickelate films we took spectra of the emission lines of the calibration lamp as reference. The spectral positions of the Neon emission lines serve as absolute reference and can reveal shifts of the energy scale due to variations of the room temperature or to mechanical drifts in the experimental setup. In all presented measurements we did not detect any shift within the experimental resolution, indicating a high stability and accuracy of the LabRAM HR800 setup.

3.2 Elastic x-ray scattering

Bundles of electromagnetic radiation with energies ranging from 100 eV to 100 keV – commonly known as x-rays – have come a long way since their discovery by W. C. Röntgen in 1895 [164]. Originally generated as diffuse rays in Crookes tubes and used to capture photographs of human bones and body parts, today's third generation light sources can produce highly collimated x-ray beams of astonishing brilliance [165]. Within these ~120 years manifold applications have emerged ranging from medical diagnosis to airport security and to full structural determination of viruses consisting of thousands of atoms. Most certainly, x-rays are one of the discoveries in the field of physics from which mankind has benefited the most and an end is still not in sight. Fourth generation light sources are coming of age with 10 orders of magnitude higher peak brilliance and coherent x-ray bundles. Few free electron laser (FEL) facilities worldwide are already available for experiments with this particular type of coherent radiation and many more will be realized in the next years and decades.

In solid state physics x-ray diffraction (XRD) is of enormous importance. State-of-the-art single-crystal or powder XRD is an accurate probe of structural properties and allows to determine atomic positions with precisions a few thousandths of an Angstrom and bond angles down to a few tenths of degrees. Scattering in resonance to atomic absorption edges allows for the investigation of novel electronic and magnetic ordering phenomena whose fingerprints are too faint to be detected with any other probe. In this work we employ x-ray diffraction and absorption spectroscopy as a non-destructive probe of structural, magnetic, charge, and orbital degrees of freedom in nickelate heterostructures.

3.2.1 Principles of x-ray scattering

The basics of x-ray physics and light-matter interaction can be found in Refs. [166–169]. The following sections briefly review the fundamental concepts as elucidated in these references, followed by a more detailed description of the principles used to analyze and interpret the experimental data shown in chapter 5.

Intensity of Bragg Reflections

In their seminal work, W.H. Bragg and W.L. Bragg derived the condition $2d\sin\theta = n\lambda$ for maximum intensity in the diffraction pattern of point charges arranged in a periodic lattice. Here, d is the distance between lattice planes irradiated by plane x-rays of wavelength λ impinging at an angle θ. The integer number n has the meaning of a reflection order. The Bragg equation is equivalent to M. v. Laue's conditions describing the relation between lattice vectors $\boldsymbol{R}$ and scattering vector $\boldsymbol{q}$ for crystals of arbitrary symmetry at the position of constructive interference.

Following this notion, in a classical description an atom can be modeled as electron density of spherical symmetry $\rho(\boldsymbol{r})$. In the simplest case of non-resonant, elastic scattering the atomic form factor f of an isolated atom with its center of mass at

$\boldsymbol{r} = 0$ reads as

$$f(\boldsymbol{q}) = \int \rho(\boldsymbol{r}) e^{-\imath \boldsymbol{q}\cdot\boldsymbol{r}} d\boldsymbol{r}, \tag{3.25}$$

with the integration over all positions $\boldsymbol{r}_i$ accounting for the unequal optical path lengths corresponding to the density distribution and yielding a phase shift between the diffracted wavefronts. The direction of the momentum transfer $\boldsymbol{q} = \boldsymbol{k}_{out} - \boldsymbol{k}_{in}$ points along the bisection of incoming and scattered light. For a set of different distance vectors $\boldsymbol{r}_i$ the variation of phase shifts $-\imath \boldsymbol{q}\cdot\boldsymbol{r}$ can be large, which together with the orbital smearing of the electron density will thus lead to a cessation of coherency and a reduction in the coherently scattered intensity. This reduction increases further for larger $\boldsymbol{q}$. In the limit of $\boldsymbol{q} = 0$ the integration is merely over the charge distribution and yields the number of electrons of the atom Z.

In Eq. 3.25 important contributions, e.g. from a quantum mechanics, are not included yet. The full atomic form factor in dependence of the photon energy $\hbar\omega$ can be expressed as

$$f^{full}(\boldsymbol{q}, \hbar\omega) = f(\boldsymbol{q}) + f'(\hbar\omega) + i f''(\hbar\omega), \tag{3.26}$$

with f' accounting for ways electrons with different binding energies respond to the incoming field, and the term f'' arising from the binding energy acting as a damping mechanism to the otherwise free electron density. In analogy to optics, f' would correspond to the refraction of light while f'' would correspond to the absorption. Tabulated values of the energy dependent form factor are given for instance in the Henke tables [170].

In a crystal lattice the atoms are arranged periodically and the contribution of each atom is summed discretely. The crystal structure factor $F^{cryst}(\boldsymbol{q})$ is given by

$$F^{cryst}(\boldsymbol{q}) = \sum_{\boldsymbol{R}_n} f(\boldsymbol{q}) e^{\imath \boldsymbol{q}\cdot\boldsymbol{R}_n} \tag{3.27}$$

with the position $\boldsymbol{R}_n$ of an atom in the crystallographic unit cell. Note that F^{cryst} is a complex quantity. The lattice vectors $\boldsymbol{R}_n$ and their corresponding reciprocal lattice vectors $\boldsymbol{G}$ are of the form

$$\boldsymbol{R}_n = n_1\boldsymbol{a}_1 + n_2\boldsymbol{a}_2 + n_3\boldsymbol{a}_3, \qquad \boldsymbol{G} = h\boldsymbol{a}_1^* + k\boldsymbol{a}_2^* + l\boldsymbol{a}_3^* \tag{3.28}$$

with the set of basis vectors $(\boldsymbol{a}_1, \boldsymbol{a}_2, \boldsymbol{a}_3)$ and n_i being integers. The $\boldsymbol{a}_i^*$ vectors are obtained by $\boldsymbol{a}_i^* = 2\pi(\boldsymbol{a}_j \times \boldsymbol{a}_k)/(\boldsymbol{a}_1 \cdot (\boldsymbol{a}_2 \times \boldsymbol{a}_3))$, where the i, j, k-indices follow cyclic permutation. It is clear from Eq. 3.27 that largest intensity $|F^{cryst}|^2$ is achieved when all scattered waves are in phase, which requires

$$\boldsymbol{q} \cdot \boldsymbol{R}_n = 2\pi \cdot \text{integer}. \tag{3.29}$$

This condition is fulfilled if and only if $\boldsymbol{q}$ coincides with a reciprocal lattice vector, equivalent to the Laue condition and therewith the Bragg condition.

The integers h, k, l may adopt any value between $-\infty$ and ∞, and the triple hkl are the Miller-indices specifying the points of intersection of the lattice planes with the unit cell edges. The structure factor thus depends on the Miller indices of the respective reflection, the positions of the atoms in the unit cell, and the atomic scattering factor. In a one atom basis it is

$$F^{cryst}(hkl) = \sum_{\boldsymbol{R}_n}^{N} f e^{2\pi\imath(hn_1+kn_2+ln_3)}. \tag{3.30}$$

The summation is up to N, denoting the number of unit cells in the crystal. For infinite N the structure factor exhibits the shape of a Dirac delta function whereas for real systems a broadening has to be taken into account. The simple cubic structure ($F^{cryst} = f$) gives rise to reflections for all combinations of hkl and all orders are observed. In symmetries lower than cubic the sum in Eq. 3.30 can become zero for specific combinations of the atomic coordinates (n_1, n_2, n_3) and the triple (hkl). These are the *selection rules* for x-ray diffraction. Probing the presence/absence of specific diffraction peaks is a powerful tool to determine the crystal structure symmetry and the crystallographic space group.

Interestingly, 'forbidden' reflections can be observed in some cases when the energy of the incoming light is tuned to the resonance of atomic absorption edges [171,172]. Such observations indicate that anisotropic crystals can distort the electronic wave function rendering the form factor into a non-trivial matrix form at resonant conditions.

For unit cells including several species of atoms the structure factor becomes

$$F^{cryst}(\boldsymbol{q}, \hbar\omega) = \sum_{\boldsymbol{r}_j}^{J} f^{full}(\boldsymbol{q}, \hbar\omega) e^{\imath\boldsymbol{q}\cdot\boldsymbol{r}_j} \sum_{\boldsymbol{R}_n}^{N} e^{\imath\boldsymbol{q}\cdot\boldsymbol{R}_n}, \tag{3.31}$$

where J is the number of distinct atoms in the unit cell. Also in this more complex case the structure factor has the mathematical form of a discrete Fourier transform, implying that the reverse transformation from the intensity of observed reflections allows to determine the real space atomic positions in the unit cell. However, the intensity scales with the product of the structure factor and its complex conjugate

$$I \propto |F^{cryst}|^2 = F^{cryst} \cdot F^{cryst\ *} \tag{3.32}$$

which entails loss of information. This is the well-known phase problem of x-ray diffraction.

Interaction of x-rays with matter in the optical approach

As already described in the scope of Raman scattering, solid state spectroscopy techniques exploit the interaction of light and matter to gain information about excitations and the physical state of condensed matter systems. The coupling of specific material properties to the light's electromagnetic field can drive the system into an out of equilibrium state which then can be probed by the spectroscopic technique of choice. In this section the emphasis is on resonant elastic x-ray scattering (REXS) which can enhance the scattering cross-section dramatically. Moreover REXS is an element-specific probe providing the possibility to measure states and excitations of certain components of the material only. As a consequence, in the past two decades

REXS has been established as one of the fundamental techniques to probe charge, spin, and orbital ordering in materials such as $3d$ transition metal oxides [75, 173–175].

Along the lines of the linear response theory of Raman scattering we use the same approach for soft x-ray scattering. In the soft x-ray regime ($\lambda \sim 15$ Å) the variation of the electric field $\boldsymbol{E} = \boldsymbol{\varepsilon} E_0 e^{-i(\omega t - \boldsymbol{k}\cdot\boldsymbol{r})}$ is still larger than the 'radius' of the XAS final state, or in other words, the electric field can be approximated as being constant at the position of the absorbing atom.

Recalling Eq. 3.2 we start with $\boldsymbol{P} = \chi \boldsymbol{E}$, where χ is the electrons's electric susceptibility and neglect higher order terms which can become relevant e.g. in pump-probe experiments on nickelates [53, 99, 100] but are not relevant for our absorption and scattering experiments with relatively low excitation fields and small perturbations. In the framework of a simple harmonic oscillator with frequency ω and the electromagnetic wave field $\boldsymbol{E}(t) = \boldsymbol{\varepsilon} E_0 e^{-i(\omega t - \boldsymbol{k}\cdot\boldsymbol{r})}$ as driving force ($\boldsymbol{\varepsilon}$ is a unit vector along the wave's polarization), velocity and acceleration of the electron are

$$\boldsymbol{j}(t) = \frac{\partial \boldsymbol{P}(t)}{\partial t} = -i\omega\chi\boldsymbol{E}(t), \qquad \boldsymbol{a}(t) = \frac{\partial \boldsymbol{j}(t)}{\partial t} = \omega^2\chi\boldsymbol{E}(t). \tag{3.33}$$

With the absorption process corresponding to the damping of the oscillatory motion of the electron the absorbed power is given by the time-averaged work

$$W = \frac{1}{T}\int_0^T \boldsymbol{F}\cdot\boldsymbol{j}dt = \langle \boldsymbol{E}\cdot\boldsymbol{j}\rangle = \frac{1}{2}Re[\boldsymbol{E}^*\cdot(-i\omega\chi)\boldsymbol{E}] \tag{3.34}$$

At this point we introduce the conductivity as $\sigma \equiv \omega\chi$. Taking into account the optical theorem and considering forward scattering ($\boldsymbol{q} \approx 0$), the scattered intensity is $I \sim |f^{full}(\hbar\omega)|^2$ and $Im[f^{full}(\hbar\omega)] \propto -E\sigma$ or

$$I_{XAS} \propto -1/E \; Im[f^{full}(\hbar\omega)], \tag{3.35}$$

with $E = \hbar\omega$. Note that this corresponds to the general notion that the XAS process is linked to the imaginary part of the atomic form factor f^{full}. It follows for the absorbed and the scattered intensities

$$I_{XAS} = \frac{1}{2}Im[\boldsymbol{\varepsilon}^*_{out}\cdot\sigma\cdot\boldsymbol{\varepsilon}_{in}], \tag{3.36}$$

$$I_{REXS}(\hbar\omega) = \frac{|\boldsymbol{E}_{out}|^2}{|\boldsymbol{E}_{in}|^2} \propto |\boldsymbol{\varepsilon}^*_{out}\cdot\;\sigma\cdot\boldsymbol{\varepsilon}_{in}|^2. \tag{3.37}$$

Generally the conductivity σ is a second rank tensor with complex entries arising from the solution to the differential equation of a damped oscillator. Real and imaginary part are Kramers-Kronig related [176].

3.2.2 X-ray absorption spectroscopy

From the near edge fine structure in the XAS the local geometric, electronic, and orbital structure of matter can be determined. Spectroscopy experiments performed

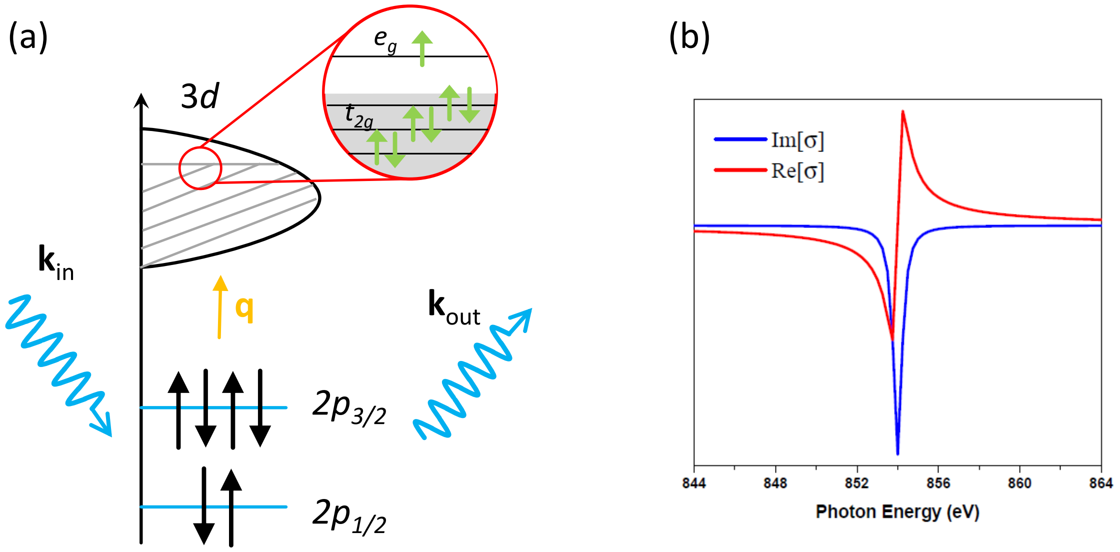

Figure 3.11 Energy level diagram of $3d$ TMO system and conductivity tensor σ. (a) Illustration of the photon-in photon-out process for $2p \rightarrow 3d$ excitations with the momentum transfer $\mathbf{q}$. A $3d^7$ system with the crystal field separating the t_{2g} and e_g levels into a low spin state is shown. Furthermore, spin-orbit coupling splits the $2p$ core-hole state into $2p_{3/2}$ and $2p_{1/2}$. The splitting is usually ~10 eV for these systems. The two resulting transitions are L_3: $2p_{3/2} \rightarrow 3d$ and L_2: $2p_{1/2} \rightarrow 3d$. (b) Real and imaginary part of σ of a typical two-level system. As an example $\omega_0 = 854$ eV and $\Gamma = 0.5$ eV is chosen. The figure is from Refs. [169, 177].

in the scope of this thesis mainly involved the dipole-allowed transitions in $3d$ TMOs corresponding to the $L_{3,2}$-edges, but also the ligand's K-edge (oxygen) and the Nd M-edge was probed, covering the soft x-ray range from 543 eV to 1003 eV. The main part of this section will refer to the quantitative analysis of the x-ray linear dichroism (XLD) at the Ni $L_{3,2}$-edges.

It is standard to derive the XAS cross section from quantum mechanical first-order perturbation theory [178]. The full light-matter interaction Hamiltonian includes terms accounting for Thomson scattering, magnetic terms, and contributions from resonant processes with one term H_{ext} related to transition rate matrix (Fermi's Golden Rule) which then can be connected to σ. Fermi's Golden Rule which is key to many spectroscopic phenomena gives the transition probability between an initial state $|i\rangle$ and a final state $|f\rangle$, i.e. the transition rate T can be expressed as

$$T = \sum_f |\langle f|H_{ext}|i\rangle|^2(\delta(\hbar\omega + E_i - E_f) + \delta(\hbar\omega - E_i + E_f)), \tag{3.38}$$

with the Dirac delta functions δ enforcing energy conservation. After evaluating the matrix element $\langle f|H_{ext}|i\rangle$, Eq. 3.38 and Eq. 3.36 can be related. Moreover, to account for a lifetime-broadening of the states the delta functions in Eq. 3.38 are replaced by Lorentzian functions

$$\delta(x) = -Im\left(\lim_{\Gamma\to 0} \frac{1}{\pi(x + +i\Gamma/2)}\right), \tag{3.39}$$

with a width Γ. For the relevant core-hole excitations of the x-ray absorption process it is further useful to express the states $|i\rangle$ and $|f\rangle$ by spherical harmonics. The evaluation of the matrix elements according to dipole selection rules then leads to an expression of the conductivity σ for of a simple two-level system

$$\sigma = \frac{2}{2\pi m^2}\left(\frac{1}{\omega + \omega_0 + i\Gamma/2} + \frac{1}{\omega - \omega_0 + i\Gamma/2}\right). \tag{3.40}$$

Here, ω_0 is the energy difference between the two states. The enhancement to the scattering for energies $\hbar\omega$ tuned to the transition is evident from the divergence of the denominators for these values. A cartoon of a two-level system is shown in Fig. 3.11(a). The example illustrates the $L_{3,2}$-edge transitions of $3d$ TMOs where the electronic states of interest lie close to the Fermi level. The Kramers-Kronig related real and imaginary parts of σ are exemplarily plotted in Fig. 3.11(b).

In TMO heterostructures the local ligand field often is of lower symmetry than cubic. The conductivity tensor relevant for the x-ray absorption process when the local symmetry is tetragonal corresponds to

$$\sigma^{tetra}(\hbar\omega) = \begin{pmatrix} \sigma_{xx} & 0 & 0 \\ 0 & \sigma_{xx} & 0 \\ 0 & 0 & \sigma_{zz} \end{pmatrix}. \tag{3.41}$$

A very important consequence is that such a tensor yields inequivalent spectra when the polarization of the incoming light is in- or out-of-plane with respect to the tetragonal distortion. The effect is the called *natural linear dichroism* and has been studied in many TMO systems to quantify orbital occupations and the magnitude of orbital energy level splitting [43, 49]. The imbalance in the orbital occupation due non-degenerate energy levels is also denoted as *orbital polarization*.

From systematic calculations of core level absorption edges of $3d$ transition metals and rare-earths [179, 180], the x-ray dichroism can be analyzed quantitatively by a sum rule analysis [181]. The sum rules relate the integrated magnetic circular dichroism to the spin and orbital magnetic moment in the ground state, but in a generalized form [182] they allow also to quantify the x-ray linear dichroism/orbital polarization of Ni e_g orbitals in a crystal field [109–113, 177].

In our case the experimentally measured integrated absorption intensity at the Ni $L_{3,2}$ edge is brought into relation with the projected density of states of the final state via the sum rule analysis. Our XAS spectra are measured with π and σ polarized photons and the intrinsic properties of the dipole operator for the two light polarizations can be obtained only by symmetry considerations, finally resulting in the sum rules. This is described in detail in Ref. [177]. For a Ni^{3+} ion in nominal $3d^7$: $\mathrm{t}_{2g}^6\ \mathrm{e}_g^1$ configuration and $2p \rightarrow 3d$ transitions one obtains the spectral intensities

$$I_x = I_y \equiv I_{E_x} = \frac{1}{6}h_{3z^2-r^2} + \frac{1}{2}h_{x^2-y^2}, \tag{3.42}$$

$$I_z \equiv I_{E_z} = \frac{2}{3}h_{3z^2-r^2}, \tag{3.43}$$

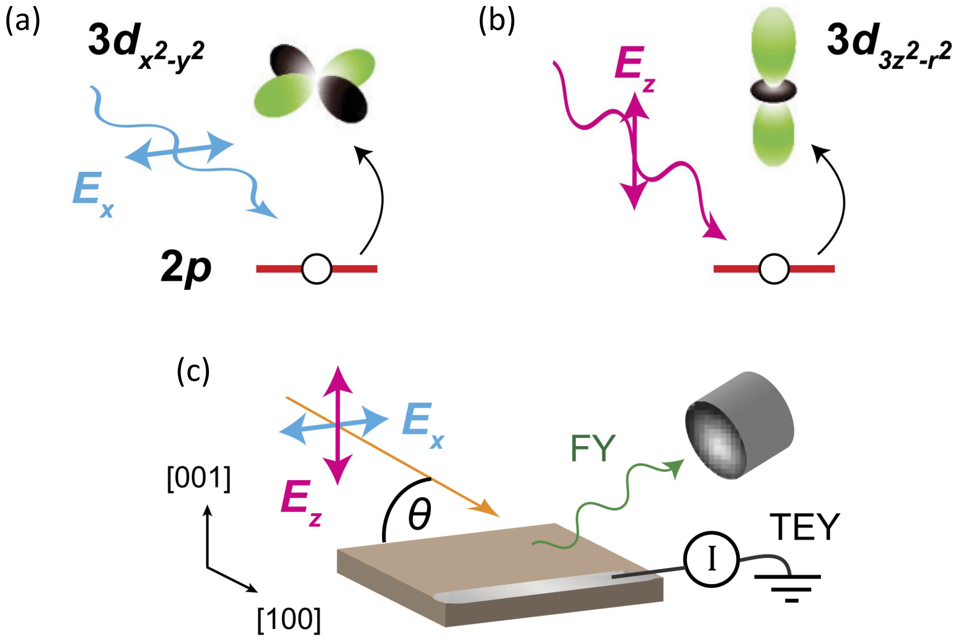

Figure 3.12 X-ray linear dichroism and orbital polarization. (a) According to the symmetry of e_g states and electric dipole selection rules, photons with E_x linear polarization probe unoccupied states of $3d_{x^2-y^2}$ orbitals. (b) Photons with E_z polarization predominantly excite into $3d_{3z^2-r^2}$ states. (c) XAS experimental scattering geometry with E_x and E_z polarized light under the incident angle θ. The linear dichroism is the difference between the XAS signals of (a) and (b). The two detection modes of the XAS signal are fluorescence yield (FY) and total electron yield (TEY). The figure is from Ref. [116].

after expressing the dipole operator in terms of spherical harmonics. Here $h_{3z^2-r^2}$ and $h_{x^2-y^2}$ are the hole occupation numbers of the respective orbitals and the intensities are for local tetragonal crystal symmetry.

The hole ratio X then can be calculated from the energy-integrated XAS intensities $I_{E_x,E_z} = \int I_{E_x,E_z}(\epsilon)d\epsilon$ across the Ni $L_{3,2}$-edge via

$$X = \frac{h_{3z^2-r^2}}{h_{x^2-y^2}} = \frac{3I_{E_z}}{4I_{E_x} - I_{E_z}}. \tag{3.44}$$

The schematic of a XAS experiment on a [001] oriented nickelate heterostructure is illustrated in Fig. 3.12. The σ polarized light couples into states with x^2-y^2 symmetry [Fig. 3.12(a)], whereas π polarized light couples predominately to $3z^2-r^2$ states for $\theta < 45°$ [Fig. 3.12(b)]. From the scattering configuration with an incident angle θ as shown in Fig. 3.12(c) it is evident that the signal of the π channel has to be corrected as a function of θ in order to obtain E_z. From the relation $I(\theta) = I_{E_x}\cos^2\theta - I_{E_z}\sin^2\theta$ [177] it follows for an incident angle $\theta = 30°$ that $I_{E_z} = 4/3I_\pi - 1/3I_{E_x}$, with I_π being the measured intensity with π polarization and $I_{E_x} = I_\sigma$.

The formal definition of the orbital polarization P is given by

$$P = \frac{n_{x^2-y^2} - n_{3z^2-r^2}}{n_{x^2-y^2} + n_{3z^2-r^2}} = \left(\frac{4}{n_{e_g}} - 1\right)\frac{X-1}{X+1}, \tag{3.45}$$

with $n_{e_g} = 4 - h_{e_g}$ being the sum of all electrons in e_g orbitals and $n_{3z^2-r^2} = 2 - h_{3z^2-r^2}$ and $n_{x^2-y^2} = 2 - h_{x^2-y^2}$ for Ni^{3+}. Quantifying n_{e_g} is however not straight-forward as hybridization between Ni d and O p states is not negligible and can be affected by epitaxial strain and proximity to another material and furthermore depends on the choice of local atomic basis.

Therefore, in the following only the hole ratio X is calculated, which already indicates the presence/absence of an orbital polarization and the type of orbital splitting. The hole ratio $X = 1$ of bulk nickelates with fully degenerate e_g orbitals was found to deviate from unity in previous studies of epitaxially strained nickelate thin films and heterostructures [111–113,115]. $X > 1$ corresponds to an enhanced electron occupation of the $d_{x^2-y^2}$ orbital, whereas for $X < 1$ the $d_{3z^2-r^2}$ orbital is preferentially occupied. For completeness it is mentioned that full orbital polarization would be achieved for $X = 2$, i.e. $x^2 - y^2$ orbital is half filled and $3z^2 - r^2$ is completely unoccupied if also there is no hybridization.

3.2.3 Magnetic x-ray scattering

Eq. 3.37 gives a very general expression of light scattering with the optical conductivity σ being a second rank tensor. In case of a cubic system with a net magnetization along the z-direction the conductivity tensor of magnetic scattering can be derived as follows. When the Lorentz force creates a Hall current in the xy-plane the electric permitivity is given by $\boldsymbol{D} = \hat{\epsilon}\boldsymbol{E} = \hat{\epsilon}' + i\boldsymbol{g} \times \boldsymbol{E}$, with $\boldsymbol{g}$ being the gyromagnetic ratio. A consequence of this form are imaginary off-diagonal elements in σ which lead e.g. to magneto optical phenomena like the Kerr and Faraday effect and x-ray magnetic circular dichroism (XMCD). In the quantum mechanical picture, spin-orbit coupling and time-reversal symmetry breaking yield the off-diagonal terms. For the cubic system the elements of the magnetic conductivity tensor then are

$$\sigma^{magnetic}(\hbar\omega) = \begin{pmatrix} \sigma_{xx} & i\sigma_{xy} & 0 \\ -i\sigma_{xy} & \sigma_{xx} & 0 \\ 0 & 0 & \sigma_{xx} \end{pmatrix}. \tag{3.46}$$

Most TMO are of lower symmetry than cubic and the magnetization can be oriented along an arbitrary direction. A formalism to derive $\sigma^{magnetic}$ for such situations has been developed in Ref. [183]. Along the lines of Ref. [4] we apply this formalism for the case of period-four antiferromagnetic order in a spherically symmetric environment.

In the following the atomic conductivity tensor of magnetic scattering is expressed by the scattering factor (see Eq. 3.35) and denoted as F. According to Ref. [183] the general form of F in spherical symmetry reads as

$$F = \begin{pmatrix} F^{(0)} + (x^2 - \frac{1}{3})F^{(2)} & -zF^{(1)} + xyF^{(2)} & yF^{(1)} + xzF^{(2)} \\ zF^{(1)} + xyF^{(2)} & F^{(0)} + (y^2 - \frac{1}{3})F^{(2)} & -xF^{(1)} + yzF^{(2)} \\ -yF^{(1)} + xzF^{(2)} & xF^{(1)} + yzF^{(2)} & F^{(0)} + (z^2 - \frac{1}{3})F^{(2)} \end{pmatrix}. \tag{3.47}$$

This form is achieved after expanding the terms of F in spherical harmonics on the unit sphere and the indices of $F^{(u)}$ (with $u \in \{0, 1, 2\}$) correspond to the respective

Legendre polynomials. In symmetries lower than spherical the expansion of the spin direction in spherical harmonics does not truncate at finite u and certain higher order elements $F^{(u)}$ would have to be taken into account as well [183].

With $\boldsymbol{\varepsilon}_{in(out)}$ representing the polarizations of the incoming (outgoing) light of the scattering process and the unit vector in the direction of the magnetization $\hat{\mathbf{m}}$, Eq. 3.47 can be transformed to

$$\begin{aligned}\boldsymbol{\varepsilon}^*_{out} \cdot F \cdot \boldsymbol{\varepsilon}_{in} = F^{(0)}(\boldsymbol{\varepsilon}_{in} \cdot \boldsymbol{\varepsilon}^*_{out}) + F^{(1)}(\boldsymbol{\varepsilon}_{in} \times \boldsymbol{\varepsilon}^*_{out} \cdot \hat{\mathbf{m}}) \\ + F^{(2)}\left[(\boldsymbol{\varepsilon}^*_{out} \cdot \hat{\mathbf{m}})(\boldsymbol{\varepsilon}_{in} \cdot \hat{\mathbf{m}}) - \frac{1}{3}(\boldsymbol{\varepsilon}_{in} \cdot \boldsymbol{\varepsilon}^*_{out})\right] \quad (3.48)\end{aligned}$$

The family of nickelates exhibits an antiferromagnetic period-four spin configuration [59]. Hence, in our model of the magnetic scattering we first neglect the term with $F^{(0)}$ as it is not depending on the magnetic moment at all.[5] Moreover the $F^{(2)}$ term is quadratic in $\mathbf{m}$, i.e. will not lead to signal modulations in antiferromagnetic systems as the antiparallel spin directions cancel out. This leaves us with the $F^{(1)}$ term proportional to $\mathbf{m}$ which is related to magnetic circular dichroism ($\Delta m_j = \pm 1$) giving rise to the first harmonic of an antiferromagnet. Hence, the magnetic scattering tensor F_i of site i can be written as

$$F_i = \mathfrak{f}_i(\hbar\omega) \cdot \begin{pmatrix} 0 & -\hat{m}_{i_z} & \hat{m}_{i_y} \\ \hat{m}_{i_z} & 0 & -\hat{m}_{i_x} \\ -\hat{m}_{i_y} & \hat{m}_{i_x} & 0 \end{pmatrix}. \quad (3.49)$$

Here, $\mathfrak{f}_i$ is the complex valued, energy dependent, magnetic circular dichroic form factor. For the analysis of the experimental data in chapter 5, $\mathfrak{f}_i(\hbar\omega)$ is calculated from the double cluster model described in Ref. [13].

Next we consider the diffraction at subsequent magnetic sites i. The scattered intensity then is

$$I = |\sum_i e^{i(\mathbf{k}_{in} - \mathbf{k}_{out})\cdot \mathbf{r}_i} \boldsymbol{\varepsilon}^*_{out} \cdot F_i \cdot \boldsymbol{\varepsilon}_{in}|^2, \quad (3.50)$$

with $\mathbf{r}_i$ the position of site i and the sum is over all sites. Note that the scattering vector $\mathbf{q}$ is defined as $\mathbf{q} = \mathbf{k}_{out} - \mathbf{k}_{in}$. For the scattering at four subsequent atomic sites corresponding to the periodicity of antiferromagnetic order in the nickelates, the phases add up and yield

$$F = F_1 + iF_2 - F_3 - iF_4, \quad (3.51)$$

which corresponds to $F = 2\,(F_{\mathrm{SB}} + iF_{\mathrm{LB}})$ for scattering at alternating SB and LB sites along the magnetic wave vector $\boldsymbol{q}_0 = (1/4, 1/4, 1/4)$, with $\mathbf{m}_1 = -\mathbf{m}_3$ and $\mathbf{m}_2 = -\mathbf{m}_4$ (see chapter 2).

Generally, four channels can be measured with π or σ polarized incoming photons and a polarization analyzer, according to $I_{in/out} \sim \boldsymbol{\varepsilon}^*_{out} \cdot F_i \cdot \boldsymbol{\varepsilon}_{in}$. In our experiments no polarization analyzer was used and the two accessible channels were $\boldsymbol{\pi} \equiv I_{\pi\sigma} + I_{\pi\pi}$ and $\boldsymbol{\sigma} \equiv I_{\sigma\pi} + I_{\sigma\sigma}$, with $I_{\sigma\sigma} = 0$ for resonant magnetic scattering [169].

---

[5] It is noted that in the specific simulations with the software ReMagX [184] and QUAD [185] in chapter 5 the term $F^{(0)}$ is taken into account.

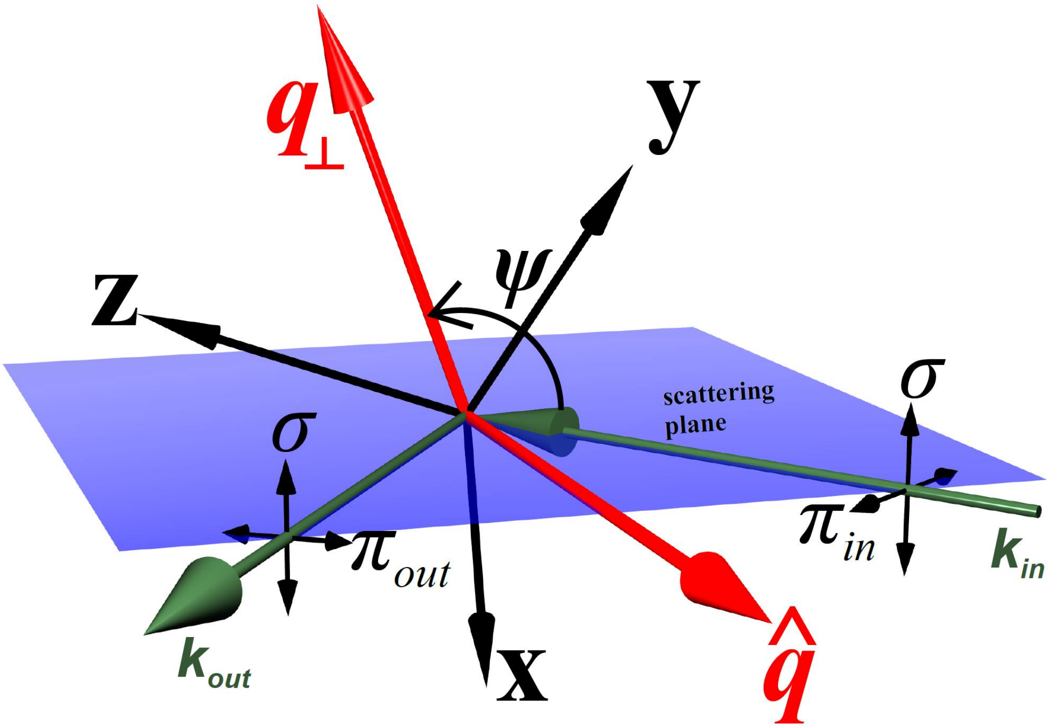

Figure 3.13 Azimuthal dependence scattering geometry. The sample (crystal frame axis x, y, z) is rotated around the azimuthal angle ψ within the fixed scattering frame (vectors of incoming and outgoing light $\mathbf{k}_{in(out)}$). The axis of rotation corresponds to the scattering vector $\boldsymbol{q}$ and the rotation is right-handed. $\psi = 0°$ is defined as the coincidence of $\boldsymbol{q}_\perp$ and the scattering plane. The intensity of the scattered light dependents on the relative orientation of the magnetic moment (not shown here) tied to the crystal frame and the π or σ polarized incoming light. The figure is from Ref. [169].

As was shown by Hannon *et al.* and others [186, 187], the intensity I of magnetic scattering depends on the relative orientation between the magnetic moments and the polarization of the incoming light. The rotation of the sample around the azimuthal angle ψ systematically varies this relative orientation and the modulation of the scattered intensity allows to deduce the local orientation of the magnetic moments [4, 12, 57, 188]. The scattering geometry for measuring such an *azimuthal dependence* is shown in Fig. 3.13.

Along the lines of Ref. [183] this bisecting scattering geometry can be described in a cartesian coordinate system by a set of geometric relations. Frano *et al.* have implemented these relations in a Mathematica® script to model their magnetic scattering data of [001] oriented nickelate heterostructures [4]. The script is published in Ref. [169]. In chapter 5 we also use these relations in combination with a script for the software OriginPro®. A least squares fit can be performed to the integrated intensities of the rocking curve of the (1/4, 1/4, 1/4) antiferromagnetic peak at each azimuthal angle ψ, simultaneously for the $\boldsymbol{\pi}$ and $\boldsymbol{\sigma}$ channel. A large set of magnetic form factors $\mathfrak{f}_i$ of the SB and LB Ni sites was calculated with the double cluster

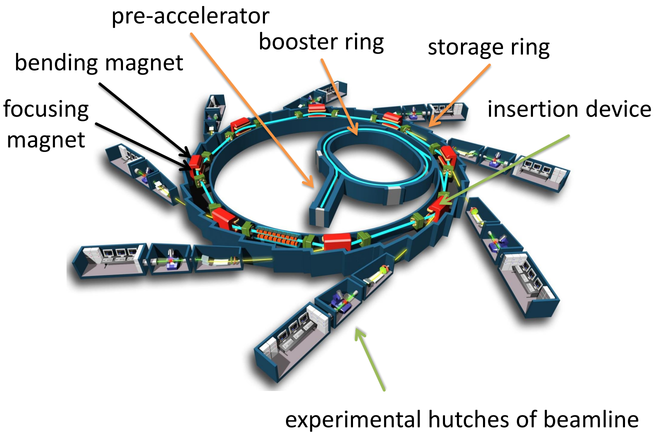

Figure 3.14 Schematic of a synchrotron light source. Electrons are accelerated to relativistic speeds by a linear pre-accelerator and the booster ring. After injection into the storage ring, bending and focusing magnets keep the electron beam on a circular orbit. Insertion devices such as special bending magnets, wigglers, and undulators periodically modulate the beam's trajectory yielding the emission of x-ray radiation The radiation is guided along the beamlines to the experimental setups in the hutches. The schematic is adapted from Ref. [189] and shows the SOLEIL synchrotron.

model [13]. The $\mathfrak{f}_i$ are a function of the energy $\hbar\omega$ and the magnitude of the breathing distortion δd. The parameters of the fit were the two angular coordinates Θ, Φ giving the orientation of the magnetic moments and the magnitude δd of breathing distortion. In chapter 5 we call this the *form factor corrected model.* Finally, absolute magnetic moments sizes were obtained from the conversion of the δd parameter by the double cluster model [13].

3.2.4 X-ray sources: synchrotron radiation

Various methods allow for the controlled generation and emission of x-rays. Among the most common x-ray sources are cathode tubes, accelerating electrons towards a specific target material. When the electrons collide with the target a typical radiation spectrum arises that originates from bremsstrahlung and dipole-allowed transitions in the electron shell of target atoms. In case of a Cu target anode K-edge excitations are involved, yielding radiation at characteristic energies of 8047.8, 8027.8 and 8905.3 eV, corresponding to the $K_{\alpha 1}$, $K_{\alpha 2}$, and K_{β} emission lines. A first characterization of crystalline properties of the samples presented in this thesis was performed with a Huber four-circle diffractometer using Cu $K_{\alpha 1}$ radiation. A detailed description of four-circle diffractometers and the technical components and physics of cathode tubes is given in Refs. [177, 190, 191] or can be found in most standard textbooks on x-ray diffraction.

For investigations of thin oxide heterostructures beyond basic structural characterization x-ray radiation generated by cathode tubes can be insufficient. A small scattering volume yields a reduced scattering signal which usually lies below detection limit for Bragg peaks related to scattering from oxygen atoms and/or faint cation displacements. Further, diffraction peaks arising from ordering phenomena such as magnetic, charge, or orbital order are inherently weak. As a consequence many phenomena can only be observed with highly brilliant and collimated x-rays and when the scattering cross section is strongly enhanced due to resonance effects [186, 192, 193], i.e. the x-rays energies have to be tuned to specific atomic absorption edges.

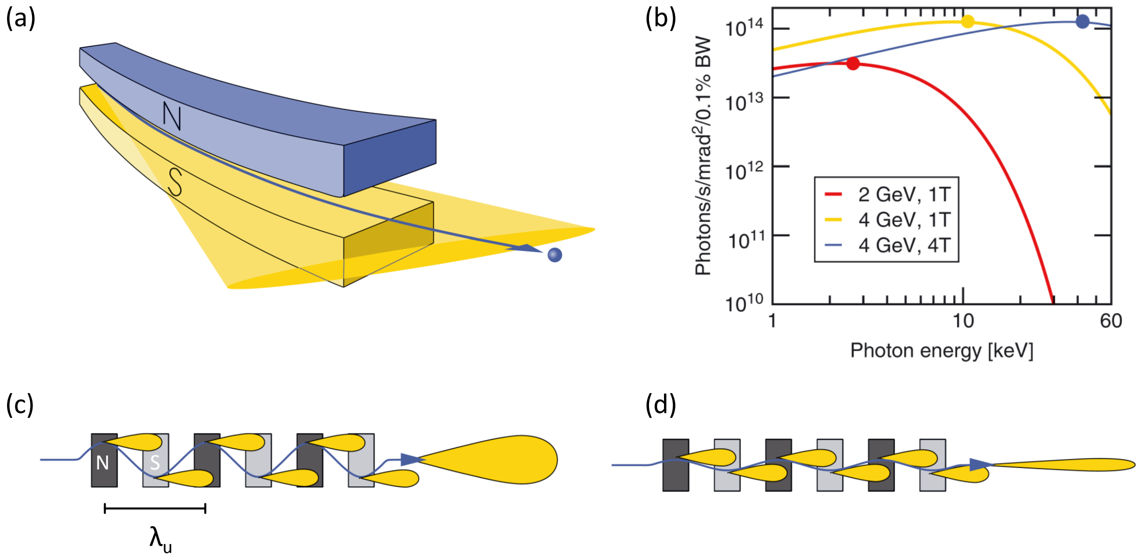

Figure 3.15 Synchrotron insertion devices. (a) Bending magnets deflect electrons to a circular orbit in the storage ring. X-ray radiation is emitted along the forward direction with propagation corresponding to a flattened cone (yellow) with a fan angle equal to the angular change of the path of the relativistic electrons. (b) Bending-magnet spectra for horizontally polarized radiation on axis for three different combinations of the storage-ring energy and magnetic-field strength. The circles indicate the critical energy $\hbar\omega_c$, dividing the total emitted power of the bending magnet in half [165]. (c) In a wiggler alternating magnetic dipoles accelerate the electrons on a sinusoidal trajectory. The periodicity of the magnet array is λ_u. The emitted radiation is more intense as compared to the bending magnet. (d) Undulators are constructed such that the emitted wavefronts interfere constructively, yielding an enhanced x-ray intensity and higher brilliance of the beam. Panel (a)-(d) are from Ref. [165].

High beam intensity with tunable energy ranges is a property of synchrotron light sources [Fig. 3.14] [165, 169]. These descend from the related *cyclotron* concept but are build with linear acceleration and bending of an electron beam by magnetic fields *synchronized* to the beam's increasing kinetic energy. As first step, electrons are accelerated close to the velocity of light by the booster ring and then are injected into the storage ring. Here, bending magnets guide the electrons along a circular orbit. The deflection of relativistic electrons by the bending magnets yields a broad emission spectrum [Fig. 3.15(a),(b)] covering a bandwidth from the infrared up to the hard x-ray range. In principal, x-rays of a specific energy can be picked from the radiation spectrum via monochromator optics and be used for experiments. The brilliance $\mathcal{B}$ of the x-ray beam is defined then by

$$\mathcal{B} = \frac{\text{photons/s}}{(\text{mrad})^2(\text{mm}^2 \text{ source area})(0.1\% \text{ bandwidth})}, \tag{3.52}$$

and is therefore the flux per unit source area and unit solid angle. Modern third generation synchrotrons, however, are complemented with *wiggler* or *undulator* insertion devices. In such device alternating magnets deflect the electron's trajectory sinusoidally, increasing the beam intensity and decreasing the divergence [Fig. 3.15(c),(d)].

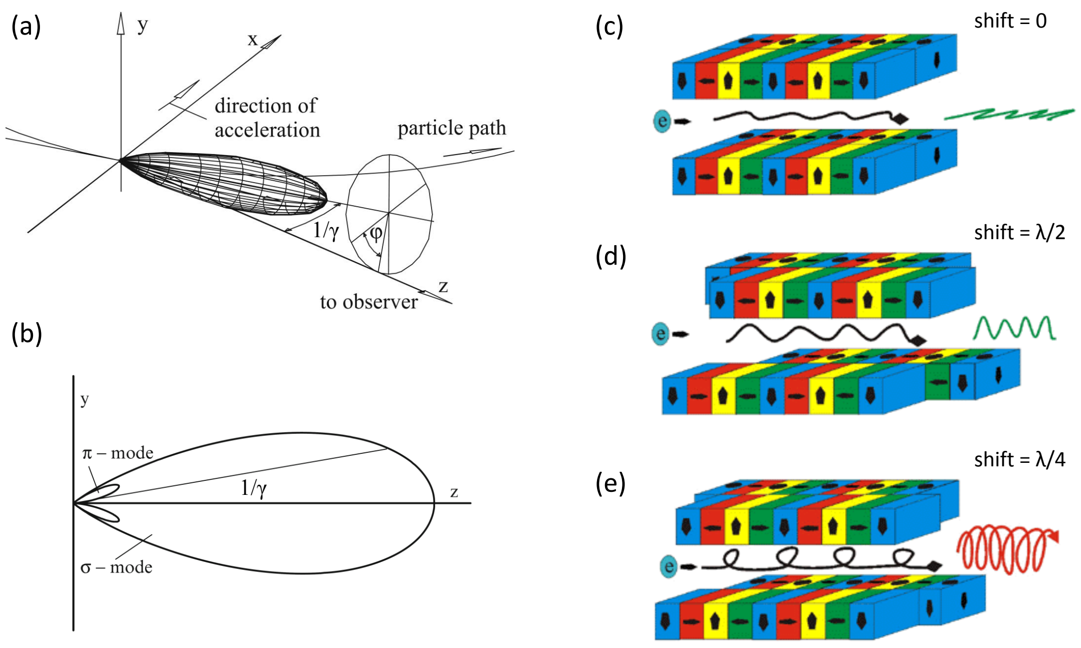

Figure 3.16 Polarized synchrotron radiation. (a) Spatial radiation distribution of an accelerated relativistic particle on a curved path. The reference frame is the laboratory system. Within the opening angle $1/\gamma$ the radiation power decreases to about one eighth of the peak intensity. (b) Radiation lobes for π -and σ-mode polarization. π-mode radiation is emitted into a lobe surrounding the forward direction at finite angles and has zero intensity in the forward direction where the σ-mode has its maximum. For higher frequencies of the radiation the angular distribution concentrates more and more in the forward direction. (c)-(e) Magnetic dipole array of undulator producing linear horizontal, linear vertical, and circular polarized light depending on the relative diagonal shift of the elements within the array. Panel (a),(b) are from Ref. [194] and panel (c)-(e) from Ref. [195].

The wiggler is an array of N alternating magnetic dipoles with a period λ_u as shown in Fig. 3.15(c). Wigglers operate with high magnetic fields B and a large number N. Basically, the repetition magnetic dipoles corresponds to a superposition of bending magnet radiators amplifying the emitted intensity by a factor $2N$ in respect to a single bending magnet. Insertion devices are classified by the number $K^* = \frac{eB\lambda_u}{2\pi m_e c}$, with m_e and c being the mass of an electron and speed of light in vacuum, respectively. Wigglers typically exhibit $K^* \gg 1$, whereas for $K^* \leq 1$ one speaks of an undulator.

For the undulator the x-ray emissions at each oscillation are in phase. This results in a coherent waveform with higher intensity $I \sim N^2$ and less divergence, i.e. the radiation is highly collimated in the forward direction [Fig. 3.15(d) and Fig. 3.16(a)]. On top of that the emitted spectral range $\Delta E/E$ is much narrower which further increases the beam's brilliance. The resulting narrow (almost discrete) undulator spectrum can be shifted by a change of the gap between the magnetic dipoles, optimizing the brightness for a specific energy range of interest. Different harmonics are used according to the energy ranges. When the intensity drops below that of the next odd harmonic at the highest accessible K^*-value (given by the minimum undulator gap) the new, higher, harmonic is used. Further description of the insertion devices and synchrotron radiation is given in Ref. [165]. More sophisticated designs corresponding to asymmetric and multipole insertion devices can be found in Ref. [194].

An important and common feature of the radiation of all three types of insertion devices is the high degree of polarization which enables e.g. an excellent coupling of the light to magnetic properties of the material. In general, two polarization directions are defined for an electric radiation field. σ (for the German word 'senkrecht' or orthogonal) is in the plane of the particle path being perpendicular to the particle velocity. π (for parallel) then is the corresponding direction perpendicular to σ [Fig. 3.16(a),(b)]. The intensities and the spatial distributions of the two polarization modes are very different [Fig. 3.16(b)]. Whereas the σ-mode is directed mainly in the forward direction π radiation is emitted into a lobe surrounding the former direction at finite angles. The result is a 100% linear polarization within the σ plane and only small deviations from 100% for moderate off-axis directions.

The array of magnets in modern *diagonal undulators* exhibits a more complex arrangement as shown in Fig. 3.15(d). Dipoles within an array can be shifted with respect to each other [Fig. 3.16(c)-(e)]. Their major advantage is the fast switching of the direction of the polarization of the incoming light with respect to the experimental setup. The shift of $\lambda/2$ in Fig. 3.16(d) rotates the light's polarization plane from Fig. 3.16(c) by 90° around the forward direction axis. These two modes are widely employed for the magnetic scattering experiments in chapter 5. The convention in diffraction experiments denotes incoming light as π polarized when the vector $\boldsymbol{\varepsilon}$ indicating linear polarization direction lies in the scattering plane and as σ for $\boldsymbol{\varepsilon}$ perpendicular to the plane.

For completeness it is mentioned that also (left -or right) circular polarized light can be produced when the shift corresponds to $\lambda/4$ and a spiral motion of the electron is induced [Fig. 3.16(e)].

Chapter 4

Tunable order parameters in nickelate heterostructures

4.1 Raman spectroscopy of ultra-thin oxide heterostructures

Raman spectroscopy is a well-established and versatile technique for the investigation of powder samples, liquid solutions, and bulk crystals [128]. Likewise, Raman scattering is employed by the thin film and heterostructure community to explore phase transitions of various types, to characterize the crystalline quality of films, and to probe the lattice dynamics in conjunction with electronic and magnetic responses of material systems grown on different substrates [5, 44, 161, 162, 196–201]. In case of thin material systems however, there are two substantial drawbacks decreasing the quality of Raman spectra obtained from films with thicknesses less than ∼100 nm. (i) The scattering volume is significantly reduced as compared to bulk materials yielding a much weaker signal. (ii) The faint scattered intensity from the thin film is overwhelmed by the strong signal coming from the substrate.

Taking advantage of resonant processes can help to increase the Raman signal of a thin slab of material [202]. For materials like ZnO an enhancement of the Raman cross-section by several orders of magnitude has been reported when the incident photon energy was in proximity of an electronic transition of the material [203]. In case of the nickelates an optical gap is formed between two bands that originate from strongly hybridized Ni $3d$ e_g and O $2p$ orbitals with a magnitude of $\sim$ 0.2 eV [53]. This corresponds to a laser wave length λ located almost in the far-infrared ($\sim$ 6 μm), which is problematic for scattering experiments as in general the scattering cross-section is proportional to λ^{-4}, i.e. no such Raman setup was not available for our experiments. Experimental tests on nickelate films with different laser wavelengths (455 nm, 532 nm, 632.8 nm) showed that the best signal-to-noise ratio is obtained with a HeNe laser of 632.8 nm. Therefore, the red HeNe laser is used in all Raman spectra shown in the following if not indicated otherwise. On top of the absence of an electronic transition at available laser energies, nickelates are relatively weak Raman scatterers as compared to famous monolayer systems such as graphene [204] or $MoSe_2$ and MoS_2 [205]. Thus, a signal enhancement might be crucial for our measurements and we considered other possible enhancement effects.

In Surface Enhanced Raman Spectroscopy (SERS) [206] the signal of thin slabs of materials can be enhanced by a factor of 10^5 [207] or even more in case of single molecules [208]. However, the main mechanisms to achieve such a boost of the signal are (i) the combination of a special substrate surface (e.g. electrochemically roughened silver) and adsorbed molecules forming a surface complex where charge is transferred either from conduction band of the metallic substrate to the unoccupied molecular orbitals or vice versa [209]. In other words the chemisorption of the molecule on the metal layer disturbs the electronic structure of the substrate and allows for a resonant excitation of a surface-induced electronically excited charge-transfer state. (ii) The deposition of metallic nanoparticles on the sample surface which are smaller in size than the incoming wavelength can lead to excitations of localized surface plasmons. Therewith the nanoparticles act as antennas which efficiently amplify the Raman cross-section [210]. However, both enhancement mechanisms are precluded in our case as very clean material systems are required and the epitaxial match to specific perovskite oxide substrates is key for the emergence of the effects we intend to study. Similar scattering signal enhancements are known from Tip Enhanced Raman Spectroscopy (TERS) [211], combining atomic force microscopy with a Raman spectrometer. With this technique basically any thin film system on a substrate can be studied, however to the best of our knowledge no TERS setup is available that allows for measurements at low temperatures.

In conclusion, it is not straight-forward to enhance the Raman signal of the nickelate films. Thus, the option that is left for achieving high quality spectra of ultra-thin films is the suppression of the strong substrate signal. The strong substrate contribution is mainly due to to the large optical penetration depth of the laser light (common wavelengths range from visible to near-infrared) in typical TMO film materials. For instance the penetration depth of a 632.8 nm laser in the well-studied TMO material YBCO is more than 300 nm. The usage of shorter laser wavelengths reduces the penetration depth, as e.g. realized in ultraviolet (UV) Raman spectroscopy setups [5]. However, this technique suffers of a low throughput efficiency, insufficient light dispersion and poor Rayleigh light rejection, precluding the observation of low energy and low intensity phonon modes in most cases. As consequence of these technical difficulties, another approach is the usage of perovskite substrates that yield low background signal and exhibit no Raman modes in the spectral region of interest of the film.

4.1.1 Perovskite oxide substrates

A selection of the most common perovskite oxide substrates used for the epitaxial growth of TMO films was screened in terms of a search for a wide free spectral range (i.e. no substrate phonon modes coinciding with film modes) and a small overall background contribution. Fig. 4.1(a) compares the Raman spectra of $SrTiO_3$, LSAT, LSAO, and $LaAlO_3$ in the spectral range relevant for our studies.

- **$SrTiO_3$**: The Raman response at ~ 80 cm^{-1}, between 200-500 cm^{-1}, and

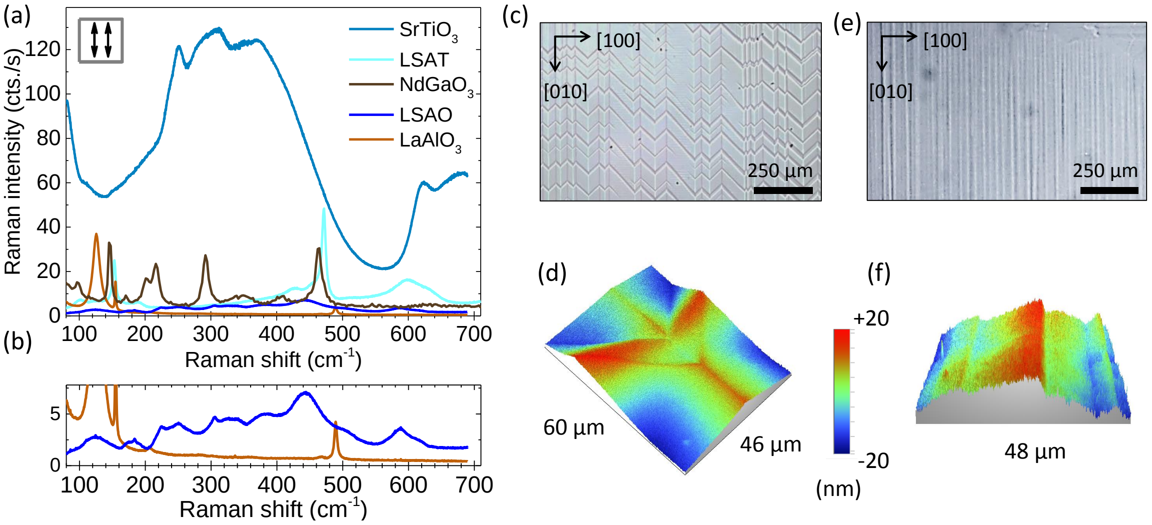

Figure 4.1 Perovskite oxide substrates. (a) Raman spectra of SrTiO$_3$, LSAT ([LaAlO$_3$]$_{0.3}$[Sr$_2$AlTaO$_6$]$_{0.7}$), NdGaO$_3$, LSAO (LaSrAlO$_4$), and LaAlO$_3$ substrates at $T = 300$ K. The inset represents the electric field's polarization vectors of the incoming and the detected light with respect to the substrate edges. All spectra are recorded with the 632.8 nm HeNe excitation line and a laser power of 1 mW. (b) Zoom-in of the low-intensity spectra of LSAO and LaAlO$_3$. (c)-(f) Structural twin domains of LaAlO$_3$. (c) Polarized light microscope image of typical tweed-like twin domains. The pseudocubic directions are indicated. (d) Topography of a tweed-like domain tiling where the walls of several domains meet in line junctions. The surface profile is recorded by a white-light interferometer. (e),(f) Typical lamellar or needle twin domains. Images are in analogy to (c),(d).

600-800 cm^{-1} is particularly strong [Fig. 4.1(a)]. At first glance this might be surprising as the crystal structure of SrTiO$_3$ is the undistorted cubic perovskite which from pure symmetry considerations does not give rise to Raman active modes[1]. However, second-order Raman processes [212] generate the typical continuous and broad spectrum observed in Fig. 4.1(a). Most of the second-order spectrum is relatively insensitive to different polarization configurations, only in the X'Y' channel the overall intensity is strongly reduced. Parts of the spectral weight at low wave numbers further vanish below the structural phase transition at $T = 130$ K [213].

As a consequence, SrTiO$_3$ is a very unfavorable substrate in terms of thin film Raman investigations. For many classes TMO thin films (nickelates, manganites, aluminates, scandates, etc.) with thicknesses of 50 nm or less the background will exceeded the film signal by more than one order of magnitude almost across

---

[1] SrTiO$_3$ is of O_h^1 symmetry (space group $Pm\bar{3}m$, no. 221). The five atoms per unit cell are all located at a point of inversion symmetry and at the Brillouin zone center the 15 degrees of freedom only yield one F_{1u} triply degenerate acoustic mode and three F_{1u} plus one F_{2u} triply degenerate optical modes. The two phonons of the second order Raman process can originate from anywhere in the Brillouin zone if only their wave vectors add up to zero. It is generally non-trivial to assign certain features in such a spectrum, since the scattering intensity does not only originate from different points in the Brillouin zone but also depends on variations in the combined density of states. For SrTiO$_3$ it is known that most spectral features originate mainly from pairs of transverse polarized phonons with wave vectors near the zone boundary [212].

the whole spectral range up to 1100 cm^{-1}. Only in specific cases Raman studies of ultra-thin TMO films on $SrTiO_3$ are feasible, for example when the vibrational features of the film are so sharp that they can be clearly distinguished from the broad background or when the mode of interest coincides with the spectral gap between 500-600 cm^{-1}, as e.g. in case of the BiO_6 octahedra breathing mode of ultra-thin $BaBiO_3$ films [196], where the film signal is additionally enhanced for 632.8 nm laser light which is in resonance with the $BaBiO_3$ optical band gap.

- **LSAT** ($[LaAlO_3]_{0.3}[Sr_2AlTaO_6]_{0.7}$): In comparison to $SrTiO_3$ the Raman background is strongly reduced across the whole spectral range. Several sharper features are observed below 200 cm^{-1} and between 350-500 cm^{-1} and a broad feature is found at around 600 cm^{-1}, but the remaining spectral range is almost free of features. Only few publications about the Raman spectrum of LSAT are available [214, 215] and yet there is no clear assignment of the modes. The LSAT double perovskite structure with space group $Fm\bar{3}m$ generally exhibits 4 zone center Raman phonons $\Gamma_{\text{Raman}} = A_{1g} + E_g + 2F_{2g}$. Additional features in Fig. 4.1(a) can originate from second order processes, similar to $SrTiO_3$ or can be explained along the lines of possible tetragonal distortions of the LSAT crystal lattice [216] or a superstructure of lower symmetry than $Fm\bar{3}m$ due to a partial ordering of the B-site cations [217].

  Considering also that the spectrum is nearly temperature independent, LSAT is a substrate well suited for thin film Raman investigations.

- **$NdGaO_3$**: The Raman spectrum of orthorhombic $NdGaO_3$ is well understood [218] with 24 active modes $\Gamma_{\text{Raman}} = 7A_{1g} + 7B_{1g} + 5B_{2g} + 5B_{3g}$ in space group $Pbnm$. The energies of the 24 modes mostly coincide with the typical energy range of the modes of other ternary TMOs such as the nickelates.

  Hence, $NdGaO_3$ substrates might not be the first choice, but the sharpness of the modes can allow for a distinction to the film modes, in particular at low temperatures [219]. Note that polarized Raman spectroscopy on $(110)_{or}$ cut $NdGaO_3$ substrates yields different spectra depending on the alignment with respect to the two in-plane directions of the substrate edges. In contrast, TMO films grown on the surface can be twinned and the Raman spectrum for the two alignments are identical, i.e. an average signal from the twin domains is detected both times.

- **LSAO** ($LaSrAlO_4$): The tetragonal $I4/mmm$ space group of LSAO yields $\Gamma_{\text{Raman}} = 2A_g + 2E_g$ Raman active modes originating from oscillations of the Sr/La and O atoms. Additional features are due to second-order processes or local lattice distortions of the oxygen octahedra. A detailed analysis and mode assignment can be found in Ref. [220].

  The weak overall intensity, the broadness of the modes [Fig. 4.1(b)], and the weak temperature dependency makes LSAO well suited for Raman investigations.

- **$LaAlO_3$**: Rhombohedral $LaAlO_3$ exhibits the widest free spectral range of all substrates discussed here. No Raman active modes are found between 175 cm^{-1}

> and 425 cm^{-1} and for energies larger than 500 cm^{-1} [Fig. 4.1(a),(b)]. The space group $R\bar{3}c$ gives rise to only five Raman active modes $\Gamma_{\mathrm{Raman}} = A_{1g} + 4E_g$, described in more detail in Refs. [149, 221–223]. However, the twin domains of LaAlO$_3$ [145, 224] can be a problem for polarized Raman spectroscopy when the size of the twins is smaller than the spatial extension of the laser focus spot. Since the films adopts the crystallographic orientation of the underlying substrate domain, several orientations can be mixed in the polarization analysis then. Typical twins are shown in Fig. 4.1(c)-(f). Here, it can help to screen and preselect the LaAlO$_3$ substrates for wide needle-like domains [Fig. 4.1(e),(f)] before deposition of the film.

From the above discussion it follows that LaAlO$_3$ is the most suitable substrate in terms of Raman spectroscopy. Depending of the aim of the experimental study, it can however be required that a specific strain state is imposed to the film, i.e. the substrate choice is predetermined. For this case, we have developed the *confocal Raman z-scan technique* which suppresses the substrate signal significantly, as described in chapter 3, and is a powerful alternative to UV Raman spectroscopy without its technical disadvantages. High-quality Raman spectra of films as thin as 4 pseudocubic unit cells (1.6 nm) can be measured from nickelates grown on LaAlO$_3$ and ~30 unit cells can be measured on SrTiO$_3$, without employing resonance effects.

As a side remark it is noted that further complications in terms of the substrate background can arise from the fluorescence response of the substrate to the incoming photons. Then not only the choice of the substrate material is important, but also the incident laser wavelength determines at which wave numbers a high background is present. However, for the substrates considered here strong fluorescence effects become only relevant at wave numbers $>$ 1000 cm^{-1}. The investigation of such spectral ranges is important e.g. in case of two-magnon processes, however, these high-energy Raman excitations are not discussed in the scope of this thesis.

Also we note that Ref. [215] has investigated oxide substrates under the aspect of applicability in Raman spectroscopy-based thin film research. There the conclusion is that MgO is the best Raman substrate in terms of the largest free spectra range and a low background. In our studies MgO is not used, mainly due to the relatively large lattice mismatch with nickelates.

4.1.2 Comparing the confocal *z*-scan to previous Raman studies

Previous Raman studies on nickelates have investigated relatively thick films $>$ 100 nm which were fully relaxed [63, 225], or thinner films between $\sim$ 20 and 100 nm grown on LaAlO$_3$ substrates [226]. In both cases the aim of the studies was not a manipulation of the intrinsic electronic, magnetic and lattice degrees of freedom, but rather bulk-like properties were investigated. Apart from the work we present in the following sections [54, 55], we know of only one very recent Raman study specifically addressing different strain states of thin nickelate films grown on different substrates [227].

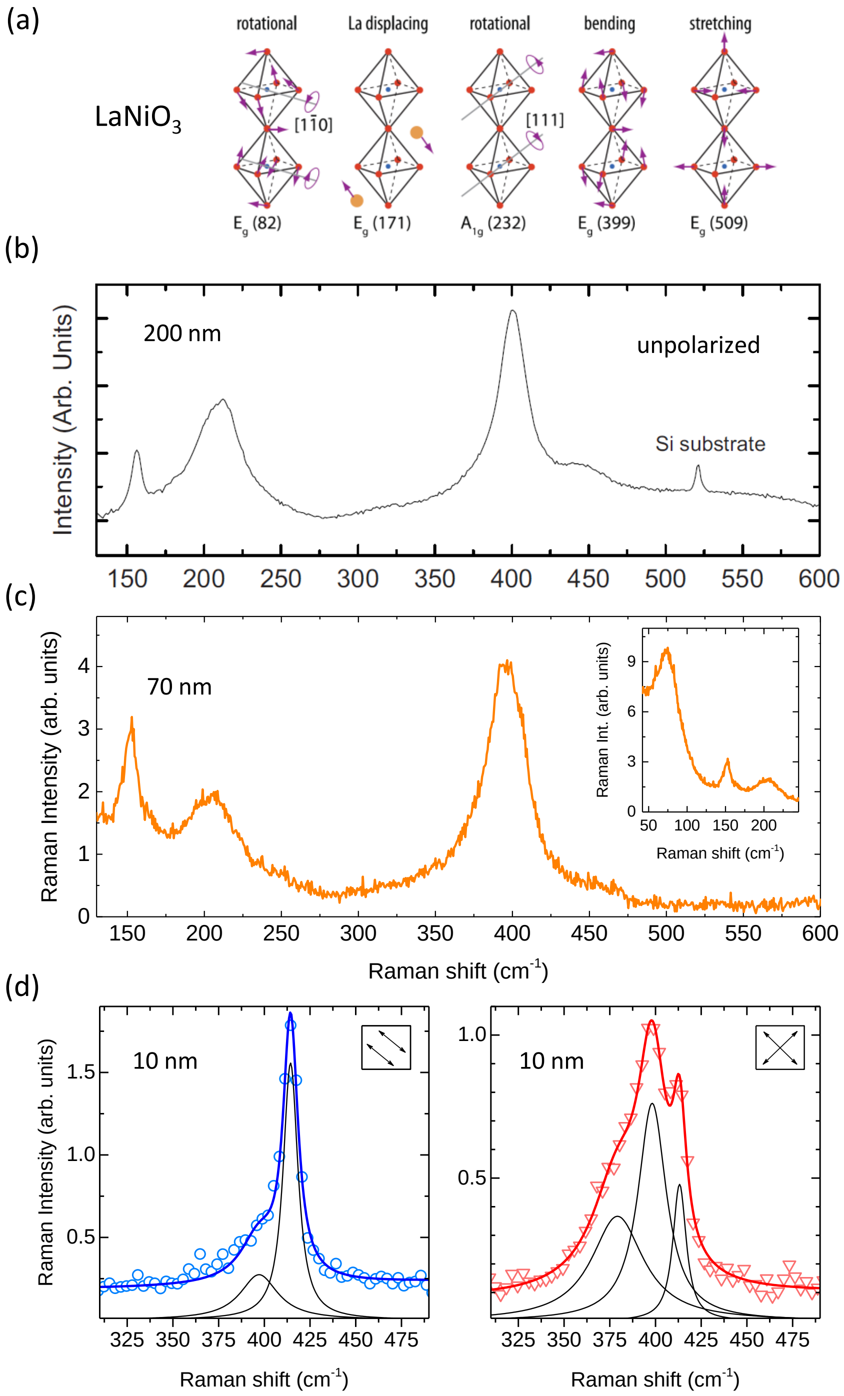

Figure 4.2 Raman spectra of LaNiO$_3$. (a) Displacement patterns of the Raman-active modes of LaNiO$_3$ in space group $R\bar{3}c$. The mode symmetry and the calculated energy in cm^{-1} are indicated. The figure is adapted from Ref. [228]. (b) Unpolarized Raman spectrum of 200 nm LaNiO$_3$ on Si substrate at $T = 300$ K. The figure is adapted from Ref. [225]. (c) Experimental data of 70 nm LaNiO$_3$ on LSAT substrate. Phonon modes in panel (b) and (c) are similar. (d) Polarized confocal z-scan spectra of 10 nm LaNiO$_3$ on LSAT substrate revealing features not present or not resolved in the unpolarized spectra of thick films. The left panel is recorded in parallel and the right in crossed polarization. Insets represent the electric field's polarization vectors of the incoming and the detected light with respect to the nickelate pseudocubic unit cell. Open circles are experimental data and solid lines represent the results of least-squares fits of the data to Voigt-profiles. The individual Voigt-profiles are shown as the black curves.

In case of a 200 nm $LaNiO_3$ grown on Si substrate, Chaban *et al.* measured a softening of the A_{1g} rotational mode [225], which suggests a decreasing rhombohedral distortion towards the ideal cubic structure at high temperatures, similar to what is known from $LaAlO_3$ crystals [149]. As a first step in our own study of the impacts of epitaxial strain and heterostructuring on nickelates and as a reference measurement a relatively thick 200 nm $LaNiO_3$ film was compared to the bulk-like spectrum in Ref. [225] and a theory calculation [228]. The energies of three of the five Raman active modes $\Gamma_{\mathrm{Raman}} = A_{1g} + 4E_g$ calculated by LSDA [228] at 171, 232, and 399 cm^{-1} are in reasonable agreement with Ref. [225] and our experimental spectrum [Fig. 4.2(a)-(c)]. The inset of Fig. 4.2(c) shows the low-energy excitations of our $LaNiO_3$ film with the experimental mode at 75 cm^{-1} to be assigned to the calculated E_g rotational mode at 82 cm^{-1}. The LSDA mode at 509 cm^{-1}, however, seems to be overestimated in energy when assigned to the shoulder in Fig. 4.2(b),(c) at 450 cm^{-1}. In Ref. [228] it is pointed out that in the calulation's relaxed lattice structure the NiO_6 rotation angle is highly sensitive to the choice of the functional and the pseudopotentials and its value has a delicate influence on the frequency not only of the A_{1g} rotational mode, but also on the high frequency oxygen breathing and stretching distortions, which could explain such a deviation in calculated frequency.

After this successful comparison to theoretical predictions and previous experimental results, as next step the ultra-thin limit is approached by measuring a 10 nm $LaNiO_3$ film and use polarization analysis. The left and right panel of Fig. 4.2(d) show the z=0 spectrum of a confocal scan and reveal new features in Raman spectra of the thin epitaxial films which were previously not present or not resolved. In particular at energies around the E_g bending mode at $\sim$400 cm^{-1} it can bee seen that the total number of modes is higher than in (b) and (c) and higher than allowed by $R\bar{3}c$ selection rules. This indicates that the lattice of thin epitaxially strained $LaNiO_3$ on LSAT substrate corresponds to a space group with a symmetry lower than $R\bar{3}c$. Hence, the confocal z-scan technique can be used to study strain effects in thin and ultra-thin nickelate films.

Very recently the effect of a symmetry reduction in $LaNiO_3$ films under distinct epitaxial strain states has been discussed in Ref. [227]. Films with thicknesses between 14 and 130 nm were grown on $LaAlO_3$ and LSAT substrates, respectively. Even though the thin film modes were not resolved in detail (there is an overlap between film and substrate bands and no polarization analysis was used), it can be recognized that the number of $LaNiO_3$ modes increases with decreasing film thickness and are distinct for tensile and compressive strain. A comparison to frequencies obtained by first-principle calculations suggests the presence of space group $C2/c$ for compressive strain, $Imma$ for low strain states, and $Fmmm$ for tensile strain. It is also pointed out that Raman spectroscopy is apparently highly sensitive to detect these faint structural deviations, whereas x-ray structural refinement [146] and similar methods could not detect a difference between compressively and tensile strained $LaNiO_3$ films.

The other compound previously studied by Raman spectroscopy is the antiferromagnetic insulator $NdNiO_3$. Zaghrioui *et al.* presented the first evidence of a structural symmetry breaking in $NdNiO_3$ from $Pbnm \rightarrow P2_1/n$ [63]. Early neutron diffraction experiments measured such a symmetry breaking in the small rare-earth compounds as e.g. $YNiO_3$ [8], however in the large rare-earth compounds $PrNiO_3$ and $NdNiO_3$ it was too faint to be detected [148]. In a combined study, new reflections in the electron-diffraction pattern and drastic changes in the Raman spectrum across the phase transition are observed [Fig. 4.3(a),(b)]. In particular a strong broadening and softening of a mode at ∼620 cm^{-1} [Fig. 4.3(b)] is interpreted as signature of the structural symmetry breaking and a charge disproportionation of the Ni^{3+} valence state into $Ni^{3+\delta}$ and $Ni^{3-\delta}$ configurations. Even though the changes in the Raman spectrum do not directly reflect the Ni valence state it is argued that the soft mode behavior is qualitatively similar to the charge ordering in PtCl chains [229] and an increase of δ gives rise to an increase of the $Ni^{3+\delta}$-O interaction greater than the decrease of the $Ni^{3-\delta}$-O one, so that the vibrational frequency, depending on the sum, increases.

Girardot *et al.* have synthesized $NdNiO_3$, $SmNiO_3$, and $Sm_{0.6}Nd_{0.4}NiO_3$ films on $LaAlO_3$ substrate [226] [Fig. 4.3(c)] and $NdNiO_3$-$SmNiO_3$ superlattices in a subsequent study [230]. The evolution of the Raman modes across the electronic and magnetic phase transitions is compared for the compounds with $T_{MIT} = T_{\mathrm{N}}$ ($NdNiO_3$) and $T_{MIT} \neq T_{\mathrm{N}}$ ($SmNiO_3$, $Sm_{0.6}Nd_{0.4}NiO_3$), respectively. In the regime $T_{\mathrm{N}} < T < T_{MIT}$ a pronounced softening by ∼40 cm^{-1} of one mode around 420 cm^{-1} is observed and brought into relation with a change in the distortion of the NiO_6 octahedra stabilizing upon cooling at the magnetic transition. In more detail, the softening is interpreted as a ferroelectric soft mode and believed to be too large to correspond to the $Ni^{3\pm\delta}$ charge disproportionation scenario from Ref. [63]. The stabilization at T_{N} can indicate a coupling between the ferroelectric and magnetic order parameters and might be a signature of possible magnetoelectric multiferroic character of the nickelates [118, 119, 231].

We have grown 12 nm $NdNiO_3$ films on LSAO and LSAT substrates, respectively [Fig. 4.3(d)]. The spectrum of the film on LSAO is closely similar to the corresponding one in Fig. 4.3(c). Both, LSAO and $LaAlO_3$ induce compressive strain to the film. The phonon modes of the film on LSAT (tensile strain), however, exhibit different frequencies and relative intensities. Here, the confocal z-scan technique will allow to study the impacts of the different lattice dynamics due to epitaxial strain in more detail, as elucidated in the following sections.

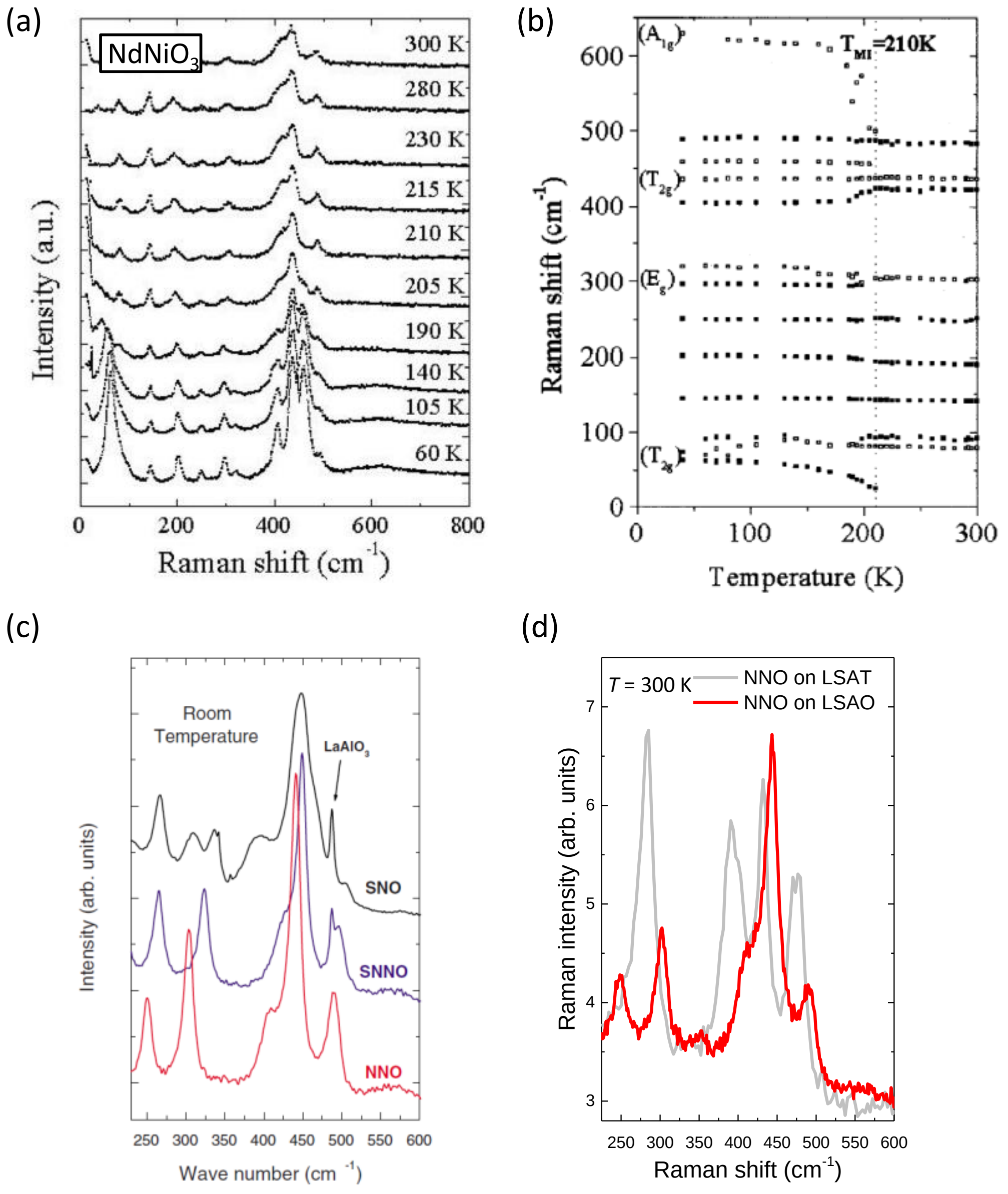

Figure 4.3 **Raman spectra of $NdNiO_3$.** (a) Temperature series of 150 nm $NdNiO_3$ on Si substrate. Spectra are unpolarized. Phonon modes below 100 cm^{-1} are assigned to Nd displacing, NiO_6 octahedral distortions correspond to the range 150-500 cm^{-1} and the band at 620 cm^{-1} (best visible at $T = 60$ K) is suggested to be octahedral breathing distortion. (b) Temperature dependence of the Raman frequencies. A renormalization of specific modes is observed at $T = 210$ K, the metal-insulator transition temperature. (a), (b) are adapted from Ref. [63]. (c) Unpolarized Raman spectra of $SmNiO_3$ (SNO), $Sm_{0.6}Nd_{0.4}NiO_3$ (SNNO), and $NdNiO_3$ (NNO) films on $LaAlO_3$ substrate. Film thicknesses are 17, 52, and 75 nm, respectively. The figure is adapted from Ref. [226]. (d) Experimental data of 12 nm $NdNiO_3$ on LSAO (red) and LSAT substrate (gray), respectively. The spectrum of the film on LSAO is closely similar to the corresponding spectrum in (c), whereas the energies and intensities of the modes of the film on LSAT differ significantly. The spectra were recorded by the confocal z-scan technique.

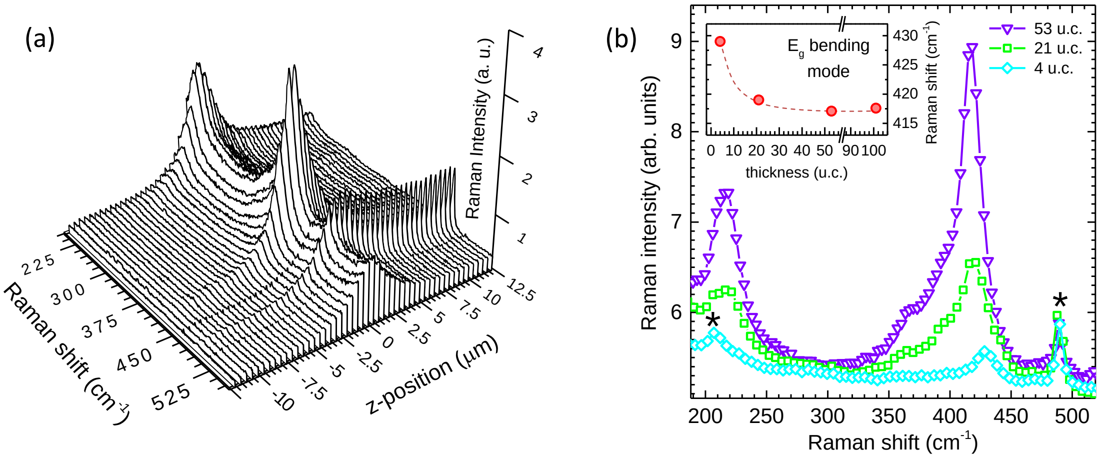

Figure 4.4 **Evolution of $LaNiO_3$ E_g-bending mode with film thickness.** (a) Confocal Raman z-scan of a 53 unit cell (21 nm) thick $LaNiO_3$ film on $LaAlO_3$ substrate at $T = 300$ K around the E_g-bending mode at ∼420 cm^{-1}. (b) Comparison of the $z = 0$ spectra for $LaNiO_3$ films of different thickness from 4 unit cells to 53 unit cells. The shift in the frequency of the $LaNiO_3$ E_g-bending mode at around 420 cm^{-1} is a consequence of the strain-relaxation in thicker films. The asterisks indicate substrate peaks of $LaAlO_3$ (here, the substrate spectrum is not subtracted from the $z = 0$ spectrum). The inset shows the frequency evolution of the E_g-bending mode with increasing film thickness. The dashed line is a guide for the eye.

4.2 Lattice dynamics of nickelate heterostructures

4.2.1 Ultra-thin $LaNiO_3$ films and the evolution of the E_g bending mode

As a first systematic study that applies the confocal z-scan the lattice dynamics of fully strained $LaNiO_3$ films with thickness as low as 4 pseudocubic unit cells was investigated [55]. With increasing film thickness a large softening of a $LaNiO_3$ E_g-bending mode is observed, indicating the relaxation of biaxial compressive strain imposed by the $LaAlO_3$ substrate.

The samples series was $LaNiO_3$ films consisting of 101 pseudocubic unit cells (u.c.) (40 nm), 53 u.c. (21 nm), 21 u.c. (8 nm), and 4 u.c. (1.6 nm), grown by PLD. Fig. 4.4(a) shows as an example the unpolarized confocal z-scan of the 53 u.c. sample in the range between 220 cm^{-1} and 550 cm^{-1}, where the strongest changes across the sample series occurred. The $z = 0$ spectra of the series of films is are compared in Fig. 4.4(b). In the range between 200 cm^{-1} and 500 cm^{-1} four $LaNiO_3$ phonon modes are observed for the 53 u.c film, namely at 215 cm^{-1}, 365 cm^{-1}, 398 cm^{-1}, and 417 cm^{-1}. The mode at 365 cm^{-1} was neither observed experimentally in bulk-like $LaNiO_3$ [225] nor obtained in the LSDA calculations for space group $R\bar{3}c$ (No. 167) [228]. Similar to our observations on thin $LaNiO_3$ on LSAT [Fig. 4.2(d)], the occurrence of additional Raman active modes indicates that the epitaxially grown thin films crystallize in a subgroup of $R\bar{3}c$ with lower symmetry. As suggested by x-ray structural refinements on similar $LaNiO_3$ films [146, 150] the subgroup can be $C2/c$ (No. 15). This would also agree with the recent report of Ref. [227] assigning the $C2/c$ symmetry to compressively strained

$LaNiO_3$.

Whereas Ref. [227] ended with film thicknesses of 14 nm, the confocal z-scan allowed us to also study thinner films with 21 u.c. (8 nm) and 4 u.c. (1.6 nm). Interestingly, the number of modes is not changing further, but particularly the frequency of the E_g-bending mode experiences a drastic shift. A reduced number of modes would be expected in case the ultra-thin $LaNiO_3$ finally adopts the substrate's $R\bar{3}c$ symmetry and larger number in case there is a further symmetry breaking. The softening with increasing film thickness is illustrated in Fig. 4.4(b) . The band softens from 429 cm^{-1} for 4 u.c. to 419 cm^{-1} for 21 u.c. and to approximately 417 cm^{-1} for 53 u.c. and 101 u.c.

In general, a stretching of bond lengths – as e.g. due to relaxation of compressive strain – leads to a decrease in the phonon frequency. In case of the rare-earth nickelates $R$$NiO_3$ the lattice mismatch to a substrate is accommodated by the R-site and Ni cation sublattice and by tilting of the NiO_6 octahedra. Whereas we found in XRD characterization of comparable $R$$NiO_3$ samples [112] that the cation sublattice is still highly strained after $\sim$ 10 nm (length scale for significant relaxation is 20 to 50 nm), a coherent relation for the octahedral tilts of the substrate and the film can usually only be established for the first few unit cells after the interface [232]. Here, likely the superposition of the two strain relaxation effects is observed, with the tilt relaxation dominating for the first few unit cells after the interface and showing a strong impact on the Raman frequency of the E_g-bending mode which is directly related to the Ni-O-Ni bond angle. For larger film thicknesses also the cation sublattice strain gradually relaxes and reaches the plateau value of 417 cm^{-1} starting from approximately 40 u.c. Significantly thicker films (101 u.c.) do not show a further softening suggesting that a strain released state is stabilized. It is further noted, that even in case of the 4 u.c. the $a^-a^-a^-$ tilt pattern of the $LaAlO_3$ is not fully adopted by the $LaNiO_3$ as the number of phonons stays constant in our sample series. Rather, the tilting magnitude is not identical in all three pseudocubic directions (in accordance with $a^-b^-b^-$ of $C2/c$), accounting for the compressive strain accommodation.

In conclusion, depth-resolved confocal Raman spectroscopy with visible laser light is a sensitive tool to probe mechanisms of strain relaxation and changes of bond angles in ultra-thin systems. For future studies of strain relaxation mechanisms it would be interesting to combine our experimental results with first-principle calculations and scanning transmission electron microscopy, mapping the oxygen positions and the octahedral tilts angles close to the substrate interface.

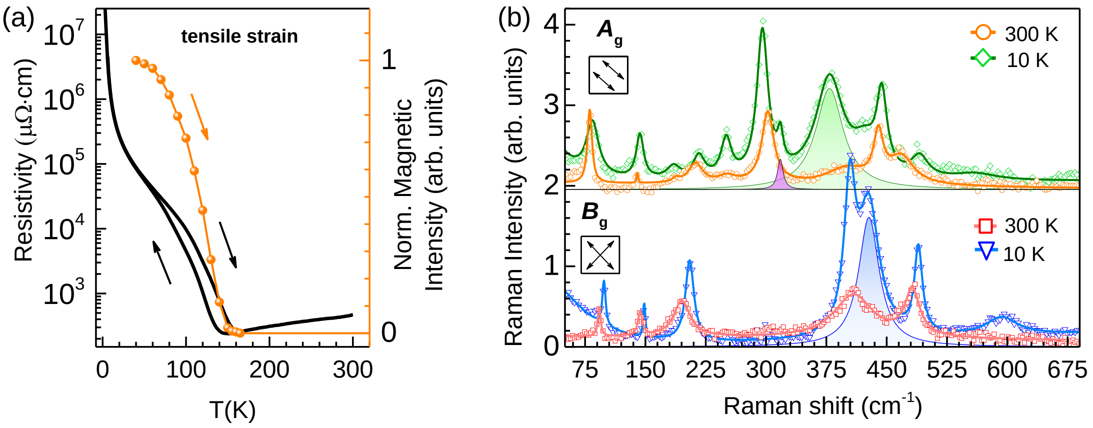

Figure 4.5 Phase transitions in $NdNiO_3$ films under tensile strain. Electrical resistivity (left scale) and normalized intensity of the antiferromagnetic (1/4, 1/4, 1/4) reflection (right scale) measured by REXS as a function of temperature. Arrows indicate warming and cooling cycles. (b) Raman spectra at T = 300 and 10 K in A_g and B_g symmetry (upper and lower subpanels, respectively). The solid lines represent the results of least-squares fits of the data to Voigt profiles. Anomalous modes at low T associated with the $P2_1/n$ phase are have shaded profiles. The arrows in the insets in (b) indicate the electric field vectors of the incoming and the scattered light with respect to the substrate edges.

4.2.2 Phase transitions of $NdNiO_3$

$NdNiO_3$ thin films with a thickness of ∼9 nm were grown by PLD on [001] oriented LSAT substrates as described in Ref. [112]. The larger in-plane lattice constants of LSAT impose moderate tensile strain to the $NdNiO_3$ lattice (see Table A.1 and Table A.2 in Appendix A). The electronic and magnetic phase transitions of bulk $NdNiO_3$ and $PrNiO_3$ are similar, with a slightly higher $T_{MIT} = T_N$ in case of $NdNiO_3$. Raman spectra of both materials grown on LSAT are found to be closely related, with few discrepancies which will be pointed out later. The current section mainly discusses $NdNiO_3$ whereas the section 'Spin density wave in $PrNiO_3$ heterostructures' will focus on the $PrNiO_3$ Raman response.

For powder samples of $NdNiO_3$ and $PrNiO_3$ the $Pbnm \rightarrow P2_1/n$ symmetry breaking at T_{MIT} has been confirmed by recent high-resolution x-ray and neutron diffraction refinements [64, 65]. In tensile strained $NdNiO_3$ films the same $Pbnm$ symmetry as in bulk was identified at room-temperature [147]. Hence, it will be assumed in the following that the $NdNiO_3$ and $PrNiO_3$ films under tensile strain also exhibit $Pbnm$ space group and undergo a symmetry reduction to $P2_1/n$ at the MIT, whose signatures can be observed by Raman scattering [63, 226].

Fig. 4.5(a) shows the electrical resistivity of the 9 nm $NdNiO_3$ film together with the intensity of the antiferromagnetic REXS Bragg reflection[2] as a function of temperature. The tensile strained film shows a MIT with a hysteresis, which is indicative of a first-

---

[2] Resistivity was measured via the van der Pauw method. REXS experiments were performed at the BESSY-II undulator beam line UE46-PGM1 at the Ni L_3 edge, following a protocol described in Ref. [4].

order transition. The intensity of the (1/4, 1/4, 1/4) Bragg reflection (pseudocubic notation) determined by REXS reflects the order parameter of non-collinear antiferromagnetism. More details about magnetic REXS can be found in chapter 3 and chapter 5. The onset of magnetic order determined by REXS coincides approximately with the MIT, as it does in bulk $NdNiO_3$ [61]. The dependence of the MIT on epitaxial strain in $NdNiO_3$ is qualitatively similar to recent findings reported in Ref. [2].

The z=0 Raman spectra corrected by the substrate contribution is displayed in Fig. 4.5(b) and supplies complementary information about charge/bond ordering, which modifies the lattice structure and hence the phonon spectrum. At high temperatures, the Raman-active phonons reflect the pseudocubic perovskite structure, with uniform NiO_6 octahedra. Upon cooling below T_{MIT}, the spectrum of $NdNiO_3$ under tensile strain exhibits three additional modes at 317 cm^{-1}, 375 cm^{-1} and 425 cm^{-1}. Polarization-resolved data in different light-field configurations (indicated in Fig. 4.5(b) as arrows relative to the substrate edges) determine the symmetry of the displacement patterns as A_{g} and $B_{1\mathrm{g}}$, respectively. The Raman spectra were fitted to a superposition of Voigt profiles resulting from a convolution of the intrinsic Lorentzian lineshape with the Gaussian spectrometer resolution (solid lines in Figs. 4.5(b)).

We call the new modes occurring below the below the MIT (shaded Voigt profiles) *anomalous modes* whereas the modes present above and below the transition are called *regular modes*. The behavior of the anomalous modes at 375 cm^{-1} and 425 cm^{-1} (green and blue shaded Voigt profile) is closely similar to the temperature evolution of $PrNiO_3$ phonon modes which will be discussed in detail below. The mode at 317 cm^{-1} (violet Voigt profile) is not observed in $PrNiO_3$. In the following we will focus onto this feature and the spectral range 200 - 335 cm^{-1} for temperatures around $T_{\mathrm{MIT}} = 140$ K.

Fig. 4.6 gives a comprehensive overview on the temperature evolution of the spectrum in the A_g channel. The Raman bands of this energy range are assigned to distortions of the NiO_6 octahedra [63]. The strongest mode at 310 cm^{-1} at $T = 300$ K corresponds to rotational displacement patterns of the octahedra [54]. As can be seen in Fig. 4.6(a) the spectral signature around ~300 cm^{-1} experiences drastic changes when the sample is cooled below the MIT. In our fits the 310 cm^{-1} mode vanishes below the transition (black Voigt profile in Fig. 4.6(b)) and a strong band at 295 cm^{-1} and one weak band at 317 cm^{-1} dominate this spectral range (orange and violet Voigt profiles). Similar observations were made in the unpolarized Raman study by Girardot *et al.* [226] and commented as potential splitting of a mode across the structural phase transition. Concerning our polarization analysis it is noted that A_g phonons are non-degenerate, i.e. the observed spectral evolution cannot be due to a monoclinic splitting of one Raman band. An explanation of the spectral features will be given later in conjunction with first-principal calculations of the $Pbnm$ and $P2_1/n$ phonon frequencies.

The detailed evolution of the integrated intensities of the modes in this spectral range is shown in Fig. 4.6(c). The intensity of the 295 cm^{-1} and 317 cm^{-1} line (orange and violet Voigt profiles) evolves in an order parameter-like manner across the MIT. Note that the evolution of the 295 cm^{-1} mode at around the phase transition can be interpreted in more than one way. In Figs. 4.6(b),(c) we have chosen to fit the spectral

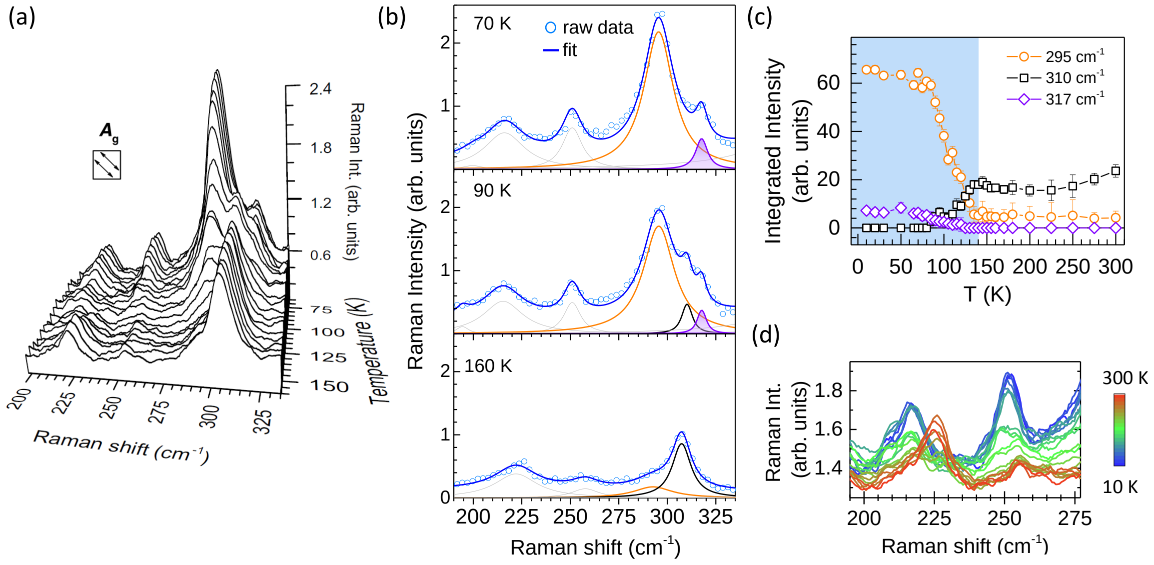

Figure 4.6 Rotational A_g modes of $NdNiO_3$ at the MIT. (a) Evolution of A_g phonon modes in the range 200 - 335 cm^{-1} around $T_{\mathrm{MIT}} = 140$ K. The subpanels of (b) show cuts of the 3-D plot from (a) at temperatures $T = 70$, 90, and 160 K. The solid lines are least-squares fits of the data to Voigt profiles which are indicated individually at the bottom of each panel. Profiles of modes related to rotational distortions of the NiO_6 octahedra are color-coded in orange, black, and green. Other modes are colored in gray. (c) Detailed temperature dependence of the integrated intensity of the phonon modes at around 295 cm^{-1}, 310 cm^{-1}, and 317 cm^{-1}. (d) Temperature-dependent changes in the spectrum for energies < 275 cm^{-1}.

weight between 280 - 300 cm^{-1} by one Voigt profile (orange) for all temperatures. This profile then experiences a hardening and strong increase in intensity with decreasing temperature. The other option is that the weak 295 cm^{-1} mode from high temperatures is also weakly present at low temperatures, but the 310 cm^{-1} mode (black Voigt profile) experiences a renormalization of its frequency and a strong increase in intensity and becomes the 295 cm^{-1} band at low-T, i.e. in this regime the original orange mode cannot be resolved any more. The detailed temperature evolution of the 317 cm^{-1} line is more clear due to the separation of the peaks [Figs. 4.6(b),(c)].

From Fig. 4.6(c) it can be deduced that there is a large phase coexistence of the orthorhombic *Pbnm* and the monoclinic $P2_1/n$ phase between 140 and 85 K. It is interesting to compare this mixed-phase region to the work by Mattoni *et al.* who used photoemission electron microscopy (PEEM) to image the switching between metallic and insulting domains as a function of temperature [233]. Upon cooling or heating, the majority of domains switches its state within a window a of few K, as extracted from the x-ray absorption data in total electron yield mode which is local probe of the film's surface region. In fluorescence yield mode which probes the entire film within the diameter of the x-ray beam spot (comparable to the 20 μm Raman laser spot) the width of the transition is $\Delta T \approx 40$ K. The remaining discrepancy to the $\Delta T \approx 55$ K observed with Raman spectroscopy can be explained e.g. by the different morphological characteristics of the terraced substrate used in Ref. [233]. Moreover, the epitaxy to the orthorhombic $NdGaO_3$ generally yields a sharper upturn

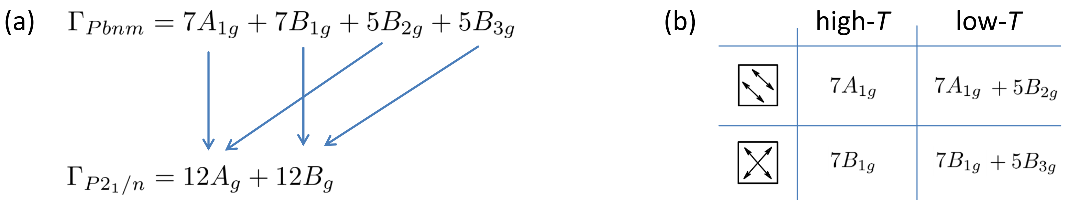

Figure 4.7 Mode symmetry analysis of the structural phase transition. (a) The high temperature orthorhombic *Pbnm* phase exhibits 24 Raman modes in total – the same number as the low temperature monoclinic $P2_1/n$ phase. The 12 A_g and 12 B_g modes of $P2_1/n$ space group result from $7A_{1g} + 5B_{2g}$ and $7B_{1g} + 5B_{3g}$ modes of *Pbnm*, respectively. (b) Expected modes in the high -and low-temperature phase for the Raman polarization configurations used in our measurements. For clarity the modes in the low temperature phase are also indicated in the *Pbnm* nomenclature.

in resistivity of the nickelate's MIT (see Fig. 5.5(c) in chapter 5) which then in turn can also be reflected in a smaller or wider Raman ΔT width.

Similar effects in the temperature evolution as discussed above are also observed for the modes in the range 200 - 275 cm^{-1}, as shown in Fig. 4.6(d).

A deeper understanding of the above characteristics in the mode evolution across the MIT can be gained from a combination of mode symmetry analysis and *ab-initio* calculations.

4.2.3 Symmetry analysis and phonon calculations

Both space groups *Pbnm* and $P2_1/n$ give rise to 24 Raman modes in total [Fig. 4.7(a)], i.e. from this point of view no extra lines are expected to occur across the phase transition. At first glance this is contradicting the occurrence of the new modes coined as anomalous modes above. However, the changes in the Raman spectra can be understood when considering the effects of the polarization configurations that were used for the measurements. In the *Pbnm* phase the Z(X'X')$\bar{\text{Z}}$ and Z(X'Y')$\bar{\text{Z}}$ configurations only probe 7A_{1g} and 7B_{1g} modes, respectively. In the $P2_1/n$ phase the same configurations probe however 12 A_g and 12 B_g modes, respectively. It can be shown that the additional 5 A_g modes result from the *Pbnm* B_{2g} channel and the 5 additional B_g modes result from the *Pbnm* B_{3g} channel [Fig. 4.7(a)]. In consequence 5 additional modes can be expected across the phase transition, for both of the polarization configurations [Fig. 4.7(b)].

To confirm this quantitatively, M. Höppner (MPI-FKF) has used Density Functional Perturbation Theory as implemented in quantum espresso [234] to calculate various nickelate phonon spectra at **q**=0. Standard local density approximation in the parametrization of Perdew/Zunger [235] and projector augmented wave pseudopotentials [236] were used. The plane wave (charge) cutoff was set to 80 Ry (960 Ry), respectively. The primitive Brillouin Zone was sampled with 5 × 5 × 5 k-points. The calculations shown here were conducted for $PrNiO_3$, note however that the experimental Raman spectra of $PrNiO_3$ and $NdNiO_3$ are closely similar. A frozen core configuration of the Pr f-shell was assumed: Pr $4f^2 = \text{Pr}^{3+}$. Prior to the phonon

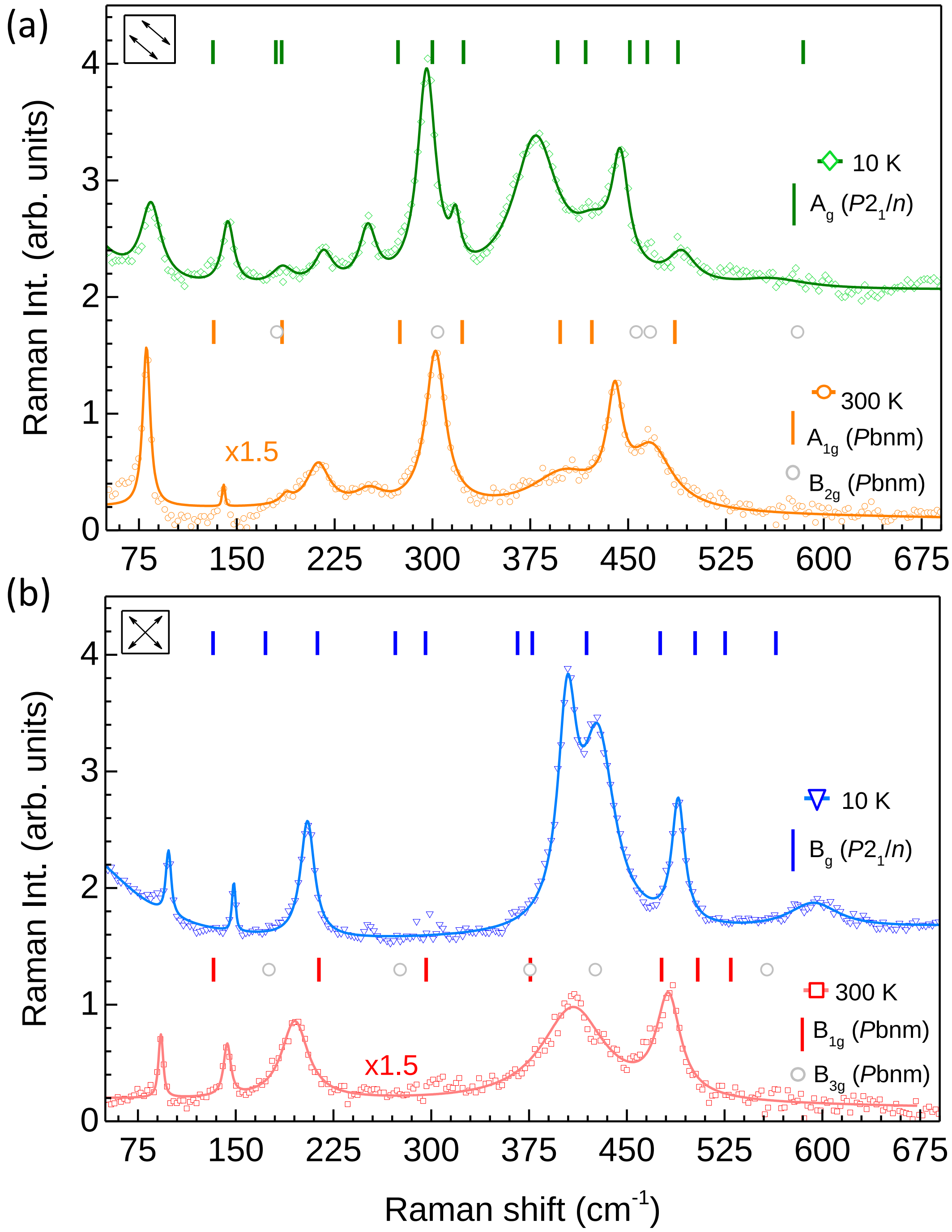

Figure 4.8 Raman frequency calculations for $YNiO_3$. (a) Comparison of calculated frequencies of $YNiO_3$ to experimental data of $NdNiO_3$ on LSAT at $T = 10$ and 300 K (green and orange curves) for $Z(X'X')\bar{Z}$ scattering configuration. At low-T 12 $P2_1/n$ modes are calculated (green dashes). At high-T 7 $Pbnm$ modes of the A_{1g} are calculated (orange dashes) and can be expected in the experimental spectrum. Additionally the frequencies of 5 modes with B_{2g} symmetry are indicated (open gray circles) but not expected to be observed in the spectrum. The correspondence between the 12 $P2_1/n$ modes and the 7 + 5 $Pbnm$ modes is obvious. (b) Same as in (a) but for the $Z(X'Y')\bar{Z}$ scattering configuration.

calculation, the forces on the atoms were minimized to be smaller than 0.3 mRy/bohr. The relaxation of the crystal lattices was performed within LDA. As starting point the experimental *Pbnm* and $P2_1/n$ structures were used [65, 237]. To simulate the influence of a substrate, additionally two-dimensional strain was applied to the unit cell prior to the force minimization.

As a first approach the Raman frequencies of $YNiO_3$ in $P2_1/n$ and *Pbnm* space group were calculated. The Yttrium's [Kr] $4d^1$ $5s^2$ electron configuration (Y^{3+}: [Kr]) avoids difficulties occurring when Density Functional Theory treats open $4f$ shell systems with their highly localized character. This would also be possible by considering $LaNiO_3$ (with La: [Xe] $5d^1$ $6s^2$ and La^{3+}: [Xe]), however, monoclinic distortions with two differently sized NiO_6 octahedra cannot be stabilized for the fully relaxed structure of this compound. As displayed in Fig. 4.8 and Tables 4.1, 4.2 the overall agreement between the calculated frequencies and the experimental $PrNiO_3$ and $NdNiO_3$ spectra is not satisfying, except for a few modes. This might not come as a surprise, since the bond lengths and distortions of the two compounds and the Y and Pr, Nd atomic masses are different. However, the trend of additional lines from the *Pbnm* B_{2g} and B_{3g} channel appearing in the low-T phase – as already deduced by the mode symmetry analysis – can be clearly recognized in the frequency calculation in Fig. 4.8(a),(b).

As next step the Raman frequencies of $PrNiO_3$ were calculated using sets of pseudopotentials to account for the impacts of the 2 electrons in the $4f$ shell of the Pr^{3+} ion. Fig. 4.9 compares the results of the calculation with the experimental $NdNiO_3$ spectra. The comparison is to the $NdNiO_3$ spectra instead of the $PrNiO_3$ spectra since the $NdNiO_3$ modes are significantly more pronounced but similar in energy to $PrNiO_3$. Starting with the 10 K spectrum of the A_g channel [Fig. 4.9(a)] there is an excellent agreement between calculation and experiment for four of the first five low-energy modes. The third mode at 185 cm^{-1} is observed ∼25 cm^{-1} higher in energy as calculated. However, the intensity of the mode is almost at the noise level. Thus, the feature in the spectrum might be just an artifact and it is possible that the actual mode corresponds to a weak shoulder of the band at ∼145 cm^{-1} which we did not consider in our fit. The first four lines in the $T = 300$ K spectrum show a discrepancy between calculation and experiment, but can be roughly assigned. Again the weak mode at 185 cm^{-1} which we have fitted by an extra Voigt profile (185 cm^{-1}) can be a noise artifact. Being a real phonon feature would imply a total number of phonons higher than the five modes allowed in the *Pbnm* A_{1g} channel. Additional peaks in the Raman spectrum can originate from leakage from other polarizations, due to insufficient impact of the polarizing optical components of the Raman spectrometer or polycrystalline fractions of the sample. Both do not apply for our case. Additional lines can also emerge from impurity phases, ordered lattice defects or a lattice symmetry lower than *Pbnm*. However, hard x-ray characterization of the samples did not show indications for any of these points.

The subsequent energy regime includes the strong A_g rotational mode at around 300 cm^{-1} and an additional weak mode at slightly higher energies in the $T = 10$ K spectrum. The detailed temperature dependence of these features was already discussed in the context of Fig. 4.6. From the calculation it can be deduced that the A_g rotational mode experiences a renormalization in frequency across the phase transition and the

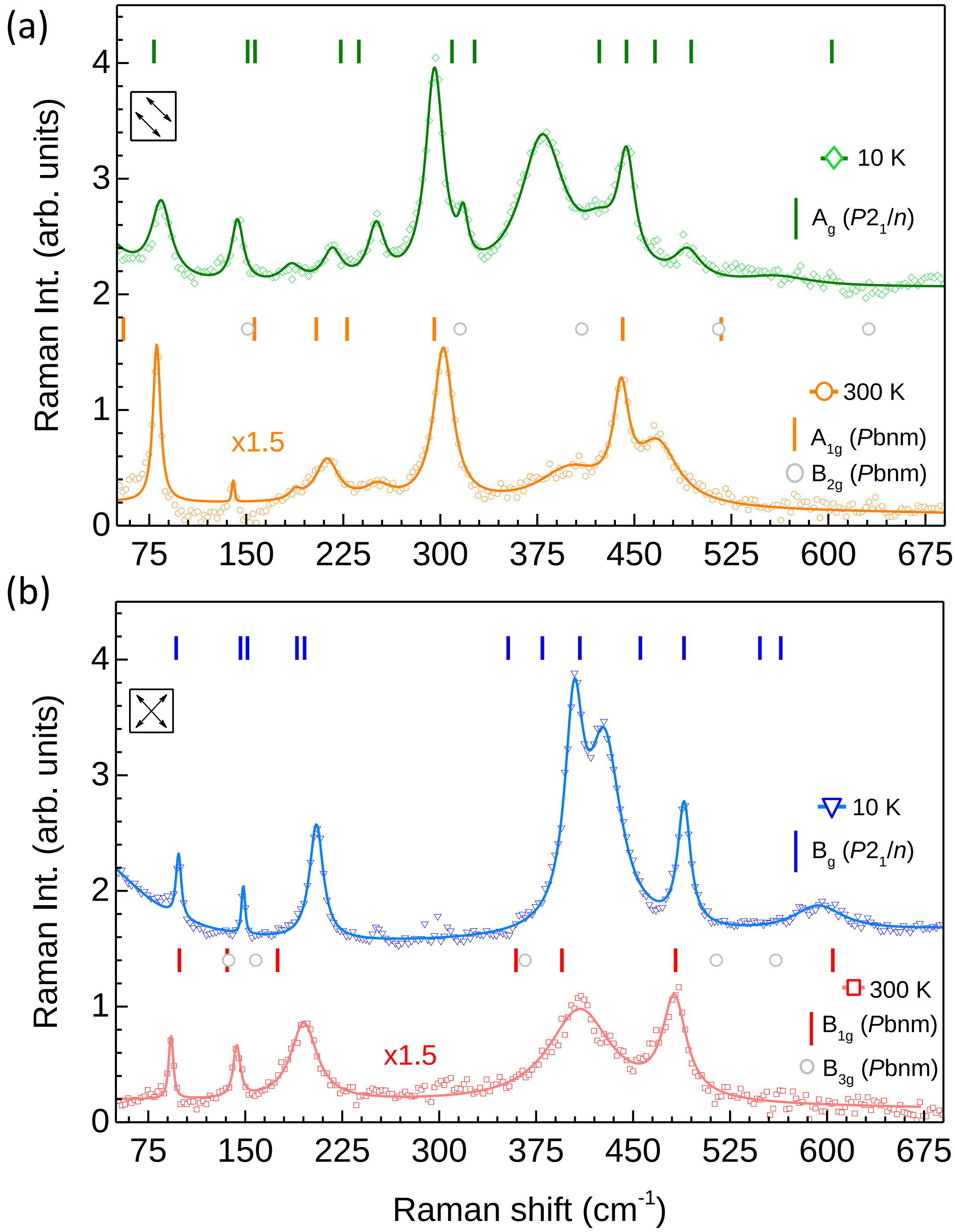

Figure 4.9 Raman frequency calculations for $PrNiO_3$. (a),(b) Comparison of calculated frequencies of $PrNiO_3$ to experimental data of $NdNiO_3$ on LSAT. Lines, symbols, and indicated Raman frequencies are analogous to Fig. 4.8.

weak mode results from a *Pbnm* B_{2g} mode which then is observed in the A_g channel at low temperatures. Both calculated $P2_1/n$ frequencies are moderately too high in energy. This tendency becomes even stronger for the modes of the massif ranging from 350 – 525 cm^{-1} and a down-shift of all calculated energies by 20 cm^{-1} or more would lead to a much better agreement between calculation and experiment in this regime. In particular the band observed at 375 cm^{-1} (corresponding to an anomalous mode discussed for $PrNiO_3$ in Fig. 4.15(c)) is calculated at 420 cm^{-1} when resulting from the 410 cm^{-1} B_{2g} high-T *Pbnm* mode. The overestimation of the calculated frequencies can be a consequence of distortions of the octahedral network of the thin films on LSAT which are not present in the bulk lattice used as starting point for the relaxed structure of the calculation. In particular elongations, compressions and bucklings can be induced to the octahedra by epitaxial strain. The strain accommodation via changes in the octahedral tilt angles mainly affects the frequency of the A_g rotational mode and not so much the massif from 350 – 525 cm^{-1}, as we will argue later. Also the frequencies of the low-energy lines might be more robust against details of the tilt angles as they are partly governed by the A-site cation displacement of the ABO_3 perovskite structure.

To further explore the impacts of octahedral distortions on the Raman spectrum virtual strain was applied to the bulk structure [65] before the phonon calculation. Namely 1% tensile strain was applied along the orthorhombic a and b direction of the $PrNiO_3$ unit cell. As can bee seen in Table 4.2 there is only a moderate change of the frequencies for the virtually strained unit cell. In conclusion, this approach of applying two-dimensional strain does not simulate the epitaxial strain accommodation of the nickelate film properly. For the future, the input from a full structural refinement of the oxygen positions in tensile strained nickelate films can help to reach a higher agreement between calculation and experiment in this energy range.

The highest calculated energy for a collective lattice displacement is ∼605 cm^{-1} and related to breathing distortions of the oxygen octahedra cage. We assign this to the weak and broad experimental line at ∼565 cm^{-1}.

In crossed polarization channel [Fig. 4.6(b)] the match between calculation and experiment is qualitatively similar to the parallel polarization [Fig. 4.6(a)]. Good agreement is achieved for low-energy modes at 10 and 300 K. In the $T = 10$ K spectrum only three of the five B_g lines are resolved experimentally, probably due to the strong overlap of the peaks. For higher energies, the agreement becomes worse again, and in particular it is difficult to relate the anomalous mode at ∼430 cm^{-1} to a mode of B_{3g} symmetry at $T = 300$ K. Again the discrepancy in frequencies could be because the octahedral distortions not captured properly in the calculation.

Table 4.1 Raman frequencies in the $P2_1/n$ phase. Phonon frequencies (cm^{-1}) extracted from the Voigt-profile fits of the experimental data of $PrNiO_3$ and $NdNiO_3$ at $T = 10$ K and calculated frequencies of $YNiO_3$ and $PrNiO_3$.

Mode	$PrNiO_3$ (exp.)	$NdNiO_3$ (exp.)	$YNiO_3$ (calc.)	$PrNiO_3$ (calc.)
A_g (1)	81	84	132	79
A_g (2)	149	144	180	151
A_g (3)	-	185	184	157
A_g (4)	200	217	274	223
A_g (5)	258	250	300	237
A_g (6)	287	295	324	309
A_g (7)	-	318	396	327
A_g (8)	372	380	417	423
A_g (9)	415	421	451	444
A_g (10)	436	443	465	466
A_g (11)	469	490	488	494
A_g (12)	550	565	584	603
B_g (1)	97	99	133	97
B_g (2)	132	149	173	146
B_g (3)	-	-	213	152
B_g (4)	-	-	272	190
B_g (5)	194	205	296	196
B_g (6)	-	-	366	353
B_g (7)	-	-	378	380
B_g (8)	396	405	419	409
B_g (9)	424	426	476	456
B_g (10)	483	490	502	489
B_g (11)	-	-	525	548
B_g (12)	-	592	564	564

Table 4.2 Raman frequencies in the *Pbnm* phase. Phonon frequencies (cm^{-1}) extracted from the Voigt-profile fits of the experimental data of $PrNiO_3$ and $NdNiO_3$ at $T = 300$ K and calculated frequencies of $YNiO_3$ and $PrNiO_3$. In the last column 1% in-plane tensile strain has been applied to the $PrNiO_3$ unit cell.

Mode	$PrNiO_3$ (exp.)	$NdNiO_3$ (exp.)	$YNiO_3$ (calc.)	$PrNiO_3$ (calc.)	str. $PrNiO_3$ (calc.)
A_{1g} (1)	-	81	132	55	58
A_{1g} (2)	151	141	185	156	154
A_{1g} (3)	185	214	275	204	204
A_{1g} (4)	280	255	323	228	225
A_{1g} (5)	-	302	398	295	297
A_{1g} (6)	433	440	422	441	447
A_{1g} (7)	474	469	486	517	481
B_{1g} (1)	-	93	133	99	98
B_{1g} (2)	-	145	214	136	128
B_{1g} (3)	165	195	296	175	167
B_{1g} (4)	-	-	376	359	363
B_{1g} (5)	391	409	477	395	399
B_{1g} (6)	473	484	504	483	480
B_{1g} (7)	-	-	530	604	573
B_{2g} (1)	-	-	181	151	154
B_{2g} (2)	-	-	304	315	317
B_{2g} (3)	-	-	456	409	396
B_{2g} (4)	-	-	467	515	519
B_{2g} (5)	-	-	580	631	624
B_{3g} (1)	-	-	176	137	140
B_{3g} (2)	-	-	276	158	166
B_{3g} (3)	-	-	376	367	360
B_{3g} (4)	-	-	426	514	476
B_{3g} (5)	-	-	558	560	591

4.2.4 Comparative Raman study of nickelates

In order to gain general insights on the lattice dynamics of nickelates we have investigated Raman spectra as a function of the rare-earth ion R. Moreover, we compare particular Raman bands corresponding to rotational distortions of the NiO_6 octahedra to previous results on similar ABO_3 perovskite compounds that comprise an universal Raman-frequency scaling law as function of octahedral tilts [238].

Films with $R = \mathrm{Sm}$ were grown by RF magnetron sputtering [3] and with $R = \mathrm{La}$, Pr, and Nd by PLD as described above. XRD characterization revealed similar crystalline quality for the films synthesized by the different techniques. The $T = 10$ K Raman spectra measured in Z(X'X')$\bar{\mathrm{Z}}$ scattering configuration are compared Figs. 4.10(a)-(d). All films are approximately 10 nm thick and grown on LSAT substrate. The films with $R = \mathrm{Sm}$, Nd and Pr are expected to exhibit identical space groups, analogous to their bulk counterparts, i.e. their spectra can be compared directly.

In general, increasing ionic radii r_R lead to decreasing lattice distortions and most of the bond lengths stretch, resulting in (i) a reduction of the Raman intensity and (ii) a softening of Raman frequencies. This behavior can be observed in Figs. 4.10(a)-(c) e.g. for the anomalous modes (green shaded Voigt profile) which decrease in (integrated) intensity from Sm to Nd and to Pr and soften from 408.1 cm^{-1} to 377.4 cm^{-1} and to 373.4 cm^{-1}, or for the regular band at 445.3 cm^{-1} softening to 442.5 cm^{-1} and to 435.7 cm^{-1}. Further, only 10 $\mathrm{A_g}$ Raman bands are resolved for $R = \mathrm{Pr}$ whereas 12 modes can be fitted for $R = \mathrm{Nd}$, Sm which is in agreement with higher distortions in the latter compounds. This is even more evident in the Z(X'Y')$\bar{\mathrm{Z}}$ scattering configuration where 11 of the 12 $\mathrm{B_g}$ modes are observed for $R = \mathrm{Sm}$ but for $R = \mathrm{Nd}$ and Pr the modes between 225 cm^{-1} and 375 cm^{-1} lie below the noise level [Fig. 4.10(e)-(g)].

One has to be careful with a direct comparison of the $R = \mathrm{La}$ spectra in Figs. 4.10(d),(h) to the other spectra of Fig. 4.10 since the $LaNiO_3$ on LSAT might exhibit a different space group. The x-ray refinement by May *et al.* [146] suggests monoclinic $C2/c$ (no. 15) symmetry for $LaNiO_3$ films under both, compressive and tensile strain. The Raman study by Weber *et al.* [227] suggests orthorhombic $Fmmm$ (no. 69) for $LaNiO_3$ under tensile conditions on LSAT. We find in total five modes in the $\mathrm{A_g}$ channel and seven modes in the $\mathrm{B_g}$ channel in agreement with $C2/c$ selection rules but contradicting a smaller number of symmetry allowed modes in $Fmmm$ space group. For a final confirmation of $C2/c$ the oxygen position of our film will have to be refined or a proper calculation of the strained $LaNiO_3$ Raman frequencies would be required. However, the number of observed modes is a strong indication that our film exhibits space group $C2/c$ or another subgroup of $R\bar{3}c$.

Most striking in Figs. 4.10(a)-(d) is the evolution of the rotational $\mathrm{A_g}$ mode (orange shaded Voigt profile) as a function of the rare-earth ion R. The dependence of the frequency of rotational modes on the A- and B-site cations of the ABO_3 perovskite structure has been studied in before in various compounds [221, 238–240]. It was observed that the Raman frequency of such modes scales linearly with the magnitude of the BO_6 tilt angles [Fig. 4.10] which in first approximation is proportional to the A-site ionic radius. Iliev *et al.* proposed the universal law for the frequency scaling to

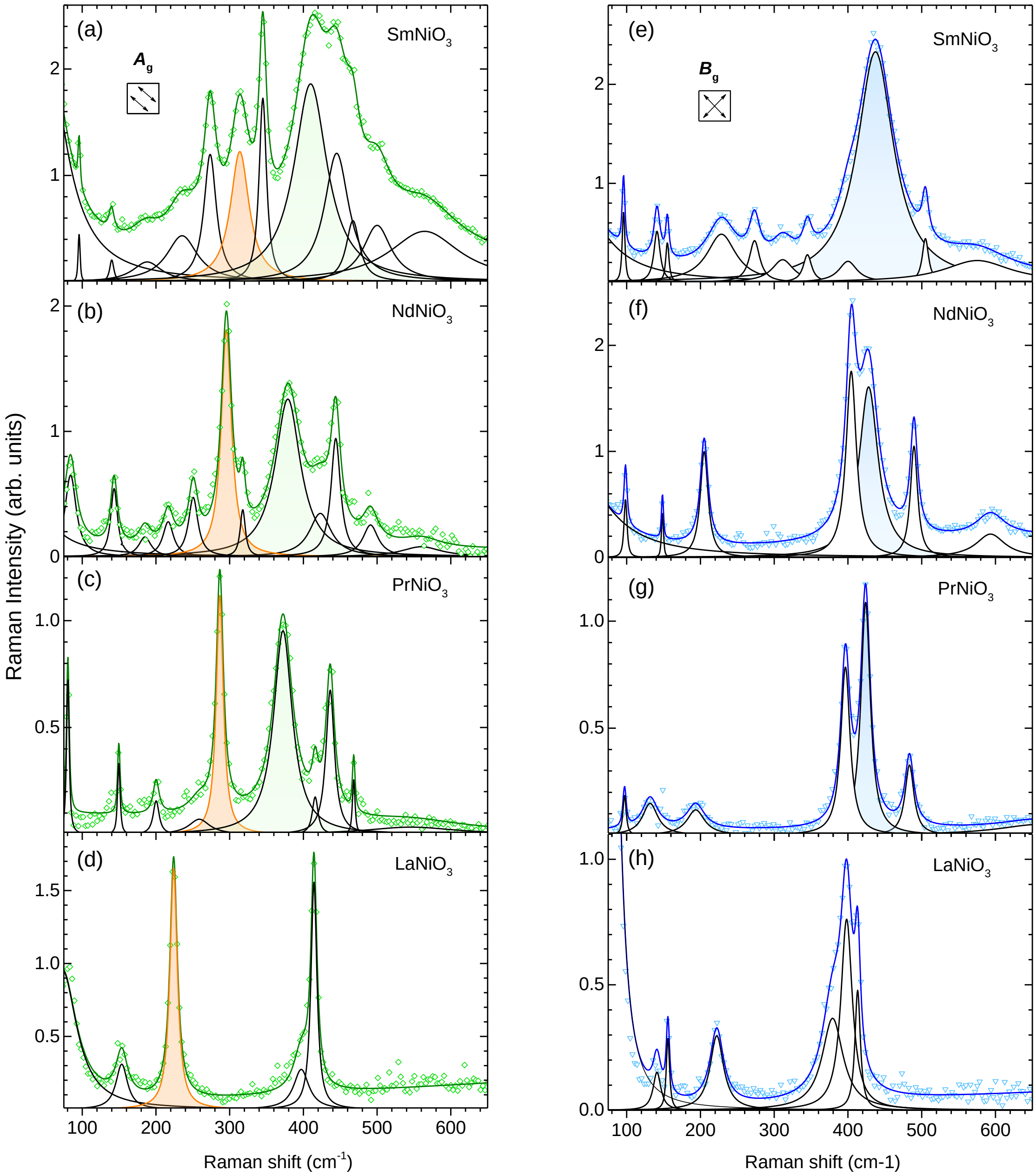

Figure 4.10 The A_g rotational mode in dependence of the RNiO$_3$ rare-earth ion. (a)-(d) Phonon modes of A_g symmetry at $T = 10$ K for RNiO$_3$ films on LSAT substrate. Film thicknesses for R = Sm, Nd, Pr, and La are 9 nm, 8 nm, 12 nm, and 9 nm, respectively. The solid lines are the superpositions of fits of the data to Voigt profiles which are indicated individually. The orange shaded profile is the A_g rotation mode. The intense anomalous mode occurring below T_{MIT} is shaded in green. (e)-(h) For comparison the corresponding modes in the B_g channel are shown. Intense anomalous mode are shaded in blue.

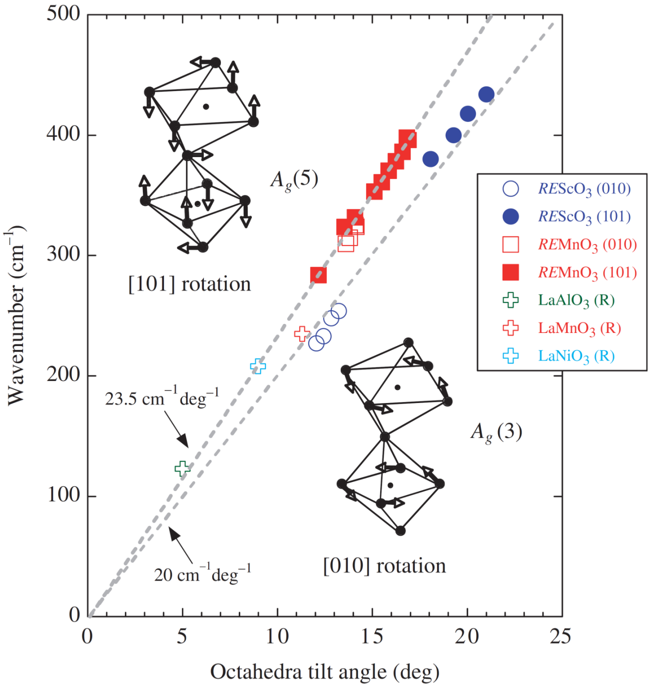

Figure 4.11 Rotational A$_g$ mode frequencies in dependence of octahedra tilt angles. A scaling law of ∼23.5 cm^{-1}/deg applies for the [101] rotational A$_g$ modes of REMnO$_3$ (filled red squares), with RE = La, Pr, Nd, Sm. Eu, Gd, Tb, Dy, Ho, and Y. The empty red squares correspond to the [010] rotational mode, of RE = Gd, Dy, and Y The [101] and [010] directions are the pseudocubic directions in the Pnma setting of space group No. 62. For REScO$_3$ the scaling law is ∼20 cm^{-1}/deg (filled and empty blue circles). Here RE = Nd. Sm, Gd, and Dy. Additionally the positions of [111] rotational modes of rhombohedral LaAlO$_3$, LaMnO$_3$, and LaNiO$_3$ are indicated. The figure is from Ref. [239] and includes data from references therein.

be ∼23.5 cm^{-1}/deg [238]. Small deviations from this scaling constant were detected when B-site cation is Sc or Cr [239, 240].

Chaban *et al.* have tested the ∼23.5 cm^{-1}/deg scaling law for bulk-like LaNiO$_3$ [225]. They calculate the octahedral tilt angle α'=9° about the [111] direction of a rhombohedral structure according to $x_{O1} = 1/2(1 - 1/\sqrt{3}\tan\alpha')$ with x_{O1} being the atomic coordinate of the oxygen position deviating from a hypothetical undistorted perovskite structure. The experimentally observed 209 cm^{-1} closely matches the 211 cm^{-1} calculated with the x_{O1} position of Ref. [148]. Moreover, it is stressed that the rotational A$_g$ mode is a soft mode of the phase transition from rhombohedral to the undistorted cubic perovskite and corresponds to zero frequency for α'=0°. In the frame-work of Landau theory, for a simple second-order phase transition the soft-mode frequency ω at $T < T_c$ is given by $\omega^2 \propto \omega_0^2(T_c - T)$ and ω^2 proportional to the octahedral rotational order parameter α'^2. A T_c of ∼1800 K can be extrapolated [225] or calculated from first-principles [228]. While this T_c is too high to be reached with the Raman setup, similar soft-mode transitions have been tracked in LaAlO$_3$ at lower temperatures [149] or under hydrostatic pressure [241].

The case of orthorhombic structures is a bit more intricate. For instance the *Pnma* structure (space group no. 62, alternative setting to *Pbnm*) can be described in terms of rotations α'_1, α'_2, and α'_3 around the pseudocubic [101], [010], and [111] axes, respectively [240]. However, it can be shown that two of the three rotation angles are already sufficient to fully characterize the crystal structure. In *Pnma* the octahedral rotations around the [101] and [010] directions [insets in Fig. 4.10] give rise to typical Raman lines, i.e. can provide information about the tilts α'_1 and α'_2, as for example in case of the orthomanganites [238, 242]. On the other hand, when the tilt angles are calculated from refined atomic positions [243] according to $\alpha'_1 = \arctan(2^{3/2}|(z_{O1})|)$ and $\alpha'_2 = \arctan(|2(x_{O2} - z_{O2})|)$ [153,238], both the [101] and the [010] rotational mode follow the ~23.5 cm^{-1}/deg law. Interestingly, the scaling factor is closely similar to rhombohedral $LaMnO_3$ and $LaAlO_3$ [Fig. 4.10], i.e. independent of the crystallographic structure and the direction of the rotational axis.

In the following the relationship between the frequency of the rotational soft modes and the octahedral tilt angle for nickelate films with $R =$ La, Pr, Nd, and Sm in investigated. LSAT substrate was used for all samples to disentangle the effects of epitaxial strain from the influence of the rare-earth ionic radii r_R. We note that the magnitude of imposed tensile strain by LSAT is different for $R =$ La, Pr, Nd, and Sm (0.8, 1.2, 1.6, and 1.9%), but judging from a shift of only ~3 cm^{-1} between $PrNiO_3$ on grown on LSAO and LSAT (-1.7% and 1.2%) [Figs. 4.15(c),(d)] the impact of epitaxial strain in Fig. 4.10 can be neglected in comparison to the much stronger impact of the R-ion substitution on the rotational A_g modes.

As first approach we plot the frequency of the [101] rotational A_g mode extracted by the fits in Fig. 4.10 as a function of the rare-earth ionic radii after Shannon [245] (ions in 3+ valence state in an eightfold environment) [Fig. 4.12(a)]. According to Refs. [238, 243] the relation between r_R and α' (and the tolerance factor T) is approximately linear, hence any of them can be used for characterization of phonon mode frequency dependencies. The nickelates with $R =$ Pr, Nd, and Sm follow the trend of a linear dependence between Raman frequency and r_R, similar to $RCrO_3$, $RMnO_3$, and $RScO_3$. However, the $R =$ La compounds deviate from the linear relation of the other rare-earths, with the strongest deviation for $LaNiO_3$ [Fig. 4.12(a)]. This might be because the $LaNiO_3$ Raman line likely corresponds to the [111] rotational A_g mode and not the [101] mode.

Eventually, the frequency scaling law as a function of the tilt angles α' is of interest. The dependency on the actual angles α' might be more accurate than using the general tabulated values of r_R [245] and non-linearities can vanish [238, 240]. However, the tilt angles α' of epitaxially grown nickelate films can differ significantly from their bulk counterparts [146, 150, 246, 247]. Thus, in Fig. 4.12(b) we only show literature data of bulk nickelates as a function of bulk tilt angles and do not include our film Raman frequencies. The experimental error in the literature data set appears to be too large to allow for a conclusion about the scaling constant of nickelates. In the future, the angle α' of the nickelate films on LSAT can be determined from the oxygen positions obtained by x-ray structural refinement in analogy to the work by May *et al.* for $LaNiO_3$ films on $LaAlO_3$ and $SrTiO_3$ substrates [146].

Then a proper comparison of the nickelate's scaling law to the ones of other ABO_3 compounds [221,238–240] will be possible. Furthermore, an established scaling constant will allow to use Raman spectroscopy as a quick and effective characterization tool of nickelate films, since a simple measurement of the Raman frequency directly yields the value of the tilt angle α' of films and heterostructures grown on various substrates. Moreover, it would be useful to include nickelate films with much smaller r_R such as $R =$ Ho or Y in the series to achieve higher confidence in the determination of the scaling constant.

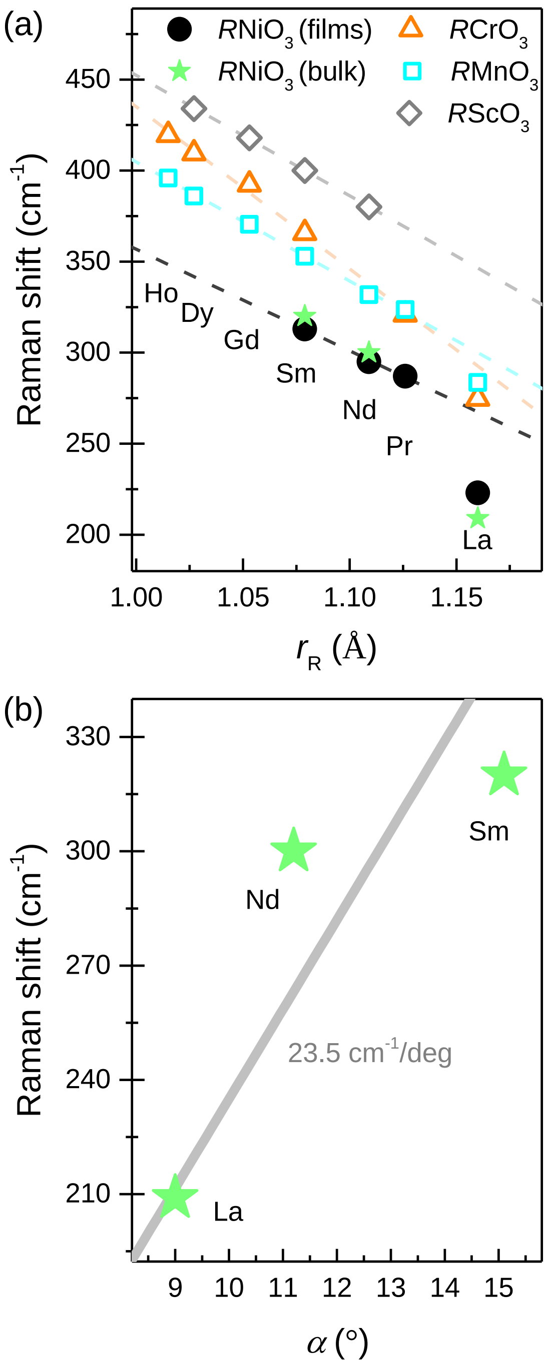

Figure 4.12 Rotational A$_g$ mode of nickelates. (a) Frequency of the [101] rotational mode as a function of the rare-earth ionic radii r_R of $R =$ Pr, Nd, and Sm (black circles). The LaNiO$_3$ data corresponds to the [111] rotational A$_g$ mode. For comparison the dependency of the [101] frequency of RCrO$_3$, RMnO$_3$, and RScO$_3$ with $R =$ La, Pr, Nd, Sm, Gd, Dy, and Ho is shown [238–240]. The bulk RNiO$_3$ data (green symbols) are from [63, 225, 244]. For $RE =$ La the dependency deviates from the linear scaling of the other rare-earth compounds (dashed lines). (b) Frequency of rotational modes of bulk RNiO$_3$ as a function of the tilt angle α'. The gray line indicates the $\sim$23.5 cm^{-1}/deg scaling law. The tilt angles of the RNiO$_3$ films are not known.

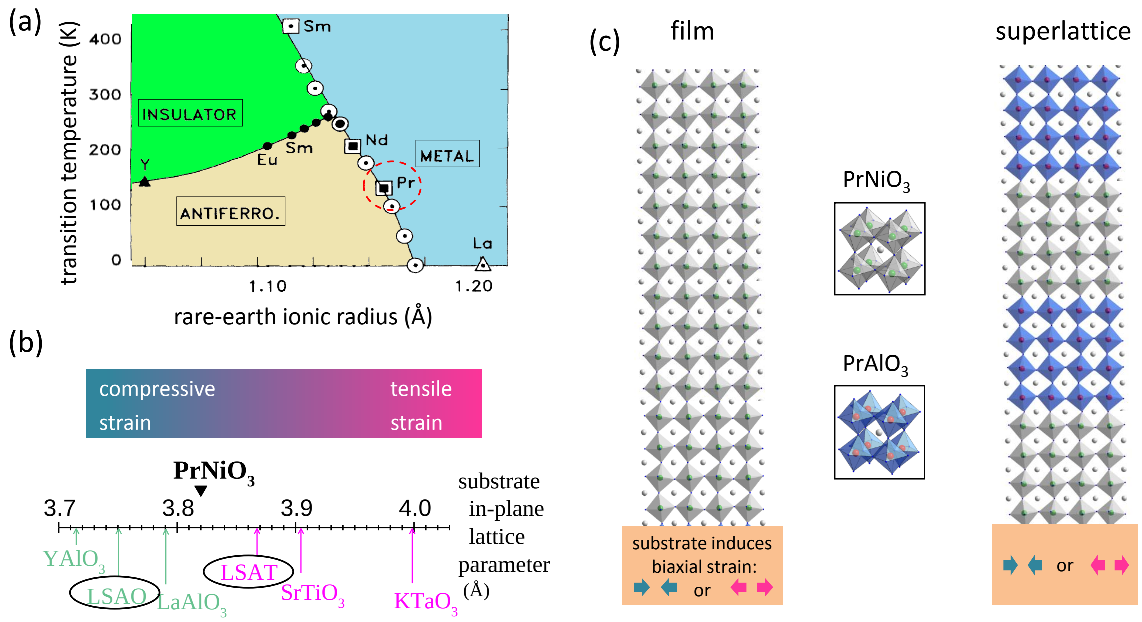

Figure 4.13 $PrNiO_3$ films and superlattices under tensile and compressive strain. (a) Section of the bulk nickelates phase diagram highlighting the position of $PrNiO_3$ with proximity to the paramagnetic metallic $LaNiO_3$ on the right hand side and nickelates with separate electronic and magnetic transitions on the left hand side. The figure is adapted from Ref. [59]. (b) Schematic showing the type of biaxially induced strain to a $PrNiO_3$ film grown on common perovskite oxide substrates. A scale with the in-plane pseudocubic lattice parameters of the substrates is given. LSAO imposes compressive and LSAT imposes tensile strain with respect to the 3.82 Å lattice constant of bulk $PrNiO_3$. (c) Sketch of the NiO_6 octahedral network of a $PrNiO_3$ film (left) and a 4//4 unit cells $PrNiO_3$-$PrAlO_3$ superlattice (right) onto which either compressive (green arrows) or tensile strain (magenta arrows) is induced. In the center, the pseudocubic unit cells of $PrNiO_3$ and $PrAlO_3$ are indicated.

4.3 Spin density wave in $PrNiO_3$ heterostructures

The different models describing the charge/bond order phase transition concomitant with the $Pbnm \rightarrow P2_1/n$ phase transition have been outlined in chapter 2. According to the model proposed by Lee *et al.* which is based on a Landau formalism and applies for the more itinerant members $R =$ Nd and Pr with $T_{\mathbf{MIT}} = T_{\mathbf{N}}$, the MIT is caused by spin density wave formation and the charge/bond order can be viewed as secondary order parameter which does not necessarily emerge in all lattice structures [6, 56]. In this framework the primacy of the charge/bond order parameter is brought into question. In the following section we will show that indeed a magnetically ordered state without the charge/bond order and concomitant monoclinic lattice distortion can be realized in specific $PrNiO_3$-$PrAlO_3$ heterostructures.

$PrNiO_3$ thin films and superlattices were grown by PLD as described in Ref. [112]. We chose the nickelate $PrNiO_3$ due to its extraordinary position in the phase diagram [Fig. 4.13(a)]: nickelates with lower lattice distortion exhibit a paramagnetic metallic ground state ($Pr_{0.5}La_{0.5}NiO_3$ and $LaNiO_3$) whereas higher distortions yield

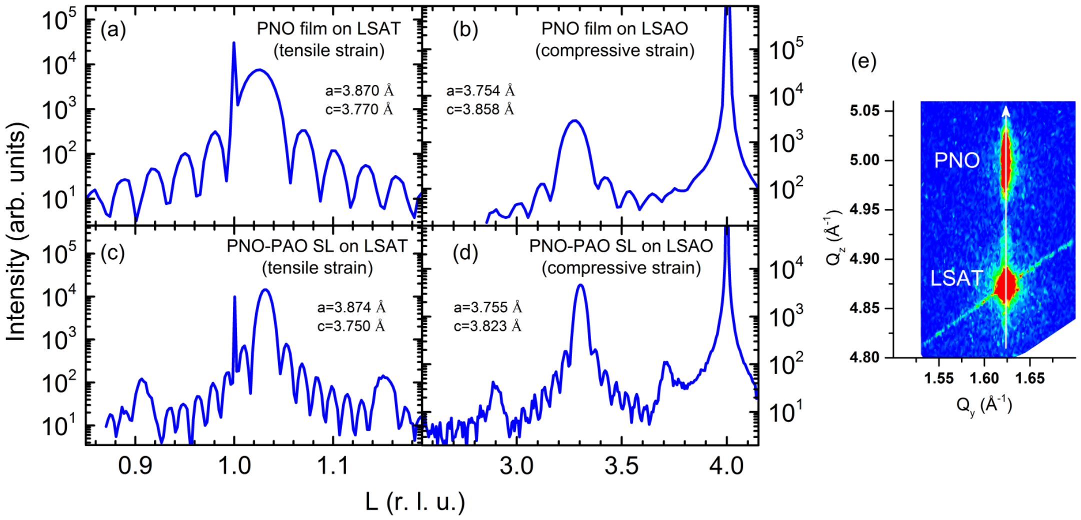

Figure 4.14 Structural characterization of $PrNiO_3$ films and superlattices. (a)-(d) L-scans around the (001) reflex for the $PrNiO_3$ thin films (PNO) and $PrNiO_3$-$PrAlO_3$ superlattices (PNO-PAO), respectively. The a and c in- and out-of plane lattice parameters obtained by XRD analysis are indicated. Panel (e) shows as an example the reciprocal space map around the (103) reflex of the $PrNiO_3$ film on LSAT with the white arrow indicating the match of the in-plane lattice constants of the nickelate and the substrate. For the measurements Cu K_α radiation (E = 8048 eV) was used.

an antiferromagnetic insulating ground state with elevated $T_{\mathbf{MIT}}$ ($NdNiO_3$) or even separated $T_{\mathbf{MIT}}$ and $T_{\mathbf{N}}$ ($SmNiO_3$). This positions renders $PrNiO_3$ particularly susceptible for manipulations towards either of the two directions. Two different [001] oriented substrates were used, inducing compressive and tensile strain, respectively [Fig. 4.13(b),(c)]. The LSAT and LSAO substrate's in-plane lattice constants are $a_{\text{sub}} = 3.868$ Å and $a_{\text{sub}} = 3.756$ Å, respectively. Bulk $PrNiO_3$ has a pseudocubic lattice constant of $a_{\text{pc}} = 3.82$ Å, hence the respective lattice mismatch $(a_{\text{sub}} - a_{\text{pc}})/a_{\text{pc}}$ leads to 1.2 % tensile strain for $PrNiO_3$ on LSAT and to -1.7 % compressive strain for $PrNiO_3$ on LSAO, i.e. similar magnitudes of biaxial strain on the compressive and tensile side. All substrates had very low mosaicity and miscut angles <0.1°. The thickness of the films was ∼12 nm corresponding to thirty-two unit cells and the superlattices were composed of eight bilayers with four unit cells $PrNiO_3$ and four unit cells of $PrAlO_3$ [Fig. 4.13(c)]. The total thickness of the samples was determined from the L-scans around the (001) pseudocubic Bragg reflex [Fig. 4.14(a)-(d)]. For the superlattices the thickness control of the individual layers was ensured by counting laser pulses, using the growth rate per pulse for $PrNiO_3$ and $PrAlO_3$ obtained from previous tests with feedback from x-ray diffraction. Fig. 4.14(e) shows as an example the reciprocal space map around the (103) reflex for $PrNiO_3$ on LSAT. The alignment between the $PrNiO_3$ film and the LSAT substrate peak (see vertical white arrow) is evidence of a high in-plane strain state. Values for the in- and out-of-plane lattice constants a and c were obtained from a quantitative analysis of the XRD pattens and are indicated in Fig. 4.14(a)-(d). For the $PrNiO_3$-$PrAlO_3$ superlattices these values represent an average for both components, assuming a tetragonal crystal structure of the overlayer. The in-plane lattice constants of all samples match closely with those

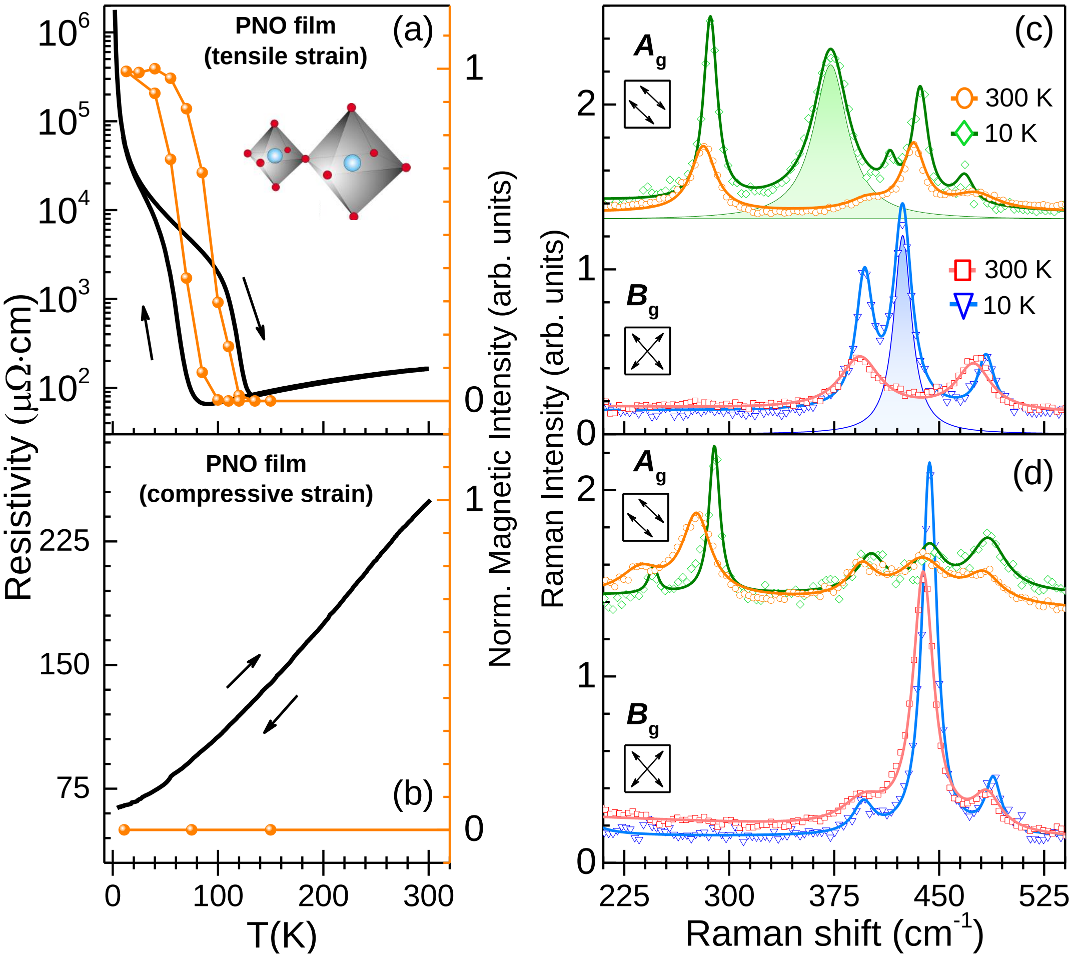

Figure 4.15 Phase transitions in PrNiO$_3$ films under tensile and compressive strain. (a),(b) Electrical resistivity (left scale) and normalized intensity of the antiferromagnetic (1/4, 1/4, 1/4) reflection (right scale) measured by REXS as a function of temperature in PrNiO$_3$ films under (a) tensile and (b) compressive strain. Arrows indicate warming and cooling cycles. (c),(d) Raman spectra of PrNiO$_3$ films under (c) tensile and (d) compressive strain at T = 300 and 10 K in A$_g$ and B$_g$ symmetry (upper and lower subpanels, respectively). The former film exhibits anomalous modes at low T associated with charge ordering (shaded in panel c), while the latter does not. The solid lines represent the results of least-squares fits of the data to Voigt profiles. The inset in (a) shows a segment of the low-T monoclinic distortion with two differently sized NiO$_6$ octahedra. The arrows in the insets in (c,d) indicate the electric field vectors of the incoming and the scattered light with respect to the substrate edges.

of their substrates indicating fully strained films and superlattices.

Fig. 4.15 shows the z=0 Raman spectra of 12 nm thick PrNiO$_3$ films on tensile and compressive strain corrected by the substrate contribution, together with the electrical resistivity and the intensity of the antiferromagnetic REXS Bragg reflection measured on the same samples. The film under tensile strain shows a MIT with significant hysteresis in the temperature range 80-130 K, which is indicative of a first-order transition [Fig. 4.15(a)]. The onset of magnetic order determined by REXS coincides with the MIT, as it does in bulk PrNiO$_3$ [61]. By contrast, the compressively

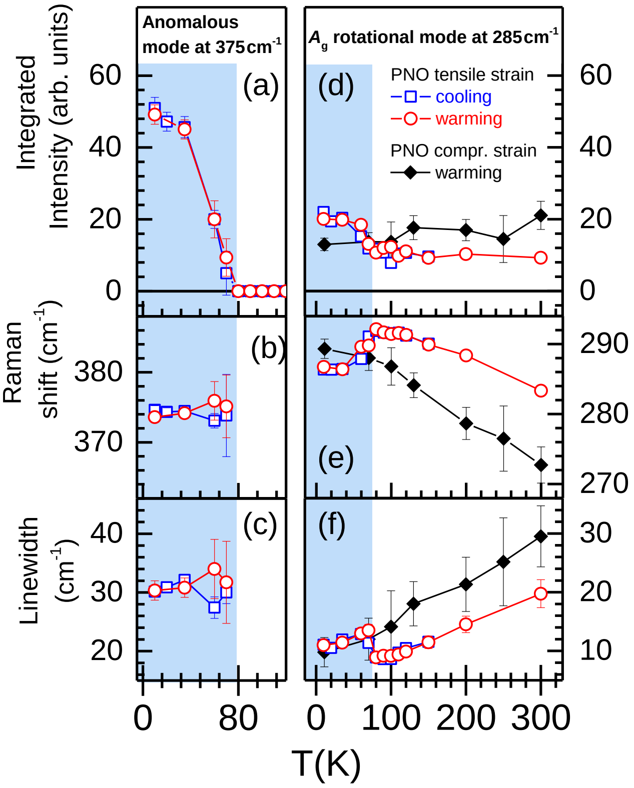

Figure 4.16 Temperature dependence of PrNiO$_3$ film Raman modes. (a)-(c) Raman intensity, frequency, and linewidth of the anomalous phonon mode at 375 cm^{-1} upon cooling (blue) and heating (red) cycles (d)-(f) Temperature dependence of the regular phonon mode at 285 cm^{-1}, corresponding to the A$_g$ rotational distortion of the NiO$_6$ octahedra. In the tensile strain case the mode experiences a significant renormalization at T_{MIT} = 80 K. In the shaded areas the film under tensile strain is insulating. No hysteresis between cooling and heating cycles is observed.

strained PrNiO$_3$ film remains metallic and paramagnetic down to lowest temperatures [Fig. 4.15(b)].

At high temperatures, the Raman-active phonons of the spectra in Figs. 4.15(c),(d) correspond to the pseudocubic perovskite structure, with uniform NiO$_6$ octahedra. Upon cooling below T_{MIT}, the spectrum of PrNiO$_3$ under tensile strain exhibits two additional modes at 375 cm^{-1} and 425 cm^{-1} [Fig. 4.15(c)], consistent with a superstructure of two differently sized NiO$_6$ octahedra, which in the bulk leads to a loss of the b mirror symmetry of $Pbnm$ and to the monoclinic space group $P2_1/n$ [63, 226, 248, 249]. The association with charge/bond ordering is supported by the absence, at low temperature, of additional phonons in the compressively strained PrNiO$_3$ film, which does not exhibit a MIT [Fig. 4.15(d)]. Polarization-resolved data in different light-field configurations (indicated in Figs. 4.15(c),(d) as arrows relative to the pseudocubic unit cell of PrNiO$_3$) determine the symmetry of the displacement patterns as A_g and B_{1g} for the modes at 375 cm^{-1} and 425 cm^{-1}, respectively. The Raman spectra were fitted to a superposition of Voigt profiles resulting from a convolution of the intrinsic Lorentzian lineshape with the Gaussian spectrometer resolution (lines in Figs. 4.15(c),(d)).

Fig. 4.15(a) shows the integrated intensity of the fits of the anomalous mode at 375 cm^{-1} characteristic of the monoclinic symmetry breaking and therewith the charge/bond ordering. Its temperature dependence exhibits behavior characteristic of the order parameter of a continuous (or weakly first-order) phase transition with critical temperature ~ 80 K. Figs. 4.15(d)-(f) display the intensity, frequency, and linewidth of a regular mode with frequency 285 cm^{-1} that corresponds to rotations of the NiO_6 octahedra in the pseudocubic perovskite structure. All of these parameters exhibit anomalies at the same temperature, reflecting changes in the electron-phonon coupling at the MIT; similar observations were reported before for R = Nd and Sm [63, 226]. In contrast, the regular phonons in the compressively strained $PrNiO_3$ film exhibit standard anharmonic behavior, without anomalies.

In the $PrNiO_3$ film under tensile strain, the phonon lineshapes carefully monitored as a function of temperature while eliminating laser heating effects. Remarkably, no hysteresis in any of the phonon lineshapes upon cycling through the MIT [Figs. 4.15(a)-(f)] is observed, in stark contrast to the behavior of the resistivity and the magnetic order parameter measured on the same sample [Fig. 4.15(a)]. Differences in the hysteretic behavior of the regular Raman phonons and the macroscopic resistivity have been noted before, and were attributed to the possible influence of defects on *dc* charge transport [226]. Similar considerations were made in interpreting differences between the macroscopic magnetic susceptibility and the *dc* resistivity [250]. The results of our experiments now allow us to compare data generated by two microscopic probes of magnetic and charge/bond order, respectively. The fact that the former persists to ~ 120 K upon heating [Fig. 4.15(a)], while the latter vanishes at ~ 80 K [Fig. 4.16], suggests that the two order parameters are only weakly coupled, and that the sublattice magnetization is the primary order parameter. This is consistent with the theoretically predicted spin density wave phase [6, 56].

We now turn to the measurements on $PrNiO_3$-$PrAlO_3$ superlattices grown under the same strain conditions as the $PrNiO_3$ films. Fig. 4.17 shows that the spatial confinement of the conduction electrons in the superlattices strengthens the magnetic correlations. In the superlattice under tensile strain, T_N grows to ~ 160 K, [Fig. 4.17(a)] while the hysteresis that characterizes the transition is greatly reduced compared to the corresponding film [Fig. 4.15(a)]. In the superlattice under compressive strain, the spatial confinement induces antiferromagnetic order with $T_N \sim 100$ K, [Fig. 4.17(b)] in a manner similar to superlattices based on $LaNiO_3$, [102] but already at an active layer thickness of four (rather than two) unit cells. The resistivity upturn upon cooling below T_N of the compressively strained $PrNiO_3$-$PrAlO_3$ superlattice is much more subtle than in the $PrNiO_3$ films and in the superlattice under tensile strain, and the superlattice remains highly conductive even below T_N. Combined with the REXS data that demonstrate similar magnetic order parameters in both samples, this suggests that differences in charge/bond order may be responsible for the different transport properties.

The Raman spectra of the SLs provide direct insight into the influence of spatial confinement and strain on charge ordering. Figs. 4.17(c),(d) presents polarized spectra of the $PrNiO_3$-$PrAlO_3$ superlattices, in a manner parallel to those of the films [Figs. 4.15(c),(d)]. Apart from the fact that the phonon profiles in the superlattices are generally broader than in the films, the energies and polarization dependences of the regular phonons in both superlattice are closely similar to those of the corresponding films. In particular, the modes at 285 cm^{-1}, 435 cm^{-1} and 465 cm^{-1} in the superlattice under tensile strain only appear in the A_g channel while the ones at 400 cm^{-1} and 480 cm^{-1} only appear in B_{1g}.

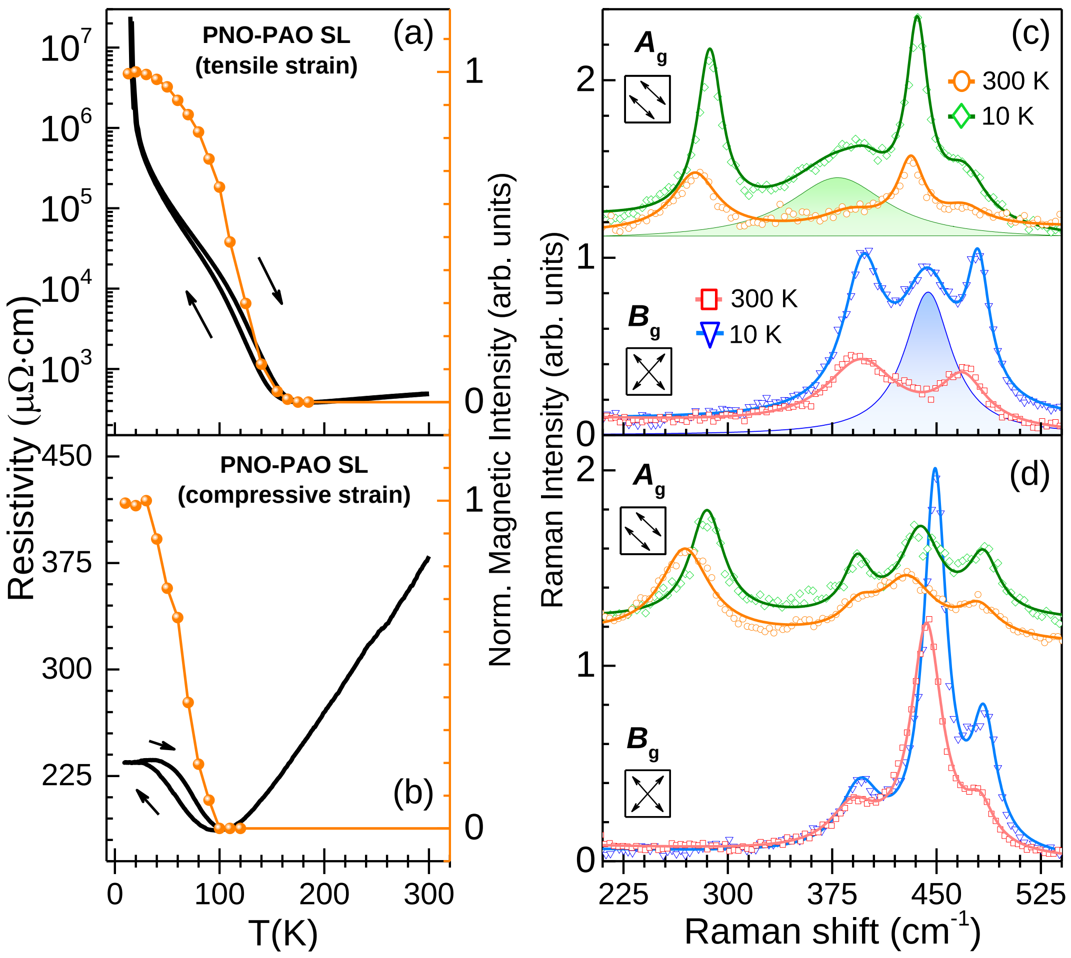

Figure 4.17 Phase transitions in PrNiO$_3$-PrAlO$_3$ superlattices under tensile and compressive strain. (a),(b) Electrical resistivity and normalized intensity of the antiferromagnetic (1/4, 1/4, 1/4) reflection measured by REXS as a function of temperature in PrNiO$_3$-PrAlO$_3$ superlattices under (a) tensile and (b) compressive strain. (c,d) Raman spectra of the superlattices under (c) tensile and (d) compressive strain at T = 300 and 10 K for the A$_g$ and B$_g$ channels. The anomalous modes at low T (shaded in (c)) are due to the monoclinic symmetry breaking. Lines and symbols in the insets are analogous to Fig. 4.15.

The broadening of the modes implies the anomalies in intensity, frequency, and linewidth across the MIT [Fig. 4.18] are not as pronounced as for the case of the films [Fig. 4.16]. However, the emergence of the anomalous mode at 375 cm^{-1} in the A_g channel [Fig. 4.18(a)] is closely similar to the order-parameter like evolution of the corresponding film mode [Fig. 4.16(a)]. The energy of the B_{1g} mode at 445 cm^{-1} is ~20 cm^{-1} higher than the one of the corresponding PrNiO$_3$ film, and both A_g and B_{1g} phonons are significantly broader in the superlattices, mirroring the broadening of the regular modes. The onset temperature of the anomalous modes [Fig. 4.18(a)] coincides with T_{MIT} within the experimental error, once again strengthening the association with charge/bond order. Their absence in the spectra of the superlattice under compressive strain [Fig. 4.17(d)] therefore implies that the amplitude of charge/bond modulation is either absent or much smaller than in the superlattice under tensile strain.

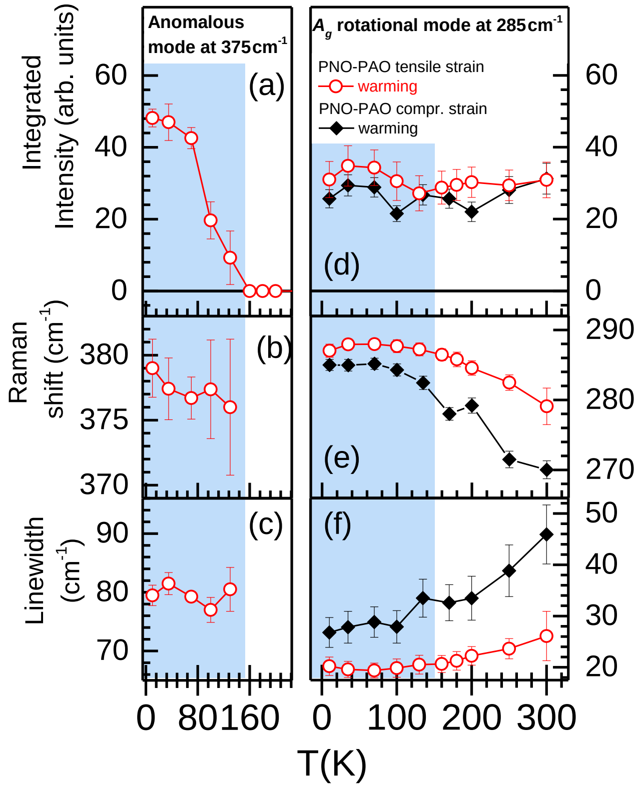

Figure 4.18 Temperature dependence of PrNiO$_3$-PrAlO$_3$ superlattice Raman modes.(a)-(c) Raman intensity, frequency, and linewidth of the anomalous phonon mode at 375 cm^{-1}. (d)-(f) Temperature dependence of the regular phonon mode at 285 cm^{-1}. Renormalization effects at T_{MIT} = 160 K are much weaker than for the films in Fig. 4.16. In the shaded areas the superlattice under tensile strain is insulating.

As an additional confirmation of the analogy between the emergence/absence of specific modes in the films and the superlattices a full polarization analysis of the samples was performed. The set of measurements shown in Fig. 4.19 helps to distinguish between different modes, especially for the ones that are either broad or close to each other. In more detail, we did not only measure in Z(X'X')$\bar{\mathrm{Z}}$ and Z(X'Y')$\bar{\mathrm{Z}}$ configurations yielding $\mathrm{A_g}$ and $\mathrm{B_{1g}}$ modes, respectively [Fig. 4.15 and Fig. 4.17], but also in Z(XX)$\bar{\mathrm{Z}}$ which yields the superposition $\mathrm{A_g}$+$\mathrm{B_{1g}}$ [Fig. 4.19]. No Raman active modes were observed with Z(XY)$\bar{\mathrm{Z}}$ polarization. At the bottom of each panel of Fig. 4.19 the individual Voigt profiles of the fits of the Z(X'X')$\bar{\mathrm{Z}}$ and Z(X'Y')$\bar{\mathrm{Z}}$ data are indicated. These fits are added up (solid lines) and superimposed to the data (open symbols) measured in the Z(XX)$\bar{\mathrm{Z}}$ channel. As can be seen by the graphs color-coded in black for T = 300 K and magenta for T = 10 K, there is excellent agreement between the solid lines and the open symbols. This behavior in the observed intensities for the different polarization configurations corresponds one-to-one with the expected selection rules shown in Table B.1 in Appendix B, supporting that the fits of the anomalous spectral weight in the Z(X'X')$\bar{\mathrm{Z}}$ and Z(X'Y')$\bar{\mathrm{Z}}$ channel used for the argumentation in relation to Fig. 4.15 and Fig. 4.17 are correct and the same structural changes related to charge/bond order occur in both tensile strained samples and are absent in compressively strained samples.

In summary, we have used two complementary, microscopic probes to elucidate the influence of temperature, epitaxial strain, and spatial confinement on charge/bond and spin order in PrNiO$_3$. The REXS data show that both superlattices have identical

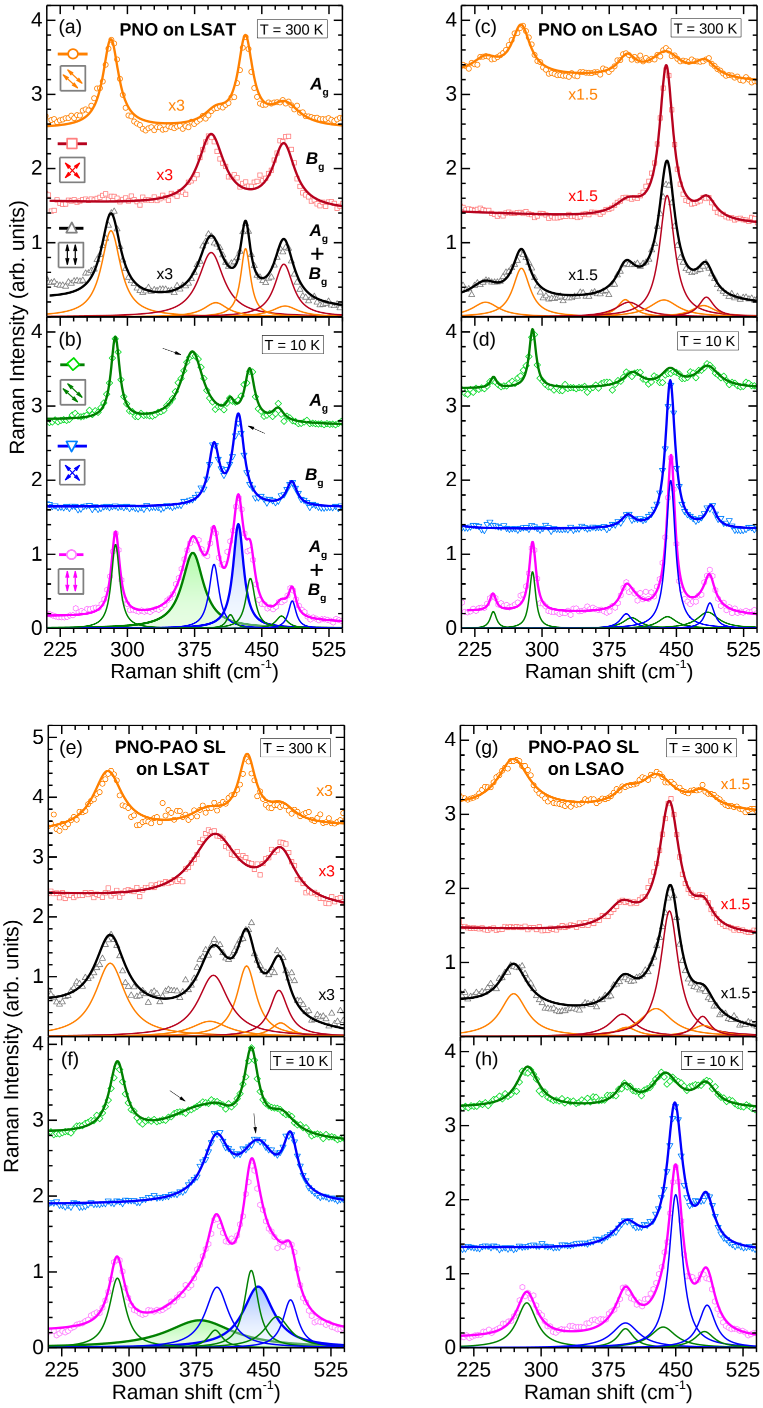

Figure 4.19 Full polarization analysis. (a)-(h) Polarized Raman spectra at 300 K and 10 K. Open symbols are raw data and solid lines are fits consisting of several Voigt profiles. At the bottom of each panel the Voigt profiles are indicated individually in the corresponding color of the A$_g$ and B$_g$ spectra. Solid lines (black at room-T and magenta at low-T) for $Z(XX)\bar{Z}$ polarization are the sum of the fits for $Z(X'X')\bar{Z}$ and $Z(X'Y')\bar{Z}$, probing modes of A_g and B$_g$ symmetry, respectively. New modes emerging below the transition are indicated with arrows and their individual Voigt profiles are shaded. Note that the room-T spectra are scaled and the spectra are shifted in vertical direction for clarity.

magnetic ground states, while our Raman scattering data imply that the amplitude of the charge/bond order differs greatly in both systems. This is consistent with the prediction by Lee *et al.* that the spin density modulation is the primary order parameter, whereas a charge/bond density modulation may or may not accompany the spin density as a secondary order parameter, depending on the specific lattice symmetry. [6, 56]

4.4 Conclusion and outlook

We have developed a measurement procedure combining confocal Raman spectroscopy and a vertical scan of the focus position (z-scan), which allows to obtain high-quality spectra from ultra-thin films and heterostructures grown on various substrates. The technique was applied to the material class of rare-earth nickelates whose rich phase diagram results from the interplay between charge, orbital, spin, and lattice degrees of freedom. In such heterostructures other diffraction methods have problems to follow the emergence and evolution of the structural order parameter, owing the small scattering signal of the atomically thin active layers and the small magnitude of the distortions. Raman spectroscopy on the other hand is very sensitive to faint changes of the lattice or symmetry reductions, given that the film and substrate signal can be disentangled.

As the most important result of this chapter we have used Raman spectroscopy to identify three different states in $PrNiO_3$ films and $PrNiO_3$-$PrAlO_3$ superlattices, only two of which were observed before in bulk RNiO$_3$: an insulating state with robust spin and charge/bond order in films and superlattices under tensile strain, and a metallic state with neither form of order in films under compressive strain. In superlattices under compressive strain, a weakly metallic state with fully developed spin order but no (or very weak) charge/bond order is realized. Further evidence of decoupling of spin and charge order comes from films under tensile strain, where it was found that superheating of magnetic order persists over a much larger temperature range than charge ordering. In contrast, we find no evidence for a charge-ordered "spin liquid" state with converse combination of both order parameters [2].

Our data thus directly confirm theoretical predictions for a spin density wave phase with charge/bond order as a secondary order parameter [6,56]. The mechanism invoked by these predictions, Fermi surface nesting, is enhanced by spatial confinement, in accord with our data on $PrNiO_3$ films and $PrNiO_3$-$PrAlO_3$ superlattice under the same (compressive) strain conditions. Spin density waves have been directly observed and characterized only in few bulk metals, including elemental chromium and its alloys [251], organic charge-transfer salts [252], and most recently the iron pnictides [7].

The separate control of magnetic and charge/bond order that is reported here for the nickelates opens up new opportunities for device applications, including designs in which metallic antiferromagnets serve as active elements [253, 254]. In addition, our determination of the energies and symmetries of the vibrational modes characteristic of charge/bond ordering, as well as their dependence on strain and spatial confinement, provides specific input for models of the MIT and electron-phonon interactions in the nickelates and related transition metal oxides [71, 77–82].

Finally, we have demonstrated that the confocal z-scan technique with visible laser light is a powerful alternative to ultraviolet Raman spectroscopy [5] for the investigation of lattice vibrations in thin films and superlattices. We thus foresee manifold applications in the determination of the structural and electronic phase behavior of oxide heterostructures.

Chapter 5

Complex magnetic order in nickelate slabs

The chapter starts with a general discussion of the peculiarities of [111] oriented crystal structures which are employed for the following experiments. This particular crystallographic direction coincides with the $\mathbf{q}_0$=(1/4, 1/4, 1/4) propagation vector of the nickelate's magnetic order, hence out-of-plane spatial confinement yields truncation along the propagation direction of the magnetic order. Important results of previous experimental studies on [111] nickelates will be reviewed and the suitability of truncated nickelate slabs as an elementary magnetic model system will be explained. A thorough experimental characterization of all synthesized samples by electrical transport, scanning transmission electron microscopy, and synchrotron x-ray diffraction then leads us to focus on a series of four specific $NdNiO_3$ slabs with different layer thickness along the [111] direction. The central point of the chapter is the REXS azimuthal dependence, which is modeled by a double cluster approach and discussed in conjunction with DFT+U calculations. Finally, implications of our findings on theories describing the magnetic order in nickelates are explained and future experiments will be outlined.

5.1 [111] oriented heterostructures and interfaces

For rare-earth nickelates with composition RNiO$_3$ (R=rare-earth ion), theory predicts new and exotic quantum many-body states when synthesized in heterostructures along the pseudocubic [111] direction. The presence of unprecedented states, such as a Dirac half-semimetal phase [255], antiferro-orbital order [60], a polar metal state [117], a multiferroic state [104], and an unusual ferromagnetic phase [256] has been suggested. It is argued that some of these states can be expected to form even in the Ni $3d^7$ electron system without strong spin-orbit coupling, since the nickelate perovskite crystal lattice is geometrically transformed into a buckled honeycomb structure when truncated along the [111] direction [Fig. 5.1(a)-(c)]. The predictions of a novel ferromagnetic state and possible multiferroicity motivates for a deeper investigation of the magnetism in [111] nickelate heterostructures. In the following it is shown how specifically designed [111] NdNiO$_3$ slabs embedded into a non-magnetic matrix can serve as a novel platform to study the intrinsic magnetic order in nickelates. The [111] orientation in our case is directly related to the periodicity and propagation of the magnetic order, i.e. it enables a truncation of the slab system along the $\mathbf{q}_0$=(1/4, 1/4, 1/4) wave vector direction. A similar truncation of the spin order was present in previously studied LaNiO$_3$-LaMnO$_3$ superlattices [107, 108], but has not been realized in nickelate slabs embedded in a non-magnetic matrix [4, 102].

For a comprehensive understanding of the impacts of the [111] orientation on the physics of a system, it is instructive to start with a very general look on the [111] crystallographic direction. Subsequently, we go into more detail for the specific case of NdNiO$_3$ on NdGaO$_3$. In general, a (pseudo)cubic structure with stoichiometry ABO$_3$ exhibits the stacking sequence B/AO$_3$ for adjacent planes along the [111] direction [Fig. 5.1(b)], which is distinct from the AO/BO$_2$ stacking of the [001] orientation. At the interface of a heterostructure or in case of two inequivalent B-sites as in the monoclinic phase of nickelates, each B-cation has three neighbors of the same and three of the other species B' [Fig. 5.1]. As a consequence, [111] interfaces exhibit an extraordinary nature which can lead to topologically nontrivial band structures [106, 257–259]. Moreover, each BO$_6$ octahedron share s three O with octahedra of the neighboring material – as opposed to one shared O for the $\langle 100 \rangle$ cases – yielding an enhanced structural interconnectivity across the (111) interface. Different stackings along the [111] direction are for instance a sequence of three distinct layers, corresponding to a three-dimensional version of the dice lattice [260]. The [111] direction in A_2B_2O$_7$ pyrochlore oxides yields alternating triangular and kagome lattice planes which can produce a Chern insulator phase [261].

Here, the focus is on the double-layer case, i.e. the buckled honeycomb lattice, which can be obtained by cutting the nickelate or the gallate unit cell in an appropriate way. Since the monoclinic angle of NdNiO$_3$ is small and NdGaO$_3$ is orthorhombic at all temperatures, an orthorhombic reference frame is considered in the following. Taking the orthorhombic/monoclinic unit cell of NdNiO$_3$ [Fig. 5.1(d)] as starting point , we examine two cuts that yield a pseudocubic body diagonal as out-of plane direction, namely the $(101)_{or}$ and the $(011)_{or}$ orthorhombic cut [Fig. 5.1(e)]. Correspondingly, the NdNiO$_3$ and NdGaO$_3$ crystals are indicated as pseudocubic [111] and $[\bar{1}11]$ oriented,

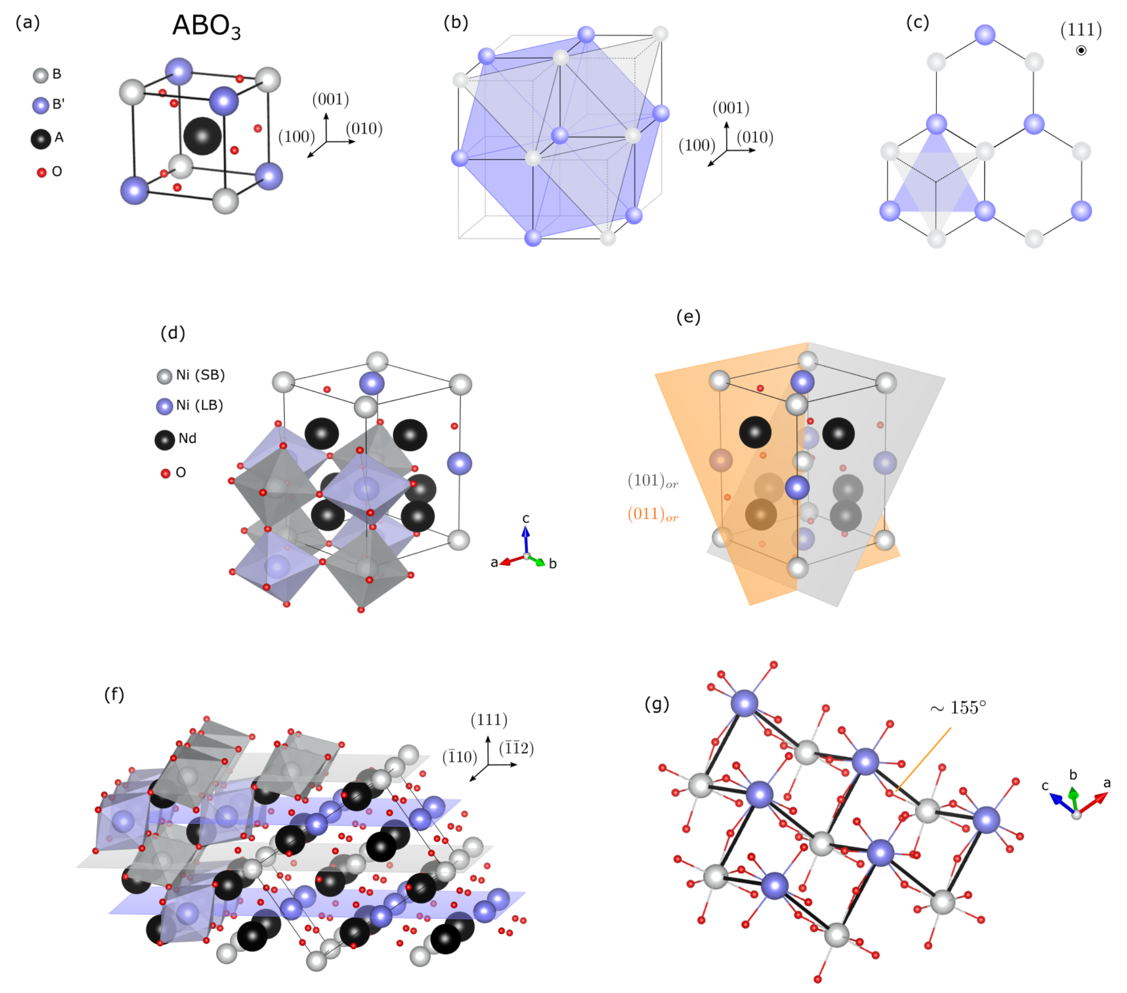

Figure 5.1 Perovskite crystal structures in [111] orientation. (a) Pseudocubic unit cell of the ABO_3 perovskite structure. B site cation positions are color-coded in gray and blue, to distinguish the two inequivalent Ni sites of the monoclinically distorted low-T phase of nickelates. (b) Planes of the two B-sites (blue and gray) are stacked alternately along the [111] direction. Additional planes of AO_3 composition are located in-between the B-site planes but omitted here for clarity. (c) A projection of the shortest Ni-Ni bonds (black lines) on the (111) plane forms a (buckled) honeycomb lattice. (d) Low-T monoclinic unit cell (black lines) with two inequivalent Ni sites, enclosed by collapsed (SB, gray) and expanded (LB, blue) oxygen octahedron, respectively. The four NiO_6 octahedra indicate the pseudocubic unit cell for which the a and b axis are 45° offset to the monoclinic a and b axis. (e) The $(101)_{or}$ and $(011)_{or}$ orthorhombic/monoclinic cut planes (gray and orange), which are orthogonal to the pseudocubic [111] and $[\bar{1}11]$ direction, respectively. (f) Along the [111] direction, planes of SB (gray) and LB NiO_6 octahedra (blue) are stacked in an alternating fashion. The monoclinic $P2_1/n$ unit cell is indicated by black lines. (g) In a side view the buckled character of the honeycomb lattice (black lines) is evident. Ni-O-Ni bond angles are indicated according to Ref [64].

respectively. The [111] oriented lattice of $NdNiO_3$ with the refined atomic positions of Ref. [64] is shown in Fig. 5.1(f). In the monoclinic low-T phase the NiO_6 octahedra split into sets of expanded and contracted octahedra with long Ni-O bonds (LB) and short bonds (SB), arranged in the typical breathing mode pattern and yielding alternating LB and SB planes along the [111] direction. A detailed side-view of the corresponding buckled honeycomb lattice together with the corresponding Ni-O-Ni bond angles is displayed in Fig. 5.1(g).

It is emphasized, that the orientation of the substrate's cut can influence the physical properties even of relatively thick film (10 to 20 nm), where one might not expect the interface to dominate the behavior. In particular, this has been observed for orthorhombic heterosystems such as $NdNiO_3$ grown on $NdGaO_3$. Typically, $NdGaO_3$ substrates in the $(110)_{or}$ cut are used for thin film synthesis [262] and the $NdNiO_3$ exhibits a sharp MIT at which the resistivity increases by more than five orders of magnitude upon cooling (see also Fig. 5.5(c) later in the text). The films grown on $(110)_{or}$ substrates are commonly referred to as [001] pseudocubic oriented [263], even though the out-of plane direction is strictly speaking the [100] or [010] direction, which then again is equivalent to [001] in the pseudocubic reference frame. Ref. [262] finds $T_{MI} = T_N$ in these films, similar to bulk $NdNiO_3$ (Ref. [59]). There are only few works on films grown on $NdNiO_3$ substrates with a $(001)_{or}$ surface – coinciding now indeed with the pseudocubic [001] direction – and first experiments indicate a significantly weaker and broader upturn of the resistivity, but again $T_{MI} = T_N$ (Ref. [264]). Conversely, Ref. [103] observed a significant strengthening of the electronic correlations in $NdNiO_3$ when grown on $(101)_{or}$ $NdGaO_3$, with $T_{MI} \gg T_N$.

One factor influencing the electronic correlations in the aforementioned heterostructures is certainly the amount and asymmetry of the epitaxial strain induced by the $NdGaO_3$ substrate [Fig. 5.2]. The lattice mismatch is calculated with respect to the bulk monoclinic $P2_1/n$ unit cell of $NdNiO_3$ via $(\alpha_{\mathrm{NGO}} - \alpha_{\mathrm{NNO}})/\alpha_{\mathrm{NNO}}$ with α being the $NdGaO_3$ and $NdNiO_3$ lattice parameters along the respective crystallographic directions [64, 265]. The larger $NdGaO_3$ lattice parameters of a=5.428 Å, b=5.498 Å, and c=7.709 Å (Ref. [265]) introduce moderate tensile strain with respect to the bulk $NdNiO_3$ lattice parameters of a=5.387 Å, b=5.383 Å, and c=7.61 Å (Ref. [64]) for all possible orientations [Fig. 5.2]. For the $(110)_{or}$ surface the lattice mismatches are similar along both main crystallographic directions [Fig. 5.2(a)]. Therewith, no additional in-plane asymmetry is imposed on the $NdNiO_3$ for this specific cut. For the $(101)_{or}$ cut on the other hand, the tensile strain along the [010] direction of ~2% is relatively high and notably larger than the ~1.2% along the [010] direction [Fig. 5.2(d)]. For similar asymmetric systems such as LSMO on $NdGaO_3$ multiple mechanisms of strain accommodation have been reported [266]. Along the small mismatch direction it is for instance possible that the mismatch strain is fully accommodated by tilts of the octahedral network whereas for larger mismatches long range sinusoidal lattice modulations can occur.

Considering the differences in the electrical transport of $NdNiO_3$-$NdGaO_3$ heterostructures on differently cut substrates, then the observed deviations cannot be a pure strain effect. It is rather suggested by Ref. [103] (and discussed in more detail in the next section) that details of the octahedra tilt pattern, which propagate from the substrate into the film, are key. Contrary to the $(110)_{or}$ and $(001)_{or}$ interfaces, at the $(101)_{or}$ interface there are Ni-O-Ga bonds for each NiO_6 octahedron [Fig. 5.3]. This might foster a long-range propagation of octahedral distortions in [111] oriented heterostructures and potentially could influence the electrical transport of a relatively

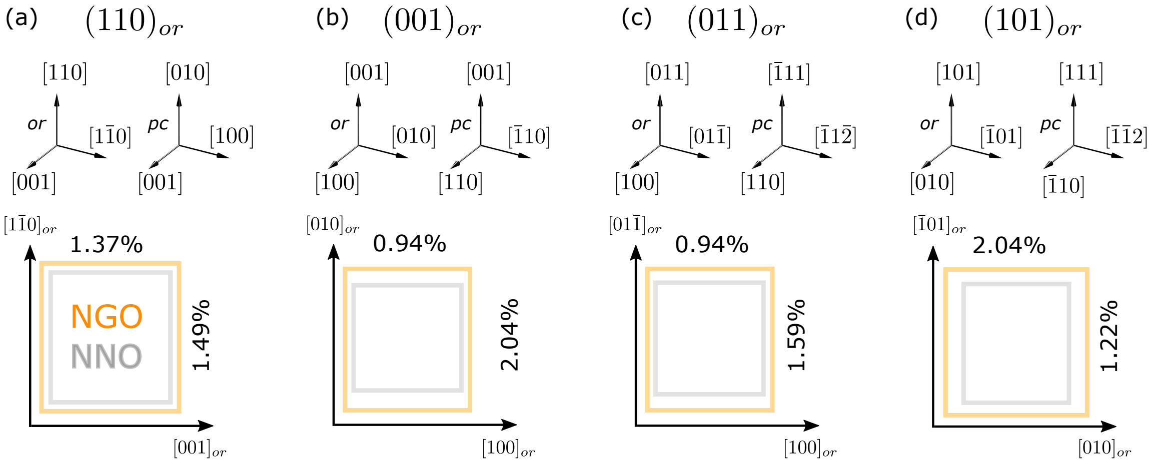

Figure 5.2 Coordinate system transformation and magnitude of tensile strain for different substrate cuts. (a)-(d) Orthorhombic and pseudocubic coordinate system for selected cuts of the $NdGaO_3$ substrate. (e)-(i) Schematics of the corresponding in-plane lattice of $NdNiO_3$ and $NdGaO_3$ and the epitaxial strain imposed to the $NdNiO_3$ along the indicated orthorhombic crystallographic directions.

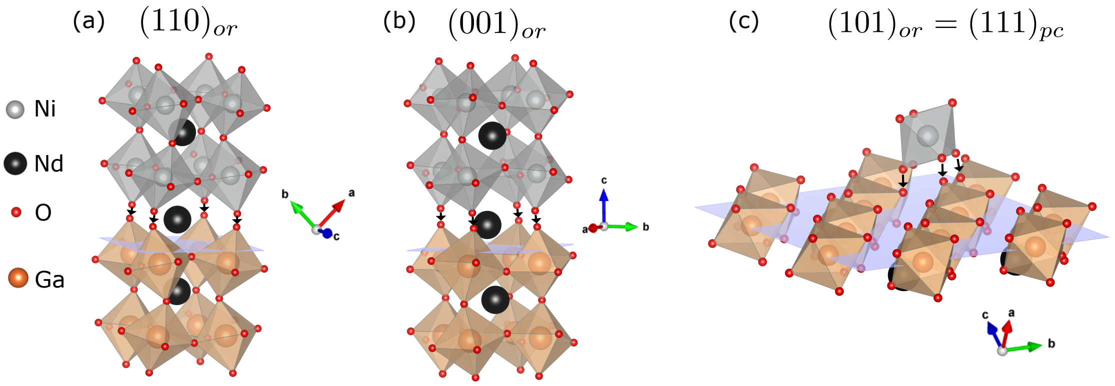

Figure 5.3 Interfaces for different substrate cuts. (a) Graphical representation of a pseudocubic $NdNiO_3$ unit cell epitaxially grown on a $NdGaO_3$ substrate in the orthorhombic $(110)_{or}$ cut. The interfacial $NdNiO_3$ and $NdGaO_3$ NiO_6 octahedra share one oxygen, as indicated by the black arrows. A (110) plane is shown in blue. The *Pbmn* orthorhombic *a, b,* and *c* lattice directions of $NdGaO_3$ are indicated by the red, green, and blue arrows. (b) For the orthorhombic $(001)_{or}$ cut the interconnectivity is similar to the $(110)_{or}$ cut. (c) In the growth mode along the $[101]_{or}$ orthorhombic direction each interfacial $NdNiO_3$ octahedron is connected to three $NdGaO_3$ octahedra. For clarity only one NiO_6 octahedron of $NdNiO_3$ is shown.

thick 17 nm $NdNiO_3$ film as discussed in Ref. [103].

Another peculiarity of the $NdNiO_3$-$NdGaO_3$ heterosystem is the matching polarity of the two constituents. Generally, perovskite materials of valence composition $A^{3+}B^{3+}O_3^{2-}$ consist of charged $(AO)^{1+}$ and $(BO_2)^{1-}$ planes stacked along the [001] direction, $(ABO)^{4+}$ and $(O_2)^{4-}$ planes stacked along the [110] direction, and $(AO_3)^{3-}$ and $(B)^{3+}$ planes stacked along the [111] direction. Here, both $NdNiO_3$ and $NdGaO_3$ exhibit the nominal 3+ valence on their A and B site cations, hence any polar mismatch across the interface is absent and no structural and electronic reconstruction effects occur (as known e.g. from $LaAlO_3/SrTiO_3$ interfaces). Moreover, the 3+ valence of the Ga ion is relatively stable, minimizing the possibility of a charge transfer between Ni and Ga across the interface.

As a final side-remark it is mentioned that also the $B-B'$ cations distances depends on the orientation of two dissimilar materials across the interface. Closer proximity to a different TMO ion can have drastic influence on the local electronic environment of the B site cation. In the case of $NdNiO_3$-$NdGaO_3$, the BO_6 octahedra are non-symmetric. Hence, the Ni-Ga distance is $\sim$3.79 Å in the $(001)_{or}$ cut and in average $\sim$3.89 Å in the $(110)_{or}$ and $(101)_{or}$ cut. The different $B-B'$ distances are probably not relevant for the films discussed above, they could however play a crucial role in the comparison of ultrathin $(001)_{or}$ and $(101)_{or}$ superlattice systems.

5.2 Truncated [111] nickelate slabs as an elementary magnetic model system

The nature of the magnetic order in nickelates is still under debate. The unusually large periodicity of the antiferromagnetic ground state is characterized by the wave vector $\mathbf{q}_0 = (1/4,\ 1/4,\ 1/4)$ in pseudocubic notation, corresponding to (1/2, 0, 1/2) in orthorhombic notation. Previous neutron diffraction experiments were not able distinguish between collinear (↑↑↓↓) and non-collinear (↑→↓←) spin arrangements. As a consequence theoretical descriptions vary from localized spin models [9] with antisymmetric exchange interactions to itinerant models [6] where the spin order arises from a nesting instability of the Fermi surface and yield diverse collinear and non-collinear ground states [118]. Moreover, several scenarios describing the magnetization of the Ni sublattices were proposed in neutron studies: two distinct Ni magnetic moments [8], equal moments sizes [10], and one of the Ni sublattices carrying zero moment [11]. Distinct Ni magnetic moments are predicted by mean field [82] and *ab-initio* calculations [83], however the magnetization of one Ni sublattice is considered being zero in other calculations [78, 267].

Along the lines of recent REXS experiments confirming the non-collinear (↑→↓←) spiral in bulk-like films [4, 12, 57] it is thus of great importance to test the validity of theoretical concepts describing the intrinsic magnetism of the nickelates. As elucidated in the following sections the specifically designed $NdNiO_3$-$NdNiO_3$ heterosystem truncated along the [111] direction emerges as a practical testing ground for current and future theories, especially in terms of possible spin configurations and tests of the amplitude ratio of magnetic moments in neighboring NiO_6 octahedra.

Previous studies investigated nickelate heterostructures with the intention to manipulate the RNiO$_3$ magnetism extrinsically via the interplay with a second magnetic material [107, 108, 268], via charge transfer [114, 269], or via an altered orbital occupation [4]. In contrast, here we aim to explore the pure effect of truncation along the [111] direction. Consequently we have chosen to stabilize the thin $NdNiO_3$ slabs through $NdGaO_3$, a well characterized paramagnetic band insulator with a stable valence Ga^{3+} ion, preventing a polar discontinuity at the interface and charge transfer to the Ni. Furthermore, the R-cation sublattice remains unchanged across the $NdGaO_3$-$NdNiO_3$ interface precluding additional symmetry breaking and intermixing. Moreover, both materials have good epitaxial matching conditions along the [111] direction including closely similar oxygen octahedra tilt angles [103]. This is of particular importance since distinct changes in the tilt angles can facilitate a realignment of the easy axis in magnetic systems [38]. Finally, the [111] orientation is expected to prevent strain induced orbital polarization of the Ni e_g orbitals [15], which was identified as the origin of reorientation of the spin spiral polarization plane in strained [001] heterostructures via the spin orbit coupling [4] and would obscure the observation of the elementary effect of [111] directional truncation.

In addition to these conditions that preclude external influences and render the truncated [111] nickelate slabs into an elementary magnetic model system, there are technical aspects making the [111] orientation particularly suited for the REXS experiments. As will be discussed in more detail below, the scattering vector $\mathbf{q}$ can coincide with the $\mathbf{q}_0 = (1/4,\ 1/4,\ 1/4)$ in a horizontal scattering geometry and no wedge as in Ref. [4] is needed. Thus no shadowing effects occur and moreover the π and σ scattered intensities can be analyzed separately.

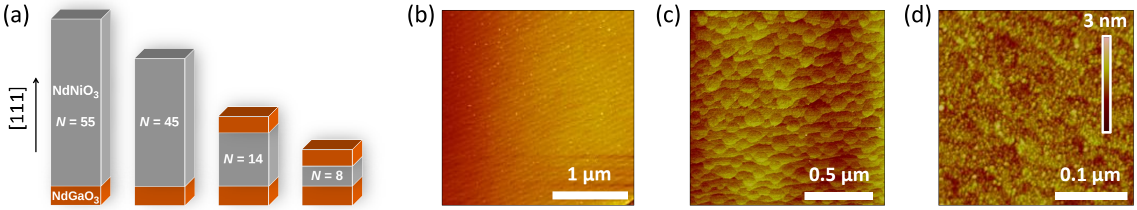

Figure 5.4 [111] oriented nickelate slabs and surface topology of NdGaO$_3$ and NdNiO$_3$. (a) Schematic of the four main samples of this chapter. NdNiO$_3$ slabs of different thickness were grown on NdGaO$_3$ substrate with N indicating the number of Ni planes along the pseudocubic [111] direction. The thin $N = 14$ and 8 samples are additionally capped with NdGaO$_3$. (b) AFM images of the surface of [111] oriented NdGaO$_3$ substrate after annealing. Well defined terraces with step edges of unit cell height have formed. (c) Results obtained by the same annealing recipe were not identical for all NdGaO$_3$ substrates. In some cases a mixed surface termination and fractured step edges emerged. (d) Typical surface topology of a NdNiO$_3$ film.

5.3 Experimental characterization of samples

The epitaxial nickelate heterostructures presented in this chapter were grown by pulsed laser deposition (PLD) as described in Ref. [112], and by off-axis radiofrequency magnetron sputtering as described in [103]. Through the extensive experimental characterization by various methods a high crystalline quality of the samples was confirmed and a distinction to the properties of [001] oriented heterostructures was assured, so that new aspects in the physics of nickelates could be explored.

Films of NdNiO$_3$ and PrNiO$_3$ – both exhibiting a MIT and a Néel transition in the bulk – were grown on NdGaO$_3$ and YAlO$_3$ substrates with one of the pseudocubic $\langle 111 \rangle$ planes as surface. The orthorhombic NdGaO$_3$ was chosen based on the results of Ref. [103], discussed in chapter 2. The effects of epitaxy to the orthorhombic YAlO$_3$ have not been studied yet. NdGaO$_3$ imposes moderate tensile strain to the nickelate crystal lattice whereas YAlO$_3$ acts compressively (see Fig. 5.2 and Table A.1 and Table A.2 in Appendix A). Such a difference in the sign of the strain states offers the possibility to disentangle influences of [111] crystal orientation and epitaxial strain [54]. However, along the different steps of characterization it was found that basically only the material combination NdNiO$_3$ on NdGaO$_3$ exhibits properties significantly distinct from the corresponding [001] heterostructures. Thus, most of this chapter is focused on a selection of four samples: Two NdNiO$_3$ slabs on NdGaO$_3$ with a thickness of $N = 55$ and 45 (N indicates the number of Ni planes along the pseudocubic [111] direction) and thin $N = 14$ and 8 samples that are additionally capped with NdGaO$_3$ [Fig. 5.4(a)].

Tests of pre-annealing of the [111] NdGaO$_3$ substrates prior to the NdNiO$_3$ deposition yielded varying results. Whereas some substrates showed well defined terraces with step edges of unit cell height after 4 h at 1000°C in oxygen atmosphere [Fig. 5.4(b)], other substrates of the same batch showed regions of different surface termination within the steps and fractured step edges [Fig. 5.4(c)]. The discrepancies can originate from the different substrate miscuts – which for the batch was indicated to range from

0.1° to 0.5° – i.e. the thermal diffusion coefficients are depending on the different cut angles. In principal, it is possible to achieve single termination by etching with NH_4Cl-based solutions or by adjusting the annealing recipe for each subtrate individually, however, in the following we chose to deposit the films on untreated surfaces with a statistical distribution of Nd and Ga as termination. Previous test with related [001] heterostructures did not show a significant difference in the macroscopic physical properties between treated and untreated substrates [112]. Moreover a detailed local mapping of the MIT on a terraced substrate revealed stripe-like patterns corresponding to step edges [233], i.e. a faceted substrate surface might also influence the spin order in a subtle way which we intend to avoid. Fig. 5.4(d) shows a typical surface of a $NdNiO_3$ film grown on [111] $NdGaO_3$. The root-mean-square roughness is below 1 nm, which is comparable to heterostructures grown along the [001] direction.

The first step of the subsequent characterization are electrical transport measurements, providing information about a change in the electronic structure as compared to [001] heterostructures and allowing a pre-selection of promising samples. By scanning transmission electron microscopy imaging of the local crystal structure and oxygen positions a pinning of the NiO_6 octahedra to the substrate was studied. and an accurate determination of the layer thicknesses and interface roughnesses was performed by on -and off resonant soft x-ray reflectivity. Moreover, the number N of magnetically active Ni layers in the [111] direction could be extracted from the magnetic peak in the resonant reflectivity. X-ray absorption spectroscopy allowed to exclude the presence of Ni e_g orbital polarization, which was identified as the origin of reorientation of the spin spiral polarization plane via the spin orbit coupling in strained [001] nickelate heterostructures [4]. Finally, the azimuthal dependence of the magnetic resonant x-ray scattering at $\mathbf{q}_0$=(1/4, 1/4, 1/4) is analyzed in combination with a double cluster model and the two main results of the chapter are derived: (i) the crossover between non-collinear and collinear spin structures depending on the $NdNiO_3$ slab thickness in the $\mathbf{q}_0$ direction and (ii) the tunability of the magnetic moments in the Ni sublattices by structural pinning of the oxygen positions in the NiO_6 octahedra. The crossover of the spin structures is then corroborated by density functional theory calculations.

All results from the different characterization methods are in very good agreement. Furthermore, the direct comparison of the magnetic structure of the samples grown by the different techniques PLD ($N = 55, 14, 8$) and sputtering ($N = 45$) are found to be closely similar, which demonstrates the robustness of our results.

5.3.1 Electrical transport

The electrical transport was measured via van der Pauw method with Pt contact pads sputtered in the corners of the samples. Fig. 5.5(a) shows the resistivity curves of the four most important $NdNiO_3$-$NdGaO_3$ heterostructures discussed in this chapter. Cooling and heating cycles exhibit a small hysteresis with a width < 5 K. The $NdNiO_3$ film with a thickness of 114 Å in the [111] direction features an upturn of ρ at $T \sim 325$ K and a typical kink related to the antiferromagnetic transition [270] at $T \sim 200$ K. The wide separation of the two features is closely similar to previous observations on 170 Å $NdNiO_3$ films [103], also grown on [111] oriented $NdGaO_3$

substrates. The features of the MIT and the magnetic transition are more pronounced in the derivative of the resistivity -d/dT ln($\rho(T)$) in Fig. 5.5(b). With decreasing $NdNiO_3$ thickness the transitions occur at lower temperatures. The magnetic onset temperatures are similar to the ones determined by resonant elastic x-ray scattering, as explained later. We note that in Refs. [12, 57] $NdNiO_3$ films were deposited on [111] $NdGaO_3$ substrates as well, however, $T_{\mathbf{MI}}$ and $T_{\mathbf{N}}$ were found to coincide at $T \sim$ 160 K upon cooling, i.e. the films showed behavior similar to bulk powder samples. The difference might be a consequence of the significantly larger film thickness in refs. [12,57] which fosters relaxation of the epitaxial strain in the [111] direction and/or accumulation of lattice defects and disorder. Furthermore, we notice that the upturn at $T_{\mathbf{MI}}$ in Fig. 5.5(a) is rather subtle for all samples and the overall shape of the resistivity curves qualitatively resemble the behavior of bulk-like $SmNiO_3$ [59]. This is in accordance with Ref. [103] relocating thin [111] oriented $NdNiO_3$ films at a position in the nickelates phase diagram that corresponds to larger octahedral distortions.

A reference sample of $NdNiO_3$ grown along the [001] direction [Fig. 5.5(c), dark blue curve] shows a much more pronounced jump of the resistivity over several orders of magnitude at $T_{\mathbf{MI}}$, which is at $T \sim$ 160 K on the cooling run. The rather gradual change of ρ at $T_{\mathbf{MI}}$ for [111] oriented heterostructures can be ascribed to the altered Ni-O-Ni bond angles [38, 103], similar to $SmNiO_3$. Further, a thicker [111] oriented $NdNiO_3$ film of 230 Å (light blue curve) shows a reduced $T_{\mathbf{MI}} \sim$ 250 K, as compared to the 114 Å film in Fig. 5.5(a). The reduction of $T_{\mathbf{MI}}$ towards the $\sim$ 160 K can be due to vanishing influence of the [111] interface with increasing film thickness and/ or accumulation of defects.

In addition, a 110 Å $NdNiO_3$ film was grown on [111] oriented $YAlO_3$ [gray curve in Fig. 5.5(c)]. Along the lines of Refs. [2, 3, 54] the MIT of nickelates can be suppressed if the amount of compressive strain induced in the (001) planes is sufficiently large. In particular, the -2.9% lattice mismatch between $NdNiO_3$ and $YAlO_3$ in the [001] orientation was found to be sufficient for a complete suppression of the MIT [2]. For [111] heterostructures the situation turns out more complex since still a weak MIT is observed, however at strongly reduced $T \sim$ 125 K. This can be a consequence of the fact that the substrate strain along the [111] direction is only a projection onto the (001) plane and the induced lattice distortion is of trigonal symmetry. Preliminary REXS experiments (not shown here) revealed only a faint magnetic peak for the films on $YAlO_3$ will require further experimental investigation.

Similar considerations apply for $PrNiO_3$ films and $PrNiO_3$-$PrAlO_3$ superlattices grown on [111] oriented $NdGaO_3$. As shown in Fig. 5.5(d) the MIT of [111] and [001] oriented $PrNiO_3$ films coincide in temperature (light green and black curve and inset) and is only slightly higher for the superlattice. Hence, an distinction between [001] and [111] orientation is not pronounced and the $PrNiO_3$ samples will not be investigated here further. Reasons for the assimilation can be the larger mismatch between the $PrNiO_3$ and $NdGaO_3$ tilt angles, i.e. octahedral interlock effects in the tilts across the interface do not occur, which might also be the case for nickelate films grown on [111] oriented $YAlO_3$.

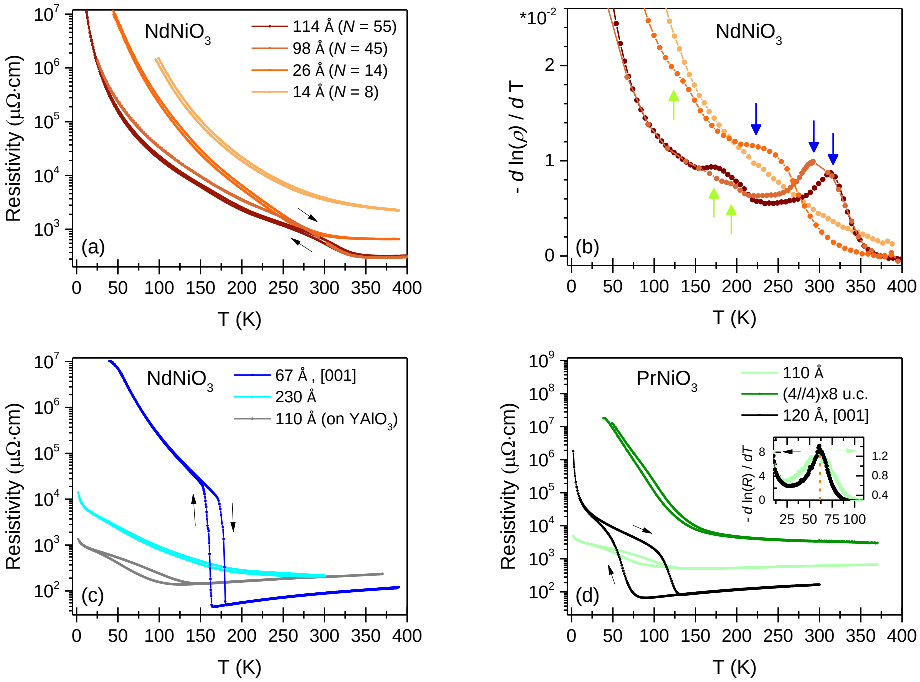

Figure 5.5 Electrical transport of [111] oriented heterostructures. (a) Resistivity ρ upon cooling and heating cycles (black arrows) for the $NdNiO_3$ on $NdGaO_3$ samples with different $NdNiO_3$ layer thickness (N indicates the number of magnetically active Ni layers, as explained later in the text). The discontinuity of the 98 Å at $T \sim 300$ K is due to measurement in two different setups. When the value of the absolute resistance exceeds the software limit of the Quantum Design PPMS the resistivity curves are cutoff at low temperatures. (b) Derivative of the resistivity -d/dT ln($\rho(T)$) upon cooling with clear features of the electronic and antiferromagnetic phase transition for the 114, 98, and 26 Å sample. Blue arrows indicate peak positions corresponding to half of the $NdNiO_3$ being metallic and the other half insulating. The green arrows indicate typical kinks related to the occurrence of antiferromagnetism. For the 14 Å sample the features are too faint for a clear assignment. (c) $NdNiO_3$ reference samples: a 67 Å film grown along the pseudocubic [001] direction exhibiting a sharp metal-insulator transition with a jump in ρ over three orders of magnitude (dark blue curve). A 230 Å thick film exhibits only a weak upturn at lower temperatures (light blue curve) than the films in (a). A film grown on [111] oriented $YAlO_3$ also shows only a weak MIT at low temperatures (gray curve). (d) For $PrNiO_3$ the T_{MI} does not depend on whether the growth is on a (111) or a (001) surface (see light green and black curve, and inset with the derivative of ρ upon cooling). Also a $PrNiO_3$-$PrAlO_3$ superlattice with layer sequence $(4//4) \times 8$ u.c. exhibits only a slightly enhanced transition temperature (dark green curve). In consequence, the samples in (c), (d) were not further investigated.

5.3.2 Scanning Transmission Electron Microscopy

Analysis by scanning transmission electron microscopy (STEM) provides valuable information about the quality and structural details of oxide heterostructures. In our case the chemical sharpness of the interfaces and the octahedral tilt angles derived from the oxygen positions were of particular interest. Cross-section specimens of the $N = 55$ and 8 sample were treated and thinned to electron transparency. Technical details about sample preparation and STEM data processing can be found in the

Supplementary Information of [271].

The high angle annular dark field (HAADF) images in Fig. 5.6(a),(b), recorded and analyzed by Y. E. Suyolcu (MPI-FKF), confirm the epitaxial layer-by-layer growth of the $NdNiO_3$-$NdGaO_3$ heterostructures. Complementary low angle annular dark-field (LAADF) images (not shown here but to be published in [272]) on a 100 nm scale gave no indications for the presence of crystallographic stacking faults or structural domains in the $NdNiO_3$. Electron energy loss spectroscopy (EELS) confirmed the chemical sharpness of the $NdNiO_3$-$NdGaO_3$ interfaces with Ni and Ga cation intermixing limited to only ~ 2 atomic layers.

The two most important pieces of information gained from the STEM study is a subtle difference in the Ni-O-Ni bond angle between the $N = 55$ and 8 sample [Fig. 5.6(c),(d)] and the crystallographic reorientation of the $N = 55$ film [Fig. 5.6(e),(f)]. These information were extracted from annular bright field (ABF) imaging data, analyzed by the Digital Micrograph software tool described in Ref. [273]. Details on the analysis will be published in [272]. The obtained difference in the Ni-O-Ni bond angle (155° for $N = 55$ and 153° for $N = 8$) is assigned to an enhanced pinning of the octahedral oxygen positions to the confining $NdGaO_3$ octahedral network, for the case of the thin nickelate slab. Note that 153° corresponds to the Ga-O-Ga bond angle of bulk $NdGaO_3$ [265], whereas 155° is similar to the bulk $NdNiO_3$ value [64]. As will be discussed later, such a structural pinning can hamper the emergence of the NiO_6 octahedral breathing distortion which has significant impact on the magnetic moment sizes in the Ni sublattices.

The second observation refers to the growth of the $N = 55$ sample on a $[\bar{1}11]$ $NdGaO_3$ surface (corresponding to the $[011]_{or}$ orthorhombic direction) and the $N = 8$ sample grown on [111] surface (corresponding to $[101]_{or}$). The oxygen bond angle analysis across the $NdNiO_3$-$NdGaO_3$ interface [Fig. 5.6(e),(f), with details to be published in Ref. [272]] reveals that the change in the tilt pattern observed along an atomic column from $NdGaO_3$ to $NdNiO_3$ corresponds to a crystallographic reorientation from $[\bar{1}11]$ to [111] within the first few atomic layers after the interface. In other words, the orthorhombic a and b axis of the *Pbnm* unit cell exchange as a function of the distance from the interface. The $N = 8$ sample grown on a [111] surface does not show any reorientation and the tilt pattern in the stays constant across all layers. In consequence, the $N = 55$ sample is directly comparable to the other samples of the series with $N = 45$, 14, and 8, since effectively they all exhibit the same [111] crystallographic orientation.

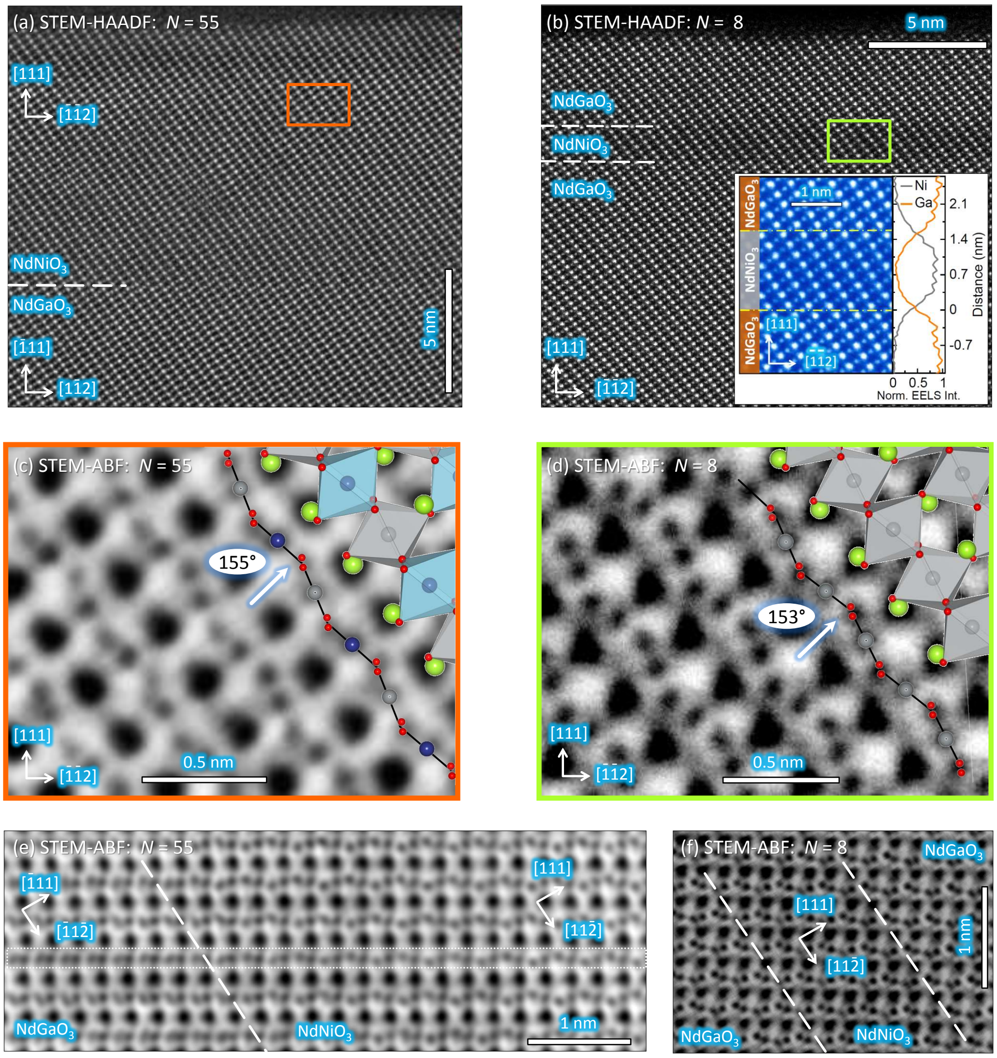

Figure 5.6 STEM images of the N = 55 and 8 Ni planes samples. (a),(b) HAADF images of Nd, Ga, and Ni atoms of the $NdNiO_3$-$NdGaO_3$ heterostructures, confirming the epitaxial growth. Interfaces are indicated by dashed lines. The inset in (b) combines the HAADF image (left) with the respective Ni and Ga $L_{3,2}$ EELS line scan profiles (right). The Ni and Ga intermixing at the $NdNiO_3$-$NdGaO_3$ interfaces is limited to only $\sim$ 2 atomic layers. (c),(d) ABF images mapping the oxygen positions within the colored boxes indicated in (a) and (b). A quantitative analysis of the Ni-O-Ni bond angles α reveals a partial relaxation in the $N = 55$ case (α=155°), whereas the oxygen positions in the $N = 8$ case (α=153°) are pinned to the confining $NdGaO_3$ oxygen octahedron network. The error bars of the bond angle determination (95% confidence interval, corresponding to 2 times the standard error) are less than 1° (Ref. [273]). (e) Analysis of the oxygen positions on a larger scale across the $NdNiO_3$-$NdGaO_3$ interface of the $N = 55$ sample reveals differences in the projected cation-oxygen bond angles along the indicated atomic columns (dotted box). The pattern changes continuously from a rather straight line in the $NdGaO_3$ to a zig-zag pattern in the $NdNiO_3$. This corresponds to a reorientation of the crystallographic unit cell as indicated by the pseudocubic directions. (f) Conversely, for the $N = 8$ sample a constant zig-zag pattern is observed from the $NdGaO_3$ substrate to the $NdNiO_3$ film and to the $NdGaO_3$ capping layer, i.e. no reorientation occurs.

Table 5.1 Structural and magnetic parameters extracted from x-ray reflectivity. Layer thickness t and interface roughnesses r_1 ($NdGaO_3$ substrate to $NdNiO_3$) and r_2 ($NdNiO_3$ to $NdGaO_3$ capping) are obtained from fits to on -and off resonant scans at $T = 300$ K. The error of t is 1-2 Å and less than 0.5 Å for r. The number N of magnetically active Ni planes in the [111] direction is deduced from the modeling of the magnetic contribution in the resonant scans at $E = 853$ eV and $T = 20$ K and the errors of N are extracted from Fig. 5.7.

sample	t $NdNiO_3$ (Å)	t $NdGaO_3$ (Å)	r_1 (Å)	r_2 (Å)	N Ni planes
$N = 55$	113.9	–	3.6	–	55 ± 3
$N = 45$	97.6	–	3.2	–	45 ± 3
$N = 14$	26.1	50.4	3.3	4.1	14 ± 1
$N = 8$	14.4	48.9	3.2	5.4	8 ± 0

5.3.3 Resonant soft x-ray reflectivity

Reflectivity of x-rays at resonance energies of specific ion absorption edges has proven to be a valuable tool in non-destructive chemical diagnostics with an atomic-scale resolution and an element sensitivity that can used for probing the properties of buried layers in heterostructures [111, 274–276]. Here the specular scattering of photons is employed with energies in the soft x-ray regime to accurately characterize structural properties of the samples. Moreover, the magnetic (1/4, 1/4, 1/4) reflection and the specular scattering direction coincide for [111] samples and in consequence the magnetic reflection is observed on a reflectivity background when energies are tuned to the Ni L_3 and Nd M_5 edge.

Structural characterization

On -and off resonant soft x-ray reflectivity was used to determine the layer thicknesses and interface roughnesses of $NdNiO_3$ and $NdGaO_3$ with the software ReMagX (Ref. [184]). The off-resonant parts of the atomic scattering factors of Nd, Ga, Ni, and O were taken from the Chantler tables [277]. The resonant parts were extracted from the corresponding x-ray absorption spectra (XAS) recorded as described in Ref. [111]. As an example the real and imaginary parts f_1 and f_2 of the Ni and Nd scattering factors of the $N = 55$ film are shown in the inset of Fig. 5.7(a) with the real part f_1 obtained by Kramers-Kronig transformation. The reflectivity curves taken at various energies and $T = 300$ K were simultaneously fitted [Fig. 5.7(a)-(d)]. The resulting set of parameters for the layer thickness t and interface roughness r are summarized in table 5.1.

Quantifying the magnetically active Ni planes

The Ni magnetic Bragg peak is observed in the resonant soft x-ray reflectivity of [111] oriented samples [103] since the $\mathbf{q}_0$=(1/4, 1/4, 1/4) propagation vector direction lies along the specular direction [Fig. 5.7(e)-(l)]. Moreover, tuning the energy to the Ni L_3 resonance allows for a detailed study of the magnetic properties since the magnetic scattering signal is significantly enhanced and vanishes within the experimental error

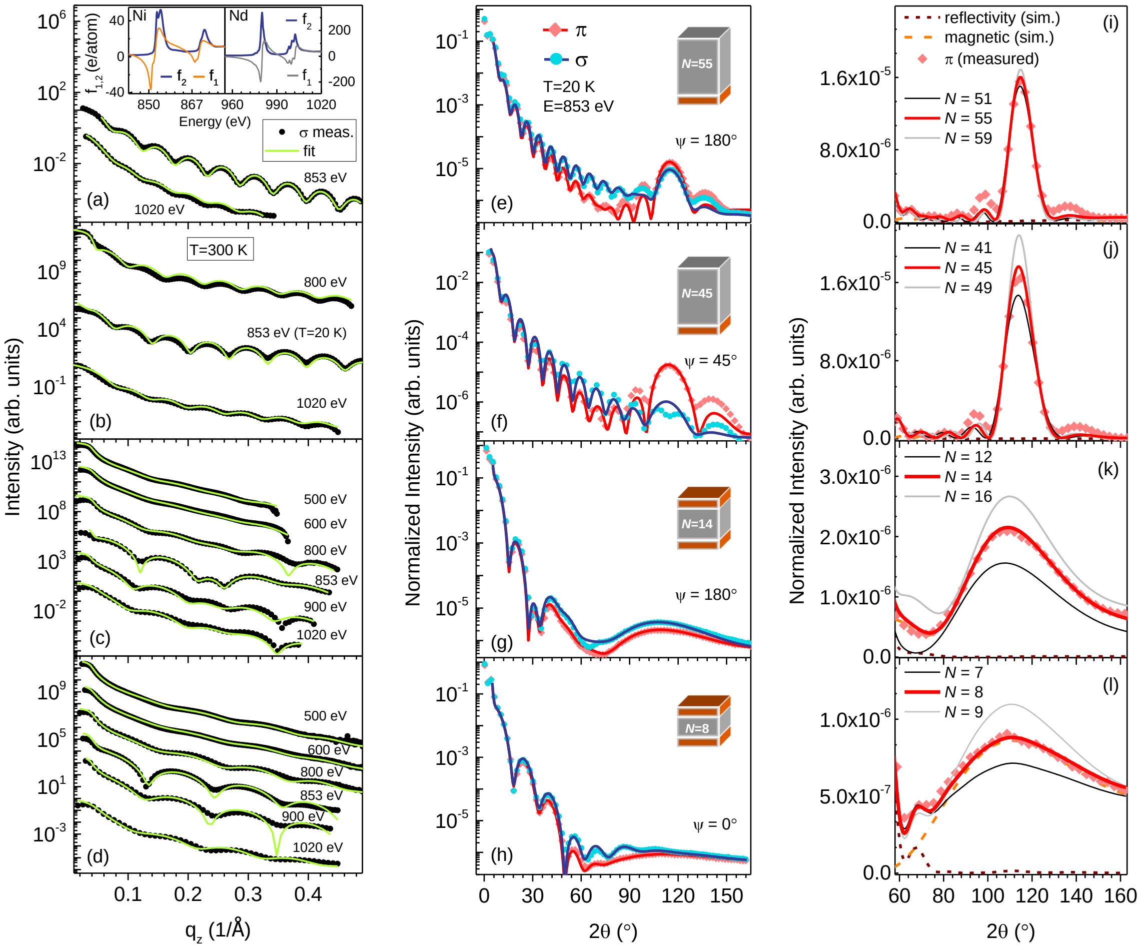

Figure 5.7 Characterization of structural and magnetic properties. (a)-(d) Reflectivity of the N = 55, 45, 14, and 8 Ni layers at various energies at T = 300 K (black symbols). The $NdNiO_3$ film thickness and the $NdGaO_3$ capping layer thickness are extracted from the fits (solid green lines). For clarity the reflectivity curves at different energies are offset. The inset in panel (a) shows the imaginary and real part (f_2 and f_1) of the Ni and Nd scattering factors, exemplary for N = 55 sample. (e)-(h) Resonant reflectivity at E = 853 eV (Ni L_3) and T = 20 K for π and σ polarized photons (red and blue symbols). The solid lines are the superposition of the structural fit at E = 853 eV from panel (a)-(d) and separate simulations to the antiferromagnetic (1/4, 1/4, 1/4) peak appearing in the reflectivity at $2\theta \sim 115°$. (i)-(l) Enlarged view of the antiferromagnetic peak in (e)-(h) on a linear intensity scale (red symbols) together with simulated curves benchmarking the error bars for the number of magnetically active Ni planes (black and gray lines). The red solid line in panels (i)-(l) is the simulation which agrees best with the measurement data. Accordingly, the results for the number of magnetically active Ni layers are N = 55 ± 3, 45 ± 3, 14 ± 1, and 8± 0.

for non-resonant energies. The software tool QUAD (Ref. [185]) was used to analyze the magnetic contribution to the reflectivity signal in the 2θ range between 60° and 165° and determined the number N of magnetically active Ni planes stacked along the [111] direction (Table 5.1). The obtained numbers are consistent with the structural thickness from the independent ReMagX fits at $T = 300$ K [Fig. 5.7(a)-(d)], where the magnetic peak is absent. The solid lines in Fig. 5.7(e)-(l) are the superposition of the magnetic QUAD fit and the structural ReMagX fit. As the number N agrees with the structural fit and the STEM analysis, we exclude magnetic dead layers at interfaces and in particular for the thinnest sample effectively 8 Ni layers are active, corresponding to two full periodicities of the period-four antiferromagnetic order.

5.3.4 X-ray absorption spectroscopy

X-ray induced core-hole excitations measured by x-ray absorption spectroscopy (XAS) give valuable information about the orbital occupation in TMO material systems. Here, we focus on the Ni $L_{3,2}$ edge, corresponding to transitions from $2p$ to unoccupied $3d$ states. The linear dichroism of the absorption spectra measured with two distinct linear polarizations of the incident photons turns out to be relevant for the understanding of the magnetism in truncated nickelate slabs. In fact, it is the absence of any orbital polarization in our [111] nickelate systems which reveals that different mechanisms than in previous studies [4, 102] must be at play.

The authors Frano *et al.* have described the change of the polarization plane of the antiferromagnetic spin spiral in [001] oriented nickelate heterosystems [4]. A combined effect of epitaxial strain and spatial confinement of the conduction electrons influences the e_g orbital occupation which in turn reorients the spin spiral via spin-orbit coupling. Depending on the sign of the epitaxial strain, the spin orientations can be pushed either into or out-of plane. A more detailed description of the experimental results of Frano *et al.* was given in chapter 2.

In the light of this important discovery the orbital polarization state of our samples needs clarification. In particular whether the observed reorientation of the spiral from (↑→↓←) to (↑↑↓↓) can be explained by a change in the e_g orbital occupancy. A quantitative determination of the linear dichroism of [111] samples probed in a horizontal scattering geometry is not straight-forward as for [001] heterostructures [111–113]. Whereas for [001] oriented samples the electric field vectors $\boldsymbol{\varepsilon}_{\parallel}$ and $\boldsymbol{\varepsilon}_{\perp}$ of the linearly polarized incident light basically coincide with the spatial extension of the lobes of the e_{g} orbitals with x^2-y^2 and $3\mathrm{z}^2$-r^2 character [Fig. 2.7] – i.e. they couple into the empty states of the respective symmetry – the corresponding directions in [111] samples are skew with respect to $\boldsymbol{\varepsilon}_{\parallel}$ and $\boldsymbol{\varepsilon}_{\perp}$. Thus, the [111] oriented $N = 55$ was mounted on a wedge with an inclination angle of 54.7° at an azimuthal angle of 45°. As a consequence the $NdNiO_3$ crystallographic directions are reoriented such that crystallographic directions correspond to the incoming light polarizations, indicated as $\boldsymbol{\varepsilon}_x$ and $\boldsymbol{\varepsilon}_z$ in correspondence to the respective orbitals [Fig. 5.8(a)]. Moreover, the XAS is not only measured at the L_2 edge [4, 60] but also at L_3 energies, since the higher absorption intensity and the smaller broadening can lead to more pronounced dichroic effects [Fig. 5.8(b)]. In the entire energy range the normalized linear dichroism

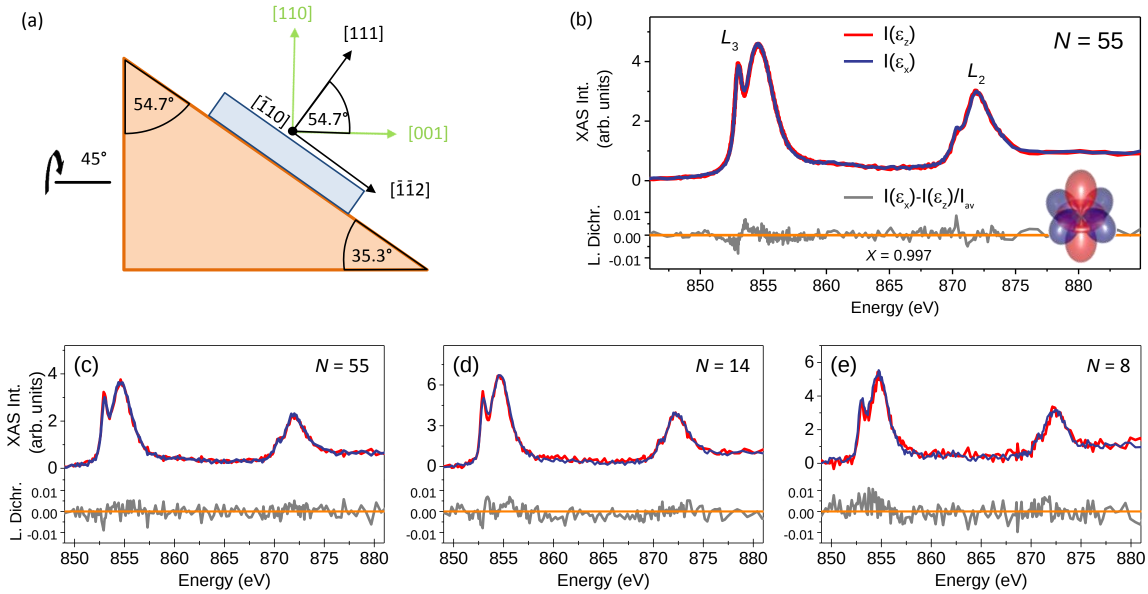

Figure 5.8 Absence of orbital polarization in [111] oriented samples. (a) Schematic of a [111] oriented sample mounted on a wedge with inclination angle of 54.7°. An additional rotation of the wedge by 45° around the azimuthal angle ψ positions the crystallographic directions such that the electric field vector directions $\boldsymbol{\varepsilon}_x$ and $\boldsymbol{\varepsilon}_z$ of the incoming light coincide with the major lobes of the $d_{3z^2-r^2}$ and $d_{3x^2-y^2}$ orbitals, respectively. (b) Fluorescence yield XAS of the $N = 55$ sample on the wedge measured at the Ni $L_{3,2}$ edge at $T = 20$ K for the two linear polarizations $\boldsymbol{\varepsilon}_x$ and $\boldsymbol{\varepsilon}_z$ of incoming photons (red and blue curve). The linear dichroism $I(\boldsymbol{\varepsilon}_x) - I(\boldsymbol{\varepsilon}_z)$ normalized by the averaged energy integral I_{av} from 850 eV to 880 eV (gray curve) is vanishingly small and the calculated hole ratio indicates the absence of an orbital polarization and its influence on the spin order. The inset with the red and blue semitransparent $d_{3x^2-y^2}$ and $d_{3z^2-r^2}$ orbitals illustrates the corresponding degeneracy of the electron density distributions. (c)-(e) XAS of the $N = 55$, 14, and 8 Ni layers measured in horizontal scattering geometry (i.e. without wedge) at $T = 20$ K. The difference spectra for the two incoming light polarizations (gray curves) are zero within the noise for all samples, i.e. there is no significant change from $N = 55$ to $N = 8$ indicating the emergence of an orbital polarization.

$I(\boldsymbol{\varepsilon}_x) - I(\boldsymbol{\varepsilon}_z)$ is vanishingly small and the calculated ratio of X (for details see Ref. [112] or chapter 2) is close to unity, indicating the degeneracy of the $d_{3z^2-r^2}$ and $d_{3x^2-y^2}$ orbitals and the absence of orbital polarization [4] influencing the spin order. This is in accordance with the expectation that a trigonal lattice distortion (here due to tensile strain in the (111) plane) is not lifting the degeneracy of e_g orbitals (see Ref. [15] and chapter 2). We note that the data of Ref. [60] show a non-zero dichroic XAS signal in a comparable scattering geometry for much thinner $N = 2$ samples of NdNiO$_3$ on LaAlO$_3$ which was interpreted as signature of antiferro-orbital order.

The XAS of the other samples in our series were taken in the same run as the REXS experiments, i.e. in a flat scattering geometry without wedge [Fig. 5.8(c)-(e)]. Here the quantitative extraction of a possible imbalance in the $d_{3z^2-r^2}$ and $d_{3x^2-y^2}$ occupation is more complex as derived in Ref. [112] and chapter 2. However, the normalized difference signals $I(\boldsymbol{\varepsilon}_x) - I(\boldsymbol{\varepsilon}_z)$ of the $N = 55$, 14 and 8 Ni planes samples is zero within the noise limit [gray curve in Fig. 5.8(c)-(e)]. The XAS of the $N = 45$ sample (not shown here) is very similar to the $N = 55$ case. Since the hole ratio X was determined to be unity for the $N = 55$ sample on the wedge and there is no change in the linear dichroism of the whole $N = 55$ to 8 series without wedge, we exclude the emergence of an orbital polarization for all samples. As a consequence orbital polarization cannot be key to the reconstruction of the spin spiral from non-collinear to collinear.

Furthermore, we emphasize that the dichroic signal of Ref. [60] interpreted as a special type of orbital order – namely antiferro-orbital order – is not observed. In bulk-like samples, Jahn-Teller-like orbital order which could explain a (↑↑↓↓) spin configuration has already been excluded in earlier studies since (1/4, 1/4, 1/4)-type reflections have not been found at the Ni K-edge [278] and moreover the measured signal of $(0kl)_{or}$ and $(h0l)_{or}$ reflections at this energy is not in agreement with the presence of an orbital superstructure [70]. For the $N = 8$ sample with a thickness of 14.4 Å these kind of measurements are unfeasible as our experience gained in the scope of the project published in Ref. [72] showed that a slab thickness of more than 100 Å is required to probe fine details in the K-edge energy dependence of such peaks. Hence, superlattices with several repetitions of the $N = 8$ layers would be required.

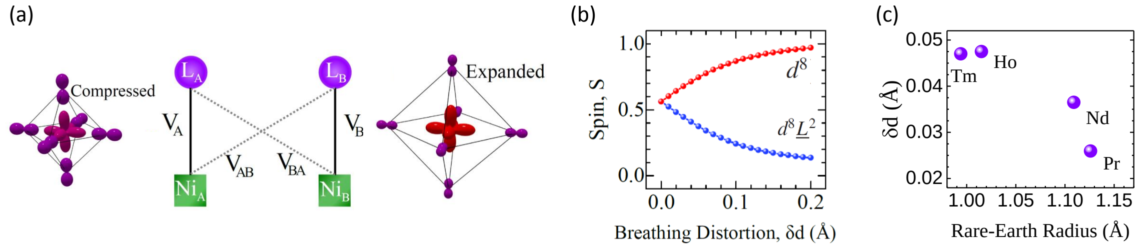

Figure 5.9 Double cluster calculation and NiO$_6$ breathing distortion. (a) Diagrammatic depictions of the two clusters A and B with Ni and ligand sites L_A and L_B and standard ligand field hopping V$_A$ and V$_B$. Additionally, intercluster coupling is introduced with the hopping parameters V$_{AB}$ and V$_{BA}$, allowing to incorporate the physics of a negative charge transfer and the NiO$_6$ breathing distortion in the calculations. The corresponding compressed and expanded NiO$_6$ octahedra are illustrated on the left and right hand side, together with the calculated hole density matrices at the Ni and O sites. Ligand hole densities are scaled by a factor of 2 for clarity. (b) Total spins S of the compressed and expanded octahedron with $d^8\underline{L}^2$ and d^8 character, respectively, as a function of the magnitude δ of the breathing distortion. (c) Experimental values of δ for powder samples of TmNiO$_3$, HoNiO$_3$, NdNiO$_3$, and PrNiO$_3$. Panel (a) and (b) are adapted from Ref. [13] and the experimental values in (c) taken from Refs. [64,65,248].

5.4 Double Cluster modeling

Core level XAS spectra are typically modeled by atomic or cluster multiplet calculations. Closely related to the XAS process is the magnetic circular dichroism from which the resonant magnetic diffraction can be derived. Previous cluster and charge transfer multiplet calculations on nickelates mostly focused either on a match with experimental XAS data [279,280] or with experimental magnetic scattering data [281]. However, after the choice of certain model parameters such as the lifetime broadening, which brings the calculated XAS spectrum in congruence with experimental XAS data, possibly the corresponding magnetic diffraction does not agree with the experiment or vice versa. A novel approach in this field is the double cluster model introduced by R.J. Green *et al.* [13], based on the negative charge transfer concept that starts from a Ni 3$d^8\underline{L}$ electron configuration with $\underline{L}$ denoting a ligand hole at the oxygen, as introduced in Ref. [14] and implemented in *ab-intio* calculations in Refs. [81,83]. The double cluster explicitly incorporates the NiO$_6$ breathing distortion [Fig. 5.9(a)] whose magnitude δd corresponds to the deviation of the long and short Ni-O bond lengths from the mean value. In the scope of this approach good agreements between the calculation and experimental data can be reached for both: the XAS and the resonant magnetic scattering [13].

One important insight that follows from the double cluster calculation – and will also be relevant later – is that the theoretical picture of a 2 Ni $d^8\underline{L} \rightarrow$ Ni d^8 + Ni $d^8\underline{L}^2$ bond disproportionation at the MIT corresponds to the rather extreme case of δd $\gg$ 0.2 Å. For values closer to the experimentally found δd [Fig. 5.9(c)] the compressed and expanded octahedra will not exhibit the configuration $(d^8\underline{L}^2)_{S=0}$ and $(d^8)_{S=1}$, i.e. one set of octahedra is carrying the full spin whereas the spin of the

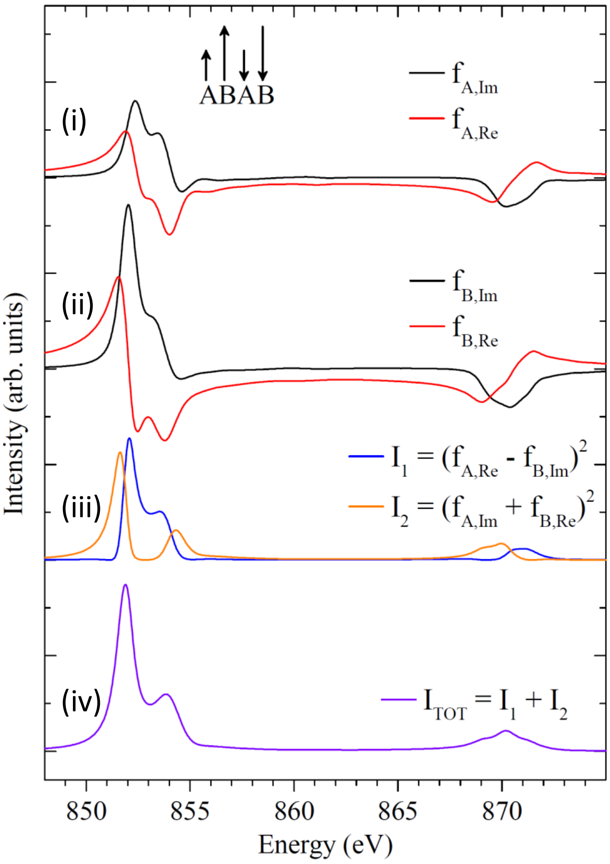

Figure 5.10 Calculated energy dependence of magnetic scattering by the double cluster model. Black and red curves in (i) and (ii) are the real and imaginary part of the magnetic form factors f of the sites **A** and **B**, respectively. **A** corresponds to a SB and **B** to a LB site. The difference between the curves in (i) and (ii) depends on the magnitude of δ and is not a simple scaling factor. (iii) Scattered intensity I_1 and I_2 from the two sites (blue and orange curve). (iv) The total scattered intensity is the sum $I_1 + I_2$. The figure is adapted from Ref. [283].

other set is zero, but both spins will be closer to $S = 1/2$ [Fig. 5.9(b)]. Experimental values of δd are given in Fig. 5.9(c) and are in the range between $\sim$ 0.02 and $\sim$ 0.05 Å. Note that δd of bulk LaNiO$_3$ is zero (in space group $R\bar{3}c$), however, recently orthorhombic/monoclinic distortions were reported in LaNiO$_3$ powder [282] which would correspond to δd$\sim$ 0.03 Å.

In the following, the resonant magnetic scattering is calculated by the double cluster approach. Such an advanced modeling of the magnetic diffraction is required since we found evidence for two inequivalent Ni sites by soft x-ray resonant scattering. As described later we deduce the imbalance between the sites from an anomaly in the energy dependence of the magnetic (1/4, 1/4, 1/4) peak. The modeling in previous studies is based on a single set of scattering factors [4, 57, 278] or considered a simple linear scaling between the scattering at the two sites. For the present work, sets of magnetic form factors $f_{\text{LB, SB}}$ for the LB and SB sites were calculated by R.J. Green and subsequently the azimuthal dependence of the magnetic scattering was modeled on basis of the different form factors.

The concept is illustrated in the following by a simple example of one spin configuration and with non-polarized photons. Consider a collinear period-four antiferromagnetic configuration at sites $A1, B1, A2, B2$. The magnetic structure factor then can be written as

$$S[\mathbf{q}_0 = (1/4,\ 1/4,\ 1/4)] = 1 \cdot f_{A1} + i \cdot f_{B1} - 1 \cdot f_{A2} - i \cdot f_{B2}, \tag{5.1}$$

with f denoting the complex valued, energy dependent, magnetic circular dichroic form factors. Generally, the magnetic circular dichroism response (or f component of the atomic scattering tensor) is obtained as the difference between left and right circular polarized spectral functions, as calculated in the double cluster model. We assume a spin configuration of ($\uparrow\Uparrow\downarrow\Downarrow$), where $\uparrow$ and $\Uparrow$ denote small and large spins, respectively. This corresponds to the nickelates case with SB and LB sites alternating along the $\mathbf{q}_0$ direction. So the structure factor simplifies to

$$S[\mathbf{q}_0 = (1/4,\ 1/4,\ 1/4)] = 2\,(f_{SB} + i \cdot f_{LB}) \tag{5.2}$$

Further, we reintroduce the dependence on the energy ω, but neglect polarization effects for simplicity. Then the spectral intensity is

$$I(\omega) \propto |f_{SB}(\omega) + i \cdot f_{LB}(\omega)|^2 = (f_{SB,Re} - f_{LB,Im})^2 + (f_{SB,Im} + f_{LB,Re})^2\,. \tag{5.3}$$

An example for δd=0.03 Å with calculated form factors $f(\omega)$ at two sites A, B and the obtained scattered magnetic intensity I (purple curve) is shown in Fig. 5.10.

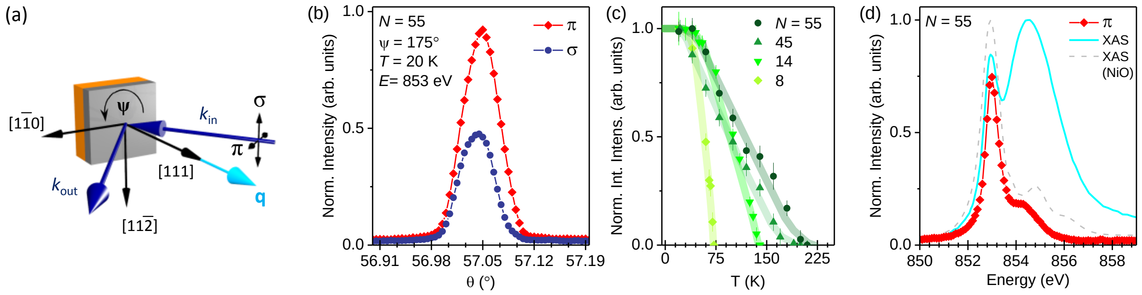

Figure 5.11 Resonant magnetic x-ray scattering. (a) Sketch of the horizontal diffraction geometry used for the magnetic scattering with π or σ polarized x-rays. The sample is rotated around the azimuthal angle ψ, with 0° defined for the crystallographic directions [111] and [1$\bar{1}$0] spanning the scattering plane and positive rotation around the scattering vector $\mathbf{q}$ is right handed. (b) Rocking curves of the antiferromagnetic (1/4, 1/4, 1/4) Bragg peak in resonance to the Ni L_3 edge at $E = 853$ eV for π and σ polarization, respectively. (c) Energy dependence of the magnetic peak intensity close to the Ni L_3 edge. The resonance maximum in the magnetic scattering intensity coincides with the energy of the first peak of the XAS multiplet (light blue curve). For comparison also the XAS of NiO powder is superimposed (gray dashed line). (d) Temperature dependence of the integrated intensity of the antiferromagnetic Bragg peak. The shaded solid lines are guides to the eye.

5.5 Magnetic azimuthal dependence

We now turn to the main experimental results of this chapter and maybe of this thesis. Before discussing the key results of the azimuthal dependence a brief description of the magnetic scattering and its peculiarities such as the energy dependence is given. A detailed description of our method and the concept of modeling the experiment can be found in chapter 3. Further it is pointed out how interfering contributions to the magnetic scattering signal are excluded.

Magnetic Scattering

The REXS experiments were performed with π and σ polarized photons in a horizontal scattering geometry [Fig. 5.11(a)] and energies tuned to the Ni L_3 edge ($2p_{3/2} \rightarrow 3d$). The antiferromagnetic (1/4, 1/4, 1/4) Bragg reflection [Fig. 5.11(b)] is observed with decreasing $T_\mathbf{N}$ for decreasing NdNiO$_3$ layer thickness N [Fig. 5.11(c)], presumably as a consequence of the reduced dimensionality of the spin system, i.e. spin fluctuations diminish the magnetization of a 2D magnetic system more strongly than for 3D magnets. Fig. 5.11(d) shows the energy dependence of the magnetic Bragg intensity at $\mathbf{q}_0$, exhibiting the typical shape reported in previous experiments [4, 12, 281] with a sharp maximum at 853 eV and a broader shoulder at higher energies. For the corresponding XAS spectrum it is known that the sharp feature is due to localized dd-excitations with a lineshape consistent with Ni $3d^8$ configuration (see also the superimposed NiO XAS), whereas the broader peak at higher energies can be interpreted as electron-hole pair excitations across the O $2p$ band, i.e. with contributions from continuum excitations [52]. For the azimuthal dependence of the magnetic scattering rocking curves at the maximum of the resonance at 853 eV were recorded. The rocking curves of the N = 55, 45, 14 and 8 sample are compared in Fig. 5.12(a) and (b).

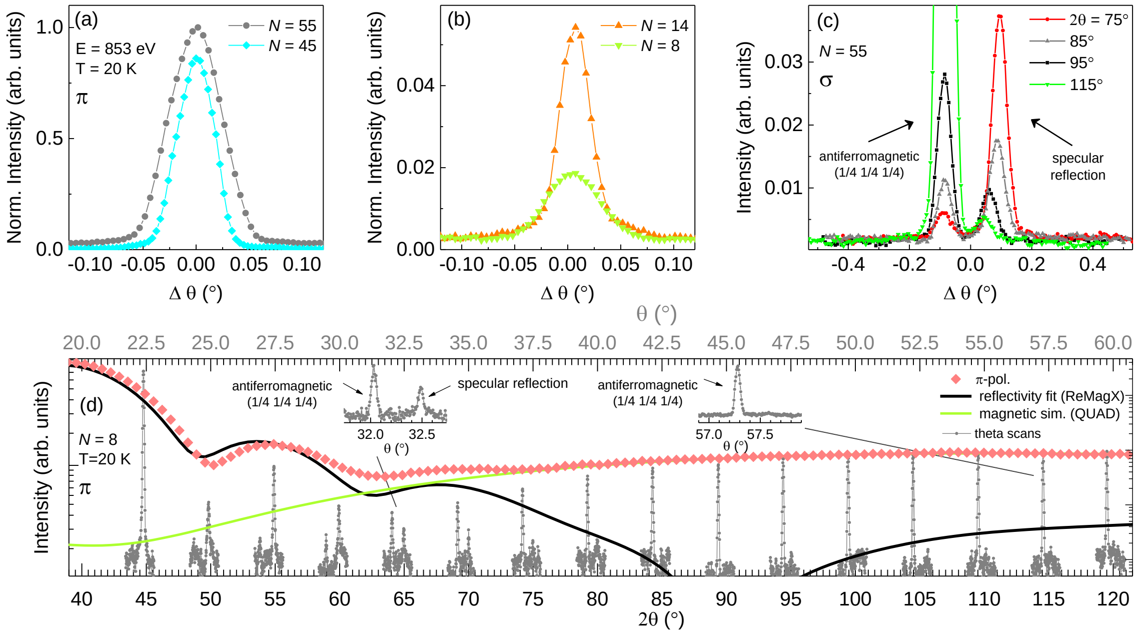

Figure 5.12 Antiferromagnetic Bragg peak and separation of magnetic and structural contributions. (a),(b) Comparison of the antiferromagnetic Bragg reflection at $\mathbf{q}_0 = (1/4, 1/4, 1/4)$ of the $N = 55$, 45, 14, and 8 Ni layers in a rocking curve recorded with a narrow detector slit. The $N = 55$ peak intensity is normalized to unity and the other curves are scaled accordingly. (c) Separation of peaks with magnetic and structural origin at different 2θ angles. The magnetic peak reaches its maximum intensity at $2\theta \sim 115°$ whereas the intensity coming from the specular crystal truncation rod drops to almost zero for high 2θ angles. In consequence, our analysis of rocking curves of the magnetic peak is free from structural contributions. (d) Detailed evolution of the structural and magnetic components. Red symbols are the reflectivity recorded with a wide slit. The solid black line is the ReMagX [184] fit to the structural part of the reflectivity, the solid green line is the QUAD [185] simulation of the magnetic peak contribution. Additionally, rocking curves (gray) were taken with a narrow slit at various 2θ angles. The intensity of the peak at smaller θ follows the magnetic simulation (green line) whereas the intensity of the peak at higher θ follows the fit of the reflectivity (black line). The observation that the green and the black curve, obtained from two independent fits, serve as envelopes for the two peaks in the rocking scans indicates that there is no (or very small) interference between the magnetic and the structural components in our data.

Separation of structural and magnetic contribution

In the θ-2θ reflectivity scans in Fig. 5.7(e)-(l) structural and magnetic contributions overlap. In order to correctly determine the variation of the magnetic scattering intensity as a function of the azimuthal angle ψ it is essential to avoid structural contributions to the detected intensity. This is achieved by using a narrower detector slit than for the reflectivity data shown in Fig. 5.7, decreasing the overall intensity but increasing the experimental resolution. The finer angular acceptance of the detector then allows the magnetic peak to be distinguished from reflectivity (specular reflection) as seen in Fig. 5.12(c). The fact that the two components are separated in the first place can be a consequence of the miscut angle of the $NdGaO_3$ substrate (here between

0.1° and 0.5°). More precisely, the substrate surface and the $NdNiO_3$ crystallographic planes (and therewith the magnetic structure) are tilted with respect to each other. Hence the specular reflection and the magnetic (1/4, 1/4, 1/4) rod do not fully coincide and the two peaks can be observed separately in a rocking curve. Furthermore, the intensity of specular reflection strongly decreases for high 2θ values and almost drops to zero at $2\theta \sim 115°$ where the intensity of the magnetic peak is strongest. As a consequence, the structural contribution is negligible in the integrated intensities of the rocking curves at $\mathbf{q}_0 = (1/4, 1/4, 1/4)$. Finally, it is pointed out that also there are no (or very weak) interference effects between the specular reflection and the magnetic peak, as evident from Fig. 5.12(d) and moreover the Brewster angle condition at $2\theta \sim 90°$ has no (or very small) influence on the magnetic signal [Fig. 5.12(d)].

Crossover between non-collinear and collinear spin structures

The intensity of magnetic scattering depends on the relative orientation between the magnetic moments and the polarization of the incoming light [186]. A rotation around the azimuthal angle ψ systematically varies this relative orientation and the ψ-dependence of the scattering for the $\boldsymbol{\pi} \equiv I_{\pi\pi} + I_{\pi\sigma}$ and $\boldsymbol{\sigma} \equiv I_{\sigma\pi}$ channels can be modeled following the formalisms described in refs. [4, 183]. Our results together with the model fits are summarized in Fig. 5.13. Panel 5.13(a) shows as reference the simulated $\boldsymbol{\pi}$ and $\boldsymbol{\sigma}$ intensities for the orthogonal spiral of bulk-like $NdNiO_3$ [Fig. 5.13(g)], as established in Ref. [12]. The shaded area corresponds to a breathing distortion with δd ranging from 0 to 0.037 Å (Ref. [64]). Its relevance will be discussed below. Two characteristic features of the azimuthal dependence are the nodes at $\psi = 90°$ and 270° and the maxima of $\boldsymbol{\pi}$ and minima of $\boldsymbol{\sigma}$ at $\psi = 0°$ and 180°. The simulated curves for collinear spin order along the [111] direction (dashed lines) predict a constant scattering signal as a function of ψ for our measurement geometry. The experimental data of the $N = 55$ sample in Fig. 5.13(b) show a shift of the first node to $\psi = 60°$ with different $\boldsymbol{\pi}$ and $\boldsymbol{\sigma}$ intensities while a crossing of $\boldsymbol{\pi}$ and $\boldsymbol{\sigma}$ occurs at the second node (240°). From our model fits we find that (i) a shift of the whole pattern in ψ is initiated by a spiraling of a spin sublattice within the (111) plane and (ii) the crossing and separation of the nodes comes from spin reorientation out of the (111) plane [Fig. 5.13(h), orange spins]. The full set of numerical values for the obtained spin angles can be found in the Supplementary Information. For the sample with $N = 45$ [Fig. 5.13(c),(i)] the entire azimuthal pattern is shifted to slightly lower ψ angles as the second spin sublattice spirals further within the (111) plane. Notable changes occur for the $N = 14$ sample, with a strongly reduced overall modulation amplitude of $\boldsymbol{\pi}$ and $\boldsymbol{\sigma}$ and the second spin sublattice increasingly misaligned to the (111) planes. For the thinnest sample with $N = 8$ the azimuthal dependence has drastically changed such that the amplitude of the modulation with ψ is almost zero. [Fig. 5.13(e)]. The symmetry of the modulation is a signature of collinear spin arrangement and the small modulation amplitude is indicative of an alignment close to the [111] direction [Fig. 5.13(k)]. Alternative model fits are discussed later in the text, however, we emphasize that the central statement of a change of the spin configuration from non-collinear to collinear is reproduced in all models.

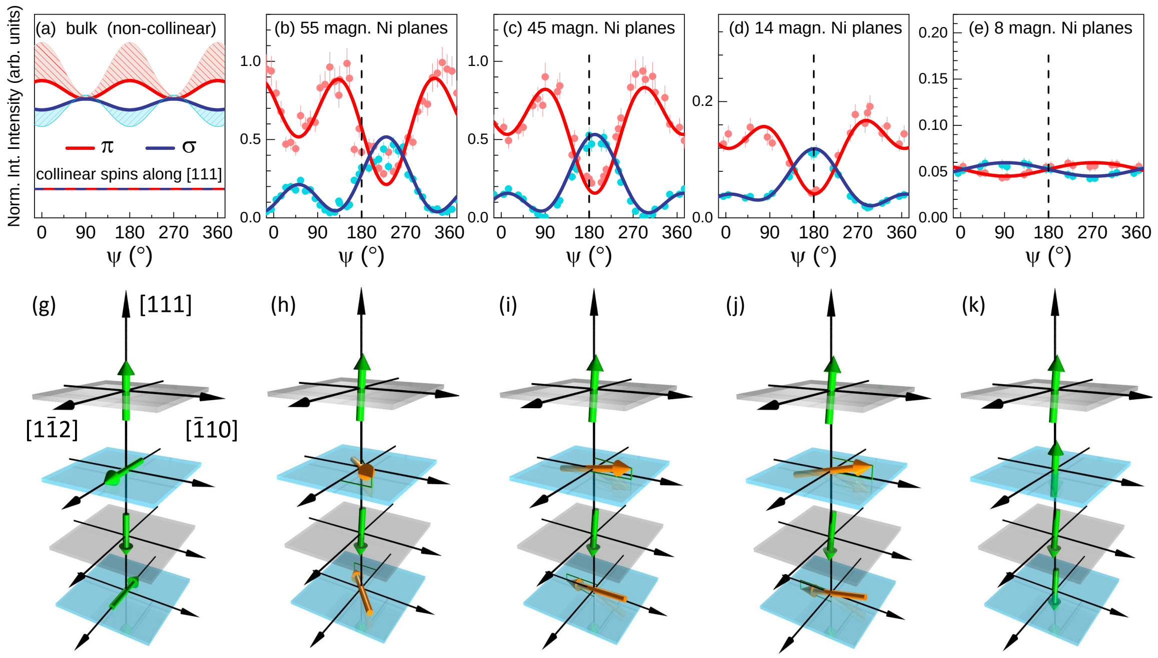

Figure 5.13 Crossover from non-collinear (↑→↓←) to collinear (↑↑↓↓) spin structures by truncation along the [111] direction. (a) Simulated dependence of the magnetic scattering on the azimuthal angle ψ for the spiral bulk model [12] with breathing distortion δd ranging from 0 (solid lines) to 0.037 Å (shaded area). The dashed lines (bottom) simulate spins entirely collinear along the [111] direction yielding no modulation with ψ in our scattering geometry. All curves are shown on an arbitrary intensity scale. (b)-(e) Normalized experimental data at $T = 20$ K and $E = 853$ eV of the $N = 55$, 45, 14, and 8 Ni samples. Solid lines are the fits from the model calculations. (g)-(k) Cartoons of the spin orientation in adjacent Ni planes. (g) is the bulk spiral and (h)-(k) show the evolution from non-collinear to collinear as obtained from the model fits in (b)-(e). For decreasing NdNiO$_3$ thickness the spins (orange) in the second and fourth planes spiral around the [111] axis and exhibit a small out-of plane component. (k) Spins in slabs truncated to 8 Ni layers are collinear (↑↑↓↓) but pointing slightly away from the [111] axis.

Tunable magnetic moments in the Ni sublattices

In addition to the changes in the magnetic moment orientation the Ni magnetic moment amplitudes are extracted from the azimuthal dependences of Fig. 5.13. Contrary to previous REXS experiments [4,12,57] a systematic anomaly in the energy dependence of the (1/4, 1/4, 1/4) peak for particular ψ angles is observed, reflected in a non-constant $\boldsymbol{\pi}/\boldsymbol{\sigma}$ ratio across the L_3 energy range [Fig. 5.14(a),(b) and insets]. We identify the anomaly as the unique signature of scattering from two inequivalent Ni sites [70,72] with distinct magnetic scattering tensors, which requires an advanced modeling of the magnetic form factors $f_{\mathrm{LB,\,SB}}$ of the LB and SB sites. To this end, the double cluster model [13] relates the magnitude δd of the NiO$_6$ breathing distortion with the magnetic moment magnitudes in the two Ni sublattices. The fits in Fig. 5.13(b),(c) yield $\delta d = 0.041$ Å for the $N = 55$ and 45 sample which corresponds to magnetic moments of $m_1 = 0.80\ \mu_B$ and $m_2 = 1.44\ \mu_B$ for the SB and LB sites, respectively [13]. The fits for the thinner NdNiO$_3$ slabs [Fig. 5.13(d),(e)] yield a reduction of the breathing distortion with decreasing N, that is $\delta d = 0.025$ Å

Table 5.2 Fit parameters in the form factor corrected model. Summary of parameters obtained from the form factor corrected model fits illustrated in Fig. 5.13. Θ is the angle between the spin vector and the [111] axis, Φ the angle to the $[11\bar{2}]$ axis (right-handed system). Indices 1, 2 indicate the first and second spin of the period-4 order, the remaining two spins are the corresponding negative vectors. For comparison the parameters of bulk $NdNiO_3$ (refs. [12, 64]) are listed. The errors of $\Theta_{1,2}, \Phi_{1,2}$, and δd are interdependent and estimated to lie between 3° and 5° for Θ and Φ, and ~ 0.002 Å for δd as evaluated from similar least χ^2 values of the fits.

sample	Θ_1 (°)	Φ_1 (°)	Θ_2 (°)	Φ_2 (°)	δd (Å)	χ^2
$N = 55$	5	176	80	39	0.041	1.19E-2
$N = 45$	6	175	76	78	0.042	2.14E-2
$N = 14$	9	179	73	87	0.019	6.81E-4
$N = 8$	8	177	5	178	0.009	8.69E-5
bulk $NdNiO_3$	0	180	90	0	0.037	–

($m_1 = 0.96\ \mu_B$, $m_2 = 1.28\ \mu_B$), and $\delta d = 0.002$ Å ($m_1 = 1.10\ \mu_B$, $m_2 = 1.14\ \mu_B$) for $N = 14$ and 8, respectively. The equalization of the moment magnitudes for $N = 8$ is in accordance with the absence of the energy scan anomaly in Fig. 5.14(c) and indicates the presence of only one crystallographic Ni site.

This is further supported by STEM ABF oxygen mapping [273] which reveals a full structural pinning of the NiO_6 octahedral network to the confining $NdGaO_3$ layers for $N = 8$, whereas subtle relaxations in the Ni-O-Ni bond angles are observed for the thick $N = 55$ film (see Supplementary Information). Hence the orthorhombic $NdGaO_3$ symmetry can be imposed on thin $NdNiO_3$ slabs and hamper the emergence of the monoclinic breathing distortion at low temperatures, resulting in antiferromagnetic order with equivalent Ni moment sizes. Presumably, this structural pinning is particularly strong due to the enhanced octahedral interconnectivity of the [111] interfaces [103, 107]. It is emphasized that the subtle change of Ni-O-Ni bond angles ($\sim 2°$) is very likely not responsible for the drastic change from non-collinear to collinear spin configurations, as indicated by the first-principles calculations (see below) which qualitatively yield the same results for cubic and orthorhombic symmetries, i.e. for much stronger changes of bond angles.

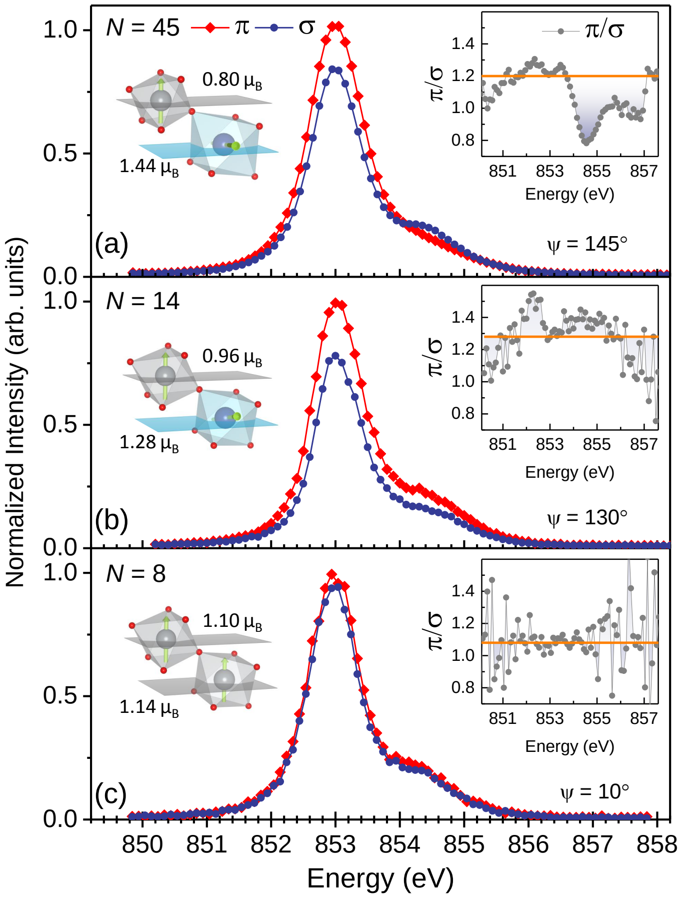

Figure 5.14 **Energy dependence of magnetic scattering and tuning of magnetic moments by structural pinning.** (a)-(c) Constant-**q** energy scans of the antiferromagnetic (1/4, 1/4, 1/4) peak with π or σ polarized x-rays at $T = 20$ K. (a),(b) The $N = 45$ and 14 samples show a variation of the $\boldsymbol{\pi}/\boldsymbol{\sigma}$ ratio as a function of the energy (see right insets), indicative of the monoclinic NiO_6 breathing distortion and two inequivalent magnetic form factors at the SB and LB Ni sites. The absolute values of the magnetic moments (left insets) can be extracted from a form factor corrected fit to the azimuthal dependence in combination with a double cluster calculation [13] (the error bar is ± 0.08 μ_B). (c) The ultra-thin $N = 8$ sample does not exhibit the anomaly, suggesting a single set of magnetic form factors and a $NdNiO_3$ crystal structure strongly pinned to the confining orthorhombic $NdGaO_3$, suppressing the NiO_6 ground state breathing distortion.

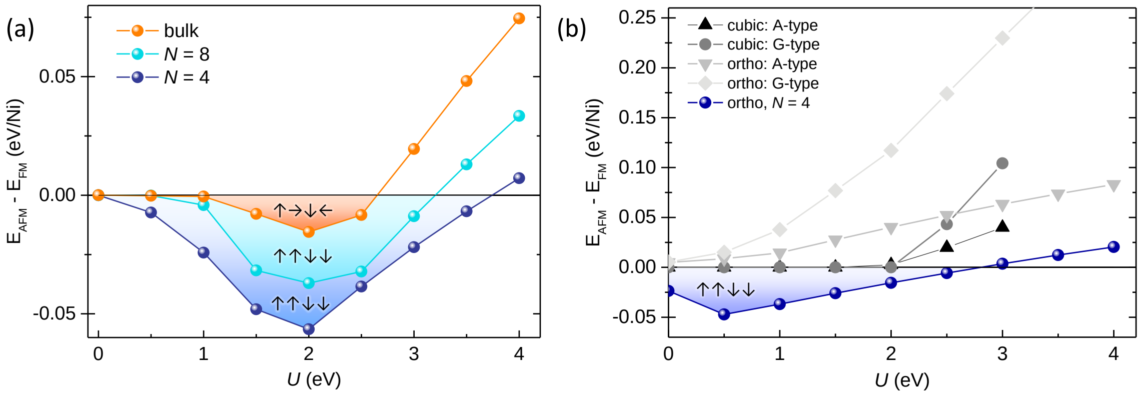

Figure 5.15 DFT magnetic ground state. (a) Comparison of the ground state energies of different antiferromagnetic (E_{AFM}) and ferromagnetic configurations (E_{FM}). Calculations in the standard cubic unit cell always result in a ferromagnetically ordered ground state (see Supplementary Information), contrary to experimental findings in nickelates. Allowing for further symmetry breaking by calculating in larger supercells with possible non-collinear spins yields new antiferromagnetic minima in the energy landscape for a distinctive range of the effective U parameter. In case of an unrestricted $NdNiO_3$ crystal structure (bulk), the antiferromagnetic minimum (orange shaded area) corresponds to the orthogonal (↑→↓←) spiral, consistent with refs. [12, 57] and closely similar to the model fits of the $N = 55$ and 45 azimuthal dependencies. In case of $NdNiO_3$-$NdGaO_3$ slabs truncated along the [111] direction ($N = 8$, 4), the orthogonal spiral is not stable and the spin configuration converges to the collinear period-four (↑↑↓↓) order (light blue and blue shaded area). (b) Comparing the total energies of typical antiferromagnetic configurations (A-type and G-type) with the corresponding ferromagnetic state, for cubic and orthorhombic $NdNiO_3$ structures, respectively (black and gray curves). The ferromagnetic ground state is favored over the antiferromagnetic one for the entire range of the effective U. A calculation in the larger supercell in the [111] reference frame yields a minimum for the antiferromagnetic (↑↑↓↓) state for $N = 4$ Ni planes of an orthorhombic $NdNiO_3$ structure (blue curve).

5.6 Density functional theory calculations

Slabs with variable thickness and truncation along specific crystallographic directions represent an interesting new testing ground for *ab-initio* theories. Motivated by the experimentally observed crossover between collinear and spiral magnetism, Z. Zhong and P. Hansmann (MPI-FKF) have performed DFT calculations with an on-site Hubbard U for fully relaxed cubic and orthorhombic structures [Fig. 5.15(a),(b)]. A comparison of the ground state energies of collinear, non-collinear, ferromagnetic, and antiferromagnetic configurations yields (i) a confirmation of the antiferromagnetic (↑→↓←) spiral as the lowest energy state in bulk $NdNiO_3$ (refs. [12, 57]) within a distinctive parameter range of the effective U (orange shaded area in Fig. 5.15(a)). (ii) Remarkably, the non-collinear orthogonal state becomes unstable for [111] directional truncation of $NdNiO_3$ with $N = 8$ Ni layers or less and the collinear antiferromagnetic (↑↑↓↓) configuration is found to be the ground state (light blue and blue shaded area in Fig. 5.15(a)).

In more detail, the calculations were performed with the VASP (Vienna ab initio simulation package) code [284] using the generalized gradient approximation GGA-

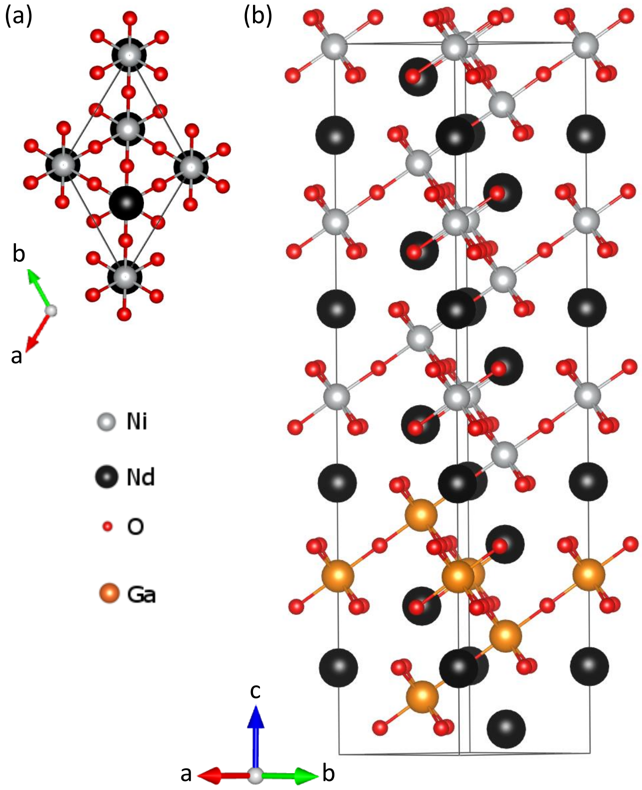

Figure 5.16 DFT supercell for [111] oriented nickelate heterostructures. (a) Top-view of the $NdNiO_3$-$NdGaO_3$ supercell. The cell is of triclinic *P1* symmetry and the a and b directions are indicated. (b) Side-view of the supercell with (111) planes of Ni or Ga stacked along the c axis, which is denoted as $(Ni)_N$-$(Ga)_{12-N}$. As an example the $N = 8$ case is shown.

PBE functional [285] for electronic exchange and correlation on fully relaxed structures of cubic symmetry. For specific cases also the corresponding $GdFeO_3$-type distorted structures (i.e. orthorhombic symmetry) were investigated and it was confirmed that the differences from the cubic case are non-significant [Fig. 5.15]. To stabilize magnetic order in the ground state in GGA+U calculations various values of Hubbard U were employed. Then total energies were compared for the symmetry broken phase to determine the ground state. The resulting magnetic configurations of the cubic $1 \times 1 \times 1$ and the orthorhombic $\sqrt{2} \times \sqrt{2} \times 2$ geometry are shown in Fig. 5.15(b) (black and gray curves). Here, the magnetic order is restricted to collinear arrangements and the resulting ground state is always ferromagnetic, which is in agreement with previous calculations [82] but in contrast to all experimental studies on nickelates.

The capturing of possible period-four non-collinear magnetic order by a direct upscaling of the supercell would make the calculation extremely expensive. However, the intrinsic symmetry of the $\mathbf{q}_0$=(1/4, 1/4, 1/4) magnetism in nickelates allows for setting up a smaller magnetic supercell within the [111] reference frame. Ferromagnetic planes are stacked along the [111] direction with the magnetic Ni sites commensurate to the $NdNiO_3$ crystal structure, and the relative spin orientation between adjacent planes is allowed to be arbitrary. A $NdNiO_3$-$NdGaO_3$ supercell is set up which and denoted as $(Ni)_N$-$(Ga)_{12-N}$, with N defining the number of subsequent Ni planes along the [111] direction and $12 - N$ the number of Ga planes [Fig. 5.16]. Since the structure is repeated periodically, $N = 12$ corresponds to bulk $NdNiO_3$ and $N < 12$ are heterostructures with $NdNiO_3$-$NdGaO_3$ interfaces. For bulk $NdNiO_3$ it is found that a (↑→↓←) spiral can be stabilized for a certain range of U values (compare orange curve in Fig. 4 of the main text). For decreasing values of N an increasing tendency to stabilize into the (↑↑↓↓) arrangement is observed and for $N = 8$ and less the ground state is the collinear (↑↑↓↓) configuration, for cubic and orthorhombic structures (cyan and dark blue curves in Fig. 5.15(a) and the blue curve in Fig. 5.15(b)).

The results of the first-principles calculations thus reproduce the slab-thickness-induced crossover from collinear to spiral magnetism, in excellent agreement with our experimental observations (Fig. 5.13). Moreover, the calculations indicate that the spin-orbit coupling is negligible, i.e. the magneto-crystalline anisotropy energy cannot be the main driver of the collinear order in $N = 8$, 4 heterostructures. The minor role of the spin orbit coupling comes as no surprise given that the predominant orbital character around the Fermi level is non-magnetic with e_g-symmetry. Rather, the truncation of the exchange path appears to be the dominant factor, upsetting the subtle balance between nearest- and next-nearest-neighbor interactions in the direction of the magnetic propagation vector $\mathbf{q}_0$.

Alternative magnetic model fits and further discussion

Fitting the azimuthal dependence doeas not always give a unique solution, i.e. different spin orientations and different moment magnitudes can yield the same pattern. To account for this we have defined the following strategy for the fitting procedure: first, we use the parameters Θ, Φ, and δd of the orthogonal (↑→↓←) bulk model [12, 57] (Table 5.2) as starting values and vary the parameters until convergence with the experimental azimuthal dependence is reached. The results of 'free fit 1' are summarized in Table 5.2 and illustrated in Fig. 5.13(h)-(k). Second, we use a large set of random starting values and let the fit converge. Most sets of starting parameters yield the same result as 'free fit 1' Table 5.2. For the $N = 55$ and 14 data there is one alternative solution ('free fit 2') with a similarly small least χ^2 (Table 5.3). Note that the 45 Ni sample behaves qualitatively similar to the 55 Ni layers, hence it will not be discussed further. For the $N = 8$ dataset all fits converge to 'free fit 1', regardless of the starting parameters. Third, we fix $|\mathbf{m}_1| = |\mathbf{m}_2|$, which corresponds to previous works considering only equivalent magnetic Ni sites [4, 12, 57] or the presence of two equally populated domains with $|\mathbf{m}_1| > |\mathbf{m}_2|$ and $|\mathbf{m}_1| < |\mathbf{m}_2|$, respectively. In this type of modeling the form factor correction is obsolete. The obtained fit parameters are summarized in Table 5.4. Fourth, we use the same modeling tool as the authors Frano *et al.* in Ref. [4] (no form factor correction) but allow a linear scaling factor between the scattering from two inequivalent Ni sites. Results are summarized as 'free fit' 1 and 2 in Table 5.4.

As the final step of our strategy we evaluate the four approaches against each other. Starting with 'free fit' 1 and 2 from Table 5.4 we notice the close similarity of the angles Θ and Φ as compared to 'free fit' 1 and 2 from the form factor corrected fits in Tables 5.2 and 5.3, illustrating the robustness of the solutions concerning the angular orientation of the spins. The $|\mathbf{m}_2|/|\mathbf{m}_1|$ ratio of 4.12 and 1.95, however, appears to be largely overestimated, considering that the highly monoclinic $HoNiO_3$ exhibits a $|\mathbf{m}_2|/|\mathbf{m}_1|$ ratio of only 2.33 (Ref. [87]). The $|\mathbf{m}_1| = |\mathbf{m}_2|$ solution of Table 5.4 is also

Table 5.3 Alternative fit parameters in the form factor corrected model. Starting from a random set of parameters Θ, Φ and δd, the fit either converges to "free fit 1" (Table 5.2) or "free fit 2". For the sample having 8 Ni layers no alternative spin orientation is listed since all fits converged to the collinear solution (within the error bars) shown in Table 5.2 .

free fit 2	Θ_1 (°)	Φ_1 (°)	Θ_2 (°)	Φ_2 (°)	δd (Å)	χ^2
$N = 55$	17	53	80	39	0.049	1.19E-2
$N = 14$	41	-113	113	-94	0.025	8.89E-4

Table 5.4 Alternative fit parameters without form factor correction. Model fit without form factor correction in analogy to Ref. [4]. First the magnitudes of the magnetic sublattices are fixed to be identical $|\mathbf{m}_1| = |\mathbf{m}_2|$, then a simple scaling factor for the magnetic scattering at the two different Ni sites is allowed ("free fit 1,2").

$\|\mathbf{m}_1\| = \|\mathbf{m}_2\|$	Θ_1 (°)	Φ_1 (°)	Θ_2 (°)	Φ_2 (°)	$\|\mathbf{m}_2\|/\|\mathbf{m}_1\|$	χ^2
$N = 55$	113	-138	92	37	1	1.13E-2
$N = 14$	46	98	94	83	1	5.23E-4
free fit 1	Θ_1 (°)	Φ_1 (°)	Θ_2 (°)	Φ_2 (°)	$\|\mathbf{m}_2\|/\|\mathbf{m}_1\|$	χ^2
$N = 55$	6	174	80	40	4.12	1.13E-2
$N = 14$	9	179	73	87	1.95	6.80E-4
free fit 2	Θ_1 (°)	Φ_1 (°)	Θ_2 (°)	Φ_2 (°)	$\|\mathbf{m}_2\|/\|\mathbf{m}_1\|$	χ^2
$N = 55$	17	53	81	39	4.42	1.12E-2
$N = 14$	41	-114	113	-95	2.01	7.78E-4

excluded as the energy dependence of the $\boldsymbol{\pi}/\boldsymbol{\sigma}$ ratio in Fig. 5.14(a),(b) indicates the presence of two significantly different Ni scattering sites. Remaining are 'free fit' 1 and 2 in the form factor corrected model (Table 5.2 and Table 5.3) with similar χ^2 values. However, regarding the spin angles and the δd of bulk-like $NdNiO_3$ (0.037 Å), the solution with the parameters of Table 5.2 are closer matching and moreover provide an almost gradual evolution from (↑→↓←) to (↑↑↓↓) with increasing [111] truncation. The slightly higher value of $\delta d = 0.041$ Å in Table 5.2 is in agreement with Ref. [103] which locates [111] oriented $NdNiO_3$ films at the position of $SmNiO_3$ in the bulk nickelate phase diagram.

None of our fits converged to a spin configuration with one magnetic sublattice carrying zero moment, corresponding to the (↑ 0 ↓ 0) model, which is widely used as starting point for theory calculations and has been discussed as one possible solution of the neutron powder diffraction refinements [11,69]. We always find two distinct magnetic sublattices with both moments $\mathbf{m}_1$, $\mathbf{m}_2$ being non-zero. This is particularly evident in the $N = 14$ case of Fig. 5.13 where an asymmetry in the modulation amplitude with respect to ψ smaller and larger than 180° is present. Such an asymmetry can only be generated from two unequal but non-zero sublattices. However, we note that for a fully collinear spin arrangement along the [111], our data analysis is not sensitive to the magnitude of the second spin lattice. The fit of the $N = 8$ data exhibits two slightly different sublattices which are effectively collinear within the error bar. Considering the systematics in the reduction of the breathing distortion from $N = 55$ to 14 and the tendency of an equalization of moments, we argue that for the $N = 8$ case $|\mathbf{m}_1| \approx |\mathbf{m}_2| \approx 1.1\ \mu_B$ is valid (within the error bar), which implies a configuration of $(\uparrow\uparrow\downarrow\downarrow)$ instead of $(\uparrow 0 \downarrow 0)$.

In addition we point out that the $(\uparrow 0 \downarrow 0)$ configuration corresponds to the extreme limit of the bond disproportionation picture. Recent bond disproportionation theories [52,81] based on the concept of a negative charge transfer gap in the nickelates [14] use the Ni $(d^8)_{S=1}$ configuration with a ligand hole $\underline{L}$ at the oxygen as starting configuration in the metallic phase, instead of the classical Ni $(d^7)_{S=1/2}$ electron configuration, and the transition to the insulating phase is described in terms of the disproportionation

$$2\,(\mathrm{Ni}\,d^8\underline{L})_{S=1/2} \rightarrow \mathrm{Ni}\,(d^8\underline{L}^2)_{S=0} + \mathrm{Ni}\,(d^8)_{S=1}, \tag{5.4}$$

where S is the total spin. The NiO_6 octahedron with the two ligand holes around the central Ni is the collapsed SB octahedron while the other octahedron expands accordingly with little net effect on the total volume. The $S = 0$ state is a result of the strong antiferromagnetic exchange interaction between the two short bond length O $2p$ holes with the two Ni $3d$ holes, or in other words: one set of octahedra is fully screened by the two ligand holes whereas the other set carries the full moment. According to the double cluster calculation [13], however, a breathing distortion of $\delta \mathrm{d} \gg 0.2$ Å would be required for a disproportionation with $S_{SB} \sim 0$ and $S_{LB} \sim 1$. Considering a magnitude of $\delta \mathrm{d} = 0.048$ Å for the strongly distorted $HoNiO_3$, less extreme values for S_{SB} and S_{LB} can be expected, which implies that both magnetic sublattices carry a magnetic moment. In particular, we argue that for the $N = 8$ case the breathing distortion is hampered due to the structural pinning of the oxygen sites, which yields similar magnetic moment sizes in both sublattices.

Further it is mentioned that in principal an additional domain with exchanged SB and LB indices (i.e. exchanged small and large moment magnitudes) can be included in our form factor corrected model. However, we find experimentally that the smaller magnetic moment of the non-collinear spiral is always aligned along the [111] axis whereas the larger moment lies within the (111) plane. Our modeling includes typical 180° antiferromagnetic domains within a (111) plane, i.e. the resulting scattered intensity is always averaged. In the case of the bulk orthogonal spiral for example, the averaging is over the configurations $(\uparrow\rightarrow\downarrow\leftarrow)$, $(\uparrow\leftarrow\downarrow\rightarrow)$, $(\downarrow\rightarrow\uparrow\leftarrow)$, and $(\downarrow\leftarrow\uparrow\rightarrow)$.

Interestingly, the electrical transport of the $N = 8$ sample shows a low electrical conductivity at high temperatures and insulating properties at low temperatures [Fig. 5.5(a)], despite our experiments indicate the absence of the breathing distortion. The insulating behavior can be the consequence of the $NdNiO_3$-$NdGaO_3$ interface (i.e. the intermixing with Ga ions in the outer layers affects and dominates the whole transport in thin slabs), or the generally enhanced effective mass of charge carriers in 2D-like systems. Moreover, it is not fully clear whether the $N = 8$ sample is insulating when measured on a local scale only. Possible inhomogeneities or other defects on a macroscopic scale can strongly reduce the effective conductivity of a very thin $NdNiO_3$ layer, when measured in van der Pauw configuration on a 5 mm × 5 mm scale. Hence, conductivity data obtained from a probe such as optical spectroscopy or local tunneling spectroscopy would be required to finally characterize the $N = 8$ slab as metallic or insulating.

5.7 Conclusion and outlook

In summary, we have introduced atomically thin slabs embedded in a non-magnetic matrix as a novel platform for the investigation of complex magnetic ordering phenomena. External influences such as charge transfer or orbital polarization obscuring the investigation of the intrinsic magnetic properties are prevented, rendering the slabs an elementary magnetic model system where the effective magnetic interactions and the relative moment magnitudes can be controlled and studied.

The observation of non-collinear and collinear spin order within the same material system has profound implications on theories attempting to establish a uniform picture of the complex magnetism in rare-earth nickelates. Possible model spin Hamiltonians will have to consider the crossover from the spiral state to the unusual (↑↑↓↓) state not as a function of crystal lattice distortions and concomitant orbital order as in the case of ternary manganites RMnO$_3$ with R=Tb, Ho (Ref. [286]) but as a function of the truncation along the magnetic wave vector $\mathbf{q}_0$. Experimentally, the magnetic excitation spectra of collinear and non-collinear order, in particular the number and the dispersion of magnon branches [9] can be explored by techniques such as resonant inelastic x-ray scattering (RIXS). A combination of the collinear (↑↑↓↓) ground state with recent findings of a non-equilibrium ferroelectric polarization in [111] NdNiO$_3$ which is stabilized by a specific octahedral tilt pattern of a LaAlO$_3$ substrate [117] might complete the long-standing quest for multiferroicity in the rare-earth nickelates. Such a state has been theoretically predicted several times [118], however conclusive experimental evidence has remained elusive so far.

Further, our analysis has made it possible to quantify and distinguish two magnetic sublattices both with non-zero moments. It is the first time that distinct moment magnitudes have been determined for NdNiO$_3$. These results are incompatible with theories restricted to (↑ 0 ↓ 0) configurations [78, 267] and provide new, specific indicators for testing future models.

Finally, it is emphasized that the concept of truncation along the $\mathbf{q}_0$ ordering vector direction has a yet unexplored potential of controlling a material's spin configuration in other transition metal oxides and in future functional devices. Targeted synthesis of model systems and synergistic application of polarized RXS and *ab-initio* theory thus provide new perspectives for research on complex magnetism in TMO heterostructures.

Appendix A

Lattice constants

Table A.1 Summary of relevant bulk nickelate lattice constants in Å at T=300 K. The pseudocubic lattice constant is a_{pc} and a, b, c are the lattice constants of the unit cell of symmetry indicated in the last column. Rhombohedral corresponds to space group $R\bar{3}c$, orthorhombic to $Pbnm$ and tetragonal to $I4/mmm$. The values are from Refs. [64,88,148,248].

nickelate	a_{pc}	a	b	c	symmetry
$LaNiO_3$	3.837	5.4573	-	13.1462	rhombohedral
$PrNiO_3$	3.820	5.4193	5.3801	7.6263	orthorhombic
$NdNiO_3$	3.807	5.3891	5.3816	7.6101	orthorhombic
$SmNiO_3$	3.796	5.3283	5.4374	7.5675	orthorhombic
$YNiO_3$	3.662	5.1792	5.5104	7.4106	orthorhombic

Table A.2 Selection of common oxide substrates with lattice constants given in Å. The parameters are from Ref. [287].

substrate	a_{pc}	a	b	c	
$NdCaAlO_4$	3.685	3.685	3.685	12.120	tetragonal
$YAlO_3$	3.708	5.180	5.310	7.350	orthorhombic
$LaSrAlO_4$	3.756	3.756	3.756	12.626	tetragonal
$LaAlO_3$	3.789	5.365	5.365	13.111	rhombohedral
$NdGaO_3$	3.858	5.428	5.498	7.709	orthorhombic
LSAT	3.868	3.868	3.868	3.868	cubic
$SrTiO_3$	3.905	3.905	3.905	3.905	cubic
$KTaO_3$	3.989	3.989	3.989	3.989	cubic

Appendix B

Raman intensities

Table B.1 Raman intensities of different backscattering configurations. The definitions of X, Y, X', Y' are such that X' is 45° offset to the direction of the Ni-O-Ni bonds, which is also the direction of the LSAT substrate edges. From perspective of the *Pbnm* unit cell X' is along the a axis. The letters $a - f$ correspond to nonzero elements of the Raman tensors as given in chapter 3.

symmetry	$X'X'$	$Y'Y'$	$X'Y'$	XX	XY
$Pbnm$					
A_g	a^2	0	$b^2 \approx a^2$	$\frac{1}{4}(a+b)^2$	$\frac{1}{4}(a-b)^2 \approx 0$
B_{1g}	0	d^2	0	d^2	0
$P2_1/n$					
A_g	a^2	0	$b^2 \approx a^2$	$\frac{1}{4}(a+b)^2$	$\frac{1}{4}(a-b)^2 \approx 0$
B_g	0	f^2	0	f^2	0

Bibliography

[1] H. Hwang, Y. Iwasa, M. Kawasaki, B. Keimer, N. Nagaosa, and Y. Tokura, "Emergent phenomena at oxide interfaces," *Nature Materials*, vol. 11, no. 2, pp. 103–113, 2012.

[2] J. Liu, M. Kargarian, M. Kareev, B. Gray, P. J. Ryan, A. Cruz, N. Tahir, Y.-D. Chuang, J. Guo, J. M. Rondinelli, J. W. Freeland, G. A. Fiete, and J. Chakhalian, "Heterointerface engineered electronic and magnetic phases of NdNiO3 thin films," *Nature Communications*, vol. 4, p. 2714, nov 2013.

[3] S. Catalano, M. Gibert, V. Bisogni, O. E. Peil, F. He, R. Sutarto, M. Viret, P. Zubko, R. Scherwitzl, A. Georges, G. A. Sawatzky, T. Schmitt, and J. M. Triscone, "Electronic transitions in strained SmNiO3 thin films," *APL Materials*, vol. 2, no. 11, pp. 0–7, 2014.

[4] A. Frano, E. Schierle, M. W. Haverkort, Y. Lu, M. Wu, S. Blanco-Canosa, U. Nwankwo, A. V. Boris, P. Wochner, G. Cristiani, H. U. Habermeier, G. Logvenov, V. Hinkov, E. Benckiser, E. Weschke, and B. Keimer, "Orbital Control of Noncollinear Magnetic Order in Nickel Oxide Heterostructures," *Physical Review Letters*, vol. 111, p. 106804, sep 2013.

[5] D. Tenne, A. Bruchhausen, N. D. Lanzillotti-Kimura, A. Fainstein, R. S. Katiyar, A. Cantarero, A. Soukiassian, V. Vaithyanathan, J. H. Haeni, W. Tian, D. G. Schlom, K. J. Choi, D. M. Kim, C. B. Eom, H. P. Sun, X. Q. Pan, Y. L. Li, L. Q. Chen, Q. X. Jia, S. M. Nakhmanson, K. M. Rabe, and X. X. Xi, "Probing Nanoscale Ferroelectricity by Ultraviolet Raman Spectroscopy," *Science*, vol. 313, no. 5793, pp. 1614–1616, 2006.

[6] S. Lee, R. Chen, and L. Balents, "Landau theory of charge and spin ordering in the nickelates," *Physical Review Letters*, vol. 106, no. 1, pp. 7–10, 2011.

[7] G. R. Stewart, "Superconductivity in iron compounds," *Reviews of Modern Physics*, vol. 83, no. 4, 2011.

[8] J. A. Alonso, J. L. García-Muñoz, M. T. Fernández-Díaz, M. A. G. Aranda, M. J. Martínez-Lope, and M. T. Casais, "Charge Disproportionation in RNiO3 Perovskites: Simultaneous Metal-Insulator and Structural Transition in YNiO3," *Physical Review Letters*, vol. 82, pp. 3871–3874, may 1999.

[9] I. R. Buitrago and C. I. Ventura, “Magnetic excitations of perovskite rare-earth nickelates: RNiO3,” *Journal of Magnetism and Magnetic Materials*, vol. 394, pp. 148–154, 2015.

[10] J. L. García-Muñoz, J. Rodríguez-Carvajal, and P. Lacorre, “Sudden Appearance of an Unusual Spin Density Wave At the Metal-Insulator Transition in the Perovskites RNiO 3 (R = Pr, Nd),” *Europhysics Letters (EPL)*, vol. 20, no. 3, pp. 241–247, 1992.

[11] A. Muñoz, J. A. Alonso, M. J. Martínez-Lope, and M. T. Fernández-Díaz, “On the magnetic structure of DyNiO3,” *Journal of Solid State Chemistry*, vol. 182, no. 7, pp. 1982–1989, 2009.

[12] V. Scagnoli, U. Staub, A. M. Mulders, M. Janousch, G. I. Meijer, G. Hammerl, J. M. Tonnerre, and N. Stojic, “Role of magnetic and orbital ordering at the metal-insulator transition in NdNiO3,” *Physical Review B*, vol. 73, no. 10, pp. 1–4, 2006.

[13] R. J. Green, M. W. Haverkort, and G. A. Sawatzky, “Bond disproportionation and dynamical charge fluctuations in the perovskite rare earth nickelates,” vol. 195127, pp. 22–27, 2016.

[14] T. Mizokawa, D. I. Khomskii, and G. a. Sawatzky, “Spin and charge ordering in self-doped Mott insulators,” *Physical Review B*, vol. 61, no. 17, p. 4, 1999.

[15] D. I. Khomskii, *Transition Metal Compounds*. Cambridge: Cambridge University Press, 2014.

[16] M. Imada, A. Fujimori, and Y. Tokura, “Metal-insulator transitions,” *Reviews of Modern Physics*, vol. 70, no. 4, pp. 1039–1263, 1998.

[17] J. van den Brink, G. Khaliullin, and D. Khomskii, “Charge and Orbital Order in Half-Doped Manganites,” *Physical Review Letters*, vol. 83, no. 24, pp. 5118–5121, 1999.

[18] A. Bhattacharya and S. J. May, “Magnetic Oxide Heterostructures,” *Annual Review of Materials Research*, vol. 44, no. 1, pp. 65–90, 2014.

[19] M. Uehara, S. Mori, C. H. Chen, and S. W. Cheong, “Percolative phase separation underlies colossal magnetoresistance in mixed-valent manganites,” *Nature*, vol. 399, pp. 560–563, 1999.

[20] Z. X. Shen and D. S. Dessau, “Electronic structure and photoemission studies of late transition-metal oxides - Mott insulators and high-temperature superconductors,” *Physics Reports*, vol. 253, no. 1-3, pp. 1–162, 1995.

[21] P. W. Anderson, “Antiferromagnetism. Theory of superexchange interaction,” *Physical Review*, vol. 79, no. 2, pp. 350–356, 1950.

[22] J. B. Goodenough, “Theory of the Role of Covalence in the Perovskite-Type Manganites [La, M(II)]MnO3,” *Physical Review*, vol. 100, no. 2, pp. 564–573, 1955.

[23] C. Zener, “Interaction between the d shells in the transition metals,” *Physical Review*, vol. 81, no. 3, pp. 440–444, 1951.

[24] I. Vrejoiu, G. Le Rhun, L. Pintilie, D. Hesse, M. Alexe, and U. Gösele, “Intrinsic Ferroelectric Properties of Strained Tetragonal PbZr0.2Ti0.8O3 Obtained on Layer-by-Layer Grown, Defect-Free Single-Crystalline Films,” *Advanced Materials*, vol. 18, no. 13, pp. 1657–1661, 2006.

[25] R. M. Bozorth, E. F. Tilden, and A. J. Williams, “Anisotropy and Magnetostriction of Some Ferrites,” *Physical Review*, vol. 99, no. 6, pp. 1788–1798, 1955.

[26] T. Kimura, S. Kawamoto, I. Yamada, M. Azuma, M. Takano, and Y. Tokura, “Magnetocapacitance effect in multiferroic BiMnO3,” *Physical Review B*, vol. 67, no. 18, p. 180401, 2003.

[27] S. N. Ruddlesden and P. Popper, “New compounds of the K2NiF4 type,” *Acta Crystallographica*, vol. 10, no. 8, pp. 538–539, 1957.

[28] A. Fujimori, “Electronic structure of metallic oxides: Band-gap closure and valence control,” *Journal of Physics and Chemistry of Solids*, vol. 53, no. 12, pp. 1595–1602, 1992.

[29] J. C. Slater, “Magnetic effects and the Hartree-Fock equation,” *Physical Review*, vol. 82, no. 4, pp. 538–541, 1951.

[30] N. F. Mott, “The transition to the metallic state,” *Philosophical Magazine*, vol. 6, no. 62, pp. 287–309, 1961.

[31] J. Hubbard, “Electron Correlations in Narrow Energy Bands,” *Proceedings of the Royal Society A: Mathematical, Physical and Engineering Sciences*, vol. 276, no. 1365, pp. 238–257, 1963.

[32] A. Fujimori and F. Minami, “Valence-band photoemission and optical absorption in nickel compounds,” *Physical Review B*, vol. 30, no. 2, pp. 957–971, 1984.

[33] J. Zaanen, G. A. Sawatzky, and J. W. Allen, “Band gaps and electronic structure of transition-metal compounds,” *Physical Review Letters*, vol. 55, no. 4, pp. 418–421, 1985.

[34] Y. F. Nie, Y. Zhu, C.-H. Lee, L. F. Kourkoutis, J. a. Mundy, J. Junquera, P. Ghosez, D. J. Baek, S. Sung, X. X. Xi, K. M. Shen, D. a. Muller, and D. G. Schlom, “Atomically precise interfaces from non-stoichiometric deposition,” *Nature Communications*, vol. 5, p. 4530, aug 2014.

[35] P. Zubko, S. Gariglio, M. Gabay, P. Ghosez, and J.-M. Triscone, "Interface Physics in Complex Oxide Heterostructures," *Annual Review of Condensed Matter Physics*, vol. 2, no. 1, pp. 141–165, 2011.

[36] D. G. Schlom, L. Q. Chen, X. Pan, A. Schmehl, and M. A. Zurbuchen, "A thin film approach to engineering functionality into oxides," *Journal of the American Ceramic Society*, vol. 91, no. 8, pp. 2429–2454, 2008.

[37] S. A. Chambers, "Epitaxial growth and properties of doped transition metal and complex oxide films," *Advanced Materials*, vol. 22, no. 2, pp. 219–248, 2010.

[38] Z. Liao, M. Huijben, Z. Zhong, N. Gauquelin, S. Macke, R. J. Green, S. Van Aert, J. Verbeeck, G. Van Tendeloo, K. Held, G. A. Sawatzky, G. Koster, and G. Rijnders, "Controlled lateral anisotropy in correlated manganite heterostructures by interface-engineered oxygen octahedral coupling," *Nature Materials*, vol. 15, no. 4, pp. 425–431, 2016.

[39] D. Kan, R. Aso, R. Sato, M. Haruta, H. Kurata, and Y. Shimakawa, "Tuning magnetic anisotropy by interfacially engineering the oxygen coordination environment in a transition metal oxide," *Nature Materials*, vol. 15, no. April, p. 432, 2016.

[40] N. Reyren, S. Thiel, A. D. Caviglia, L. F. Kourkoutis, G. Hammerl, C. Richter, C. W. Schneider, T. Kopp, A.-S. Rüetschi, D. Jaccard, M. Gabay, D. A. Muller, J.-M. Triscone, and J. Mannhart, "Superconducting Interfaces Between Insulating Oxides," *Science*, vol. 317, no. 5842, pp. 1196–1199, 2007.

[41] G. Herranz, M. Basletić, M. Bibes, C. Carrétéro, E. Tafra, E. Jacquet, K. Bouzehouane, C. Deranlot, A. Hamzić, J. M. Broto, A. Barthélémy, and A. Fert, "High mobility in LaAlO3/SrTiO3 heterostructures: Origin, dimensionality, and perspectives," *Physical Review Letters*, vol. 98, no. 21, pp. 3–6, 2007.

[42] K. S. Takahashi, M. Kawasaki, and Y. Tokura, "Interface ferromagnetism in oxide superlattices of CaMnO3/CaRuO3," *Applied Physics Letters*, vol. 79, no. 9, pp. 1324–1326, 2001.

[43] J. Chakhalian, J. W. Freeland, H. Habermeier, G. Cristiani, G. Khaliullin, M. V. Veenendaal, and B. Keimer, "Orbital Reconstruction and Covalent Bonding at an Oxide Interface," *Science*, vol. 318, no. November, pp. 1114–1117, 2007.

[44] N. Driza, S. Blanco-Canosa, M. Bakr, S. Soltan, M. Khalid, L. Mustafa, K. Kawashima, G. Christiani, H.-U. Habermeier, G. Khaliullin, C. Ulrich, M. Le Tacon, and B. Keimer, "Long-range transfer of electronphonon coupling in oxide superlattices," *Nature Materials*, vol. 11, no. 8, pp. 675–681, 2012.

[45] N. A. Pertsev, A. G. Zembilgotov, and A. K. Tagantsev, "Effect of Mechanical Boundary Conditions on Phase Diagrams of Epitaxial Ferroelectric Thin Films," *Physical Review Letters*, vol. 80, no. 9, pp. 1988–1991, 1998.

[46] T. J. Anderson, S. Ryu, H. Zhou, L. Xie, J. P. Podkaminer, Y. Ma, J. Irwin, X. Q. Pan, M. S. Rzchowski, and C. B. Eom, “Metastable honeycomb SrTiO3/SrIrO3 heterostructures,” *Applied Physics Letters*, vol. 108, no. 15, 2016.

[47] E. Bousquet and A. Cano, “Non-collinear magnetism in multiferroic perovskites,” *Journal of Physics: Condensed Matter*, vol. 28, no. 12, p. 123001, 2016.

[48] J. Chakhalian, A. J. Millis, and J. Rondinelli, “Whither the oxide interface,” *Nature Publishing Group*, vol. 11, no. 2, pp. 92–94, 2012.

[49] J. Chakhalian, J. W. Freeland, A. J. Millis, C. Panagopoulos, and J. M. Rondinelli, “Colloquium : Emergent properties in plane view: Strong correlations at oxide interfaces,” *Reviews of Modern Physics*, vol. 86, no. 4, pp. 1189–1202, 2014.

[50] J. Mannhart and D. G. Schlom, “Oxide interfaces–an opportunity for electronics.,” *Science (New York, N.Y.)*, vol. 327, no. 5973, pp. 1607–1611, 2010.

[51] I. Žutić, J. Fabian, and S. Das Sarma, “Spintronics: Fundamentals and applications,” *Reviews of Modern Physics*, vol. 76, no. 2, pp. 323–410, 2004.

[52] V. Bisogni, S. Catalano, R. J. Green, M. Gibert, R. Scherwitzl, Y. Huang, V. N. Strocov, P. Zubko, S. Balandeh, J.-m. Triscone, G. Sawatzky, and T. Schmitt, “Ground-state oxygen holes and the metal-insulator transition in the negative charge-transfer rare-earth nickelates,” *Nature Communications*, vol. 7, p. 13017, 2016.

[53] A. D. Caviglia, M. Först, R. Scherwitzl, V. Khanna, H. Bromberger, R. Mankowsky, R. Singla, Y.-D. Chuang, W. S. Lee, O. Krupin, W. F. Schlotter, J. J. Turner, G. L. Dakovski, M. P. Minitti, J. Robinson, V. Scagnoli, S. B. Wilkins, S. A. Cavill, M. Gibert, S. Gariglio, P. Zubko, J.-M. Triscone, J. P. Hill, S. S. Dhesi, and A. Cavalleri, “Photoinduced melting ofmagnetic order in the correlated electron insulator NdNiO3,” *Physical Review B*, vol. 88, p. 220401, dec 2013.

[54] M. Hepting, M. Minola, A. Frano, G. Cristiani, G. Logvenov, E. Schierle, M. Wu, M. Bluschke, E. Weschke, H. U. Habermeier, E. Benckiser, M. Le Tacon, and B. Keimer, “Tunable charge and spin order in PrNiO3 thin films and superlattices,” *Physical Review Letters*, vol. 113, no. 22, 2014.

[55] M. Hepting, D. Kukuruznyak, E. Benckiser, M. Le Tacon, and B. Keimer, “Raman light scattering on ultra-thin films of LaNiO3 under compressive strain,” *Physica B: Condensed Matter*, vol. 460, pp. 196–198, 2015.

[56] S. Lee, R. Chen, and L. Balents, “Metal-insulator transition in a two-band model for the perovskite nickelates,” *Physical Review B*, vol. 84, no. 16, pp. 1–18, 2011.

[57] V. Scagnoli, U. Staub, Y. Bodenthin, M. García-Fernández, A. M. Mulders, G. I. Meijer, and G. Hammerl, “Induced noncollinear magnetic order of Nd3+ in

NdNiO3 observed by resonant soft x-ray diffraction," *Physical Review B*, vol. 77, no. 11, pp. 14–17, 2008.

[58] L. Medarde, "Structural, magnetic and electronic properties of RNiO3 perovskites (R = rare earth)," *J. Phys.: Condens. Matter*, vol. 1679, pp. 1679–1707, 1997.

[59] G. Catalan, "Progress in perovskite nickelate research," *Phase Transitions*, vol. 81, no. 7-8, pp. 729–749, 2008.

[60] S. Middey, D. Meyers, D. Doennig, M. Kareev, X. Liu, Y. Cao, Z. Yang, J. Shi, L. Gu, P. J. Ryan, R. Pentcheva, J. W. Freeland, and J. Chakhalian, "Mott Electrons in an Artificial Graphene-like Crystal of Rare-Earth Nickelate," *Physical Review Letters*, vol. 116, no. 5, p. 056801, 2016.

[61] J. B. Torrance, P. Lacorre, A. I. Nazzal, E. J. Ansaldo, and C. Niedermayer, "Systematic study of insulator-metal transitions in perovskites RNiO3 (R=Pr,Nd,Sm,Eu) due to closing of charge-transfer gap," *Physical Review B*, vol. 45, no. 14, pp. 8209–8212, 1992.

[62] M. Medarde, J. Mesot, S. Rosenkranz, P. Lacorre, W. Marshall, S. Klotz, J. Loveday, G. Hamel, S. Hull, and P. Radaelli, "Pressure-induced orthorhombic-rhombohedral phase transition in NdNiO3," *Physica B: Condensed Matter*, vol. 234-236, pp. 15–17, 1997.

[63] M. Zaghrioui, A. Bulou, P. Lacorre, and P. Laffez, "Electron diffraction and Raman scattering evidence of a symmetry breaking at the metal-insulator transition of NdNiO3," *Physical Review B*, vol. 64, no. 8, p. 081102, 2001.

[64] J. L. García-Muñoz, M. A. G. Aranda, J. A. Alonso, and M. J. Martínez-Lope, "Structure and charge order in the antiferromagnetic band-insulating phase of NdNiO3," *Physical Review B*, vol. 79, no. 13, p. 134432, 2009.

[65] M. Medarde, M. T. Fernández-Díaz, and P. Lacorre, "Long-range charge order in the low-temperature insulating phase of PrNiO3," *Physical Review B*, vol. 78, p. 212101, dec 2008.

[66] V. M. Goldschmidt, "Die Gesetze der Krystallochemie," *Die Naturwissenschaften*, vol. 14, no. 21, pp. 477–485, 1926.

[67] S. Yunoki, A. Moreo, and E. Dagotto, "Phase Separation Induced by Orbital Degrees of Freedom in Models for Manganites with Jahn-Teller Phonons," *Physical Review Letters*, vol. 81, no. 25, pp. 5612–5615, 1998.

[68] J.-S. Zhou and J. B. Goodenough, "Chemical bonding and electronic structure of RNiO3," *Physical Review B*, vol. 69, p. 153105, apr 2004.

[69] J. Rodríguez-Carvajal, S. Rosenkranz, M. Medarde, P. Lacorre, M. Fernandez-Díaz, F. Fauth, and V. Trounov, "Neutron-diffraction study of the magnetic and orbital ordering in 154SmNiO3 and 153EuNiO3," *Physical Review B*, vol. 57, no. 1, pp. 456–464, 1998.

[70] U. Staub, G. I. Meijer, F. Fauth, R. Allenspach, J. G. Bednorz, J. Karpinski, S. M. Kazakov, L. Paolasini, and F. D'Acapito, "Direct Observation of Charge Order in an Epitaxial NdNiO3 Film," *Physical Review Letters*, vol. 88, no. 12, p. 126402, 2002.

[71] I. I. Mazin, D. I. Khomskii, R. Lengsdorf, J. A. Alonso, W. G. Marshall, R. M. Ibberson, A. Podlesnyak, M. J. Martínez-Lope, and M. M. Abd-Elmeguid, "Charge ordering as alternative to Jahn-Teller distortion," *Physical Review Letters*, vol. 98, no. 17, pp. 1–4, 2007.

[72] Y. Lu, A. Frano, M. Bluschke, M. Hepting, S. Macke, J. Strempfer, P. Wochner, G. Cristiani, G. Logvenov, H.-U. Habermeier, M. W. Haverkort, B. Keimer, and E. Benckiser, "Quantitative determination of bond order and lattice distortions in nickel oxide heterostructures by resonant x-ray scattering," *Physical Review B*, vol. 93, no. 16, p. 165121, 2016.

[73] M. Medarde, C. Dallera, M. Grioni, B. Delley, F. Vernay, J. Mesot, M. Sikora, J. A. Alonso, and M. J. Martínez-Lope, "Charge disproportionation in RNiO3 perovskites (R=rare earth) from high-resolution x-ray absorption spectroscopy," *Physical Review B*, vol. 80, no. 24, p. 245105, 2009.

[74] Y. Murakami, J. Hill, D. Gibbs, M. Blume, I. Koyama, M. Tanaka, H. Kawata, T. Arima, Y. Tokura, K. Hirota, and Y. Endoh, "Resonant X-Ray Scattering from Orbital Ordering in LaMnO3," *Physical Review Letters*, vol. 81, no. 3, pp. 582–585, 1998.

[75] T. A. W. Beale, G. Beutier, S. R. Bland, A. Bombardi, L. Bouchenoire, O. Bunu, S. Di Matteo, J. Fernández-Rodríguez, J. E. Hamann-Borrero, J. Herrero-Martín, V. L. R. Jacques, R. D. Johnson, A. Juhin, T. Matsumura, C. Mazzoli, A. M. Mulders, H. Nakao, J. Okamoto, S. Partzsch, A. J. Princep, V. Scagnoli, J. Strempfer, C. Vecchini, Y. Wakabayashi, H. C. Walker, D. Wermeille, and Y. Yamasaki, "REXS contribution to electronic ordering investigation in solids," *European Physical Journal: Special Topics*, vol. 208, no. 1, pp. 89–98, 2012.

[76] J. Kokubun and V. E. Dmitrienko, "Anisotropic resonant X-ray scattering: Beauty of forbidden reflections," *European Physical Journal: Special Topics*, vol. 208, no. 1, pp. 39–52, 2012.

[77] A. Blanca-Romero and R. Pentcheva, "Confinement-induced metal-to-insulator transition in strained LaNiO 3/LaAlO3 superlattices," *Physical Review B*, vol. 84, no. 19, pp. 1–7, 2011.

[78] D. Puggioni, A. Filippetti, and V. Fiorentini, "Ordering and multiple phase transitions in ultrathin nickelate superlattices," *Physical Review B*, vol. 86, no. 19, pp. 1–4, 2012.

[79] P. V. Balachandran and J. M. Rondinelli, "Interplay of octahedral rotations and breathing distortions in charge-ordering perovskite oxides," *Physical Review B*, vol. 88, no. 5, pp. 1–13, 2013.

[80] R. Jaramillo, S. D. Ha, D. M. Silevitch, and S. Ramanathan, "Origins of bad-metal conductivity and the insulator-metal transition in the rare-earth nickelates," *Nature Physics*, vol. 10, no. 4, pp. 304–307, 2014.

[81] S. Johnston, A. Mukherjee, I. Elfimov, M. Berciu, and G. A. Sawatzky, "Charge Disproportionation without Charge Transfer in the Rare-Earth-Element Nickelates as a Possible Mechanism for the Metal-Insulator Transition," *Physical Review Letters*, vol. 112, no. 10, p. 106404, 2014.

[82] B. Lau and A. J. Millis, "Theory of the magnetic and metal-insulator transitions in RNiO3 bulk and layered structures," *Physical Review Letters*, vol. 110, no. 12, pp. 1–6, 2013.

[83] H. Park, A. J. Millis, and C. A. Marianetti, "Site-selective Mott transition in rare-earth-element nickelates," *Physical Review Letters*, vol. 109, no. 15, pp. 1–5, 2012.

[84] A. Subedi, O. E. Peil, and A. Georges, "Low-energy description of the metal-insulator transition in the rare-earth nickelates," *Physical Review B*, vol. 91, no. 7, p. 075128, 2015.

[85] T. Mizokawa, H. Namatame, A. Fujimori, K. Akeyama, H. Kondoh, H. Kuroda, and N. Kosugi, "Origin of the Band Gap in the Negative Charge-Transfer-Energy Compound NaCuO2," *Physical Review Letters*, vol. 67, no. 12, pp. 1638–1641, 1991.

[86] J. B. Goodenough, "Covalent Exchange vs Superexchange in Two Nickel Oxides," *Journal of Solid State Chemistry*, vol. 127, no. 1, pp. 126–127, 1996.

[87] M. T. Fernández-Díaz, J. A. Alonso, M. J. Martínez-Lope, M. T. Casais, and J. L. García-Muñoz, "Magnetic structure of the HoNiO3 perovskite," *Physical Review B*, vol. 64, no. 14, p. 144417, 2001.

[88] J. L. García-Muñoz, J. Rodríguez-Carvajal, and P. Lacorre, "Neutron-diffraction study of the magnetic ordering in the insulating regime of the perovskites RNiO3 (R=Pr and Nd)," *Physical Review B*, vol. 50, no. 2, pp. 978–992, 1994.

[89] J. E. Lorenzo, J. L. Hodeau, L. Paolasini, S. Lefloch, J. A. Alonso, and G. Demazeau, "Resonant x-ray scattering experiments on electronic orderings in NdNiO3 single crystals," *Physical Review B*, vol. 71, no. 4, p. 045128, 2005.

[90] T. Saito, M. Azuma, E. Nishibori, M. Takata, M. Sakata, N. Nakayama, T. Arima, T. Kimura, C. Urano, and M. Takano, "Monoclinic distortion in the insulating phase of PrNiO3," *Physica B: Condensed Matter*, vol. 329-333, no. II, pp. 866–867, 2003.

[91] S. Middey, J. Chakhalian, P. Mahadevan, J. Freeland, A. Millis, and D. Sarma, "Physics of Ultrathin Films and Heterostructures of Rare-Earth Nickelates," *Annual Review of Materials Research*, vol. 46, no. 1, pp. 305–334, 2016.

[92] Y. Liu, C. G. Pappas, M. Shayegan, L. N. Pfeiffer, K. W. West, and K. W. Baldwin, "Observation of reentrant integer quantum hall states in the lowest landau level," *Physical Review Letters*, vol. 109, no. 3, pp. 1–5, 2012.

[93] R. Eguchi, Y. Okamoto, Z. Hiroi, S. Shin, A. Chainani, Y. Tanaka, M. Matsunami, Y. Takata, Y. Nishino, K. Tamasaku, M. Yabashi, and T. Ishikawa, "Structure and photoemission spectroscopy of strain-controlled metal-insulator transition in NdNiO3 thin films," *Journal of Applied Physics*, vol. 105, no. 5, p. 056103, 2009.

[94] X. K. Lian, F. Chen, X. L. Tan, L. F. Wang, X. F. Xuan, G. Y. Gao, S. W. Jin, and W. B. Wu, "Controlling the sharpness of room-temperature metal-insulator transition in epitaxial Sm0.5Nd0.5NiO3 films," *AIP Advances*, vol. 3, no. 6, p. 062133, 2013.

[95] A. Venimadhav, I. C. Lekshmi, and M. S. Hegde, "Strain-induced metallic behavior in PrNiO3 epitaxial thin films," vol. 37, pp. 201–208, 2002.

[96] R. Scherwitzl, P. Zubko, I. G. Lezama, S. Ono, A. F. Morpurgo, G. Catalan, and J. M. Triscone, "Electric-field control of the metal-insulator transition in ultrathin NdNiO3 films," *Advanced Materials*, vol. 22, no. 48, pp. 5517–5520, 2010.

[97] S. Asanuma, P. H. Xiang, H. Yamada, H. Sato, I. H. Inoue, H. Akoh, A. Sawa, K. Ueno, H. Shimotani, H. Yuan, M. Kawasaki, and Y. Iwasa, "Tuning of the metal-insulator transition in electrolyte-gated NdNiO3 thin films," *Applied Physics Letters*, vol. 97, no. 14, pp. 103–106, 2010.

[98] J. Shi, S. D. Ha, Y. Zhou, F. Schoofs, and S. Ramanathan, "A correlated nickelate synaptic transistor," *Nature Communications*, vol. 4, p. 2676, oct 2013.

[99] A. D. Caviglia, R. Scherwitzl, P. Popovich, W. Hu, H. Bromberger, R. Singla, M. Mitrano, M. C. Hoffmann, S. Kaiser, P. Zubko, S. Gariglio, J. M. Triscone, M. Först, and A. Cavalleri, "Ultrafast strain engineering in complex oxide heterostructures," *Physical Review Letters*, vol. 108, no. 13, 2012.

[100] M. Först, A. D. Caviglia, R. Scherwitzl, R. Mankowsky, P. Zubko, V. Khanna, H. Bromberger, S. B. Wilkins, Y.-D. Chuang, W. S. Lee, W. F. Schlotter, J. J. Turner, G. Dakovski, M. P. Minitti, J. Robinson, S. R. Clark, D. Jaksch, J.-M. Triscone, J. P. Hill, S. S. Dhesi, and A. Cavalleri, "Spatially resolved ultrafast magnetic dynamics initiated at a complex oxide heterointerface," *Nature Materials*, vol. 14, no. 9, pp. 883–888, 2015.

[101] R. Scherwitzl, S. Gariglio, M. Gabay, P. Zubko, M. Gibert, and J. M. Triscone, "Metal-insulator transition in ultrathin LaNiO3 films," *Physical Review Letters*, vol. 106, no. 24, pp. 3–6, 2011.

[102] A. V. Boris, Y. Matiks, E. Benckiser, A. Frano, P. Popovich, V. Hinkov, P. Wochner, M. Castro-Colin, E. Detemple, V. K. Malik, C. Bernhard,

T. Prokscha, A. Suter, Z. Salman, E. Morenzoni, G. Cristiani, H.-U. Habermeier, and B. Keimer, “Dimensionality control of electronic phase transitions in nickel-oxide superlattices.,” *Science (New York, N.Y.)*, vol. 332, no. 6032, pp. 937–940, 2011.

[103] S. Catalano, M. Gibert, V. Bisogni, F. He, R. Sutarto, M. Viret, P. Zubko, R. Scherwitzl, G. A. Sawatzky, T. Schmitt, and J. Triscone, “Tailoring the electronic transitions of NdNiO3 films through (111) pc oriented interfaces,” *APL Materials*, vol. 3, no. May, p. 062506, 2015.

[104] D. Doennig, W. E. Pickett, and R. Pentcheva, “Confinement-driven transitions between topological and Mott phases in (LaNiO3)N/(LaAlO3)M(111) superlattices,” *Physical Review B*, vol. 89, no. 12, p. 121110, 2014.

[105] S. Middey, D. Meyers, M. Kareev, E. J. Moon, B. A. Gray, X. Liu, J. W. Freeland, and J. Chakhalian, “Epitaxial growth of (111)-oriented LaAlO3/ LaNiO3 ultra-thin superlattices,” *Applied Physics Letters*, vol. 101, no. 26, pp. 2–5, 2012.

[106] S. Okamoto, “Doped mott insulators in (111) bilayers of perovskite transition-metal oxides with a strong spin-orbit coupling,” *Physical Review Letters*, vol. 110, no. 6, pp. 1–5, 2013.

[107] M. Gibert, P. Zubko, R. Scherwitzl, J. Íñiguez, and J.-M. Triscone, “Exchange bias in LaNiO3LaMnO3 superlattices,” *Nature Materials*, vol. 11, no. 3, pp. 195–198, 2012.

[108] M. Gibert, M. Viret, P. Zubko, N. Jaouen, J.-M. Tonnerre, A. Torres-Pardo, S. Catalano, A. Gloter, O. Stéphan, and J.-M. Triscone, “Interlayer coupling through a dimensionality-induced magnetic state,” *Nature Communications*, vol. 7, p. 11227, 2016.

[109] J. W. Freeland, J. Liu, M. Kareev, B. Gray, J. W. Kim, P. Ryan, R. Pentcheva, and J. Chakhalian, “Orbital control in strained ultra-thin LaNiO3/LaAlO3 superlattices,” *EPL (Europhysics Letters)*, vol. 96, no. 5, p. 57004, 2011.

[110] J. Chakhalian, J. M. Rondinelli, J. Liu, B. A. Gray, M. Kareev, E. J. Moon, N. Prasai, J. L. Cohn, M. Varela, I. C. Tung, M. J. Bedzyk, S. G. Altendorf, F. Strigari, B. Dabrowski, L. H. Tjeng, P. J. Ryan, and J. W. Freeland, “Asymmetric orbital-lattice interactions in ultrathin correlated oxide films,” *Physical Review Letters*, vol. 107, no. 11, pp. 1–4, 2011.

[111] E. Benckiser, M. W. Haverkort, S. Brück, E. Goering, S. Macke, A. Frañó, X. Yang, O. K. Andersen, G. Cristiani, H.-U. Habermeier, A. V. Boris, I. Zegkinoglou, P. Wochner, H.-J. Kim, V. Hinkov, and B. Keimer, “Orbital reflectometry of oxide heterostructures,” *Nature Materials*, vol. 10, no. 3, pp. 189–193, 2011.

[112] M. Wu, E. Benckiser, M. W. Haverkort, A. Frano, Y. Lu, U. Nwankwo, S. Brück, P. Audehm, E. Goering, S. Macke, V. Hinkov, P. Wochner, G. Christiani, S. Heinze, G. Logvenov, H.-U. Habermeier, and B. Keimer, "Strain and composition dependence of orbital polarization in nickel oxide superlattices," *Physical Review B*, vol. 88, p. 125124, sep 2013.

[113] M. Wu, E. Benckiser, P. Audehm, E. Goering, P. Wochner, G. Christiani, G. Logvenov, H.-U. Habermeier, and B. Keimer, "Orbital reflectometry of PrNiO3/PrAlO3 superlattices," *Physical Review B*, vol. 91, no. 19, p. 195130, 2015.

[114] M. N. Grisolia, J. Varignon, G. Sanchez-Santolino, A. Arora, S. Valencia, M. Varela, R. Abrudan, E. Weschke, E. Schierle, J. E. Rault, J.-P. Rueff, A. Barthélémy, J. Santamaria, and M. Bibes, "Hybridization-controlled charge transfer and induced magnetism at correlated oxide interfaces," *Nature Physics*, vol. 12, no. 5, pp. 484–492, 2016.

[115] A. S. Disa, D. P. Kumah, A. Malashevich, H. Chen, D. A. Arena, E. D. Specht, S. Ismail-Beigi, F. J. Walker, and C. H. Ahn, "Orbital engineering in symmetry-breaking polar heterostructures," *Physical Review Letters*, vol. 114, no. 2, pp. 1–6, 2015.

[116] A. S. Disa, F. J. Walker, S. Ismail-Beigi, and C. H. Ahn, "Research Update: Orbital polarization in LaNiO3-based heterostructures," *APL Materials*, vol. 3, no. 6, p. 062303, 2015.

[117] T. H. Kim, D. Puggioni, Y. Yuan, L. Xie, H. Zhou, N. Campbell, P. J. Ryan, Y. Choi, J.-W. Kim, J. R. Patzner, S. Ryu, J. P. Podkaminer, J. Irwin, Y. Ma, C. J. Fennie, M. S. Rzchowski, X. Q. Pan, V. Gopalan, J. M. Rondinelli, and C. B. Eom, "Polar metals by geometric design," *Nature*, vol. 533, p. 68, 2016.

[118] G. Giovannetti, S. Kumar, D. Khomskii, S. Picozzi, and J. Van Den Brink, "Multiferroicity in rare-earth nickelates RNiO3," *Physical Review Letters*, vol. 103, no. 15, pp. 1–4, 2009.

[119] J. van den Brink and D. I. Khomskii, "Multiferroicity due to charge ordering," *Journal of Physics: Condensed Matter*, vol. 20, no. 43, p. 434217, 2008.

[120] J. Chaloupka and G. Khaliullin, "Orbital order and possible superconductivity in LaNiO3/LaMO3 superlattices," *Physical Review Letters*, vol. 100, no. 1, pp. 3–6, 2008.

[121] P. Hansmann, X. Yang, A. Toschi, G. Khaliullin, O. K. Andersen, and K. Held, "Turning a Nickelate Fermi Surface into a Cupratelike One through Heterostructuring," *Physical Review Letters*, vol. 103, no. 1, pp. 1–4, 2009.

[122] J. Ruppen, J. Teyssier, O. E. Peil, S. Catalano, M. Gibert, J. Mravlje, J. M. Triscone, A. Georges, and D. Van Der Marel, "Optical spectroscopy and the nature of the insulating state of rare-earth nickelates," *Physical Review B*, vol. 92, no. 15, pp. 1–11, 2015.

[123] C. Piamonteze, M. Gibert, J. Heidler, J. Dreiser, S. Rusponi, H. Brune, J.-M. Triscone, F. Nolting, and U. Staub, “Interfacial properties of LaMnO3/LaNiO3 superlattices grown along (001) and (111) orientations,” *Physical Review B*, vol. 92, no. 1, p. 014426, 2015.

[124] R. Aso, D. Kan, Y. Shimakawa, and H. Kurata, “Octahedral tilt propagation controlled by a-site cation size at perovskite oxide heterointerfaces,” *Crystal Growth and Design*, vol. 14, no. 5, pp. 2128–2132, 2014.

[125] W. Abney and E. R. Festing, “On the influence of the Atomic Grouping in the Molecules of Organic Bodies on Their Absorption in the Infrared Region of the Spectrum,” *Phil. Trans. Roy. Soc.*, vol. 172, pp. 887–918, 1882.

[126] C. V. Raman and K. S. Krishnan, “A New Type of Secondary Radiation,” *Nature*, vol. 121, no. 3048, pp. 501–502, 1928.

[127] P. Vandenabeele, *Practical Raman Spectroscopy - An Introduction.* Chichester, UK: John Wiley & Sons, Ltd, 2013.

[128] T. P. Devereaux and R. Hackl, “Inelastic light scattering from correlated electrons,” *Reviews of Modern Physics*, vol. 79, no. 1, pp. 175–233, 2007.

[129] M. Cardona, ed., *Light Scattering in Solids I*, vol. 8 of *Topics in Applied Physics.* Berlin, Heidelberg: Springer Berlin Heidelberg, 1983.

[130] M. Cardona and G. Güntherodt, eds., *Light Scattering in Solids II*, vol. 50 of *Topics in Applied Physics.* Berlin, Heidelberg: Springer Berlin Heidelberg, 1982.

[131] W. H. Weber and R. Merlin, eds., *Raman Scattering in Materials Science*, vol. 42 of *Springer Series in Materials Science.* Berlin, Heidelberg: Springer Berlin Heidelberg, 2000.

[132] M. Rahlenbeck, *Raman light scattering study on phonon anomalies in unconventional superconductors.* PhD thesis, University Stuttgart, 2010.

[133] S.-M. Souliou, *High Pressure Study of High-Temperature Superconductors.* PhD thesis, University Stuttgart, 2014.

[134] J. Ziman, *Electrons and Phonons.* Oxford University Press, 2001.

[135] G. J. Ackland, M. C. Warren, and S. J. Clark, “Practical methods in ab initio lattice dynamics,” *J. Phys.: Condens. Matter*, vol. 9, pp. 7861–7872, 1997.

[136] S. Baroni, S. De Gironcoli, A. Dal Corso, and P. Giannozzi, “Phonons and related crystal properties from density-functional perturbation theory,” *Reviews of Modern Physics*, vol. 73, no. 2, pp. 515–562, 2001.

[137] P. Taylor and O. Heinonen, *A Quantum Approach to Condensed Matter Physics.* Cambridge University Press, 2002.

[138] U. Fano, “Effects of configuration interaction on intensities and phase shifts,” *Physical Review*, vol. 124, no. 6, pp. 1866–1878, 1961.

[139] W. Hayes and R. Loudon, *Scattering of Light by Crystals.* Wiley New York, 1978.

[140] M. I. Aroyo, ed., *International Tables for Crystallography*, vol. A. Chester, England: International Union of Crystallography, 2015.

[141] D. L. Rousseau, R. P. Bauman, and S. P. S. Porto, “Normal mode determination in crystals,” *Journal of Raman Spectroscopy*, vol. 10, no. 1, pp. 253–290, 1981.

[142] M. a. Islam, J. M. Rondinelli, and J. E. Spanier, “Normal mode determination of perovskite crystal structures with octahedral rotations: theory and applications.,” *Journal of physics. Condensed matter: an Institute of Physics journal*, vol. 25, no. 17, p. 175902, 2013.

[143] A. M. Glazer, “The classification of tilted octahedra in perovskites,” *Acta Crystallographica Section B Structural Crystallography and Crystal Chemistry*, vol. 28, no. 11, pp. 3384–3392, 1972.

[144] A. M. Glazer, “Simple ways of determining perovskite structures,” *Acta Crystallographica Section A*, vol. 31, no. 6, pp. 756–762, 1975.

[145] S. Bueble, K. Knorr, E. Brecht, and W. W. Schmahl, “Influence of the ferroelastic twin domain structure on the {100} surface morphology of LaAlO3 HTSC substrates,” *Surface Science*, vol. 400, no. 1-3, pp. 345–355, 1998.

[146] S. J. May, J. W. Kim, J. M. Rondinelli, E. Karapetrova, N. A. Spaldin, A. Bhattacharya, and P. J. Ryan, “Quantifying octahedral rotations in strained perovskite oxide films,” *Physical Review B*, vol. 82, no. 1, pp. 1–7, 2010.

[147] I. C. Tung, P. V. Balachandran, J. Liu, B. A. Gray, E. A. Karapetrova, J. H. Lee, J. Chakhalian, M. J. Bedzyk, J. M. Rondinelli, and J. W. Freeland, “Connecting bulk symmetry and orbital polarization in strained RNiO3 ultrathin film,” *Physical Review B*, vol. 88, p. 205112, nov 2013.

[148] J. L. Garcia-Muñoz, J. Rodríguez-Carvajal, P. Lacorre, and J. B. Torrance, “Neutron-diffraction study of RNiO3 (R=La,Pr,Nd,Sm): Electronically induced structural changes across the metal-insulator transition,” *Physical Review B*, vol. 46, no. 8, 1992.

[149] J. F. Scott, “Raman Study of Trigonal-Cubic Phase Transitions in Rare-Earth Aluminates,” *Physical Review*, vol. 183, no. 3, pp. 823–825, 1969.

[150] M. K. Kinyanjui, Y. Lu, N. Gauquelin, M. Wu, A. Frano, P. Wochner, M. Reehuis, G. Christiani, G. Logvenov, H. U. Habermeier, G. A. Botton, U. Kaiser, B. Keimer, and E. Benckiser, “Lattice distortions and octahedral rotations in epitaxially strained LaNiO3/LaAlO3 superlattices,” *Applied Physics Letters*, vol. 104, no. 22, pp. 1–5, 2014.

[151] O. Bock and U. Mueller, "Symmetrieverwandtschaften bei Varianten des Perowskit-Typs," *Acta Crystallographica Section B*, pp. 594–606, 2002.

[152] U. M. Gebhardt, *Strukturelle Relaxation von epitaktischen, dunnen La/Sr-Manganitfilmen in Abhangigkeit von der Schichtdicke.* PhD thesis, University Stuttgart, 2007.

[153] M. Abrashev, J. Bäckström, L. Börjesson, V. Popov, R. Chakalov, N. Kolev, R.-L. Meng, and M. Iliev, "Raman spectroscopy of CaMnO3: Mode assignment and relationship between Raman line intensities and structural distortions," *Physical Review B*, vol. 65, no. 18, p. 184301, 2002.

[154] D. A. Long, "Handbook of Raman spectroscopy. From the research laboratory to the process line.Edited by Ian R. Lewis and Howell G. M. Edwards. Marcel Dekker, New York and Basel, 2001. Price$225.," *Journal of Raman Spectroscopy*, vol. 35, no. 1, pp. 91–91, 2004.

[155] "HORIBA JOBIN YVON LABRAM HR800 USER MANUAL," tech. rep.

[156] N. Everall, "Depth Profiling With Confocal Raman microscopy," *Spectroscopy*, vol. 19, no. 11, pp. 16–24, 2004.

[157] N. A. Freebody, A. S. Vaughan, and A. M. MacDonald, "On optical depth profiling using confocal Raman spectroscopy," *Analytical and Bioanalytical Chemistry*, vol. 396, no. 8, pp. 2813–2823, 2010.

[158] B. Marton, L. G. J. Van Der Ven, C. Otto, N. Uzunbajakava, M. A. Hempenius, and G. J. Vancso, "A depth-resolved look at the network development in alkyd coatings by confocal Raman microspectroscopy," *Polymer*, vol. 46, no. 25, pp. 11330–11339, 2005.

[159] J. P. Tomba and J. M. Pastor, "Confocal Raman microspectroscopy with dry objectives: A depth profiling study on polymer films," *Vibrational Spectroscopy*, vol. 44, no. 1, pp. 62–68, 2007.

[160] M. Branescu and C. Naudin, "Depth Raman spectra and laser-induced structural and oxygenation changes in thick YBa2Cu3O7- i films," *Journal of Optoelectronics and Advanced Materials*, vol. 9, no. 3, pp. 661–663, 2007.

[161] M. Branescu, C. Naudin, M. Gartner, and G. Nemes, "Depth profiling Raman spectroscopy of a thin YBa2Cu3O7 film," *Thin Solid Films*, vol. 516, no. 22, pp. 8190–8194, 2008.

[162] J. Kreisel, M. C. Weber, N. Dix, F. Sanchez, P. A. Thomas, and J. Fontcuberta, "Probing individual layers in functional oxide multilayers by wavelength-dependent raman scattering," *Advanced Functional Materials*, vol. 22, no. 23, pp. 5044–5049, 2012.

[163] A. Sanson, M. Giarola, E. Napolitani, G. Impellizzeri, V. Privitera, A. Carnera, and G. Mariotto, "Study of carrier concentration profiles in Al-implanted Ge by micro-Raman spectroscopy under different excitation wavelengths," *Journal of Raman Spectroscopy*, vol. 44, no. 5, pp. 665–669, 2013.

[164] W. C. Röntgen, "On a New Kind of Rays," *Nature*, vol. 53, no. 1369, pp. 274–276, 1896.

[165] P. Willmott, *An Introduction to Synchrotron Radiation.* Chichester, UK: John Wiley & Sons, Ltd, 2011.

[166] J. Als-Nielsen and D. McMorrow, *Elements of Modern X-ray Physics.* Wiley, 1 ed., 2001.

[167] N. W. Ashcroft and D. N. Mermin, *Solid state physics.* Toronto: Thomson Learning, 1 ed., 1976.

[168] M. Birkholz, *Thin Film Analysis by X-Ray Scattering.* WILEY-VCH, 2006.

[169] A. Frano, *Spin Spirals and Charge Textures in Transition-Metal-Oxide Heterostructures.* Springer Theses, Cham: Springer International Publishing, 2014.

[170] B. L. Henke, E. M. Gullikson, and J. C. Davis, "X-Ray Interactions: Photoabsorption, Scattering, Transmission, and Reflection at E = 50-30,000 eV, Z = 1-92," *Atomic Data and Nuclear Data Tables*, vol. 54, no. 2, pp. 181–342, 1993.

[171] D. H. Templeton and L. K. Templeton, "Polarized X-ray absorption and double refraction in vanadyl bisacetylacetonate," *Acta Crystallographica Section A*, vol. 36, no. 2, pp. 237–241, 1980.

[172] K. D. Finkelstein, Q. Shen, and S. Shastri, "Resonant x-ray diffraction near the iron K edge in hematite (alpha-Fe_2O_3)," *Physical Review Letters*, vol. 69, no. 10, pp. 1612–1615, 1992.

[173] J. Fink, E. Schierle, E. Weschke, and J. Geck, "Resonant elastic soft x-ray scattering.," *Reports on Progress in Physics*, vol. 76, no. 5, p. 056502, 2013.

[174] J. E. Lorenzo, Y. Joly, D. Mannix, and S. Grenier, "Charge order as seen by resonant (elastic) X-ray scattering," *European Physical Journal: Special Topics*, vol. 208, no. 1, pp. 121–127, 2012.

[175] M. Takeshi, Matsumura; Hironori, Nakao; Youichi, "Resonant X-ray Scattering Experiments on the Ordering of Electronic Degrees of Freedom," *Journal of the Physical Society of Japan*, vol. 82, pp. 1–18, 2013.

[176] G. B. Arfken, H. J. Weber, and F. E. Harris, *Mathematical Methods for Physicists, Sixth Edition: A Comprehensive Guide.* Academic Press, 6 ed., 2005.

[177] M. Wu, *Orbital Reflectometry of Nickel Oxide Heterostructures.* PhD thesis, University Stuttgart, 2015.

[178] C. Cohen-Tannoudji, B. Diu, and F. Laloe, *Quantum Mechanics.* Wiley-Interscience, 2006.

[179] G. van der Laan and B. T. Thole, "Strong magnetic x-ray dichroism in 2 p absorption spectra of 3 d transition-metal ions," *Physical Review B*, vol. 43, no. 16, pp. 13401–13411, 1991.

[180] J. B. Goedkoop, B. T. Thole, G. Van Der Laan, G. A. Sawatzky, F. M. F. De Groot, and J. C. Fuggle, "Calculations of magnetic x-ray dichroism in the 3d absorption spectra of rare-earth compounds," *Physical Review B*, vol. 37, no. 4, pp. 2086–2093, 1988.

[181] B. T. Thole, P. Carra, F. Sette, and G. Van Der Laan, "X-ray circular dichroism as a probe of orbital magnetization," *Physical Review Letters*, vol. 68, no. 12, pp. 1943–1946, 1992.

[182] G. van der Laan, "Sum Rules and Fundamental Spectra of Magnetic X-Ray Dichroism in Crystal Field Symmetry," *Journal of the Physical Society of Japan*, vol. 63, pp. 2393–2400, jun 1994.

[183] M. W. Haverkort, N. Hollmann, I. P. Krug, and A. Tanaka, "Symmetry analysis of magneto-optical effects: The case of x-ray diffraction and x-ray absorption at the transition metal L2,3 edge," *Physical Review B - Condensed Matter and Materials Physics*, vol. 82, no. 9, pp. 1–14, 2010.

[184] S. Macke, "ReMagX, X-Ray Reflectivity Tool, http://remagx.org/wiki/doku.php."

[185] S. Macke, "QUAD, X-Ray Dynamical Diffraction Tool, http://quad.x-ray.center/wiki/dokuwiki/doku.php."

[186] J. P. Hannon, G. T. Trammell, M. Blume, and D. Gibbs, "X-ray Resonance Exchange Scattering (XRES)," *Hyperfine Interactions*, vol. 50, no. 1-4, pp. 477–479, 1989.

[187] M. Blume, "Magnetic scattering of x-rays," *Journal of Applied Physics*, vol. 57, no. 8, p. 3615, 1985.

[188] S. Macke, J. E. Hamann-Borrero, R. J. Green, B. Keimer, G. A. Sawatzky, and M. W. Haverkort, "Dynamical Effects in Resonant X-Ray Diffraction," *Physical Review Letters*, vol. 117, no. 11, p. 115501, 2016.

[189] "SOLEIL synchrotron, http://www.synchrotron-soleil.fr/images/File/Presse/Dossier/Dossier181206-A.pdf," tech. rep., 2016.

[190] B. D. Cullity and S. R. Stock, *Elements of X-Ray Diffraction.* Prentice Hall, 3 ed., 2001.

[191] A. Frano, “X-ray Scattering Investigations of Transition-Metal-Oxide Heterostructures, Master’s thesis, University Stuttgart,” 2010.

[192] P. Carra and B. T. Thole, “RMP Colloquia,” *Reviews of Modern Physics*, vol. 66, no. 4, pp. 1509–1515, 1994.

[193] J. P. Hill and D. F. McMorrow, “X-ray resonant exchange scattering: polarization dependence and correlation functions,” *Acta Crystallographica*, vol. A52, pp. 236–244, 1996.

[194] E. J. Jaeschke, S. Khan, J. R. Schneider, and J. B. Hastings, eds., *Synchrotron Light Sources and Free-Electron Lasers*. Cham: Springer International Publishing, 2016.

[195] H. Schulte-Schrepping, J. Viefhaus, A. Wefer, and T. Wroblewski, “Commissioning of the APPLE II undulator,” Tech. Rep. 1, 2002.

[196] G. Kim, M. Neumann, M. Kim, M. D. Le, T. D. Kang, and T. W. Noh, “Suppression of Three-Dimensional Charge Density Wave Ordering via Thickness Control,” *Physical Review Letters*, vol. 115, no. 22, pp. 1–5, 2015.

[197] J. Kreisel, G. Lucazeau, C. Dubourdieu, M. Rosina, and F. Weiss, “Raman scattering study of La0.7Sr0.3MnO3/SrTiO3 multilayers,” *Journal of Physics: Condensed Matter*, vol. 5201, no. 14, p. 5201, 2002.

[198] P. Zhang, T. Haage, H.-U. Habermeier, T. Ruf, and M. Cardona, “Raman spectra of ultrathin YBaCuO7 films,” *Journal of Applied Physics*, vol. 80, no. 5, p. 2935, 1996.

[199] Y. M. Xiong, T. Chen, G. Y. Wang, X. H. Chen, X. Chen, and C. L. Chen, “Raman spectra in epitaxial thin films of La1xCaxMnO3 (x=0.33, 0.5) grown on different substrates,” *Physical Review B*, vol. 70, no. 9, p. 094407, 2004.

[200] A. Antonakos, D. Palles, E. Liarokapis, M. Filippi, and W. Prellier, “Evaluation of the strains in charge-ordered Pr[1-x]Ca[x]MnO[3] thin films using Raman spectroscopy,” *Journal of Applied Physics*, vol. 104, no. 6, p. 063508, 2008.

[201] A. Bartasyte, O. Chaix-Pluchery, J. Kreisel, C. Jimenez, F. Weiss, A. Abrutis, Z. Saltyte, and M. Boudard, “Investigation of thickness-dependent stress in PbTiO3 thin films,” *Journal of Applied Physics*, vol. 103, no. 1, 2008.

[202] B. B. Johnson and W. L. Peticolas, “The Resonant Raman Effect,” *Ann. Rev. Phys. Chem.*, vol. 27, no. Gm 15547, pp. 465–91, 1976.

[203] J. Calleja and M. Cardona, “Resonant Raman scattering in ZnO,” *Physical Review B*, vol. 16, no. 8, pp. 3753–3761, 1977.

[204] L. M. Malard, M. A. Pimenta, G. Dresselhaus, and M. S. Dresselhaus, “Raman spectroscopy in graphene,” *Physics Reports*, vol. 473, no. 5-6, pp. 51–87, 2009.

[205] H. Li, Q. Zhang, C. C. R. Yap, B. K. Tay, T. H. T. Edwin, A. Olivier, and D. Baillargeat, “From bulk to monolayer MoS 2: Evolution of Raman scattering,” *Advanced Functional Materials*, vol. 22, no. 7, pp. 1385–1390, 2012.

[206] M. Fleischmann, P. J. Hendra, and A. J. McQuillan, “Raman spectra of pyridine adsorbed at a silver electrode,” *Chemical Physics Letters*, vol. 26, no. 2, pp. 163–166, 1974.

[207] M. G. Albrecht and J. A. Creighton, “Anomalously intense Raman spectra of pyridine at a silver electrode,” *Journal of the American Chemical Society*, vol. 99, pp. 5215–5217, 1977.

[208] K. Kneipp, Y. Wang, H. Kneipp, L. T. Perelman, I. Itzkan, R. R. Dasari, and M. S. Feld, “Single molecule detection using surface-enhanced Raman scattering (SERS),” *Physical Review Letters*, vol. 78, no. 9, pp. 1667–1670, 1997.

[209] J. F. Arenas, I. López-Tocón, J. L. Castro, S. P. Centeno, M. R. López-Ramírez, and J. C. Otero, “Resonant charge transfer on the nanoscale: Studying doublet states of adsorbates by surface-enhanced Raman scattering,” *Journal of Raman Spectroscopy*, vol. 36, no. 6-7, pp. 515–521, 2005.

[210] K. A. Willets and R. P. Van Duyne, “Localized surface plasmon resonance spectroscopy and sensing,” *Annu. Rev. Phys. Chem.*, vol. 58, pp. 267–297, 2007.

[211] E. Bailo and V. Deckert, “Tip-enhanced Raman scattering,” *Chemical Society Reviews*, vol. 37, no. 5, p. 921, 2008.

[212] W. G. Nilsen, “Raman Spectrum of Strontium Titanate,” *The Journal of Chemical Physics*, vol. 48, no. 5, p. 2240, 1968.

[213] R. Ouillon, P. Ranson, and P. Pruzan, “A Raman scattering study of the phase transitions in SrTiO3 and in the mixed system (Sr1-xCax)TiO3 at ambient pressure fromT = 300 K down to 8 K,” *Journal of Physics: Condensed Matter*, vol. 2079, 2002.

[214] C. Zhao, Y. Hang, X. He, L. Zhang, J. Yin, P. Hu, M. He, and E. Ma, “Optical characterization and evaluation of the laser properties of Yb 3 + -doped (La, Sr)(Al, Ta)O 3 single crystals,” *Journal of Physics: Condensed Matter*, vol. 23, no. 12, p. 125401, 2011.

[215] L. Gasparov, T. Jegorel, L. Loetgering, S. Middey, and J. Chakhalian, “Thin film substrates from the Raman spectroscopy point of view,” *Journal of Raman Spectroscopy*, vol. 45, no. 6, pp. 465–469, 2014.

[216] J. Xiao, M. Shao, Y. Tian, W. Huang, A. Wang, and S. Yin, “Czochralski growth and topographic study of tetragonal (La,Sr)(Al,Ta)O3 single crystals,” *Journal of Crystal Growth*, vol. 236, no. 4, pp. 671–675, 2002.

[217] S. Okada, S. Kobayashi, K. Ohashi, N. Nishikawa, T. Tokunaga, K. Sasaki, and T. Yamamoto, "Direct observation of B-site ordering in LSAT: (La0.3Sr0.7)(Al0.65Ta0.35)O3 single crystal," *Applied Physics Letters*, vol. 108, no. 25, p. 251905, 2016.

[218] J. Suda, T. Mori, H. Saito, O. Kamishima, T. Hattori, and T. Sato, "First-order Raman spectra and lattice dynamics of a NdGaO3 crystal," *Physical Review B*, vol. 66, no. 17, p. 174302, 2002.

[219] D. Savytskii, L. Vasylechko, a. Senyshyn, a. Matkovskii, C. Bähtz, M. Sanjuán, U. Bismayer, and M. Berkowski, "Low-temperature structural and Raman studies on rare-earth gallates," *Physical Review B*, vol. 68, no. 2, p. 024101, 2003.

[220] V. G. Hadjiev, M. Cardona, I. Ivanov, V. Popov, M. Gyulmezov, M. N. Iliev, and M. Berkowski, "Optical phonons probe of the SrLaAlO4 crystal structure," *Journal of Alloys and Compounds*, vol. 251, pp. 7–10, 1997.

[221] M. Abrashev, a. Litvinchuk, M. Iliev, R. Meng, V. Popov, V. Ivanov, R. Chakalov, and C. Thomsen, "Comparative study of optical phonons in the rhombohedrally distorted perovskites LaAlO3 and LaMnO3," *Physical Review B*, vol. 59, no. 6, pp. 4146–4153, 1999.

[222] V. G. Sathe and A. Dubey, "Broken symmetry in LaAlO3 single crystal probed by resonant Raman spectroscopy," *J. Phys: Cond. Matt.*, vol. 19, no. 38, p. 382201, 2007.

[223] S. A. Hayward, F. D. Morrison, S. A. T. Redfern, E. K. H. Salje, J. F. Scott, K. S. Knight, S. Tarantino, A. M. Glazer, V. Shuvaeva, P. Daniel, M. Zhang, and M. A. Carpenter, "Transformation processes in LaAlO3: Neutron diffraction, dielectric, thermal, optical, and Raman studies," *Physical Review B*, vol. 72, no. 5, p. 054110, 2005.

[224] G. Yao, S. Hou, and M. Dudley, "Synchrotron x-ray topography studies of twin structures in lanthanum aluminate single crystals," *Journal of Materials Research*, vol. 7, no. 7, pp. 1847–1855, 1992.

[225] N. Chaban, M. Weber, S. Pignard, and J. Kreisel, "Phonon Raman scattering of perovskite LaNiO3 thin films," *Applied Physics Letters*, vol. 97, no. 3, pp. 1–4, 2010.

[226] C. Girardot, J. Kreisel, S. Pignard, N. Caillault, and F. Weiss, "Raman scattering investigation across the magnetic and metal-insulator transition in rare earth nickelate RNiO3 (R=Sm, Nd) thin film," *Physical Review B*, vol. 78, no. 10, p. 104101, 2008.

[227] M. C. Weber, M. Guennou, N. Dix, D. Pesquera, F. Sánchez, G. Herranz, J. Fontcuberta, L. López-Conesa, S. Estradé, F. Peiró, J. Iñiguez, and J. Kreisel, "Multiple strain-induced phase transitions in LaNiO3 thin films," *Physical Review B*, vol. 94, no. 1, p. 014118, 2016.

[228] G. Gou, I. Grinberg, A. M. Rappe, and J. M. Rondinelli, “Lattice normal modes and electronic properties of the correlated metal LaNiO3,” *Physical Review B*, vol. 84, no. 14, p. 144101, 2011.

[229] M. Bulout, R. J. Donohoe, and B. I. Swanson, “Phenomenological description of the longitudinal vibrations of the quasi-one-dimensional solid PtCl : calculation of the valence defect frequencies Phenomenological description of the longitudinal vibrations of the quasi-one-dimensional solid PtCI : calcu,” *Journal of Phys Condens. Matter Condens. Matter*, vol. 1709, 1991.

[230] C. Girardot, S. Pignard, F. Weiss, and J. Kreisel, “SmNiO3/NdNiO3 thin film multilayers,” *Applied Physics Letters*, vol. 98, no. 24, pp. 2011–2014, 2011.

[231] S.-W. Cheong and M. Mostovoy, “Multiferroics: a magnetic twist for ferroelectricity,” *Nature Materials*, vol. 6, no. 1, pp. 13–20, 2007.

[232] H. Y. Qi, M. K. Kinyanjui, J. Biskupek, D. Geiger, E. Benckiser, H. U. Habermeier, B. Keimer, and U. Kaiser, “Local octahedral rotations and octahedral connectivity in epitaxially strained LaNiO3/LaGaO3 superlattices,” *Journal of Materials Science*, vol. 50, no. 15, pp. 5300–5306, 2015.

[233] G. Mattoni, P. Zubko, F. Maccherozzi, A. J. H. van der Torren, D. B. Boltje, M. Hadjimichael, N. Manca, S. Catalano, M. Gibert, Y. Liu, J. Aarts, J.-M. Triscone, S. S. Dhesi, and A. D. Caviglia, “Striped nanoscale phase separation at the metal-insulator transition of heteroepitaxial nickelates,” *Arxiv*, no. 001, p. 1602.04445, 2016.

[234] P. Giannozzi, S. Baroni, N. Bonini, M. Calandra, R. Car, C. Cavazzoni, D. Ceresoli, G. L. Chiarotti, M. Cococcioni, I. Dabo, A. Dal Corso, S. de Gironcoli, S. Fabris, G. Fratesi, R. Gebauer, U. Gerstmann, C. Gougoussis, A. Kokalj, M. Lazzeri, L. Martin-Samos, N. Marzari, F. Mauri, R. Mazzarello, S. Paolini, A. Pasquarello, L. Paulatto, C. Sbraccia, S. Scandolo, G. Sclauzero, A. P. Seitsonen, A. Smogunov, P. Umari, and R. M. Wentzcovitch, “QUANTUM ESPRESSO: a modular and open-source software project for quantum simulations of materials,” *Journal of Physics: Condensed Matter*, vol. 21, no. 39, p. 395502, 2009.

[235] J. P. Perdew and A. Zunger, “Self-interaction correction to density-functional approximations for many-electron systems,” *Physical Review B*, vol. 23, no. 10, pp. 5048–5079, 1981.

[236] A. Dal Corso, “Pseudopotentials periodic table: From H to Pu,” *Computational Materials Science*, vol. 95, pp. 337–350, 2014.

[237] J. A. Alonso, M. J. Martínez-Lope, M. T. Casais, J. L. García-Muñoz, M. T. Fernández-Díaz, and M. A. G. Aranda, “High-temperature structural evolution of RNiO3 (R=Ho, Y, Er, Lu) perovskites: Charge disproportionation and electronic localization,” *Physical Review B*, vol. 64, no. 9, p. 094102, 2001.

[238] M. N. Iliev, M. V. Abrashev, J. Laverdière, S. Jandl, M. M. Gospodinov, Y. Q. Wang, and Y. Y. Sun, “Distortion-dependent Raman spectra and mode mixing in R MnO3 perovskites (R=La,Pr,Nd,Sm,Eu,Gd,Tb,Dy,Ho,Y),” *Physical Review B - Condensed Matter and Materials Physics*, vol. 73, no. 6, pp. 3–8, 2006.

[239] O. Chaix-Pluchery and J. Kreisel, “Raman scattering of perovskite SmScO3 and NdScO3 single crystals,” *Phase Transitions*, vol. 84, no. 5-6, pp. 542–554, 2011.

[240] M. C. Weber, J. Kreisel, P. A. Thomas, M. Newton, K. Sardar, and R. I. Walton, “Phonon Raman scattering of RCrO 3 perovskites (R=Y, La, Pr, Sm, Gd, Dy, Ho, Yb, Lu),” *Physical Review B - Condensed Matter and Materials Physics*, vol. 85, no. 5, pp. 1–9, 2012.

[241] J. Bouvier, P. and Kreisel, “Pressure-induced phase transition in LaAlO3,” *Journal of Physics: Condensed Matter*, vol. 14, pp. 3981–3991, 2002.

[242] M. N. Iliev, H.-G. Lee, V. N. Popov, Y. Y. Sun, C. Thomsen, R. L. Meng, and C. W. Chu, “Raman spectroscopy of orthorhombic perovskitelike YMnO3 and LaMnO3,” *Physical Review B*, vol. 57, no. 5, pp. 2872–2877, 1998.

[243] B. Dabrowski, S. Kolesnik, A. Baszczuk, O. Chmaissem, T. Maxwell, and J. Mais, “Structural, transport, and magnetic properties of RMnO3 perovskites (R=La, Pr, Nd, Sm, 153Eu, Dy),” *Journal of Solid State Chemistry*, vol. 178, no. 3, pp. 629–637, 2005.

[244] N. Ihzaz, S. Pignard, J. Kreisel, H. Vincent, J. Marcus, J. Dhahri, and M. Oumezzine, “Synthesis and characterization of SmNiO3 thin films,” *Physica Status Solidi C: Conferences*, vol. 1, no. 7, pp. 1679–1682, 2004.

[245] R. D. Shannon, “Revised effective ionic radii and systematic studies of interatomic distances in halides and chalcogenides,” *Acta Crystallographica Section A*, vol. 32, no. 5, pp. 751–767, 1976.

[246] J. Hwang, J. Y. Zhang, J. Son, and S. Stemmer, “Nanoscale quantification of octahedral tilts in perovskite films,” *Applied Physics Letters*, vol. 100, no. 19, pp. 2012–2015, 2012.

[247] J. Y. Zhang, H. Kim, E. Mikheev, A. J. Hauser, and S. Stemmer, “Key role of lattice symmetry in the metal-insulator transition of NdNiO3 films,” *Scientific Reports*, vol. 6, no. April, p. 23652, 2016.

[248] J. A. Alonso, M. J. Martínez-Lope, M. T. Casais, and M. T. Fernández-Díaz, “Room-temperature monoclinic distortion due to charge disproportionation in RNiO3 perovskites with small rare-earth cations (R=Ho, Y, Er, Tm, Yb, and Lu): A neutron diffraction study,” *Physical Review B*, vol. 61, no. 3, pp. 1756–1763, 2000.

[249] C. Piamonteze and H. Tolentino, “Local structural distortion and electronic modifications in PrNiO3 across the metal insulator transition,” *AIP Conf. Proc.*, vol. 450, no. 2003, 2003.

[250] D. Kumar, K. P. Rajeev, J. A. Alonso, and M. J. Martínez-Lope, "Spin-canted magnetism and decoupling of charge and spin ordering in NdNiO3," *Physical Review B*, vol. 88, no. 1, p. 014410, 2013.

[251] E. Fawcett, H. L. Alberts, V. Y. Galkin, D. R. Noakes, and J. V. Yakhmi, "Spin-density-wave antiferromagnetism in chromium alloys," *Reviews of Modern Physics*, vol. 66, no. 1, pp. 25–127, 1994.

[252] G. Grüner, *Density Waves in Solids.* Addison-Wesley Publishing Company, 89 ed., 1994.

[253] A. H. MacDonald and M. Tsoi, "Antiferromagnetic metal spintronics.," *Philosophical transactions. Series A, Mathematical, physical, and engineering sciences*, vol. 369, no. 1948, pp. 3098–114, 2011.

[254] J. Sinova and I. Žutić, "New moves of the spintronics tango," *Nature Materials*, vol. 11, no. 5, pp. 368–371, 2012.

[255] K. Y. Yang, W. Zhu, D. Xiao, S. Okamoto, Z. Wang, and Y. Ran, "Possible interaction-driven topological phases in (111) bilayers of LaNiO3," *Physical Review B - Condensed Matter and Materials Physics*, vol. 84, no. 20, pp. 2–5, 2011.

[256] A. Rüegg, C. Mitra, A. A. Demkov, and G. A. Fiete, "Electronic structure of (LaNiO3)2/(LaAlO3)N heterostructures grown along [111]," *Physical Review B*, vol. 85, no. 24, p. 245131, 2012.

[257] D. Xiao, W. Zhu, Y. Ran, N. Nagaosa, and S. Okamoto, "Interface engineering of quantum Hall effects in digital transition metal oxide heterostructures.," *Nature communications*, vol. 2, p. 596, 2011.

[258] A. Rüegg and G. A. Fiete, "Topological insulators from complex orbital order in transition-metal oxides heterostructures," *Physical Review B - Condensed Matter and Materials Physics*, vol. 84, no. 20, pp. 1–5, 2011.

[259] D. Doennig, W. E. Pickett, and R. Pentcheva, "Massive symmetry breaking in LaAlO3/SrTiO3(111) quantum wells: A three-orbital strongly correlated generalization of graphene," *Physical Review Letters*, vol. 111, no. 12, pp. 1–5, 2013.

[260] F. Wang and Y. Ran, "Nearly flat band with Chern number C=2 on the dice lattice," *Physical Review B - Condensed Matter and Materials Physics*, vol. 84, no. 24, pp. 1–5, 2011.

[261] X. Hu, A. Rüegg, and G. A. Fiete, "Topological phases in layered pyrochlore oxide thin films along the [111] direction," *Physical Review B - Condensed Matter and Materials Physics*, vol. 86, no. 23, pp. 1–11, 2012.

[262] Z. Liao, R. J. Green, N. Gauquelin, S. Macke, L. Li, J. Gonnissen, R. Sutarto, E. P. Houwman, Z. Zhong, S. Van Aert, J. Verbeeck, G. A. Sawatzky, M. Huijben, G. Koster, and G. Rijnders, "Long-Range Domain Structure and Symmetry Engineering by Interfacial Oxygen Octahedral Coupling at Heterostructure Interface," *Advanced Functional Materials*, 2016.

[263] H. Boschker, M. Mathews, E. P. Houwman, H. Nishikawa, A. Vailionis, G. Koster, G. Rijnders, and D. H. A. Blank, "Strong uniaxial in-plane magnetic anisotropy of (001)- and (011)-oriented La0.67 Sr0.33 MnO3 thin films on NdGaO3 substrates," *Physical Review B - Condensed Matter and Materials Physics*, vol. 79, no. 21, pp. 1–6, 2009.

[264] R. J. Green, "private communication," 2016.

[265] L. Vasylechko, L. Akselrud, W. Morgenroth, U. Bismayer, A. Matkovskii, and D. Savytskii, "Crystal structure of NdGaO3 at 100 K and 293 K based on synchrotron data," *Journal of Alloys and Compounds*, vol. 297, no. 1-2, pp. 46–52, 2000.

[266] A. Vailionis, H. Boschker, W. Siemons, E. P. Houwman, D. H. A. Blank, G. Rijnders, and G. Koster, "Misfit strain accommodation in epitaxial ABO3 perovskites: Lattice rotations and lattice modulations," *Physical Review B - Condensed Matter and Materials Physics*, vol. 83, no. 6, pp. 1–10, 2011.

[267] S. Yamamoto and T. Fujiwara, "Charge and Spin Order in RNiO3 (R=Nd, Y) by LSDA+U Method," *Journal of the Physical Society of Japan*, vol. 71, no. 5, pp. 1226–1229, 2002.

[268] S. Dong and E. Dagotto, "Quantum confinement induced magnetism in LaNiO3-LaMnO3 superlattices," *Physical Review B - Condensed Matter and Materials Physics*, vol. 87, no. 19, pp. 1–7, 2013.

[269] J. Hoffman, I. C. Tung, B. B. Nelson-Cheeseman, M. Liu, J. W. Freeland, and A. Bhattacharya, "Charge transfer and interfacial magnetism in (LaNiO3) n/(LaMnO3)2 superlattices," *Physical Review B - Condensed Matter and Materials Physics*, vol. 88, no. 14, pp. 1–7, 2013.

[270] P. H. Xiang, S. Asanuma, H. Yamada, I. H. Inoue, H. Akoh, and A. Sawa, "Room temperature Mott metal-insulator transition and its systematic control in Sm1-xCaxNiO3 thin films," *Applied Physics Letters*, vol. 97, no. 3, pp. 5–8, 2010.

[271] M. Hepting, R. J. Green, Z. Zhong, M. Bluschke, Y. Eren Suyolcu, S. Macke, A. Frano, S. Catalano, M. Gibert, R. Sutarto, F. He, G. Cristiani, G. Logvenov, Y. Wang, P. A. van Aken, P. Hansmann, M. Le Tacon, J.-M. Triscone, G. A. Sawatzky, B. Keimer, and E. Benckiser, "Complex magnetic order in nickelate slabs (unpublished)." 2016.

[272] Y. Eren Suyolcu, Y. Wang, and P. A. van Aken, “Crystallographic reorientation of NdNiO3 films grown on [111] NdGaO3 substrates. (unpublished).” 2016.

[273] Y. Wang, U. Salzberger, W. Sigle, Y. Eren Suyolcu, and P. A. van Aken, “Oxygen octahedra picker: A software tool to extract quantitative information from STEM images,” *Ultramicroscopy*, vol. 168, pp. 46–52, 2016.

[274] S. Macke, A. Radi, J. E. Hamann-Borrero, A. Verna, M. Bluschke, S. Brück, E. Goering, R. Sutarto, F. He, G. Cristiani, M. Wu, E. Benckiser, H. U. Habermeier, G. Logvenov, N. Gauquelin, G. A. Botton, A. P. Kajdos, S. Stemmer, G. A. Sawatzky, M. W. Haverkort, B. Keimer, and V. Hinkov, “Element specific monolayer depth profiling,” *Advanced materials (Deerfield Beach, Fla.)*, vol. 26, no. 38, pp. 6554–6559, 2014.

[275] J. M. Tonnerre, M. De Santis, S. Grenier, H. C. N. Tolentino, V. Langlais, E. Bontempi, M. García-Fernández, and U. Staub, “Depth Magnetization Profile of a Perpendicular Exchange Coupled System by Soft-X-Ray Resonant Magnetic Reflectivity,” *Physical Review Letters*, vol. 100, no. 15, p. 157202, 2008.

[276] H. Wadati, D. G. Hawthorn, J. Geck, and G. A. Sawatzky, “Resonant soft X-ray scattering studies of interface reconstructions in SrTiO3/LaAlO3 superlattices,” *Journal of Applied Physics*, vol. 106, 2009.

[277] C. Chantler, “Theoretical Form Factor, Attenuation and Scattering Tabulation for Z=1-92 from E=1-10 eV to E=0.4-1.0 MeV,” *Journal of Physical and Chemical Reference Data*, vol. 24, p. 71, 1995.

[278] V. Scagnoli, U. Staub, M. Janousch, A. M. Mulders, M. Shi, G. I. Meijer, S. Rosenkranz, S. B. Wilkins, L. Paolasini, J. Karpinski, S. M. Kazakov, and S. W. Lovesey, “Charge disproportionation and search for orbital ordering in NdNiO3 by use of resonant x-ray diffraction,” *Physical Review B*, vol. 72, no. 15, pp. 1–7, 2005.

[279] C. Piamonteze, F. M. F. De Groot, H. C. N. Tolentino, A. Y. Ramos, N. E. Massa, J. A. Alonso, and M. J. Martínez-Lope, “Spin-orbit-induced mixed-spin ground state in RNiO3 perovskites probed by x-ray absorption spectroscopy: Insight into the metal-to-insulator transition,” *Physical Review B*, vol. 71, no. 2, pp. 2–5, 2005.

[280] J. W. Freeland, M. Van Veenendaal, and J. Chakhalian, “Evolution of electronic structure across the rare-earth RNiO3 series,” *Journal of Electron Spectroscopy and Related Phenomena*, vol. 208, pp. 56–62, 2016.

[281] Y. Bodenthin, U. Staub, C. Piamonteze, M. García-Fernández, M. J. Martínez-Lope, and J. A. Alonso, “Magnetic and electronic properties of RNiO3 (R = Pr, Nd, Eu, Ho and Y) perovskites studied by resonant soft x-ray magnetic powder diffraction,” *Journal of Physics: Condensed Matter*, vol. 23, no. 3, p. 036002, 2011.

[282] B. Li, D. Louca, S. Yano, L. G. Marshall, J. Zhou, and J. B. Goodenough, "Insulating Pockets in Metallic LaNiO3," *Advanced Electronic Materials*, p. 1500261, 2015.

[283] R. J. Green, "private communication," 2016.

[284] G. Kresse, "From ultrasoft pseudopotentials to the projector augmented-wave method," *Physical Review B*, vol. 59, no. 3, pp. 1758–1775, 1999.

[285] J. P. Perdew, K. Burke, and M. Ernzerhof, "Generalized Gradient Approximation Made Simple," *Physical Review Letters*, vol. 77, no. 18, pp. 3865–3868, 1996.

[286] T. Kimura, S. Ishihara, H. Shintani, T. Arima, K. T. Takahashi, K. Ishizaka, and Y. Tokura, "Distorted perovskite with eg1 configuration as a frustrated spin system," *Physical Review B*, vol. 68, no. 06, p. 060403(R), 2003.

[287] "CrysTec Data-Sheets, http://www.crystec.de/datasheets-e.html," 2016.

List of publications

Published

1. M. Hepting, M. Minola, A. Frano, G. Cristiani, G. Logvenov, E. Schierle, M. Wu, M. Bluschke, E. Weschke, H.-U. Habermeier, E. Benckiser, M. Le Tacon, and B. Keimer. "Tunable Charge and Spin Order in $PrNiO_3$ Thin Films and Superlattices." Phys. Rev. Lett **113**, 227206 (2014), *Editors' Suggestion.*

2. M. Hepting, D. Kukuruznyak, E. Benckiser, M. Le Tacon, and B. Keimer. "Raman light scattering on ultra-thin films of $LaNiO_3$ under compressive strain." Physica B **460**, 196 (2015).

3. Y. Lu, A. Frano, M. Bluschke, M. Hepting, S. Macke, J. Strempfer, P. Wochner, G. Cristiani, G. Logvenov, H.-U. Habermeier, M. W. Haverkort, B. Keimer, and E. Benckiser. "Quantitative determination of bond order and lattice distortions in nickel oxide heterostructures by resonant x-ray scattering" Phys. Rev. B **93**, 165121 (2016).

Unpublished

1. M. Hepting, R. J. Green, Z. Zhong, M. Bluschke, Y. E. Suyolcu, S. Macke, A. Frano, S. Catalano, M. Gibert, R. Sutarto, F. He, G. Cristiani, G. Logvenov, Y. Wang, P. A. van Aken, P. Hansmann, M. Le Tacon, J.-M. Triscone, G. A. Sawatzky, B. Keimer, E. Benckiser. "Complex magnetic order in nickelate slabs." *manuscript under review for publication*

Acknowledgements

This PhD thesis would not have been possible without the help and support of many people. Let me thank you in the following.

First and foremost I would like to express my deepest gratitude to Prof. Bernhard Keimer for the chance to carry out my PhD thesis in his group at the Max Planck Institute. The work environment and his support gave me valuable chances to visit international summer schools and conferences and develop myself further, in scientific and in personal aspects. One highlight of my PhD certainly was the three-month visit at UBC Vancouver. I am very grateful that I had this opportunity.

I sincerely thank Prof. Mathieu Le Tacon and Dr. Eva Benckiser for their day-to-day supervision. Mathieu introduced me to Raman spectroscopy and I profited a lot from his knowledge about the technique and physics in general. From Eva I learned so many things about the nickelates and she was giving me guidance and advise for the x-ray diffraction experiments and data analysis. Many thanks to both of you for your patience, trust, and fantastic support.

Special thanks to Prof. George A. Sawatzky for welcoming me in his group at UBC Vancouver. It was a great opportunity for me and I enjoyed the weekly group meetings which were more like a precious lecture on condensed matter physics and chemistry, providing unique insights into a variety of topics. Also I'd like to thank Dr. Robert Green. It was a pleasure to work with you at UBC and at CLS. I am hoping for many more collaborations in the future. I had a great time in Canada!

At MPI Stuttgart I particularly thank my office mate Christopher Dietl. You became a dear friend of mine! Your programming skills and the helpful discussions on physics have decreased the total duration of my PhD significantly! Also I am grateful that you have joined countless ANKA beam times. This similarly applies to Friederike Wrobel. It was great to have your support on beam times and at the institute. Also, it is a pleasure to look back on all of the summer schools and conferences where I have been with Christopher and/or Friederike. Do you remember Zuoz, Dresden, Cargese, Grenoble, Geneva, San Antonio, Nijmegen? Credits go to Martin Bluschke for joining the CLS beam times and for many fruitful discussions in Stuttgart. It was always entertaining to work with you or when you showed me around in Neukölln at night. With Stuttgart nightlife I rather associate Timofei Larkin. However, I am glad you have settled down now and I wish you and your family all the best for the future. Thanks to Sebastian Macke for his support in Vancouver and in Stuttgart. You are incredibly talented in computer science and programming! In the last phase of my PhD I was lucky to work with Eren Y. Suyolcu who performed STEM investigations on my samples. You've done a great job! But even more I appreciate you for being a good friend of mine. I'd like to thank Alex Frano for meeting me in Berkely and Aliaksei Charnukha for meeting me in San Diego. Michaela Souliou, you were a great coach of our soccer team! I acknowledge the many insightful discussion with 'Prof.' Yi Lu. With Matteo Minola I enjoyed working together on the thin film Raman measurements. Moreover, many thanks for useful advices during the last months! I'd like to thank Marc Höppner for the phonon calculations. I am sure you will have a great future in Copenhagen. My special thanks go to Georg Cristiani. Without your excellent samples none of our experiments would not have been possible! Unfortunately, Alireza Akbari is not in the Keimer group any more. When will you visit next time so we can go to the Persian restaurant again? To my office mates Jorge Sauceda and Gideok Kim I'd like to say it was great to have you around!

Many thanks also to all other current and former members of the Keimer group: Daniel Pröpper, Juan Porras, Joel Bertinshaw, Meng Wu, Hun-ho Kim, Toshinao Loew, Katrin Fürsich (in particular for reading the German summary), Maximilian Krautloher, Daniel Putzky, Nakheon Sung, B.J. Kim, Hlynur Gretarsson, Padma Radhakrishnan, Alexander Boris, Giniyat Khalliulin, George Jackeli, Alexander Yaresko, Santi Blanco-Canosa, Gert Friemel, Sungkyun Choi, Hakuto Suzuki, Kentaro Ueda, Robert Dawson, Roberto Ortiz, Namrata Gung, Luqman Mustafa, Nadir Driza, Martin Rahlenbeck, Darren Peets, Giorgi Ghambashidze, Ayman Akil, and Youngje Um. Furthermore, I'd like to thank Stephan Heinze for supporting me with the thermoelectricity measurements I did in the beginning of my PhD. In the same way, I'd like to thank Gennady Logvenov, Hanns-Ulrich Habermeier, Petar Yordanov, and the rest of the technology group. Special thanks go to my external supervisor Jone Zabaleta. For the first-principles calculations I thank Zhicheng Zhong and Philipp Hansmann. Furthermore, I would like to thank the Geneva group of Jean-Marc Triscone and in particular Sara Catalano for the successful collaboration and sample exchange.

Many thanks to the technicians, especially Manfred Ohl who always gave friendly and helpful advice, to Benjamin Bruha, Heiko Uhlig, and Michael Schulz. I'd like to thank Armin Schulz for his assistance and support for the Raman setups. Also, I offer many thanks to our secretary Sonja Balkema.

I greatly appreciated the support during various synchrotron beam times. In particular Peter Wochner shared his valuable knowledge and expertise at ANKA and at MPI. Also Shyjumon Ibrahimkutty supported our ANKA experiments. At BESSY II Enrico Schierle and Eugen Weschke were of great help. At CLS it was my pleasure to work with Ronny Sutarto and Feizhou He. However, I still haven't had a BBQ in Saskatoon yet! I hope I will not miss it again next time I'll be there.

Let me also mention some of the most pleasant colleagues I met during my PhD, many of them even became friends of mine. I very much enjoyed my coffee and tea breaks with Pinar and all the other occasions when we had the chance to spend time together. Also I remember our great team of former PhD representatives: Marcel, Matthias M., Umut, Ekin, and Ingrid. At some times working on the PhD was tough, but luckily Tanja provided me with croissants and coffee when I needed it the most. Chrissy unfortunately left MPI, but still we had plenty of fun moments. It also was a great pleasure to meet Katalin, Luca, Daniil, Dennis, Raquel, Vincent, Daniel, Katha, Mostafa, Avaise, Luzia, Nikolaj, Andrew, and of course the Canadians Arash, Eprahim, and Kathleen. Thank you for an amazing time! Last but not least let me thank Andres for being a great friend to me since so many years!

Finally, I express my deepest gratitude to my parents Christine and Josef, to my brother Steffen and to the rest of my family. Thank you for the trust in me from my first day of study until the last day of my thesis.